Mechanical Behavior and Radiation Effects
2019 Principal Investigators' Meeting

August 13-15, 2019
Washingtonian Marriott, Gaithersburg, MD

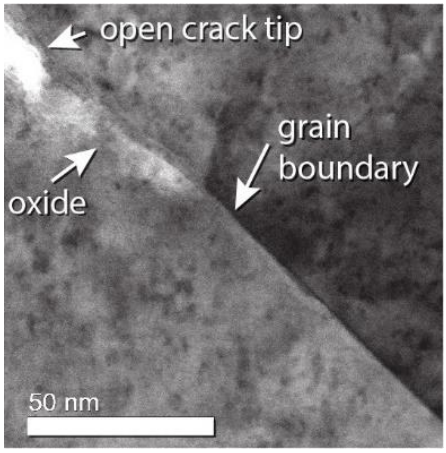

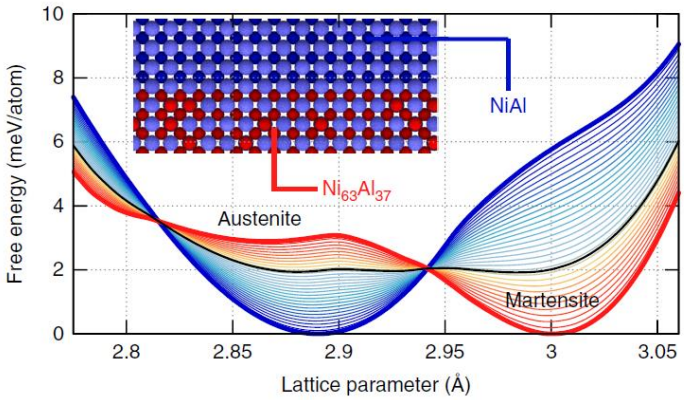

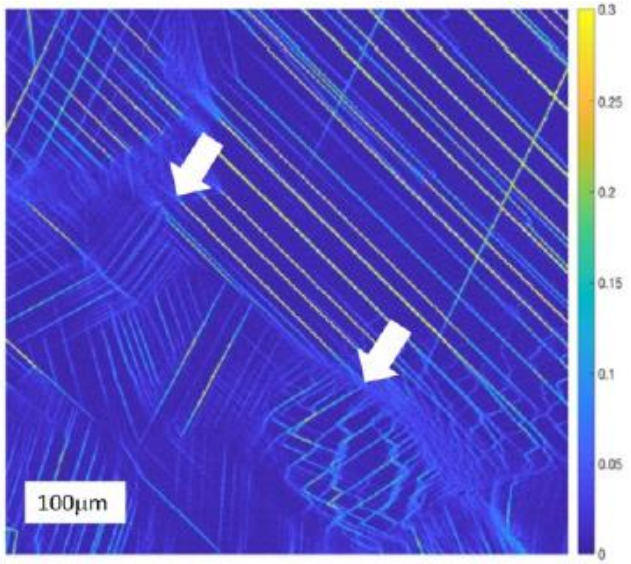

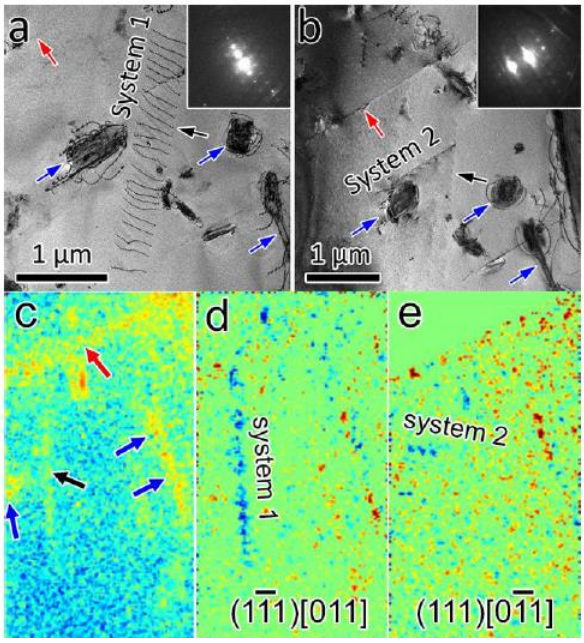

U.S. DEPARTMENT OF ENERGY | Office of Science

Materials Sciences and Engineering Division
Office of Basic Energy Sciences

Cover

Top Left: TEM of a crack tip following corrosion of a Ni-4Al alloy in high-T water. Subsequent EDS analysis reveals selective oxidation of Al and concomitant depletion of Al from the local grain boundary (Bruemmer et al, PNNL)

Top Right: Free energy as a function of in-plane lattice parameter from MD simulations of bulk $Ni_{63}Al_{37}$ and NiAl, interpolated with rule of mixtures. The combination of 65 at% $Ni_{63}Al_{37}$ (thick red) and 35 at% NiAl (thick blue) is highlighted in black to show the possibility of ultra-low stiffness. The inset (above) shows the schematic of the epitaxial interface between these two phases where Al atoms are light blue, Ni in NiAl is dark blue, and Ni in $Ni_{63}Al_{37}$ is red. (Strachan et al, Purdue)

Bottom Left: A map of maximum shear in a deformed RR1000 Ni-based alloy. Analysis indicates a strain gradient from the middle area of the grain towards the grain boundaries at each end of the slip band (between the two arrows). This is used to calculate dislocation spacing and resultant backstress on the dislocation closest to the boundary. (Fullwood and Homer, BYU and Wagoner, OSU)

Bottom Right: Comparison between EBSD and TEM-based dislocation characterization. A-B) TEM bright field images of two dislocation systems (marked by black arrows) near a twin boundary (marked by red arrow). C) Log scale GND map of same region, colored arrows indicate same locations as are shown in (a-b). Legend is 10^{13} to 10^{15} m^{-2}. D-E) Log scale GND density resolved onto different slip systems showing System 1 and System 2 with system labeled in each figure. Dislocation systems appear as blue.

This document was produced under contract number DE-SC0014664 between the U.S. Department of Energy and Oak Ridge Associated Universities.

The research grants and contracts described in this document are supported by the U.S. DOE Office of Science, Office of Basic Energy Sciences, Materials Sciences and Engineering Division.

Foreword

This volume comprises the scientific content of the 2019 Mechanical Behavior and Radiation Effects Principal Investigators' (PI) Meeting sponsored by the Materials Sciences and Engineering Division in the Office of Basic Energy Sciences (BES) of the U. S. Department of Energy. The meeting, held on August 13–15, 2019, at the Marriott Washingtonian, Gaithersburg, Maryland, is the seventh such meeting on this topic and is one among a series of research theme-based PI meetings being held by BES. The meeting's focus is on research in mechanical behavior and radiation effects of materials, and it also features research that cuts across several other BES core research program areas and Energy Frontier Research Centers where appropriate and relevant.

The studies of mechanical behavior and radiation effects have a long and important history with respect to the generation, transmission, utilization and conservation of energy. It is a tribute to the researchers that they have continued to move the field forward into a number of important areas, as can be seen by the diversity of projects being presented at this meeting. Attendees will note a number of new projects and research directions since the previous meeting including three new recipients of Early Career Research Program awards. These new projects add to the exciting areas of research and cutting-edge techniques that are a hallmark of this program.

The purpose of the Mechanical Behavior and Radiation Effects PI Meeting is to bring together researchers funded by BES in this important area of research on a periodic basis (approximately every two years) in order to facilitate the exchange of new results and research highlights, to nucleate new ideas and collaborations among the participants, and to identify needs of the research community. The meeting will also help DMS&E in assessing the state of the program, identifying new research directions and recognizing programmatic needs.

I would like to thank all of the attendees for their active participation and for sharing their ideas and new research results. I would also like to express my sincere gratitude to Ms Teresa Crockett in DMS&E, and Ms Linda Severs (plus others) of the Oak Ridge Institute for Science and Education (ORISE) for their dedicated and outstanding work in taking care of all the logistical aspects of the meeting. Additionally, I would like to thank Professor Irene Beyerlein for helping make this a better meeting through her comments and suggestions as it was being organized.

John Vetrano
Program Manager
Mechanical Behavior and Radiation Effects
Division of Materials Sciences and Engineering
Office of Basic Energy Sciences
U.S. Department of Energy

Table of Contents

Mechanical Behavior and Radiation Effects
Principal Investigators' Meeting Agenda

Tuesday, August 13, 2019

7:30 – 8:30 am	**Breakfast**
8:40 – 8:50 am	*Welcome from Meeting Chair* **Irene Beyerlein**
8:50 – 9:10 am	*Introductory Remarks and Program Overview* **John Vetrano**
Session I	Chair: **Kevin Hemker –** Johns Hopkins
9:10 – 9:30 am	**Krystyn Van Vliet – MIT** *Chemomechanics of Far-From-Equilibrium Interfaces (COFFEI)*
9:30 – 9:50 am	**Elisa Riedo – NYU** *NanoMechanics: Elasticity and Friction in Nano-Objects*
9:50 – 10:10 am	#**Frederic Sansoz – Vermont** *Role of Heterogeneous Segregation on Shear Localization Mechanisms in Nanocrystalline Alloys*
10:10 – 10:40 am	**Coffee Break**
Session II	Chair: **Maryam Ghazisaeidi –** Ohio State
10:40 – 11:00 am	#**John Balk – Kentucky** *Discovery, Design, Synthesis and Testing of High Performance Structural Alloys*
11:00 – 11:20 am	**Easo George – ORNL** *Multiscale Mechanical Properties and Alloy Design*
11:20 – 11:40 am	**Katerina Aifantis – Florida** *The Role of Grain Boundary Structure and Chemistry in Materials*
11:40 – 1:30 pm	**Working Lunch** **- Poster Introductions (Vetrano)** **- Linda Horton,** BES-DMSE Director *Overview of BES Materials Sciences Division*
Poster Session I	
1:30 – 3:30 pm	**Posters/Discussions**

Session III Chair: **Mohsen Asle Zaeem** – Colorado School of Mines

3:30 – 3:50 pm **Bill Weber – ORNL**
Electronic and Atomic Response of Ceramic Structures to Irradiation

3:50 – 4:10 pm ***Jessica Krogstad – UIUC**
Dynamic, Robust, Radiation-Resistant Ceramics: Harnessing Thermodynamic and Kinetic Driving Forces

4:10 – 4:30 pm [#]**Brian Sheldon – Brown**
Toughening Mechanisms in Ceramic Nanocomposites with One and Two Dimensional Reinforcements

4:30 – 4:50 pm **Izabela Szlufarska – Wisconsin**
Coupled Effects of Radiation and Chemical Environment on Interfaces in SiC

4:50 – 5:10 pm **Reiner Dauskardt – Stanford**
Mechanical Behavior of Hybrids with Hyper-Connected Molecular Networks

5:30 – 7:30 pm **Working Dinner – Programmatic Discussions**

*Early Career
[#]New since last meeting

Wednesday August 14, 2019

7:30 – 8:30 am	**Breakfast**
Session IV	Chair: **Sean Agnew** – Virginia
8:40 – 9:00 am	**Lin Li – Alabama** *Multiscale Modeling of Shear Banding in Metallic Glasses*
9:00 – 9:20 am	**Laurent Capolungo – LANL** *Multi-Scale Study of the Role of Microstructure in the Deformation Behavior of Hexagonal Materials*
9:20 – 9:40 am	#***Haixuan Xu – Tennessee** *Mesoscale Defect Interaction Mechanisms in Structural Alloys*
9:40 – 10:00 am	**Rob Ritchie – LBNL** *Damage-Tolerance in Structural Materials*
10:00 – 10:30 am	**Coffee Break**
Session V	Chair: **Lin Shao** – Texas A&M
10:30 – 10:50 am	**Jian Gan – INL** *The Role of Anisotropy on the Self-Organization of Gas Bubble Superlattices*
10:50 – 11:10 am	#**Pascal Bellon – UIUC** *Global Aspects of Microstructural Evolution in Irradiated Alloys: Effects of Self-Organization*
11:10 – 11:30 am	#***Assel Aitkaliyeva – Florida** *Establishing Defect-Property Relationships for 2D-Nanomaterials*
11:30 – 12:00 am	**Panel Discussion: Examples of Lab-University Collaborations** Brad Boyce, Dan Schrieber, Jessica Krogstad and Tony Rollett
12:00 – 1:30 pm	**Working Lunch and Poster Introductions (Beyerlein)**
Poster Session II	
1:30 – 3:30 pm	**Posters and Discussion**
Session VI	Chair: **Qizhen Li** – Washington State
3:30 – 3:50 pm	**Amit Misra – Michigan** *Plasticity of High-Strength Multiphase Metallic Composites*
3:50– 4:10 pm	**Chris Schuh – MIT** *Microparticle Supersonic Impact: A Testbed for the Exploration of Metals under Extreme Conditions*

4:10 – 4:30 pm ***Josh Kacher – Georgia Tech**
Fundamental Study of Fatigue Crack Initiation at Grain Boundaries in Austenitic Stainless Steel

4:30 – 4:50 pm **Brad Boyce – SNL**
Nanomechanics and Nanometallurgy of Boundaries

4:50 – 5:10 pm ***Tim Rupert – UC Irvine**
Doping Metallic Grain Boundaries to Control Atomic Structure and Damage Tolerance

5:30 – 7:30 pm **Working Dinner – Collaboration Discussions**

Thursday August 15, 2019

7:30am – 8:20am	**Breakfast**
Session VII	Chair: **Wei Cai** - Stanford
8:20 –8:40 am	**David Fullwood – BYU** *Fundamental Mechanisms Controlling Dislocation-Obstacle Interactions in Metals and Alloys*
8:40 – 9:00 am	**Anter El-Azab – Purdue** *Dislocation in Patterning in Deforming Crystals: Theory, Computational Predictions, and Validation*
9:00 – 9:20 am	**Karl Sieradzki – ASU** *Dynamic Fracture in Dealloying Induced Stress Corrosion Cracking*
9:20 – 9:40 am	**Diana Farkas – Virginia Tech** (Gary Was) *Localized Deformation and Intergranular Fracture of Irradiated Alloys under Extreme Environmental Conditions*
9:40 – 10:00 am	**Dan Schreiber – PNNL** (Steve Bruemmer) *Crack-Tip Mechanisms Driving Environmental Degradation*
10:00am – 10:20am	**Break**
Session VIII	Chair: **Seok-Woo Lee** - Connecticut
10:20 – 10:40am	**Blas Uberuaga – LANL** *Disorder and Diffusion in Complex Oxides: Towards Prediction and Control*
10:40 – 11:00am	**Peter Anderson – Ohio State** (Mike Mills) *Taming Martensitic Transformations by Defect Engineering*
11:00 – 11:20 am	**Philip Eisenlohr – Michigan State** (Carl Boehlert) *Characterization and Modeling of Deformation Induced Damage in Hexagonal Metals*
11:20 – 11:40 pm	**John Allison – Michigan** *Software Center for Predictive Theory and Modeling*
11:40 pm	**Closing Remarks by John Vetrano**

Mechanical Behavior and Radiation Effects Principal Investigators' Meeting

POSTER SESSION I
Tuesday, August 13, 2019

1) #**Understanding Multiscale Defect Formation Process and Phase-Switching Behavior in Shape Memory Functional Oxides**
Mohsen Asle Zaeem, Colorado School of Mines

2) #**Global Aspects of Microstructural Evolution in Irradiated Alloys: Effects of Self-Organization**
Qun Li and Pascal Bellon, University of Illinois, Urbana-Champaign

3) #**The Role of Subgrain Heterogeneous Processes in Slip Localization in Polycrystalline Metals During Cyclic Plasticity**
Kelly Nygren and Irene Beyerlein, University of California, Santa Barbara

4) **Nanomechanics and Nanometallurgy of Boundaries**
Remi Dingreville and Brad Boyce, Sandia National Laboratories

5) #**Effect of Gradient Architectures on the Strength, Deformation and Failure of Nanoglasses**
Paulo Branicio, University of Southern California

6) **Data Driven Approach to Dislocation-Based Plasticity Models of Face-Centered Cubic Metals**
Wei Cai, Stanford University

7) #**Improving Radiation Response of Solid-State Interfaces via Control of Curvature**
Kelvin Xie and Michael Demkowicz, Texas A&M University

8) **WastePD (EFRC)**
Seong Kim and Jerry Frankel, Ohio State University

9) **The Role of Anisotropy on the Self-Organization of Gas Bubble Superlattices**
Yiping Gao and Jian Gan, Idaho National Laboratory

10) **Atomic Scale Computational and Experimental Investigation of Twinning Mechanisms in HCP Systems**
Maryam Ghazisaeidi, The Ohio State University

11) **Computational and Experimental Investigation of Cryogenic Grain Boundary Motion for Enhanced Mechanical Properties**
Greg Thompson and Eric Homer, Brigham Young University

12) #**Mechanical Properties of Metals at The Micrometer Scale in Different Environments**
Seok-Woo Lee, University of Connecticut

13) **Radiation Response of Low Dimensional Carbon Systems**
Lin Shao, Texas A&M University

14) [#]**Toughening Mechanisms in Ceramic Nanocomposites with One and Two Dimensional Reinforcements**
Jun Lou and Brian Sheldon, Brown University

15) **Role of nanoscale coherent precipitates on the thermo-mechanical response of martensitic materials**
Alejandro Strachan, Purdue University

16) **Chemomechanics of Far-From-Equilibrium Interfaces (COFFEI)**
Ten-Ting Chi and Krystyn Van Vliet, Massachusetts Institute of Technology

17) **Electronic and Atomic Response of Ceramic Structures to Irradiation**
William Weber, Oak Ridge National Laboratory

18) ***[#]Irradiation Tailoring of Deformation-Induced Phase Transformation**
Janelle Wharry, Purdue University

19) **EDDE (EFRC)**
Yanwen Zhang, Oak Ridge National Laboratory

[#]New since last meeting
***Early Career**

Mechanical Behavior and Radiation Effects Principal Investigators' Meeting

POSTER SESSION II
Wednesday, August 14, 2019

1) #**Solute Effects on Dislocation Motion and Recovery in Mg Alloys**
Sean Agnew, University of Virginia

2) **Software Center for Predictive Theory and Modeling**
Lian Qi and John Allison, University of Michigan

3) #**Quantifying the Role of APB Tubes on the Work-hardening of Ordered Phases**
Ian Baker, Dartmouth

4) #**The Role of Subgrain Heterogeneous Processes in Slip Localization in Polycrystalline Metals During Cyclic Plasticity**
Matt Miller, Cornell and Irene Beyerlein, UCSB

5) **Characterization and Modeling of Deformation Induced Damage in Hexagonal Metals**
Songyang Han and Carl Boehlert, Michigan State University

6) **Crack-Tip Mechanisms Driving Environmental Degradation**
Kevin Rosso, Dan Schreiber and Stephen Bruemmer, Pacific Northwest National Lab

7) **Multi-Scale Study of the Role of Microstructure in the Deformation Behavior of Hexagonal Materials**
Arul Kumar and Laurent Capolungo

8) **Multiscale Mechanical Properties and Alloy Design**
Ying Yang and Easo George, Oak Ridge National Laboratory

9) **A Fundamental Study on the Link between Mechanical Properties and Atomic-level Microstructure in Nano-sized Metallic Glasses**
Anthony Kwong and Julia Greer, California Institute of Technology

10) **Understanding extreme strength and plasticity in nanotwinned NiMoW alloys**
Kevin Hemker, Johns Hopkins University

11) **TETI (EFRC)**
Janelle Wharry, Purdue and David Hurley, Idaho National Laboratory

12) **Low Temperature Cyclic Deformation Behavior of Ultrafine-grained Pure Magnesium**
Qizhen Li, Washington State University

13) **Plasticity of High-Strength Multiphase Metallic Composites**
Jian Wang, University of Nebraska-Lincoln and Amit Misra, University of Michigan

14) #**Fundamental Investigation of Grain Boundary Dislocation Mechanisms in Ultrafine Grained Metallic Films**
Olivier Pierron, Georgia Institute of Technology

15) **Damage-Tolerance of Structural Materials**
Jun Ding and Rob Ritchie, Lawrence Berkeley National Laboratory

16) #**Probing Fundamental Mechanisms of Plastic Deformation with High Energy X-rays**
Tony Rollett, Carnegie Mellon University

17) **Correlating Structure, Local Atomic Dynamics, and Composition to Reveal the Origin of Fracture Toughness in Metallic Glasses**
Sebastian Kube and Jan Schroers, Yale University

18) #**Grain Boundary Microstates: Exploring the Metastability of Sink Efficiency**
Mitra Taheri, Johns Hopkins University

19) **FUTURE (EFRC)**
Blas Uberuaga, Los Alamos National Laboratory

20) **Disorder and Diffusion in Complex Oxides: Towards Prediction and Control**
Cortney Kreller and Blas Uberuaga, Los Alamos National Laboratory

21) **Fundamental Mechanisms Controlling Dislocation-Obstacle Interactions in Metals and Alloys**
Robert Wagoner, The Ohio State University and David Fullwood and Eric Homer, BYU

22) **Deformation Mechanisms of Nanotwinned Al and Al Alloys**
Xinghang Zhang, Purdue University

#New since last meeting
***Early Career

Abstracts

Solute effects on dislocation motion and recovery in Mg alloys

Sean R. Agnew, Dept. of Materials Science and Engineering, University of Virginia

Program Scope

One of the greatest obstacles to broader application of wrought Mg alloys, for energy-efficient transportation and defense systems, is their poor low temperature formability, which is linked to strong plastic anisotropy of the hexagonal close packed (HCP) crystal structure. The most successful avenue to directly combat this Achilles heel is solid solution alloying. Unlike many other metals, where the pure material is more ductile than its alloys, there are many Mg alloys, which boast much higher ductility than pure Mg polycrystals. Solute are known to have a distinct impact upon the strength of the individual slip and twinning modes. The objective of the proposed research is to develop a firmer understanding of the interactions between substitutional solute atoms and dislocations within Mg alloys. A series of hypotheses, which have been advanced to explain the phenomena of solute hardening, softening, dynamic strain aging and associated effects on dislocation structure evolution, will be examined.

Recent Progress

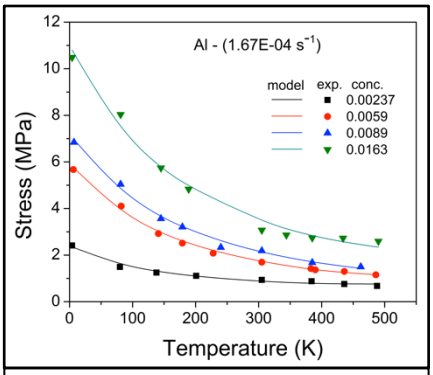

Critical resolved shear stress data of Mg-Al solid solution single crystals reproduced from ref. [2] and modeled per modern thermally activated slip theory.

Historic single crystal [e.g., 1, 2] and polycrystal [3] data has been reanalyzed through the lens of modern theories of thermally activated plasticity. Many aspects which confused previous generations of researchers are now clarified, yet outstanding gaps in our understanding are highlighted. For example, an explanation is proposed for the observed athermal plateau in crystals oriented for basal slip in terms of the solute concentration-dependent, grown-in forest dislocation density. On the other hand, the strong solute softening behavior exhibited by single crystals oriented for prismatic slip at low temperature [4] remains only qualitatively understood [5], despite very active research on the part of atomistic modelers [6]. It is hypothesized that this may be associated with a distinction in the cross-slip mechanism which is observed at low temperatures, where the softening mechanism is most obvious, and the higher temperatures upon which recent modelers focused, perhaps due to a practical interest in the potential to describe the warm forming behavior of Mg alloys.

Numerous dilute Mg-Ca and Mg-Sn binary and Mg-Ca-Zn ternary alloys have been obtained from unfunded collaborator, Prof. Michele V. Manuel (University of Florida), and the samples have been heat treated and machined into small mechanical test specimens designed for testing at cryogenic temperatures. Finally, a liquid nitrogen cooled 671 Cryo Straining Holder straining holder was purchased from Gatan for use in the FEI Titan at the University of Virginia.

Future Plans

Textured, polycrystalline samples are planned for many of the explorations of pure Mg and solid solution alloy behavior. Polycrystal plasticity modeling will be used to assist in developing slip system-level behavior from these polycrystal tests. The alloys from the University of Florida and other commercial alloys will be subjected to repeated load relaxation tests, in order to obtain true activation volumes over a range of temperatures, including cryogenic temperatures at which solute softening has previously been reported. These experiments will determine if Ca and Sn induce solute softening, as was previously observed for other solute including Zn [4] and Li [7]. In-situ straining experiments are designed to determine if there is a transition in the cross-glide control from double-kink (or jog) pairs to constricted bowing. Finally, care will be taken to examine possible strain hardening and recovery mechanisms such as dislocation junction formation and dipole annihilation, as a function of alloy content.

References

[1] Conrad, H., Hays, L., Schoeck, G., & Wiedersich, H. (1961). On the rate-controlling mechanism for plastic flow of Mg crystals at low temperatures. *Acta Metallurgica*, *9*(4), 367-378.

[2] Akhtar, A., & Teghtsoonian, E. (1969). Solid solution strengthening of magnesium single crystals—I alloying behaviour in basal slip. *Acta Metallurgica*, *17*(11), 1339-1349.

[3] Sastry, D. H., Prasad, Y. V. R. K., & Vasu, K. I. (1970). The rate-controlling dislocation mechanism for plastic flow in polycrystalline magnesium. *Current Science*, 97-100.

[4] Akhtar, A., and E. Teghtsoonian. "Solid solution strengthening of magnesium single crystals—ii the effect of solute on the ease of prismatic slip." *Acta Metallurgica* 17.11 (1969): 1351-1356.

[5] Sato, A., & Meshii, M. (1973). Solid solution softening and solid solution hardening. *Acta Metallurgica*, *21*(6), 753-768.

[6] Yasi, J. A., Hector Jr, L. G., & Trinkle, D. R. (2012). Prediction of thermal cross-slip stress in magnesium alloys from a geometric interaction model. *Acta Materialia*, *60*(5), 2350-2358.

[7] Urakami, A., & Fine, M. E. (1972). Solid solution softening by double kink catalysis. *Mechanical Behavior of Materials, ed. S. Taira and M. Kunugi (Kyoto, 1971)*, 87-96.

Publications

None to date.

The Role of Grain Boundary Structure and Chemistry in Materials

Katerina E. Aifantis
Associate Professor and Faculty Fellow
Mechanical and Aerospace Engineering, University of Florida

Program Scope

This project builds on the hypothesis that the presence of grain boundaries during deformation can be captured by mechanically induced interface energies (Φ_{gb}). Φ_{gb} depends on the plastic strain at the grain boundary (GB) and is therefore a measure of the energy change that the grain boundary undergoes during plastic deformation, rather than the thermodynamics (or static) energy (γ_{gb}) that is commonly used to characterize GBs. Although the materials science community has not explicitly introduced such mechanically induced GB energy terms, their existence can be alluded to by *in situ* transmission electron microscopy (TEM) studies that examine dislocation-grain boundary interactions [1-3] and capture dislocation absorption/emission/transmission. Molecular dynamics simulations have also recognized that γ_{gb} on its own cannot characterize the GB strength, and the concept of an energy barrier [4] was introduced, which however, cannot capture continuous GB deformation, but only the first slip.

Φ_{gb} can be incorporated within the continuum theory of gradient plasticity, allowing the prediction of the critical stress at which GBs begin deforming plastically (GB yield stress/σ_{gb}). It is therefore possible to measure Φ_{gb} and understand its origin by performing experiments and simulations that can track defect-GB interactions and provide the strain state of the material.

Throughout this project molecular dynamics simulations are used to determine the values of Φ_{gb} for different types of GBs and chemistries, making it possible to tune the material response by selecting the segregant atoms and GB geometry. The simulations are tested against in situ TEM experiments on bicrystal nanospheres.

Recent Progress

As a first step to confirming the "existence" of Φ_{gb} nanoindentation experiments were used since it has been shown that indenting in close proximity to GBs allows for second pop-ins to be obtained in the load-displacement curve, which can be assumed to indicate slip transmission, i.e. GB yielding. A brief summary is provided below but detailed information can be found in our recent published paper [5]. By indenting near GBs of Fe-3wt% Si and performing scanning probe microscopy (SPM) it was possible to verify that indeed slip transmission was present when a secondary pop-in took place, as seen in Fig. 1.

From the load-displacement curves it is possible to obtain an approximation through Tabor's rule of the stress present during the second pop-in, which corresponds to the GB yield stress, σ_{gb}, which is predicted by gradient plasticity as

$$s_{gb} = (x_{gb} / 2l)\coth(d / l). \quad (1)$$

d is a fixed length during deformation, β is the hardening modulus, l is the internal length which is a parameter indicating a critical length scale, and ξ_{gb} is an interface parameter directly related with Φ_{gb}. Fitting Eq. (1) to the experimentally obtained points for σ_{gb} against the GB-indenter distance (d) showed that indeed introduction of mechanical energy terms is capable of capturing the resistance of GBs to deformation, since an excellent fit was obtained (Fig. 2). Comparing the

ξ_{gb} values for the various GBs examined did not indicate a correlation with misorientation, however, a dependence with the grain boundary plane was noted in [5], which is similar to the dependence of the thermodynamic grain boundary energy on misorientation and GB plane.

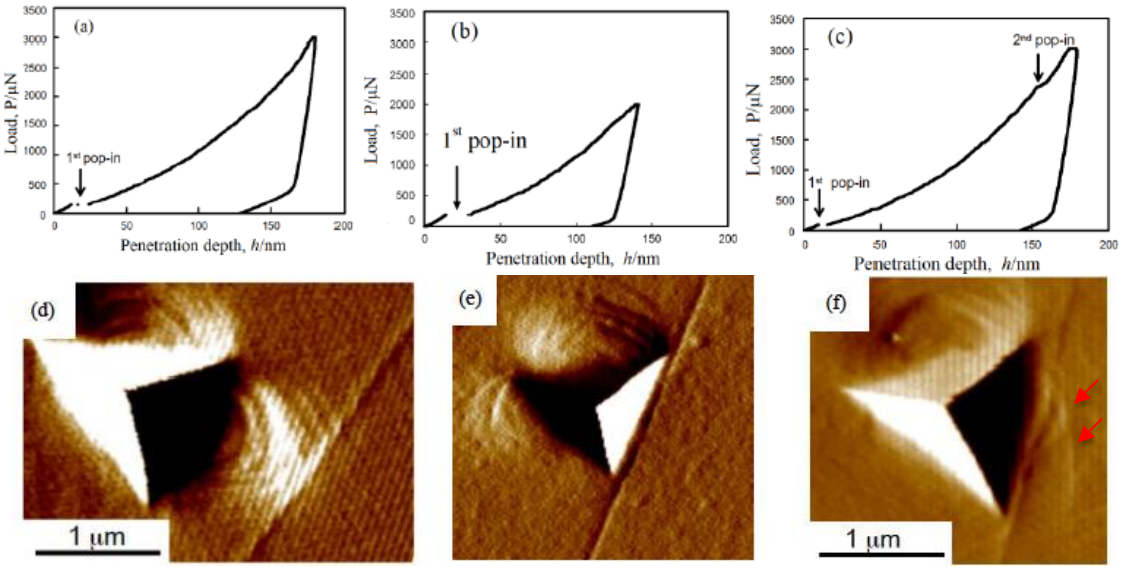

Fig. 1. Representative nanoindentation load-depth curves and SPM images obtained when the grain boundary had a 42.0°<100> misorientation: (a) indentation in the grain interior ; (b) indentation near the GB with the maximum load being 2 mN ; and (c) indentation near the GB with the maximum load being 3 mN ; (d) SPM image of indent in grain interior, taken after the curve shown in (a) ; (e) SPM image of surface after the indentation curve shown in (b) ; (f) SPM image of the surface after the indentation show in (c). It is seen that for the case that a second pop-in occurs slip is transmitted to the neighboring grain. Taken from [5]. Arrows indicate slip transmission.

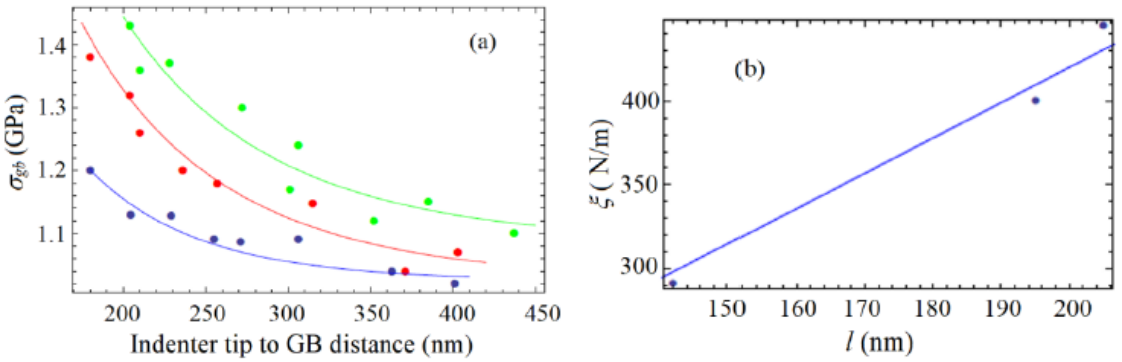

Fig. 2 (a) Fits of Eq. (1) to experimental data (dots) of the grain boundary yield stress in Fe-3wt%Si bicrystals. Each color indicates a different GB: green- 42°<110>,{120}A//{015}B, red- 22.5°<110>,{121}A//{211}B, blue- 44.6°<110>, {013}A//{323}B. (b) Plot of values obtained for ξ_{gb} and l; it is seen that a linear best fit is obtained. Taken from [5].

Although the results obtained for slip transmission through ex-situ indentation are promising, it is difficult to vary the segregation content. Therefore, molecular dynamics (MD) indentation was carried out for pure Fe or doped with either C or Si. Similarly as in the experiments distinct pop-ins in the load-displacement curves occurred during dislocation formation. The occurrence of such pop-ins was more common, however, due to the sensitivity of the simulations to individual defect formation. The simulations allowed for a clear observation of the stress at which the GBs began deforming plastically. For most of the systems considered, thus far,

significant dislocation absorption took place prior to transference and therefore σ_{gb} was computed at the onset plastic strain at the GB as seen in Fig. 3 (b). Comparing the simulation data with the analytical expression σ_{gb} (Eq. (1)) allowed to determine ξ_{gb} as 11.1 N/m for pure Fe, and 13.5 N/m for Fe-0.3wt%Si using the potential of [6] and 10.4 N/m for pure Fe, and 11.9 N/m for Fe-0.012wt%C using the potential of [7], indicating that the segregation of C and Si increase ξ_{gb}. The results shown in Fig. 3 are for a Σ5 GB, however, additional configurations have been considered with different GB planes and also higher segregation contents in order to capture the interplay between segregation and GB structure.

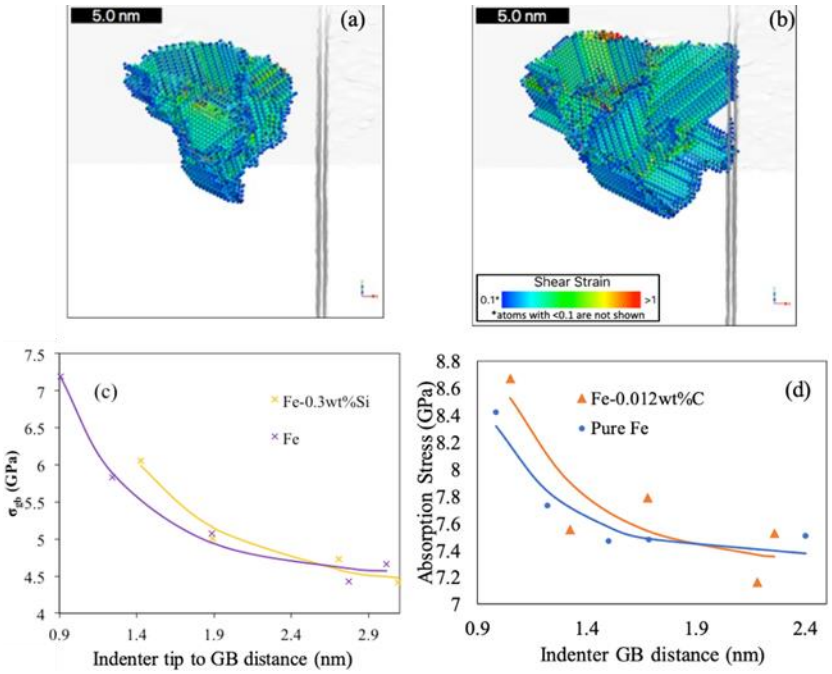

Fig. 3: (a)&(b) depict the strain field surrounding the indenter tip during indentation near a Σ5 symmetric tilt GB in BCC Fe. In (a) the GB has not yielded, while in (b) GB yielding occurs as strain develops. From (b) it is possible to deduce the GB yield stress. In (c)&(d) the simulation data (points) are compared with the theoretical predictions (solid lines), allowing to determine the value for the interface parameter ξ_{gb}. C and Si segregant atoms are added to the GBs, allowing to determine how segregation affects ξ_{gb}.

Figs 2&3 demonstrate the ability of mechanical interface terms to predict the GB yield stress, however, it is of interest to also capture the whole stress-strain response. MD simulations are therefore used to compress a bicrystal Fe containing either twist or asymmetric tilt GBs. Fig. 4 (a)&(b) depict the stress-strain curve, while Fig. 4 (c)&(d) the von Mises strain map. It can be seen that this response is reminiscent to a tri-linear curve, and can be divided into three stages as shown in Fig. 4(b). The first "knee" at a strain of ~2% corresponds to grain yielding which occurs by dislocation nucleation at the top corners and immediate slip towards the GB (Fig. 4c), while a second "knee" at a strain of ~4% occurs once deformation initiates at the lower grain, by dislocation emission at the GB. This second "knee" is indicative of GB yielding and was predicted by incorporating Φ_{gb} in gradient plasticity. Therefore, the previously obtained (through gradient plasticity) tri-linear stress-strain curves [8] are fitted (green lines) to the data as seen in Fig. 4(b), and allow the determination of ξ_{gb} and l.

Our results thus far indicate that consideration of a mechanical interface energy allows for analytical expressions that are in agreement with experimental and simulation data.

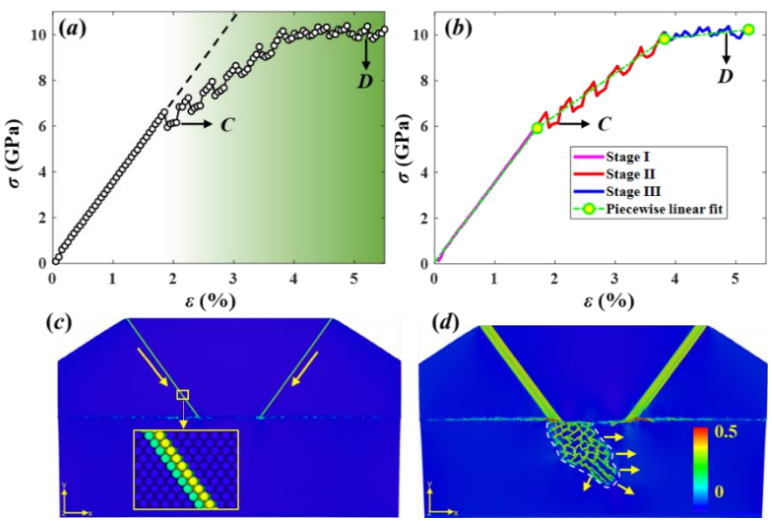

Fig. 4: (a) σ-ε curve obtained for simulation, (b) fit of gradient plasticity expressions to simulations data, (c)&(d) snapshots of von Mises atomic strain at points *C* and *D* in (b).

Future Plans

Currently data similar to that of Fig. 4 are being analyzed for different types of grain boundaries and repeated with the addition of P and H impurities in order to obtain a relationship between the ξ_{gb} and the grain boundary structure and segregant content. Once this is completed spherical nanoparticles will be examined under compression using both MD simulations and in situ TEM, in order to directly compare the values obtained for ξ_{gb} through simulations and experiments.

References

1. T. C. Lee, I. M. Robertson and H. K. Birnbaum, TEM in sity deformation study of the interaction of lattice dislocations with grain boundaries in metals, Philos. Mag. A 62, 131-153, 1990.
2. T. C. Lee, I. M. Robertson, H. K. Birnbaum, Interaction of dislocations with grain boundaries in Ni3Al, Acta metall. mater. 40, 2569-2579, 1992.
3. J. Kacher, I. M. Robertson. Philos. Mag. A 94, 814-829, 2014.
4. M. D. Sangid, T. Ezaz, H. Sehitoglu and I. M. Robertson, Energy of slip transmission and nucleation at grain boundaries, Acta Mater. 59, 283-296, 2011.
5. Aifantis K.E., Deng H., Shibata H., Tsurekawa S., Lejček P., Hackney S.A., Interpreting slip transmission through mechanically induced interface energies: a Fe–3% Si case study, Journal of Materials Science 54, 1831-1843, 2019.
6. B. Jelinek, S. Groh, M. F. Horstemeyer, J. Houze, S. G. Kim, G. J. Wagner, A. Moitra, and M. I. Baskes, Modified embedded atom method potential for Al, Si, Mg, Cu, and Fe alloys, Phys. Rev. B 85, 245102, 2012
7. L. S. I. Liyanage, S.0 G. Kim, J. Houze, S. Kim, M. A. Tschopp, M. I. Baskes, and M. F. Horstemeyer, Structural, elastic, and thermal properties of cementite (Fe3C) calculated using a modified embedded atom method, Phys. Rev. B 89, 094102, 2014.
8. Zhang X., Aifantis K.E., Ngan A.H.W., Interpreting the stress-strain response of Al micropillars through gradient plasticity. Materials Science and Engineering: A, 591, 38–45, 2014.

Publications

1. Soman, P.P., Herbert, E.G., Aifantis, K.E., Hackney, S.A., Analysis of Local Grain Boundary Strengthening Utilizing the Extrinsic Indentation Size Effect, Journal of Materials Research 34, 2347-2369, 2019.
2. Kuhr, B.R., Aifantis, K.E., Interpreting the inverse Hall-Petch relationship and capturing segregation hardening by measuring the grain boundary yield stress through MD indentation, Materials Science and Engineering: A, 745, 107-114, 2019.
3. Aifantis K.E., Deng H., Shibata H., Tsurekawa S., Lejček P., Hackney S.A., Interpreting slip transmission through mechanically induced interface energies: a Fe–3% Si case study, Journal of Materials Science 54, 1831-1843, 2019.
4. Kuhr B.R., Aifantis K.E., The Formation and Evolution of Defects in Nanocrystalline Fe During Indentation: The Role of Twins in Pop-Ins. Phys Status Solidi Basic Res 256, 1800370, 2019.
5. Soman, P.P., Herbert, E.G., Aifantis, K.E., Hackney, S.A., Effect of Processing on Nix-Gao Bilinear Indentation Results Obtained for High Purity Iron, MRS Advances 3, 477-486, 2018.

Establishing defect-property relationships for 2D-materials

PI: Assel Aitkaliyeva, University of Florida

Program Scope

This project aims to provide insight into the evolution of non-equilibrium concentration of defects in two-dimensional nanomaterials (2DNMs). The main goals of the project are to: i) tailor defect configurations and defect densities in 2DNMs using irradiation, ii) use defects to control physical properties of 2DNMs, and ii) investigate self-healing mechanisms in low dimensional materials. The project was designed to include both experimental and modeling components. Molybdenum disulfide (MoS_2) has been selected as a model system for establishing defect-property relationships in 2DNMs. The modeling component includes density-functional theory (DFT) calculations, analytic solutions to diffusion, and kinetic Monte Carlo (KMC) simulations to guide experimental irradiation campaigns needed to obtain a comprehensive understanding of the formation and evolution of defects in MoS_2 in response to radiation. Experimental approach is based on thorough characterization of intrinsic defect densities in MoS_2, various in-situ and ex-situ irradiation campaigns, and characterization (and property measurements) of irradiated specimens.

Recent Progress

In Year 1, the group established expertise in fabricating freestanding mono-, bi, and tri-layer MoS_2. We developed procedures to exfoliate MoS_2 from bulk specimen and deposit them on various substrates (Si, SiO_2, GaAs, TEM grid). The example of as-fabricated mechanically exfoliated specimen is provided in Figure 1.The exfoliated specimens were examined using various techniques including Raman spectroscopy, photoluminescence (PL), electron microscopy (TEM), X-ray photoelectron spectroscopy (XPS), and Kelvin force probe microscopy. Literature review suggests that mechanically exfoliated specimens should have higher carrier mobility and lower number of intrinsic defects than those grown through chemical vapor deposition (CVD) methods. In addition to mechanical exfoliation, the group is growing MoS_2 through CVD to determine which method leads to lower number of intrinsic defects. Specimens fabricated using both techniques will be evaluated and compared to determine the methodology most suited for irradiation campaigns.

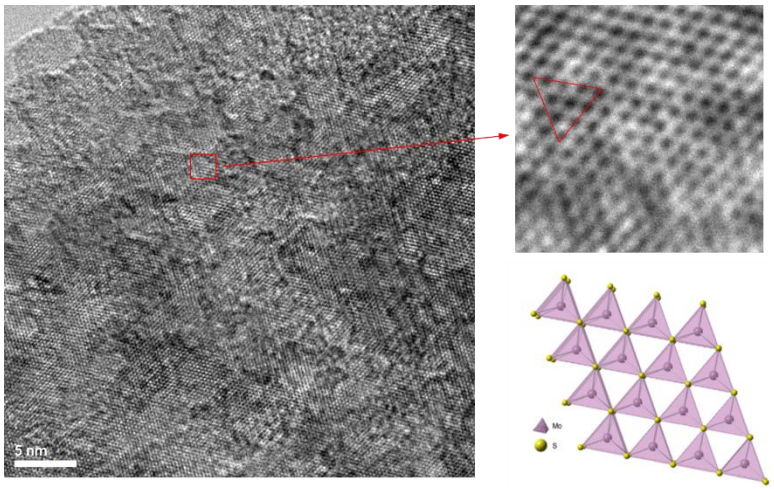

Figure 1. TEM micrograph of unirradiated MoS_2: low magnification overview: red box denotes the area from which higher magnification micrograph (on the right) was acquired. The structure of the MoS_2 is provided on the bottom right for convenience.

DFT calculations identified sulfur vacancy as the most favorable defect in MoS_2, which was experimentally validated in transmission electron microscope (TEM) during in-situ electron irradiation. The group worked on evaluating the computational issues associated with modeling of charged defects in 2D, and implementing necessary correction schemes needed to correctly model defects in MoS_2. A charged defect will increase strain of the system in its vicinity, which will lead to reduction of the symmetry due to Jahn-Teller distortion. For example, sulfur vacancy (V_s^{1-}, Figure 2) breaks 3-fold symmetry in MoS_2 due to Jahn-Teller distortion, which would lead to electric and magnetic dipole states (Figures 2a and 2b). DFT calculations (Figure 2c) further show that charged defects in MoS_2 display interesting spin states, which can allow manipulation of electronic properties of the MoS_2 through defect engineering.

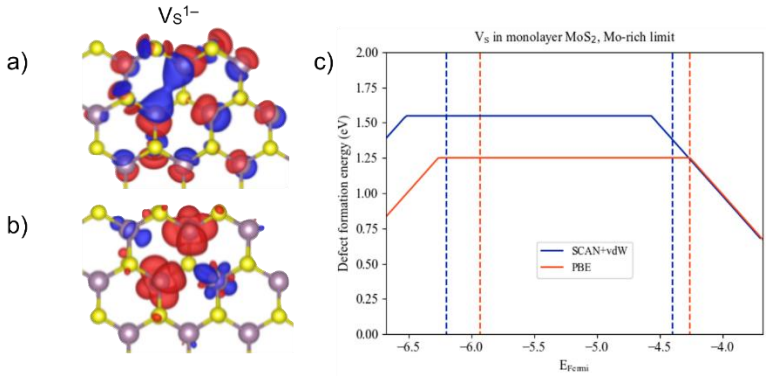

Figure 2. Preliminary DFT results for MoS_2: a) charge and b) spin states that can be produced by sulfur vacancy (V_s^{1-}), and c) charge state of sulfur vacancy in MoS_2.

It is known that energetic particles will interact with atoms of the material via electronic or nuclear components, and we will attempt to separate these two components. Electronic excitations in MoS_2 can alter density of states and charge, which we should be able to achieve using targeted irradiation campaigns. Based on our modeling results, novel spin states can be attained in 2DNMs using defect engineering. We are in the process of designing and executing appropriate experiments that will allow realizing theoretical predictions. In-situ and ex-situ ion irradiation campaigns have been scheduled at Sandia National Laboratories and Texas A&M University in collaboration with Khalid Hattar and Lin Shao, respectively. In-situ electron beam irradiations are ongoing at University of Florida.

Future Plans

Year 1 was dedicated to producing high quality samples and ensuring that defect densities and configurations in MoS_2 can be altered using irradiation. In addition, the group concentrated on establishing computational capabilities, which would aid experiment design. In year 2 of the project, we plan to focus our efforts on establishing thermal and radiation stability of defects and defect sinks in radiation response of MoS_2.

- Specifically, we will alter defect, charge, and spin states of the mechanically exfoliated and CVD grown freestanding MoS_2 and monolayer MoS_2 on a substrate. The formation energies and charge transition levels of relevant defects will be determined using DFT, and in-situ irradiation will be used to verify theoretical predictions. The result of the DFT calculations for the defect formation energies will provide the necessary data to map experimentally observed defects to specific atomic defect structures. Furthermore, the dependence of the defect formation energies on charge will be tested by irradiating and annealing 2DNM under different electrostatic conditions.

- Both in-situ and ex-situ irradiation experiments will be conducted with the goal of identifying the mechanisms governing radiation damage in 2DNMs. The radiation response of monolayer 2DNMs will be compared to that of a bilayer, and a bulk material, and the differences in their radiation response will be discerned.
- The role of substrate and interface effects on radiation stability of MoS_2 will be investigated.
- Physical properties of the as-fabricated MoS_2 will be measured.

Publications

In preparation.

Center for PRredictive Integrated Structural Materials Science – PRISMS Center

PI: J. Allison, University of Michigan (UM)
Co-PIs: S. Daly, University of California-Santa Barbara (UCSB), S. DeWitt (UM), V. Gavini (UM), M. Hedstrom (UM), E. Marquis (UM), A. Misra (UM), B. Puchala (UM), L. Qi (UM), V. Sundararaghavan (UM), K. Thornton (UM), A. Van der Ven (UCSB).

Program Scope

The overarching goal of the PRISMS Center is to establish a unique scientific platform that will enable accelerated predictive materials science. The platform has three key thrust areas:

1. **PRISMS Integrated Computational Software:** Develop and establish a suite of integrated, multi-scale, open-source computational tools for predicting the microstructural evolution and mechanical behavior of structural metals.
2. **The Materials Commons:** Develop and deploy "The Materials Commons," a knowledge repository and virtual collaboration space for curating, archiving and disseminating information from experiments and computations.
3. **PRISMS Integrated Science Use Cases:** The use cases demonstrate the application of the integrated PRISMS platform of experiments, theory and simulation for making major advances in the quantitative and predictive understanding of microstructural evolution and mechanical behavior of magnesium alloys.

Recent Progress and Future Plans

In addition to eleven faculty members, the PRISMS Center currently has four full time staff members and over the past two years twenty graduate students and post-doctoral fellows. Over this time period six students have completed their PhDs. We hold an annual workshop to develop our external PRISMS collaborative community and to train external users of PRISMS software tools and Materials Commons and have trained more than 150 users. Additional information can be found at http://prisms-center.org.

PRISMS Integrated Computational Software

Currently four primary codes make up the PRISMS Open Source Integrated software: *CASM*, *PRISMS-PF*, *PRISMS-Plasticity* and *DFT-FE* are available on GitHub (see descriptions below). Three of these codes were first released in 2015 and have had at least four major upgrades since then. A new code, DFT-FE was first released in 2018. The GitHub pages for these codes have been viewed more than 100,000 times and over 1680 unique clones (copies) have been downloaded by users as shown in Figure 1. 600 of these clones occurred over the past 12 months. Each software package includes a substantial user manual, formulation notes, commented source code and unit tests.

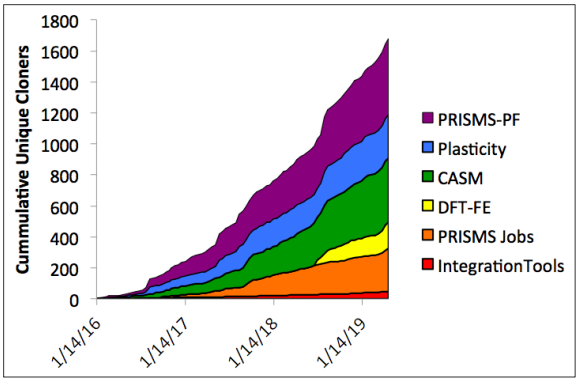

Figure 1. Cumulative clones of PRISMS codes since January 2016.

CASM: CASM, a Clusters Approach to Statistical Mechanics, provides functionality for symmetry identification, enumeration of symmetrically unique supercells and configurations, use of automatically determined or custom reference states for formation energy calculation, and convex hull identification. *CASM* has been generalized to enable the construction of Hamiltonians that couple lattice strain, chemical disorder, vibrational excitations and on-site magnetic degrees of freedom. Progress has also been made on fitting and sampling coupled Hamiltonians, improving ease of customization and sharing *CASM* projects via *Materials Commons*. Future plans include incorporation of kinetic Monte Carlo calculations of non-dilute diffusion coefficients. *https://github.com/prisms-center/CASMCode*

PRISMS-PF: The *PRISMS-PF* phase field code uses the finite element (FE) method, and is a massively scalable numerical framework for implementing phase field models for the multiscale materials modeling effort of PRISMS. The PRISMS FE framework using the deal.ii open-source finite element library has been implemented. *PRISMS-PF* has been upgraded to include support for nonlinear quasi-static governing equations, which is necessary for the corrosion application. Grain remapping functionality has been added which allows a single order parameter to store multiple grains in a polycrystalline system. A plug-in for *PRISMS-PF* has been developed for sharing results and meta-data via *Materials Commons*. Future plans include incorporation of implicit time-stepping. *https://github.com/prisms-center/phaseField*

PRISMS-Plasticity: The *PRISMS-Plasticity* code is a massively parallel numerical framework for implementing continuum and crystal plasticity finite element (CPFE) models using the deal.ii open source library. Various crystal and continuum plasticity material models have been implemented. A major improvement is development of a new physically based twinning and detwinning model along with the implementation a new kinematic hardening model to capture the material response during cyclic loading. An automated work-flow has been established for integration with EBSD data sets using DREAM.3D. Integration of the *PRISMS-Plasticity* software with the *Materials Commons* was also completed. The ability to carry out simulations using gradient plasticity and crack paths is planned for future release. *https://github.com/prisms-center/plasticity*

DFT-FE: *DFT-FE* is a massively parallel code for large-scale real-space DFT calculations using spatially adaptive higher-order finite-element basis was first released in 2018. It was recently chosen as a finalist for the Gordon Bell Prize. Key features include: (i) adaptive spatial resolutions using the FE basis informed by error estimates; (ii) computationally efficient and scalable algorithms for the solution of the KS-DFT problem; (iii) treatment of non-periodic and semi-periodic boundary conditions; (iv) treatment of density and gradient-density dependent XC functionals; (v) geometric optimization using configuration forces. Future plans include extending the implementation of *DFT-FE* to take advantage of GPU acceleration on heterogeneous computing architectures. *https://github.com/dftfeDevelopers/dftfe*

The Materials Commons *https://materialscommons.org*

The *Materials Commons* is an information repository and virtual collaboration space for curating, storing and disseminating materials information from experiments and computations. It has been designed to explicitly cover the entire data lifecycle, from data acquisition through sharing and analysis to reuse. The *Materials Commons* provides a common site for materials researchers to store, share, curate, analyze, publish, and reuse experimental and computational materials data collaboratively. The uniqueness and strength of the *Materials Commons* is that it is both a collaboration space and an information repository, where the types of collaborations supported are familiar tasks in materials research and the underlying data model for the information repository

is tailored for materials data, workflow, and analysis. Provenance is captured automatically and seamlessly as part of the scientific workflow. Over 350 users have registered on the *Materials Commons* and have uploaded over 1.5 million files. New features include a robust Python API that allows integration of computational applications with *Materials Commons*, a spreadsheet loader that allow users to directly their data from spreadsheets into *Materials Commons* and integration with Globus for fast, reliable upload/download of large sets of data such as that generated at APS or CHESS. Future plans include improvements in search and contextual understanding and cloud-based storage capability.

PRISMS Use Cases

The PRISMS Use Cases serve as demonstrations and test beds for the development and demonstration of the PRISMS platform combining experiments, theory and simulation. Highlights from these use cases are summarized below.

Grain Strengthening Use Case

Theoretical/computational methods have been integrated with advanced experiments to understand grain size strengthening behavior in Mg alloys. This involves atomistic to continuum multiscale investigation of how texture, grain and twin boundaries, and chemistry affects the micro-Hall Petch coefficients used to capture grain size effects in *PRISMS-Plasticity*. At the atomistic scale, an efficient genetic code has been developed for predicting minimum energy structures of grain boundaries by considering both macroscopic and microscopic degrees of freedom. An example of which is shown in Figure 2.

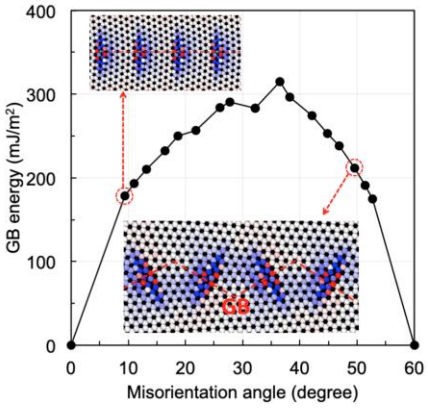

Figure 2. *This figure shows GB energies and structures for [0001]-tilted grain boundary in Mg generated by our code. All these GBs are composed of <a>-type edge dislocations on prismatic planes. They can transform from the flat GB plane at small tilted angles to the faceted GB plane at large tilted angles.*

A new high resolution EBSD (HREBSD) technique has been established to study the interaction of slip bands and grain boundaries and reconstruct the stress distribution imposed by a slip band on an adjacent grain. An analytical pile-up model was developed to predict this stress distribution. A high throughput technique is being developed to identify micro-Hall Petch coefficients in individual grains. HEDM (CHESS) has been used to provide 3D measurement of grain size effects on stress-strain behavior of Mg-Nd alloy specimens. These results were used to validate *PRISMS-Plasticity* simulation parameters. SEM-DIC methods have been substantially improved for characterizing slip and twinning during loading on large field of views (100 million data points).

Fatigue Behavior Use Case

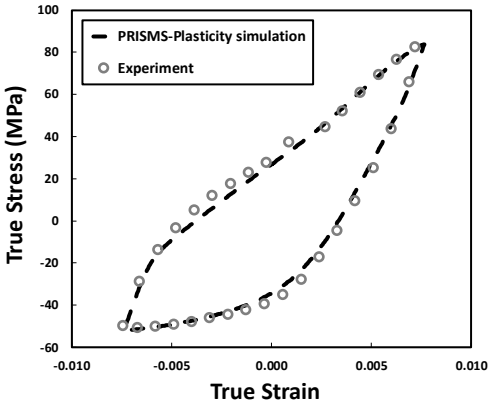

Prediction of microstructural and alloying effects on cyclic deformation and fatigue behavior of Mg alloys is being accomplished by integrating *PRISMS-Plasticity* and advanced experimental methods. The twinning and detwinning behavior of extruded fine-grained unalloyed Mg and Mg-4Al were characterized using in-situ HEDM (CHESS) measurements during cyclic deformation. These results were used to calibrate the new *PRISMS-Plasticity* twinning-detwinning model, an example of which is shown in Figure 3.

Figure 3*. Experiment and PRISMS-Plasticity simulation of cyclic stress-strain response unalloyed Mg.*

The growth of fatigue cracks through grain boundaries has been characterized in 3D using HEDM (APS). These results will be used with a new fracture model being implemented for use with the *PRISMS-Plasticity* code. This work is being done in collaboration with Professor Ashley Spear, U. Utah, who obtained an NSF supplement to a DMREF to work directly with the PRISMS Center on this topic.

Corrosion Use Case

This use case explores a new application of the PRISMS framework and is focused on coupling *PRISMS-PF* simulations with advanced in-situ corrosion experiments. A *PRISMS-PF* application using phase-field and smoothed boundary methods was developed to simulate localized pitting corrosion. The model employed describes the evolution of a metal/electrolyte interface which is governed by Butler-Volmer-type electrochemical kinetics coupled to ionic transport within the electrolyte.

In situ electrochemical/hydrogen evolution measurements with optical imaging and post-mortem microstructural analyses were conducted for pure Mg and Mg alloys, including Mg-Zn and Mg-Ca-Zn alloys. The values of corrosion potential and corrosion current, critical input to the phase field model, were determined. The corroded samples after various corrosion conditions and with different compositions showed a range of morphologies, i.e., uniform and filiform, which provides insights into how the corrosion parameters depend on the alloy composition.

Complex Alloy Use Case

This use case is combining information from our previous work on Mg-Nd-Y alloys to demonstrate the ability to integrate the PRISMS Tools to optimize a complex quaternary alloy and heat treatment, specifically the Mg-Nd-Y-Ca system. Design of the multiscale optimization framework/code, *prisms.multiscale*, has been completed. The framework integrates *CASM*, *PRISMS-PF* and *Materials Commons* and new multi-fidelity models using the open source integration and optimization framework, OpenMDAO. A multi-fidelity Gaussian Process surrogate model was developed to predict precipitate shape based on information calculated by *CASM*. As shown in Figure 4, sharp interface model (low-fidelity, inexpensive) calculations are combined with *PRISMS-PF* phase field (high-fidelity, more expensive) calculations, to make high-fidelity predictions at a much lower cost.

CASM was used to perform DFT calculations for energetics of Mg-Ca, Mg-Nd-Y and Mg-

Nd-Y-Ca. To validate this predictions, quaternary Mg-Nd-Y-Ca alloys have been obtained and are under experimental characterization. Substantial improvements to the dislocation dynamics (DD) code, ParaDis, were made to enable direct input of *PRISMS-PF* phase field simulation results and accurate calculation of interaction forces between dislocations and precipitates. These simulations are being integrated with and validated by in-situ TEM experiments.

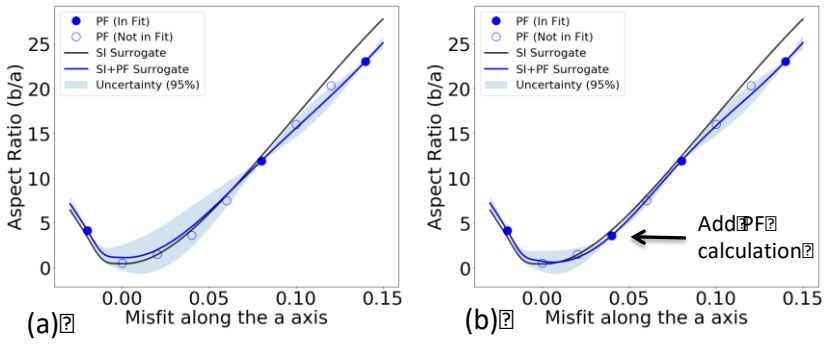

Figure 4*. A Gaussian-process-based multi-fidelity model for equilibrium precipitate aspect ratio in Mg-Nd enhances a (lower fidelity, inexpensive) sharp interface (SI) model with (higher-fidelity, more expensive) phase field (PF) calculations.*

2017-2019 PRISMS Center Publications acknowledging DOE-BES support

1. E. Solomon, V. Araullo-Peters, J.E. Allison, E.A. Marquis, Early precipitate morphologies in a Mg-Nd-(Zr) Alloys. Scripta Materialia 128;14-17 (2017)
2. C. Heinrich, V. Sundaraghavan, "A method to predict fatigue crack initiation in metals using dislocation dynamics" Corrosion Reviews, 35 (4-5) pp 325-341(2017).
3. A. R. Natarajan, A. Van der Ven, "A unified description of ordering in HCP Mg-RE alloys" Acta materialia, 124, p620-632, (2017).
4. S. DeWitt, E. Solomon, A. Natarajan, V. Araullo-Peters, S. Rudraraju, L. Aagesen, E. Marquis, A. van der Ven, K. Thornton, and J. Allison, " Misfit-Driven β''' Precipitate Composition and Morphology in Mg-Nd Alloys" Acta Mat. (2017) 136, 378-389, 2017.
5. G. H. Teichert, N. S. H. Gunda, S. Rudraraju, A. R. Natarajan, B. Puchala, K. Garikipati, A. Van der Ven, "A comparison of Redlich-Kister polynomial and cubic spline representations of the chemical potential in phase field computations", Comp. Mater. Sci. **128**, (2017) 127-139.
6. E. Solomon, T. Chan, A Chen, B Uttal-Veroff, E. Marquis "Aging behavior of Mg alloys containing Nd and Y" Magnesium Technology. (2017) 349-352
7. P. Acar, S. Srivastava, V. Sundararaghavan, Stochastic Design Optimization of Microstructures with Utilization of a Linear Solver, AIAA Journal, Vol. 55 (9) pp. 3161-3168 (2017).
8. A. R. Natarajan, A. Van der Ven, "First principles investigation of phase stability in the Mg-Sc binary alloy," Physical Review B, (2017).
9. J. C. Thomas, A. Van der Ven, "The exploration of nonlinear elasticity and its efficient parameterization for crystalline materials," Journal of the Mechanics and Physics of Solids, (2017).

10. Z. Wang, J. Siegel, K. Garikipati, "Intercalation driven porosity effects on the electro-chemo-thermo-mechanical response in continuum models for battery material electrodes," Journal of the Electrochemical Society, **164**, A2199-A2212, 2017.
11. K. Sagiyama, S. Rudraraju, K. Garikipati , **"**A numerical study of branching and stability of solutions to three-dimensional martensitic phase transformations using gradient-regularized, non-convex, finite strain elasticity**",** Journal of the Mechanics and Physics of Solids (2017).
12. ELS Solomon, EA Marquis, Deformation behavior of β' and β"' precipitates in Mg-RE alloys, Materials Letters (2017) 216(1) 67-69.
13. P-W Chu, E LeMire, EA Marquis, Microstructure of Localized Corrosion Front on Mg Alloys and the Relationship with Anodic Hydrogen Evolution, Corrosion Science (2017) *128 253-264*
14. Das, S., Gavini, V., Electronic structure study of screw dislocation core energetics in Aluminum and core energetics informed forces in a dislocation aggregate, *J. Mech. Phys. Solids*, 104, 115-143 (2017).
15. S. DeWitt and K. Thornton "Phase Field Modeling of Microstructural Evolution" *Computational Materials System Design*, D. Shin and J. Saal, Eds., Springer Nature, London, (2018)
16. L.K. Aagesen, J. Miao, J. E. Allison, S. Aubry, A. Arsenlis, "Prediction of Precipitation Strengthening in the Commercial Mg Alloy AZ91 Using Dislocation Dynamics", Metallurgical and Materials Trans.Vol 49 (5) pp. 1908-1915 (2018).
17. Aeriel D. Murphy and John E. Allison, "The Recrystallization Behavior of Unalloyed Mg and a Mg-Al Alloy," Metallurgical and Materials Transactions, Vol 49 (5) 1492-1508 (2018)
18. Zhihua Huang, John E. Allison and Amit Misra, "Interaction of Glide Dislocations with Extended Precipitates in Mg-Nd alloys", Scientific Reports, Article number: 3570 (2018).
19. Shardul Panwar and Veera Sundararaghavan, Dislocation theory-based cohesive model for microstructually short fatigue crack growth" Materials Science and Engineering A, 708, pp 395-404 (2017).
20. A. Natarajan, J. Thomas, B. Puchala, A Van der Ven, "Symmetry-adapted order parameters and free energies for solids undergoing order-disorder phase transitions", Phys Rev B, 96 134204 (2017)
21. S. Sun, A. Ramazani, V. Sundararaghavan, A hybrid multi-scale model of crystal plasticity for handling stress concentrations, Metals, 7(9), 345, 2017.
22. P. Acar, A. Ramazani, V. Sundararaghavan, Crystal Plasticity Modeling and Experimental Validation with an Orientation Distribution Function for Ti-7Al Alloy, Metals, 7(11), p.459, 2017.
23. J. Luo, A. Ramazani, V. Sundararaghavan, Simulation of Micro-Scale Shear Bands Using Peridynamics with an Adaptive Dynamic Relaxation Method, International Journal of Solids and Structures, 130, pp.36-48, (2018).
24. S. Panwar, J. Adams, J. Allison, J. W. Jones, V. Sundararaghavan, "A grain boundary interaction model for microstructurally short fatigue cracks", International Journal of Fatigue Volume 113, pp 401-406 (2018).
25. P. Motamarri, V. Gavini, "Configurational forces in electronic structure calculations using Kohn Sham density functional theory" Physical Review B (2018) 97, 165132 (2018)
26. L. K. Aaegesen, J. F. Adams, J. E. Allison, B. Andrews, V. Araullo-Peters, T. Berman, Z. Chen, S. Daly, S. Das, S. DeWitt, S. Ganesan, K. Garikipati, V. Gavini, A. Githens, M. Hedstrom, Z. Huang, H.V. Jagadish, J.W. Jones, J. Luce, E.A. Marquis, A. Misra, D. Montiel, P. Motamarri, A. D. Murphy, A. R. Natarajan, S. Panwar, B. Puchala, L. Qi, S. Rudraraju, K.

Sagiyama, E.L.S. Solomon, V. Sundararaghavan, G. Tarcea, G. H. Teichert, J. C. Thomas, K. Thornton, A. Van der Ven, Z. Wang, T. Weymouth, C. Yang. " PRISMS - An Integrated, Open Source Framework for Accelerating Predictive Structural Materials Science, JOM.(2018) October, p 1-17.

27. E. L.S. Solomon, A. R. Natarajan, A. Roy, V. Sundararaghavan, A. Van der Ven, E. A. Marquis, "Stability and strain-driven evolution of β' precipitation in Mg-Y alloys, Acta Materialia, 166 (2019) 148-157.
28. Aeriel D. Leonard-Murphy, Darren C. Pagan, Armand Beaudoin, Matthew P. Miller, John E. Allison "Quantification of Twinning-Detwinning Behavior During Low-Cycle Fatigue of Pure Magnesium Using High Energy X-Ray Diffraction" International Journal of Fatigue, 125 (2019) 314-323.
29. Zhihua Huang, Chaoming Yang, Liang Qi, John E. Allison, Amit Misra, "Dislocation pile-ups at β1 precipitate interfaces in Mg-rare earth (RE) alloys" Materials Science and Engineering A, 742 (2019) 278-286
30. J. Luo, V. Sundararaghavan, Stress point method for stabilizing zero energy modes in non-ordinary state based peridynamics, International Journal of Solids and Structures Volume 150, Pages 197-207, 2018.
31. P. Acar, V. Sundararaghavan, Stochastic Design Optimization of Microstructural Features using Linear Programming for Robust Material Design, AIAA Journal,Vol. 57(1), 2019.
32. P. Acar, V. Sundararaghavan, Do Epistemic Uncertainties Allow for Replacing Microstructural Experiments with Reconstruction Algorithms, AIAA Journal, 57(3), 1078-1091, 2019.
33. A Van der Ven, JC Thomas, B Puchala, AR Natarajan, "First-principles statistical mechanics of multicomponent crystals," Annual Review of Materials Research 48, 27-55 (2018)
34. W. Lenthe, JC Stinville, M Echlin, Z Chen, S Daly, T Pollock. Advanced Detector Signal Acquisition and Electron Beam Scanning for High Resolution SEM Imaging. *Ultramicroscopy,* 195, 193-100, (2018).
35. Chen Z, Lenthe W., Stinville J.C., Echlin M., Pollock T., Daly S. High-Resolution Deformation Mapping Across Large Fields of View Using Scanning Electron Microscopy and Digital Image Correlation. *Experimental Mechanics,*58(9): 1407-1421 (2018).
36. Chen Z. and Daly S. Daly S. Deformation Twin Identification in Magnesium through Clustering and Computer Vision. *Materials Science and Engineering A,* 736: 61-75 *(*2018).
37. Mohammadreza Yaghoobi, Sriram Ganesan, Srihari Sundar, Aaditya Lakshmanan, Shiva Rudraraju, John E. Allison, Veera Sundararaghavan, "PRISMS-Plasticity: An open-source crystal plasticity finite element software" Computational Materials Science, 169, 109078, (2019).

Quantifying the Role of APB Tubes on the Work-hardening of Ordered Phases

Principal Investigator: I. Baker

Thayer School of Engineering, Dartmouth College, Hanover, NH 03755.
Ian.Baker@Dartmouth.edu

Program Scope

The concept of an anti-phase boundary (APB) tube was originally proposed by Vidoz and Brown (1962) in order to explain the much greater work-hardening rate (50% increase) observed when an alloy, such as Ni_3Fe, is ordered. Their existence was only definitively confirmed by Chou and Hirsch in 1981 using weak-beam imaging with superlattice reflections in a transmission electron microscope. In this project, we aim to study three major unresolved issues: (1) there have been no studies in which an APB tube model has been directly linked to experimental measurements of APB tube density to quantitatively describe the work-hardening rate (WHR) in an ordered alloy, (2) how gliding dislocations interact with APB tubes has been theorized but such interactions have not been directly observed, and (3) the proposed APB tube formation mechanisms all rely on *post-mortem* TEM observations.

In this project, we are:

(1) determining the APB tube formation mechanisms via TEM *in situ* straining experiments;
(2) performing tensile tests to various strains and measuring the APB tube and dislocation density using a combination of TEM, calorimetry, and possibly electron channeling contrast imaging in a scanning electron microscope at each strain, and using these data to model the work-hardening rate;
(3) annealing out the APB tubes (but not the mobile dislocations) from strained specimens and determining the effect on the subsequent flow stress and work-hardening rate in order to provide insight into the mechanisms of APB tube strengthening;
(4) relating synchrotron X-ray diffraction (XRD) measurements and neutron diffraction measurements of APB tube density to the flow stress continuously using *in situ* deformation experiments; and
(5) examining the chemistry of the APB tubes using atom probe tomography (APT).

The work is being performed on the two most common ordered phases, B2 and $L1_2$, i.e.

(1) single crystals of B2 FeAl since there is extensive documentation of its deformation; and
(2) the $L1_2$ phase in the two-phase HEA $AlCoCrFeNi_{2.1}$ (Wani et al., 2016a, 2016b, 2017a, 2017b; Lu et al., 2017) both as a stand-alone alloy and then as part of the (B2 + $L1_2$) HEA $AlCoCrFeNi_{2.1}$.

Recent Progress

FeAl: Preliminary tests have been undertaken to observe the effect of annealing out APB tubes in B2 Fe-40Al. Large-grained polycrystalline samples were annealed at 1200°C for 10 hours to minimize chemical segregation and then annealed at 400°C for 5 days to minimize thermal vacancies (Nagpal and Baker, 1990). The samples were then compressed at a rate of 1×10^{-3} s^{-1} to 5%, 14%, and 19% strain. After straining, samples were unloaded, annealed at 120°C for 2 h, and then compressed to failure. Because the samples had to be completely removed from the testing set-up for annealing, interrupted compression tests were performed without annealing to ensure repeatability. The interrupted tests showed the same flow stress within ± 2% after reloading.

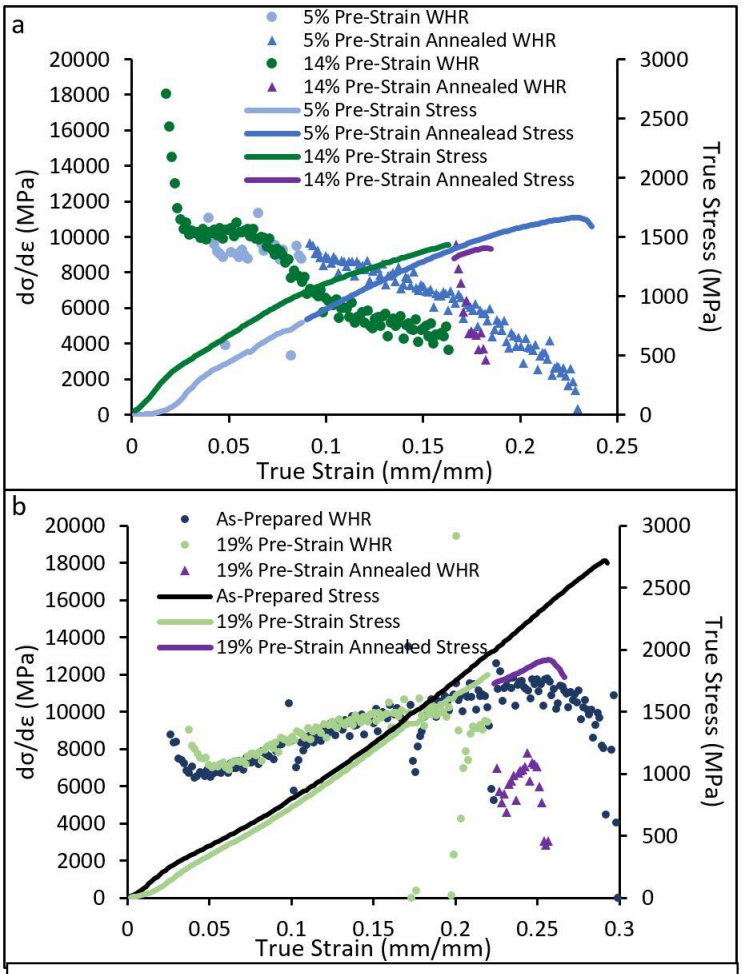

Figure 1. (a) Work-hardening rate (filled shapes) and true stress (lines) versus true strain for 5% and 14% strained, and (b) work-hardening rate (filled shapes) and true stress (lines) versus true strain for as-prepared and strained 19% samples.

Figure 1 shows the stress-strain and WHR-strain curves for four samples. For the samples strained 14% and 19%, the flow stress drops by 4% and 8%, respectively, after annealing. Such a drop was not observed in the sample strained 5%, suggesting a lower limit before the annealing has an effect. The sample strained 19% shows a greater than 25% drop in WHR after annealing. However, the 14% pre-strained sample shows an 8% increase in WHR after annealing. The curves may be different due to anisotropy of the large-grain polycrystals, which only have 2-3 grains across the diameter of the sample. The decrease in work-hardening rate observed after 19% straining indicates that APB tubes act as obstacles for gliding dislocations. As not all data show a decrease in WHR, these tests are being repeated on both single crystals and fine-grained polycrystals of Fe-40Al using tension rather than compression tests, as well as on pure iron for comparison.

It may be possible to see the effects of APB tubes using synchrotron X-ray diffraction. Fe-40Al single crystal were grown in a modified Bridgman furnace and annealed at 1200°C for 10 hours and at 400°C for 5 days (Nagpal and Baker, 1990). Samples of two different orientations were cold-rolled to ~16% thickness reduction, and part of each sample was annealed at 120°C for 2 h to remove the APB tubes. Figure 2 shows the X-ray diffraction pattern for one orientation obtained using the synchrotron at Argonne National Laboratory. Table 1 lists the percent change from the cold-rolled to cold-rolled plus annealed state for the X-ray peak position, full width half maximum, and peak height. It was anticipated that the annealed sample would have narrower peaks, as the strain energy from APBs would have been removed. However, this is not evident. These tests are being repeated on single crystals that have been deformed to much greater thickness reductions. 16% thickness reduction may not generate a high enough APB tube density to see effects on the X-ray diffraction data.

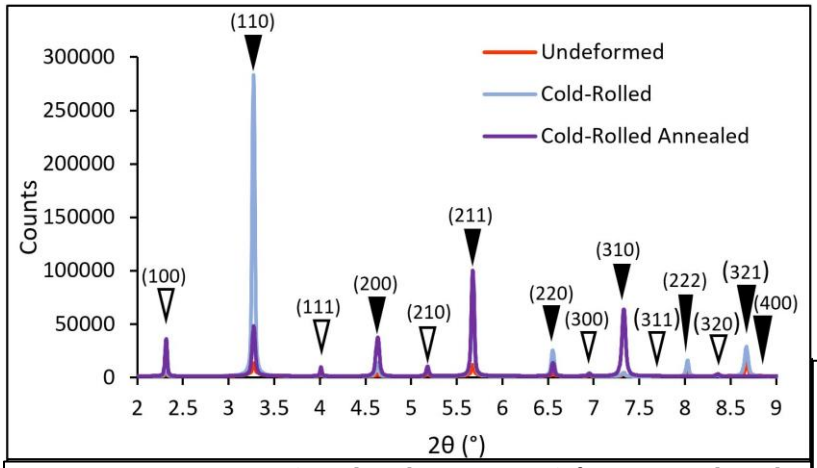

Figure 2. XRD patterns (wavelength 0.01173 nm) for a Fe-40Al single crystal in the undeformed, cold rolled (CR), and cold-rolled plus annealed (CR + A) states. Open triangles indicate superlattice peaks.

hkl	2θ	FWHM	Height
(100)	0.0778	10.6	218.1
(110)	0.0734	26.7	-84.3
(111)	0.0299	0.0	36.6
(200)	0.0670	10.5	200.8
(210)	0.0560	-9.9	6.4
(211)	0.0476	9.0	11.6
(220)	0.0458	-3.7	-47.3
(300)	0.0821	7.6	-36.3
(310)	0.0259	-9.8	1963.1

Table 1. Percent change in peak position, full-width half maximum, and peak height between the CR and CR + A samples. Blue background indicates superlattice peaks.

$AlCoCrFeNi_{2.1}$ Eutectic High Entropy Alloy: Polycrystalline $AlCoCrFeNi_{2.1}$ was arc melted from elemental materials with 99.9+% purity. XRD confirmed that the material is two-phase $L1_2$ and B2. The ordered $L1_2$ phase was further confirmed in the TEM, see Figure 3. The alloy has a dendritic microstructure composed of large dendrites of the $L1_2$ phase (tens of microns) with finer interdendritic region of mixed $L1_2$ and B2 lamella (~1μm thick), see Figure 4a. The $L1_2$ phase is Fe, Cr, and Co rich and appears lighter in the SEM; the B2 phase is Al and Ni rich, and appears darker. A stress-strain curve of the two-phase material is shown in Figure 4b. The yield strength and ultimate tensile strength are in good agreement with Wani et al., 2016a. The effects of low temperature anneals on tensile properties are being determined.

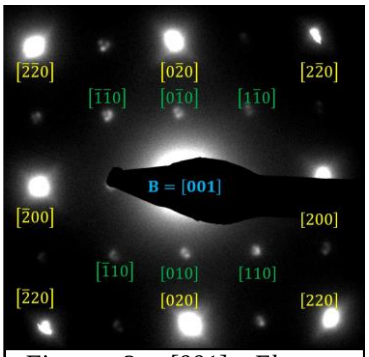

Figure 3. [001] Electron diffraction pattern from $L1_2$ phase of $AlCoCrFeNi_{2.1}$. Yellow – fundamental spots; green - superlattice spots.

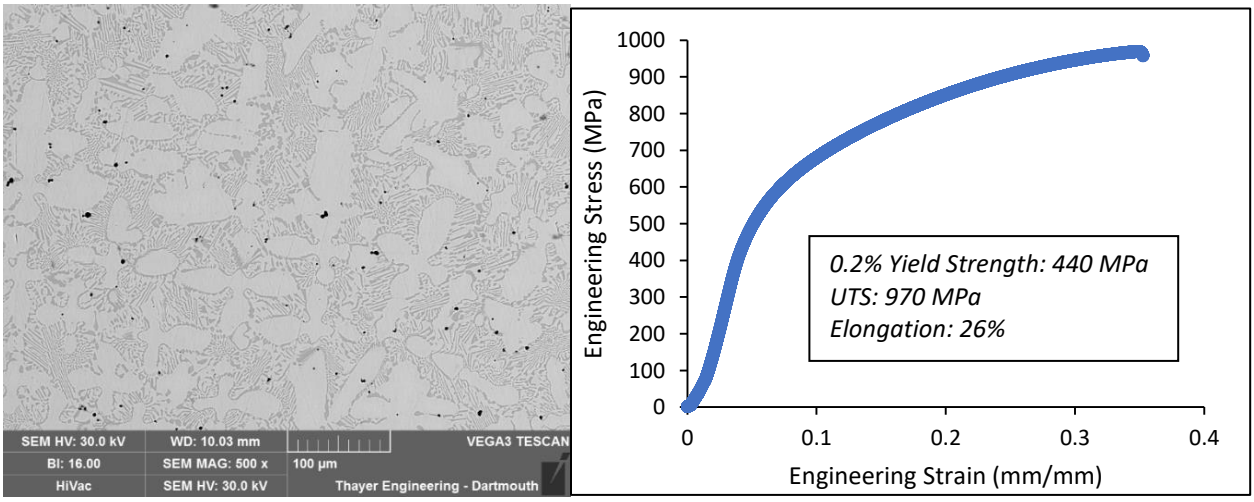

Figure 4. (a) SEM micrograph and (b) engineering stress-strain curve of $AlCoCrFeNi_{2.1}$ as-cast.

Future Plans

1. Examine effects of low-temperature, APB-tube removing anneals on the flow stress and WHR of FeAl single crystals and polycrystalline $AlCoCrFeNi_{2.1}$.
2. Fe-40Al single crystal specimens have been sent to Dr. Andrew Payzant at ORNL for neutron diffraction in as-grown, strained 50% and annealed at 120^{o}C for 2 h condition (to remove APB tubes) to determine the effect of APB tubes on neutron diffraction patterns.
3. Additional Fe-40Al single crystal specimens have been sent to Dr. Si Chen at ANL in the as-grown, strained 50% (much higher strain than previously used) and annealed at 120^{o}C for 2 h condition tubes to determine the effect of APB tubes on X-ray diffraction patterns.
4. Lightly-strained (5%) Fe-40Al-3Cu single crystal specimens have been sent to Dr. Baptiste Gault at MPIE, Germany for atom probe tomography study of the local chemistry in APB tubes.

References

Chou, C.T. and P.B. Hirsch, "Antiphase Domain Boundary Tubes in Plastically Deformed Ordered Fe-30.5 at. % Al Alloy", Philosophical Magazine A, 44 (1981): 1415.

Lu, Y., X. Gao, L. Jiang, Z. Chen, T. Wang, J. Jie, H. Kang, Y. Zhang, S. Guo, H. Ruan, Y. Zhao, Z. Cao, and T. Li, "Directly cast bulk eutectic and near-eutectic high entropy alloys with balanced strength and ductility in a wide temperature range," Acta Materialia, 124 (2017): 143.

Nagpal, P. and Baker, I, "Effect of Cooling Rate on Hardness of FeAl and NiAl," Metallurgical Transactions A, 21A (1990): 2281.

Wani, I.S., T. Bhattacharjee, S. Sheikh, Y.P. Lu, S. Chatterjee, P.P. Bhattacharjee, S. Guo, and N. Tsuji, "Ultrafine-grained $AlCoCrFeNi_{2.1}$ eutectic high-entropy alloy," Materials Research Letters, 4 (2016a): 174.

Wani, I.S., T. Bhattacharjee, S. Sheikh, Y.P. Lu, S. Chatterjee, S. Guo, P.P. Bhattacharjee, and N. Tsuji, "Effect of severe cold-rolling and annealing on microstructure and mechanical properties of $AlCoCrFeNi_{2.1}$ eutectic high entropy alloy," IOP Conference Series: Materials Science and Engineering, 194 (2017a): 012018-1-5.

Wani, I.S., T. Bhattacharjee, S. Sheikh, P.P. Bhattacharjee, S. Guo, and N. Tsuji, "Tailoring nanostructures and mechanical properties of $AlCoCrFeNi_{2.1}$ eutectic high entropy alloys using thermo-mechanical processing," Materials Science and Engineering A, 675 (2016b): 99.

Wani, I.S., T. Bhattacharjee, S. Sheikh, I.T. Clark, M.H. Park, T. Okawa, S. Guo, P.P. Bhattacharjee, and N. Tsuji, "Cold-rolling and recrystallization of textures of a nano-lamellar $AlCoCrFeNi_{2.1}$ eutectic high entropy alloy," Intermetallics, 84 (2017b): 42.

Vidoz, A.E., and L.M. Brown, "On work-hardening in ordered alloys," Philosophical Magazine A, **7** (1962) 1167.

Publications

"Microband Induced Plasticity and the temperature dependence of the mechanical properties of a carbon-doped FeNiMnAlCr high entropy alloy" Z. Wang, H. Bei and I. Baker, Materials Characterization, **139** (2018) 373-381.

"Eutectic/Eutectoid Multi-Principal Component Alloys: A Review", I. Baker, M. Wu and Z. Wang, Materials Characterization**, 147** (2019) 545-557.

The effects of carbon on the phase stability and mechanical properties of heat-treated FeNiMnCrAl high entropy alloys, M. Wu, Z. Li, B. Gault, P. Munroe and I. Baker, Materials Science and Engineering A, **748** (2019) 59-73.

Patent

United States Patent 1,0190,197 "Oxidation Resistant High-Entropy Alloys", 1/29/19, Ian Baker and Zhangwei Wang.

Discovery, Design, Synthesis and Testing of High Performance Structural Alloys

Thomas John Balk

Department of Chemical and Materials Engineering, University of Kentucky

Program Scope

The overarching goal of this project is to understand the phase stability and mechanical behavior of non-stoichiometric multi-principal element alloy (MPEA) materials, which will ideally serve as models for other MPEA systems. MPEAs represent a rapidly growing area of alloy research, with reports of novel materials exhibiting greatly improved properties, especially regarding mechanical behavior [1, 2]. MPEAs, also known as "high-entropy alloys" or "compositionally complex alloys," contain five or more alloying elements. This leads to a wide range of possible alloy compositions and an even broader spectrum of microstructures and properties [3]. Systematic evaluations of certain MPEA systems have been performed, and these have yielded promising MPEAs, often with simple stoichiometries. However, understanding how deviations from stoichiometric compositions influence certain mechanical properties has been hindered by the experimental difficulty of producing and studying sufficiently wide alloy variations in a systematic and feasible manner. Addressing this bottleneck will provide fundamental knowledge relating alloying effects to mechanical behavior in MPEAs and will facilitate the discovery and design of new, high performance structural alloys.

In order to identify suitable alloys, we are using a combinatorial thin film screening approach, in collaboration with scientists at Lawrence Berkeley National Laboratory who are performing computational work as well as complementary experimental work. Specific tasks include the fabrication, using thin film deposition from six sputtering targets, of combinatorial samples with multi-dimensional gradients in composition and microstructure. These samples are studied to screen MPEA systems for promising candidate alloys with specific composition(s), based on characterization of composition, structure and mechanical behavior across the thin film. We want to produce single-phase MPEAs with chemical homogeneity in a given thin film region, simple grain structures, and no intermetallic phases present. Gradient films facilitate first-pass screening for desirable characteristics and inform the next stage of work that involves fabrication of bulk MPEA specimens for (tensile) mechanical testing and characterization. To make the bulk alloys, metal (elemental) pieces are melted to form MPEAs, followed by thermomechanical processing to homogenize the composition and microstructure. A subset of alloys will also be cast, using vacuum arc melting, to yield larger samples (diameter ~1 cm and length ~5-10 cm) and these will allow us to assess viability of scale-up for the alloys in structural applications. Further processing plans include rolling and heat treatment to recrystallize selected

bulk MPEAs and grow grains to different extents, in order to investigate mechanical size effects in MPEAs. Mechanical testing (primarily in tension) is planned to assess mechanical behavior over a range of temperatures.

Recent Progress

Two MPEA systems are under investigation in this project. The first system is similar to the Cantor alloy, but includes Cu instead of Cr. Thin film composition gradient samples were characterized, and single-phase regions were identified using x-ray diffraction, to identify candidate alloys for bulk fabrication. In parallel, a bulk alloy processing approach was employed to identify alloy compositions that should be single-phase and thermally stable. An equiatomic alloy of CrMnFeCoNiCu was melted in a furnace and then slowly cooled, resulting in a multi-phase microstructure consisting of acicular Cr-rich particles in a non-equiatomic MPEA matrix ($Mn_{17}Fe_{22}Co_{24}Ni_{24}Cu_{13}$). This slow cooling approach has proven to provide an alternative path for identifying stable, single-phase alloys, and is a good complement to the combinatorial thin film approach. Although this slow cooling approach does not yield a wide alloy space for exploration, it does generate stable alloys, since the system tends to approach this composition on its own. We processed an equivalent alloy using rolling and heat treatment to obtain equiaxed grain structures, with a range of grain sizes. Tensile testing has shown that alloy strength and ductility are both high. These results are shown in Figure 1, where the non-equiatomic alloy is seen to exhibit better tensile mechanical properties than its equiatomic counterpart.

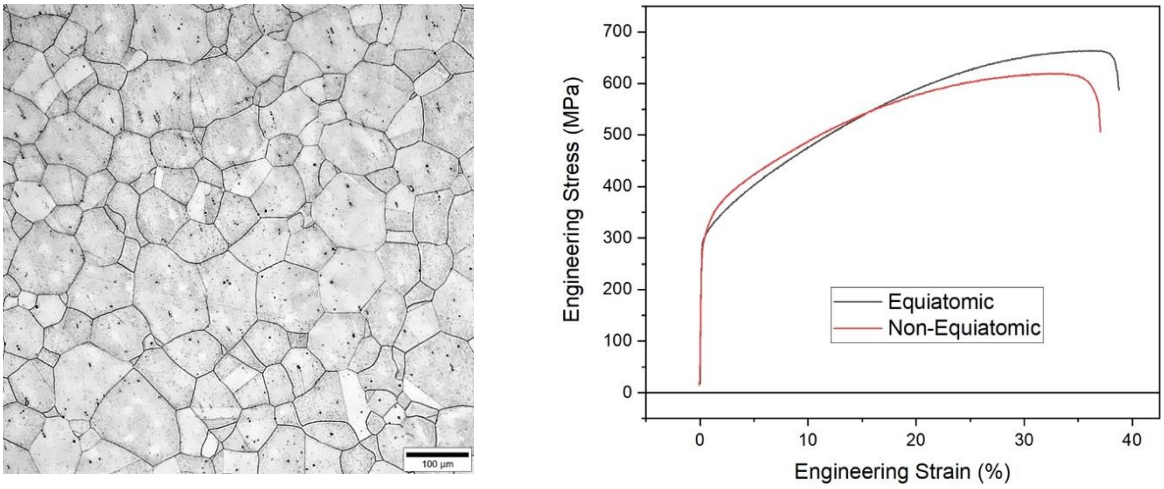

Figure 1. Optical micrograph of rolled and heat treated non-equiatomic MPEA $Mn_{17}Fe_{21}Co_{24}Ni_{24}Cu_{14}$. Tensile stress-strain curves for the non-equiatomic MPEA and its equiatomic counterpart MnFeCoNiCu.

The thermal stability of this non-equiatomic alloy is also significantly better than the equiatomic alloy. Samples of both materials were homogenized using rolling and recrystallization, then were annealed to assess the impact on microstructure. As shown in Figure 2, the non-equiatomic alloy retained its homogenous composition and elemental distribution, while the equiatomic alloy decomposed into a multi-phase microstructure. Moreover, we have

performed preliminary oxidation testing on the alloy $Mn_{17}Fe_{21}Co_{24}Ni_{24}Cu_{14}$, and it exhibits significantly better oxidation resistance than the equiatomic alloy (and the Cantor alloy).

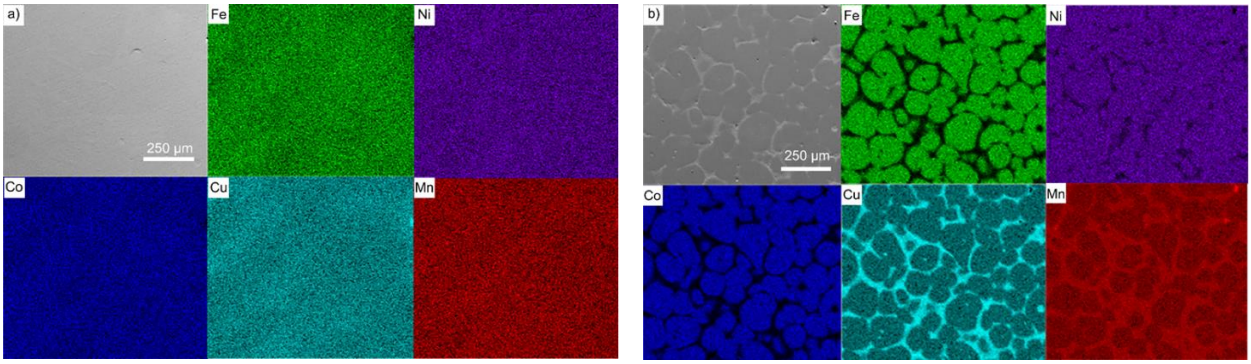

Figure 2. Optical micrographs and EDS maps of (a) annealed non-equiatomic MPEA $Mn_{17}Fe_{21}Co_{24}Ni_{24}Cu_{14}$ and (b) annealed equiatomic MnFeCoNiCu, which formed a multi-phase microstructure.

Additional work was performed on a BCC refractory MPEA system, motivated by a collaboration with LBNL scientists (Chrzan, Asta and Minor). Combinatorial thin film samples were prepared for the refractory system chosen for this project (VNbMoTaW). This system was chosen because it had been predicted that as Mo is replaced by Nb, meaning that the alloy composition approaches VNb_2TaW, the system should transition from highly brittle to highly ductile. In order to accomplish the goals of the project and also gauge the extent of the alloy space available for producing bulk single-phase MPEA samples over this composition range, we have gone through several iterations of combinatorial thin film samples. A challenge in this area has been the accurate determination of alloy composition at each film location. Because we initially deposited films on silicon substrates, there was overlap between the Si peak and the Ta/W peaks of the film. This made it difficult to know whether the compositions were correct. Subsequent depositions were performed on alternate substrates (Kapton and sapphire), which enabled accurate determination of composition at each location. The characterization of MPEA crystal structure at each film location delivered a positive result, namely that the extent of single-phase BCC stability for these MPEAs is broad. In fact, most of the film locations indicated a single-phase BCC structure, with only a small number of locations yielding different structure. Specifically regarding the trade-off between Nb and Mo, the film remains single-phase BCC when half of the Mo is replaced by Nb (and vice-versa) relative to the equiatomic composition. Therefore, we are confident that bulk alloys in the VNbMoTaW can be made such that Nb replaces Mo, with all alloys retaining the same crystal structure. This will require thermomechanical processing that we could not access at the time of proposal submission. However, the PO recently acquired a new piece of equipment that should allow the thermomechanical processing of refractory MPEAs, as well as high-temperature tensile testing in a controlled atmosphere.

Future Plans

Our research plan for the near term includes a continued focus on the links between thin film screening and bulk alloy fabrication. In the FCC system (similar to the Cantor alloy composition), we will expand the alloy space around ($Co_{24}Fe_{22}Ni_{24}Mn_{17}Cu_{13}$) using combinatorial gradient films and then fabricate suitable samples for mechanical testing. In the BCC system, we will fabricate several bulk alloys and thermomechanically process them to achieve a suitable microstructure for assessing their mechanical properties in tension. This is important for the collaborative efforts with LBNL. The PI has recently acquired a new piece of equipment (Gleeble 3500) that can process/test alloys under conditions that mimic those used in industry. The Gleeble will allow us to take as-cast MPEA samples and subject them to rolling conditions at high temperature, followed by heat treatment to achieve equiaxed grain structures. The Gleeble is also able to perform hot tension experiments under controlled environment (vacuum or controlled gas), and bulk MPEA samples will be tested to assess their ductility.

References

1. Gludovatz, B., Hohenwarter, A., Catoor, D., Chang, E.H., George, E.P. and Ritchie, R.O., "A fracture-resistant high-entropy alloy for cryogenic applications," *Science* **345**, 1153 (2014).
2. Gludovatz, B., George, E.P. and Ritchie, R.O., "Processing, Microstructure and Mechanical Properties of the CrMnFeCoNi High-Entropy Alloy," *JOM* **67**, 2262 (2015).
3. Miracle, D.B. and Senkov, O.N., "A critical review of high entropy alloys and related concepts," *Acta Materialia* 122, 448 (2017).

Publications

No publications yet for this BES-supported work

Global aspects of microstructural evolution in irradiated alloys: Effects of self-organization

Pascal Bellon, Robert S. Averback, Shen J. Dillon

Department of Materials Science and Engineering, University of Illinois at Urbana-Champaign, Urbana, IL

Program Scope

The next generation of nuclear power systems requires structural materials that can operate safely and economically in harsh conditions, in particular resisting to high levels of radiation damage at elevated temperature. Such materials, driven far from equilibrium, constitute dissipative systems that have a strong tendency for developing self-organized microstructures. One strong attractive characteristic of these self-organized microstructures is they are stable steady states, thus ensuring that materials properties are stable over time. Furthermore, it has been recognized recently that some of these microstructures contain a high number density of nanoscale features that can promote trapping and recombination of point defects, and trapping of rare gas atoms, thus improving the overall performance under irradiation. Most of the past works on self-organization under irradiation focused on isolated elements of the microstructure, such as precipitates [1], voids and bubbles, [2,3] grain boundaries [4-6]. Recent results, as well as critical re-analysis of past results, suggests however that self-organization takes place globally, coupling all the elements of the microstructure. Our new research effort aims at elucidating these global aspects of microstructural evolution under irradiation, including the validity of a local forcing analysis and the dynamical coupling of sub-systems of the microstructure. Fundamental understanding of global self-organization under irradiation is expected to offer new ideas about designing new radiation resistant materials. This research could have far broader impact by stimulating and guiding research on other aspects of self-organization in dissipative materials systems, the so-called driven alloys.

Research Plans

Our project will investigate the microstructural evolution of two-phase Ni-based alloys during energetic particle irradiation, determining how compositional patterning (CP) couples to other parts of the microstructure, such as dislocation loops, chemical ordering, and grain boundaries. The project includes both experimental and theoretical modeling to achieve our goals. The experiments involve, primarily, irradiations of two-phase Ni-Al and Ni-Si γ-γ' alloys. We will first determine if these alloys form a precipitate structure that self-selects in steady state a fixed length scale, i.e., precipitate size, morphology, and density, as well as fixed alloy compositions in the γ and γ' phases. We will then determine how this "compositionally patterning" couples to

other parts of the microstructure. Characterization of the alloys will be performed using atom probe tomography, transmission electron microscopy and scanning transmission electron microscopy to measure in particular the density, size, composition and order of precipitates, their location in relationship to dislocation loops and grain boundaries, as well as the solute concentration in the matrix and at grain boundaries.

The experimental component of the research will be supported by theoretical modeling, primarily through the development of a phase field model to explore how different kinetic parameters influence the microstructural evolution of the alloys and to provide guidance for interpreting the experimental results. The modeling consists of three tasks, first studying composition patterning in isolation in ordering alloys such as Ni-Al and Ni-Si, then assessing the influence of net fluxes on compositional patterning, and lastly investigating the coupling between compositional patterning and defect sinks such as dislocation loops and grain boundaries.

1. *Coupling between CP and dislocation loops: basic processes*

We first consider the coupling between CP and irradiation-induced dislocation loops. A first possible consequence of coupling is the suppression of loop nucleation and growth arising from the competition between loops and a high density of nanoprecipitates for freely migrating defects. Similar consequences of CP would be expected for void swelling and creep. Our focus is on the broader issues outlined in Fig. 1. For example, in Fig. 1(a) we envision the possible coupling between CP and dislocation loops, and will explore it using γ-γ' Ni-Al alloys as a model system. This choice is motivated, in part, by the works of Nelson et al [7] and Schmitz et al. [8], but also by its relevance to precipitation-hardened alloys such as PE-16.

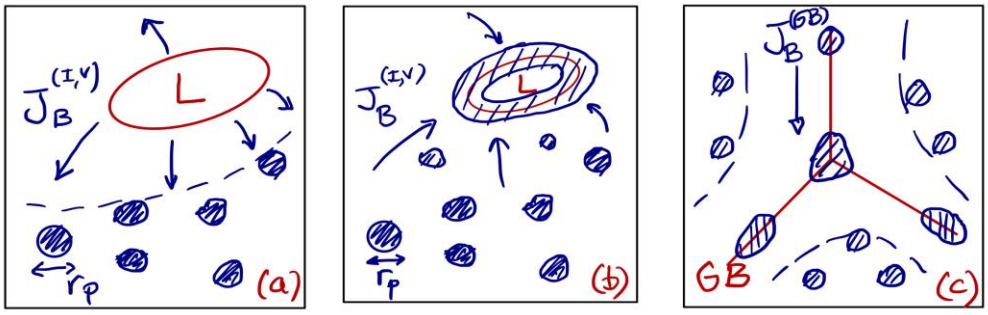

Fig. 1 Schematic microstructures of possible interactions under irradiation between nanoprecipitates of radius r_p stabilized by compositional patterning (CP) and elements of the microstructures, such as dislocation loops (L) in (a,b) and grain boundaries (GB) in (c). In (a) an inverse Kirkendall effect induces a solute flux J_B^V that depletes the region near the loop resulting in the possible absence of CP there, while in (b) solute drag to the loop leads to precipitation on the loop and may extend patterning. In (c), even in the absence of flux coupling, fast thermal diffusion along grain boundaries $J_B^{(GB)}$ competes with solute recoil into the matrix, which could result in a stable steady-state size for GB precipitates.

The first task will be to establish that CP does indeed occur in Ni-Al γ-γ' alloys, as assumed in Fig. 1(a). Potter and Hoff [9] had shown that after an irradiation dose of ~ 5 dpa at 550 °C, the region in the vicinity of loops becomes depleted of γ', Fig. 2(a), and sketched in Fig. 1(a). One possible explanation for this behavior, suggested by Potter and Hoff involves radiation-induced segregation. Alternative explanations arise, however, if dislocation loops are the dominant sink for point defects, since the defect concentrations nears sinks are dramatically reduced. Such a reduction would increase the forcing parameter, γ_b. Furthermore, our recent phase field simulations suggest that CP leads to an inverse Gibbs-Thomson effect, which should also contribute to the coupling between the dislocation loops and the regions far from the loops. Lastly, the chemical order parameter of the precipitates near the dislocation loops should also couple to their size, thus affecting their stability. This alloy system represents thus a rich model alloy to gain an understanding of the underlying coupling mechanisms.

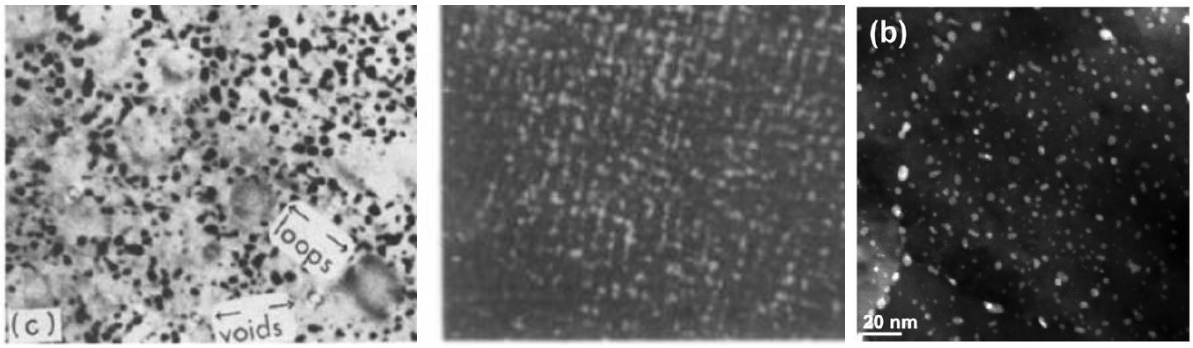

Fig. 2 Microstructures of irradiated alloys similar to the schematic ones sketched in Fig. (2): (a) bright-field TEM of Ni-14 at% Al irradiated with 3.2 MeV Ni ions at 550 ˚C to 1.7 dpa with dose rate 2.7x10^{-3} dpa-s^{-1} [9]; (b) superlattice dark-field TEM Ni-6 at% Si irradiated with Ni ions at 400 ˚C to a dose of 10 dpa [10]; (c) Z-contrast STEM Cu-1.5at% W irradiated with 1.8 MeV Kr ions at 600 ˚C to 80 dpa [11].

2. *Coupling between CP and dislocation loops: radiation-induced segregation*

We will then investigate the coupling between CP and segregation more directly using the Ni-Si alloy system, where strong binding of interstitial atoms to Si leads to robust RIS effects. Si is known to segregate to GB's and forms γ' precipitates (Ni_3Si), even in nominally understaturated alloys, as sketchd in Fig. 1(b) and illustrated in Fig. 2(b). Barbu and Ardell showed such precipitation for alloys with Si concentrations as low as 2 at.% [12]. Our goal here is determine whether these γ' precipitates undergo compositional patterning. Unlike the case of Ni-Al, the competing dynamics is between recoil mixing and RED tending to homogenize the alloy versus the segregation flux leading to precipitation.

3. *Coupling between CP and grain boundaries*

Our proposed research for elucidating the coupling between CP and GBs follows our approach for studying CP coupling with dislocations. GB's like dislocation loops are a sink for point defects and therefore will lead to local variations in γ_b and possibly also to segregation by the

inverse Kirkendall effect. Examining the interaction of CP with GB's, however, is somewhat simplified since the grain size can be fixed from the outset, and it is expected to change only slowly with irradiation dose. GB's, however, add a new dimension to the problem since, as sketched in Fig. 1(c), grain boundary diffusion can introduce in a new anisotropic forcing parameter, g_b^{GB}, in the boundaries. This may lead to CP on the GB's, but with different control variables as those for the grain interiors. The thrust of the experiments, therefore, is to carefully characterize the microstructure as a function of composition, temperature, and dose to map out the interplay between CP and GBs. The first tasks will be to determine whether CP can take place at grain boundaries, and if so, to determine the influence of CP at grain boundaries on the stability of intragranular CP.

Perspectives

Our program is expected to impact several aspects of the field of driven alloys. If our hypotheses regarding the strong influence of compositional patterning in these materials bears out, we believe it will dramatically alter our current thinking about the response of these materials to irradiation, not only calling for revision of past explanations of experiments, but also revising our ideas about designing new radiation resistant materials. Specifically, a key finding of this work will be to demonstrate the importance of the local nature of the nonequilibrium forcing introduced by irradiation, and its coupling with the permanent defect fluxes imposed by irradiation.

References

[1] R. A. Enrique and P. Bellon, Phys Rev Lett **84**, 2885 (2000).
[2] Y. P. Gao, Y. F. Zhang, D. Schwen, C. Jiang, C. Sun, and J. Gan, Materialia **1**, 78 (2018).
[3] Y. P. Gao, Y. F. Zhang, D. Schwen, C. Jiang, C. Sun, J. Gan, and X. M. Bai, Sci Rep **8**, 6629, 6629 (2018).
[4] N. M. Ghoniem and D. Walgraef, *Instabilities and self-organization in materials* (Oxford University Press, Oxford ; New York, 2008), Oxford science publications, 63.
[5] A. J. Ardell and P. Bellon, Curr Opin Solid St M **20**, 115 (2016).
[6] M. Nastar and F. Soisson, in *Comprehensive Nuclear Materials*2012), pp. 471.
[7] R. S. Nelson, D. J. Mazey, and J. A. Hudson, J Nucl Mater **44**, 318 (1972).
[8] G. Schmitz, J. C. Ewert, F. Harbsmeier, M. Uhrmacher, and F. Haider, Phys Rev B **63**, 224113, 224113 (2001).
[9] D. I. Potter and H. A. Hoff, Acta Metall Mater **24**, 1155 (1976).
[10] A. Barbu and G. Martin, Scripta Metall Mater **11**, 771 (1977).
[11] S. P. Shu, X. Zhang, J. A. Beach, P. Bellon, and R. S. Averback, Scripta Mater **115**, 155 (2016).
[12] A. Barbu and A. J. Ardell, Scripta Metall Mater **9**, 1233 (1975).

Publications

J. Lee, J. Beach, P. Bellon, R. S. Averback, “High thermal coarsening resistance of irradiation-induced nanoprecipitates in Cu-Mo-Si alloys”, Acta Mater. **132**, 432-443 (2017).

S. J. Dillon, D. C. Bufford, G. S. Jawaharram, X. Liu, C. Lear, K. Hattar, and R. S. Averback, Irradiation-induced creep in metallic nanolaminates characterized by In situ TEM pillar nanocompression, Journal of Nuclear Materials **490**, 59 (2017).

G. S. Jawaharram, S. J. Dillon, and R. S. Averback, Hardening mechanisms in irradiated Cu-W alloys, Journal of Materials Research **32**, 3156 (2017).

Z. Li and D. R. Trinkle, Mesoscale modeling of vacancy-mediated Si segregation near an edge dislocation in Ni under irradiation, Physical Review B **95**, 144107 (2017).

T. Schuler, D. R. Trinkle, P. Bellon, R. S. Averback, “Design principles for radiation-resistant solid solutions”, Phys. Rev. B **95**, 174102 (2017).

D. R. Trinkle, Automatic numerical evaluation of vacancy-mediated transport for arbitrary crystals: Onsager coefficients in the dilute limit using a Green function approach, Philosophical Magazine **97**, 2563 (2017).

X. Liu, R. Hao, S. Mao, and S. J. Dillon, Shear strengths of FCC-FCC cube-on-cube interfaces, Scripta Materialia **130**, 178 (2017).

C. Lear, P. Bellon, R. S. Averback, “Novel mechanism for order patterning in alloys driven by irradiation”, Phys. Rev. B **96**, 104108 (2017).

Y. Ashkenazy, N. Pant, J. Zhou, P. Bellon, R. S. Averback, “Phase evolution of highly immiscible alloys under shear deformation: Kinetic pathways, steady states, and the lever-rule”, Acta Materialia **139**, 205-214 (2017).

J. A. Beach, M. Wang, P. Bellon, S. Dillon, Y. Ivanisenko, T. Boll, R. S. Averback, “Self-organized, size-selection of precipitates during severe plastic deformation of dilute Cu-Nb alloys at low temperatures”, Acta Materialia **140**, 217-223 (2017).

T. Schuler, P. Bellon, D. R. Trinkle, R. S. Averback, “Modeling the long-term evolution of dilute solid solutions in the presence of vacancy fluxes”, Phys. Rev. Mater. **2**, 073605 (2018).

G. S. Jawaharram, P. M. Price, C. M. Barr, K. Hattar, R. S. Averback, and S. J. Dillon, High temperature irradiation induced creep in Ag nanopillars measured via in situ transmission electron microscopy, Scripta Materialia **148**, 1 (2018).

C. Lear, R. Averback, P. Bellon, A. E. Sand, M. Kirk, "Unusual irradiation-induced disordering in Cu3Au near the critical temperature: An in situ study using electron diffraction", J. Mater. Res. 33, pp. 3841-3848 (2018).

K. Nordlund, S. J. Zinkle, A. E. Sand, F. Granberg, R. S. Averback, R. E. Stoller, T. Suzudo et al. "Improving atomic displacement and replacement calculations with physically realistic damage models." Nature communications **9**, 1084 (2018).

K. Nordlund, Kai, S. J. Zinkle, A. E. Sand, F. Granberg, R. S. Averback, R. E. Stoller, T. Suzudo et al. "Primary radiation damage: a review of current understanding and models." J. Nucl. Mater. **512**, 450-479 (2018).

D. R. Trinkle, Variational Principle for Mass Transport, Physical Review Letters **121**, 235901 (2018).

N. Verma, N. Pant, J. A. Beach, J. Ivanisenko, Y. Ashkenazy, S. J. Dillon, P. Bellon, R. S. Averback, "Effects of ternary alloy additions on the microstructure of highly immiscible Cu alloys subjected to severe plastic deformation: an evaluation of the effective temperature model", Acta Mater. **170**, 218-230 (2019).

The role of subgrain heterogeneous processes in slip localization in polycrystalline metals during cyclic plasticity

Irene J. Beyerlein, University of California at Santa Barbara

Program Scope

Improved prediction of the behavior of materials under the monotonic and cyclic loading conditions encountered in structural components is critical to ensure reliable, long-term performance and to guide the design of new materials that can withstand extreme environments. For most classes of metallic materials, a major challenge in advancing prediction still lies in the strong dependence of highly localized plastic deformation processes on seemingly many microstructural features presiding at the nanoscale, microscale and mm-scale. Recent advances in experimentation and modeling are now enabling assessments in real time and within a microstructural framework. In this program, which began in August 2018, we bring these to bear to study microstructure-sensitive slip band localization in metals. Our overarching goal is to build the fundamental understanding of the slip-based processes that eventually lead to fatigue crack initiation, such as the formation of intense slip bands and chains of such intense bands across a microstructure, to a depth that enables prediction and material design.

The approach we use involves three sets of new methods, which, when combined, provide a complete picture of when, where, and which slip processes form during monotonic and cyclic loading. The first technique is *in-situ* High Energy X-ray Diffraction Microscopy (HEDM). Possessing both global scope and local resolution, HEDM can interrogate the distribution of orientations and strains within every crystal inside a deforming polycrystal with subcrystalline resolution. Time-resolved HEDM data can detect *when* slip heterogeneities form. The second method is a set of spatially resolved microstructure data generated via the new 3D TriBeam and advanced in situ HR-DIC approaches. These are integrated with the other efforts to determine *where* heterogeneities form. The third component is a series of recent time- and spatially resolved crystal plasticity gradient-based microstructure materials models. We extend these to identify *which* slip processes cause slip bands to form and transmit across grain boundaries.

Recent Progress

Role of microstructure on strain concentrations. Upon macroscopic loading and while the material is still globally elastic, many grains undergo highly localized plastic deformation in the form of slip bands. At the onset of globally plastic deformation, a few of these slip bands intensify, strengthen, and serve as precursors to persistent slip bands and eventual crack initiation. Experiments show that the more intense slip bands often form at coherent twin boundaries. While this is a frequent occurrence in many fcc metals containing annealing twins, it is not clear why these bands prefer to develop most often (but not always) along a twin boundary.

In this research, we first focused on the role mesoscale microstructure plays on the early developments of localized elastic strain concentrations. In the experiment, a Ni based superalloy was strained to different levels, below and above the macroscopic elastic-plastic transition. Figure 1 shows one such localized slip band identified in the material after a small amount of externally applied deformation, at a level still lying in the elastic regime. A series of 3D crystal plasticity microstructure calculations were carried out in which the same explicit microstructure was (a) idealized with elastic isotropy, (b) less elastic anisotropy or (f) idealized with simplified neighborhood. Nearly identical strain fields develop in the grain, including the intense localization, with elastic anisotropy, even when the microstructural details of the neighborhood are averaged out as a homogeneous matrix. This result suggests that the high elastic strain concentration results from the grain being surrounded entirely by elastically harder nearest neighbors. Specifically, with these calculations we uncover that elastic strain localization is favored when: (i) the grain is elastically softer than all nearest neighbors, (ii) the grain has a non-equiaxed shape with sharp corners as potential stress concentrators created by traversing twin boundary planes; and (iii) the loading axis to twin plane orientation causes a high shear boundary traction.

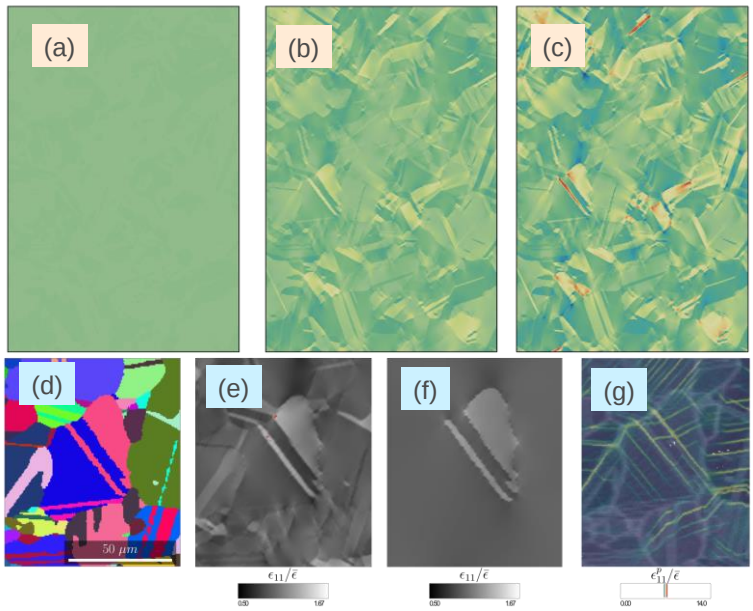

Figure 1. (a) EBSD map of a twin (g4) in a parent grain (g1) containing a slip band at the twin boundary. (b) DIC lattice rotation map exposing an orientation gradient zone at the tip of a slip band, (c) micromechanical model of a slip band in the same local neighborhood and (d) calculated lattice rotation map

These results explain how the presence of annealing twins significantly increases the probability of localization. First, given the large misorientation characteristic of fcc twin boundaries and elastic anisotropy, it becomes highly probable that either the grain or annealing twin across the twin boundary are elastically softer than its annealing twin or grain neighbor. Second, the presence of annealing twins increases the number of high-aspect ratio grains and creates sharp corners, which serve as stress and strain concentrators.

Irreversibility in orientation gradients. Fatigue crack initiation is intimately linked to plasticity processes on the grain scale and below and these processes induce lattice orientation heterogeneities. In this project, we use multiple experimental characterization methodologies,

capable of quantifying structure (including lattice orientations) on different length scales, to study changes in the crystal orientation distributions during cyclic loading. We analyze far-field HEDM data to track the distribution of lattice orientations within every crystal as a commercially pure copper test specimen is cyclically loaded. As changes in the distribution of orientations within a crystal can be linked directly to slip system activity, we posit that slip band localization correlates with grains exhibiting the greatest changes in their lattice orientation distributions. We examine the lattice orientation "cloud" or grain orientation envelope (GOE) within each copper crystal in orientation space to specifically study how the size of each GOE evolves during cyclic loading. In the HEDM experiment, the crystals that had the 40 largest GOEs at the tensile loop tip in the first loading cycle through subsequent cycles are tracked. Figure 2 depicts *changes* in the average cloud size of these top 40 crystals to the rest of the crystals in the aggregate for cycles 2 and 256 at various points around the hysteresis loops. The top 40 average cloud size remains larger than the rest of the aggregate, which we suspect indicates that these 40 crystals are the ones most susceptible to microcrack initiation. An important finding achieved within the first year of this project is that the dispersion in the orientation within a grain are irreversible. Further, these intragranular orientation gradients are seen to grow with each cycle.

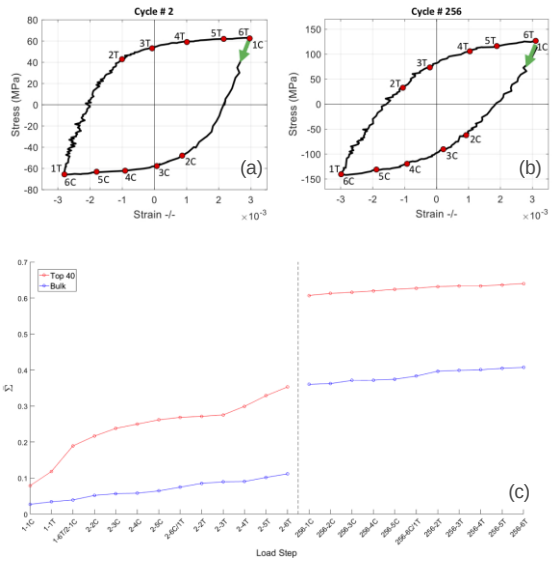

Figure 2 (a-b) Hysteresis loops from cycles 2 and 256 *in situ* cyclic loading / HEDM experiment on copper. Red markers indicate where HEDM experiments were conducted. (c) Changes in average cloud size for the top 40 crystals compared to the remaining bulk crystals within the copper aggregate at the load steps in the HEDM experiment. The first number in a load step corresponds to the cycle number (1, 2 or 256).

Future Plans

In the next year we plan to identify the sources for orientation gradients during deformation. By combining 3D micromechanical modeling of orientation development in 3D, in-situ DIC and in-situ HEDM, we hope to identify those grains and grain neighborhood properties that prompt the locally high stresses, slip band formation, and irreversible orientation gradients. Figure 3 shows some initial results using two methods, H-DIC and micromechanical modeling of slip bands. The H-DIC lattice rotation map in Fig. 3(b) displays an example of one prevailing origin of orientation gradient, which lies at the tips of intense slip bands, in the neighboring grain. Here a prominent orientation-gradient zone emanates and extends in the neighboring grain. Explicit modeling of the slip band in Fig. 3(c) within this same local neighborhood reveals a similar zone (Fig. 3d), one that is extensive due to the intensity of the slip band and the particular orientation of the neighboring

grain. With these tools, we have the opportunity to study the micromechanics behind slip band transmission and development of growing orientation gradients near intense slip bands observed experimentally.

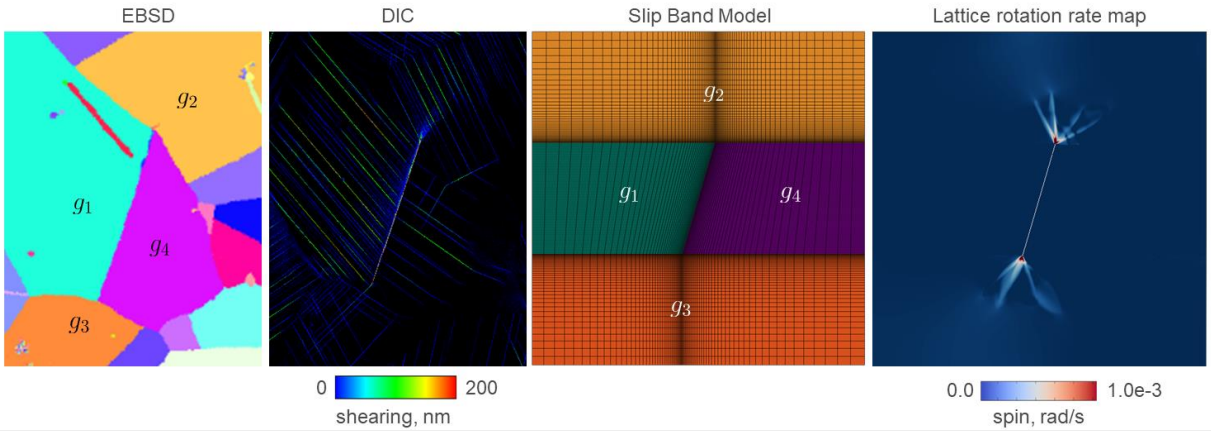

Figure 3. (a) EBSD map of a twin (g4) in a parent grain (g1) containing a slip band at the twin boundary. (b) DIC lattice rotation map exposing a orientation gradient zone at the tip of a slip band, (c) micromechanical model of a slip band in the same local neighborhood and (d) calculated lattice rotation map

Also, in the next year, we aim to identify the orientation gradient-driven processes and their relationship to the strengthening of slip bands during cyclic loading. We plan to combine two in-situ techniques, H-DIC and HEDM, to study the development of localized orientation gradients in 2D and 3D at different strain points in the cycle (Fig. 4). The key is to use the formation of those extensive zones of high orientation gradient generated at the tips of slip bands seen in H-DIC (Fig. 3b) as a "signature" of intense slip band development in 3D HEDM. The *in-situ* HEDM studies will be conducted to capture the stress and orientation evolution within each crystal at different points in the hysteresis loop, and from one cycle to the next. The full stress tensor and GOE will be extracted for each grain. 3D spatial maps of the orientations will be collected (Fig. 4). These data will be used to build an understanding of plastic responses during fatigue, and to prepare for an *in-situ* study that combines both modalities, obtaining datasets for the same grains in the same volume at different stages of cyclic loading.

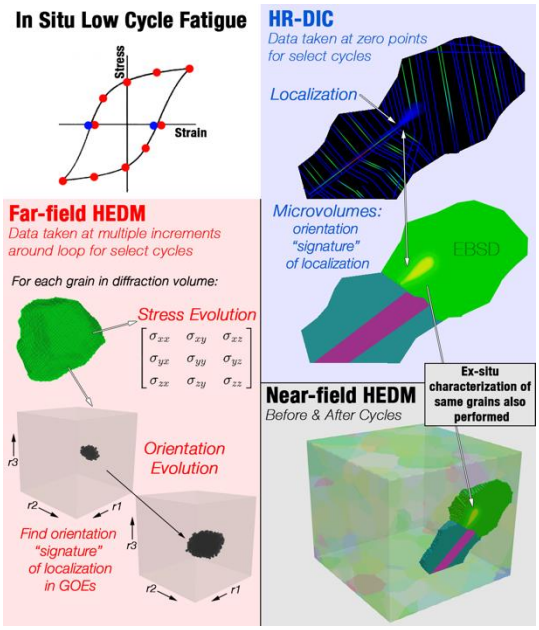

Figure 4. In-situ H-DIC and HEXM low cycle fatigue experiments for identifying when slip localization occurs and in which grains in the cycle

Publications

J.C. Stinville, P.G. Callahan, M.A. Charpagne, M.P. Echlin, V. Valle, T.M. Pollock, "Direct Measurements of Slip Irreversibility in a Nickel Base Superalloy using High Resolution Digital Image Correlation", Submitted to *Acta Materialia* (2019)

Marat I. Latypov, Jean-Charles Stinville, Jason R. Mayeur, Tresa M. Pollock, Irene J. Beyerlein, "Micromechanical study of elastic strain localization in René 88DT with annealing twin boundaries", Submitted to *Scripta Materialia* (2019)

Matt Miller, Chris Budrow, Tim Long, and Mark Obstalecki, "Understanding the evolving state of deforming polycrystals using synchrotron x-rays", Submitted to the *40th Risø Symposium* (2019)

Characterization and Modeling of Deformation Induced Damage in Hexagonal Alloys

Principal Investigators: C.J. Boehlert, T.R. Bieler, M.A. Crimp, and P. Eisenlohr
Michigan State University, 428 S. Shaw Lane, Rm 2100 Engr. Bldg., East Lansing, MI 48824

Program Scope

Over the course of this program, we have used synergistic experimental and computational approaches to examine heterogeneous deformation processes that lead to damage nucleation at interfaces in hexagonal titanium alloys. Characterization methods have included slip trace analysis, nanoindentation, and synchrotron based 3-D X-ray diffraction tomography to identify local strains and orientation gradients. Crystal plasticity finite element and Fast-Fourier based solvers have been used to simulate deformation of experimentally characterized microstructures. These simulations have enabled direct comparisons between models and experiments, revealing where better modeling approaches are necessary to establish a paradigm in which the physical processes responsible for damage nucleation in polycrystals can be simulated.

Recent Progress

A critical part of crystal plasticity models is to quantitatively identify how slip systems operate in Ti alloys, and three of our recent efforts focusing on this theme are: 1) Three different experimental methods were used to *determine the critical resolved shear stress (CRSS)* in the same material [1]. These results show that the CRSS values depend on the method, so the credibility of these methods has been assessed. In addition, by combining slip trace analysis, TEM, 3D X-ray measurements, and simulated deformation of a particular experimentally characterized microstructure patch, mechanistic phenomena not easily explained using only experimental or modeling approaches alone have been clarified. 2) A method to enable *identification of localized slip system activity* in 1 micron voxels, located hundreds of microns below the surface, has been developed. This capability greatly extends the opportunity to examine dislocation substructure mechanisms in 3-D, well beyond commonly used EBSD based GND analysis on a 2-D surface, without requiring any sample surface preparation. 3) Two approaches to *investigate slip transfer of dislocation activity through grain boundaries* have been developed; one that reveals new insights on the mechanisms of the subsurface slip transfer process (described below), and another experimental and computational modeling approach, in collaboration with IMDEA Materiales during Bieler's sabbatical in Madrid, that introduces slip transfer into crystal plasticity models (described in [2,3]).

1. Assessment of various methods for measuring critical resolved shear stress (CRSS) values

The plastic anisotropy of hexagonal materials makes the numerical prediction of their plastic behavior challenging and depends critically on the knowledge of CRSS values. We assessed the reliability of three experimental methods to quantify CRSS values of the different hexagonal slip families with simulations based upon: (a) the *statistics of observed surface slip traces* in a deformed polycrystal; (b) *an inverse indentation method where CRSS values are adjusted iteratively* until a simulated indentation into a particular crystal orientation matches the corresponding computational experiment in terms of the load–displacement response and the residual surface topography of the indent; (c) *direct measurement of the resolved shear stress at yield; i.e. observed RSS = CRSS* (using lattice strains from in-situ high-energy X-ray diffraction microscopy, HEDM) in grains for which single-family slip can be deduced from specific lattice reorientation conditions. To compare these three methods, virtual experiments were performed on synthetic microstructures to assess how reliably each method recovers a prescribed set of CRSS values using a phenomenological constitutive material description. The resulting CRSS values using method (a) strongly depend on the ability to observe slip traces from all

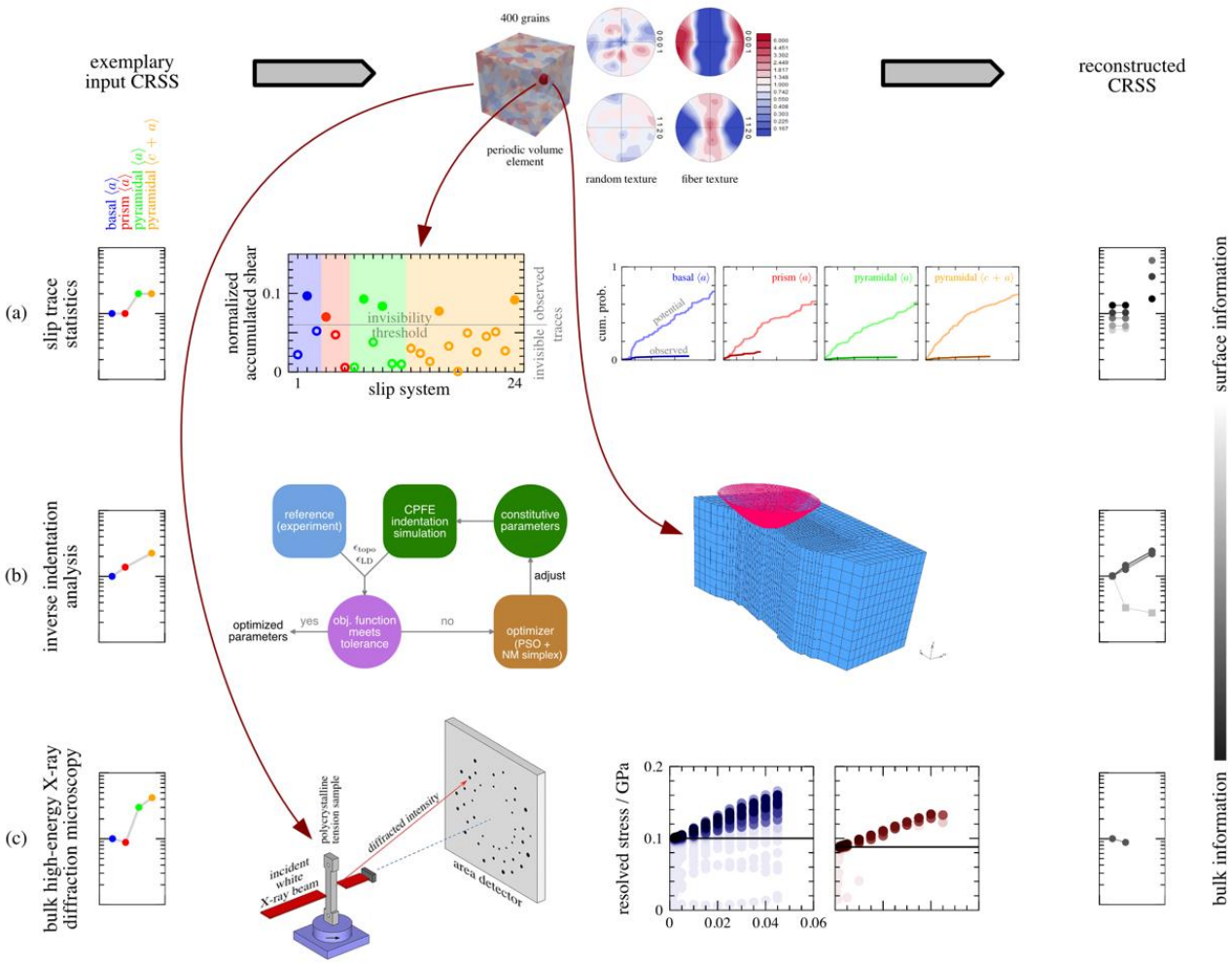

active slip systems, which introduces experimental uncertainty. For the *inverse indentation method* (b), the predicted CRSS values are within 8% of their reference CRSS values for the two cases investigated with different orientations. The simulation of the HEDM method (c) determined CRSS values for basal and prism slip reliably, but the method lacks a suitable criterion to assess pyramidal slip. In summary, the HEDM method (c) appears to be more accurate than either the inverse indentation analysis (b) or statistical slip trace analysis (a). From a broader perspective, it is noteworthy that the slip trace measurements are strictly surface measurements. In contrast, the HEDM is a bulk measurement, while inverse indentation analysis is a combination of both surface and interior slip behavior (but without any complicating factors associated with grain boundaries). The inability of extracting bulk plastic behavior from surface slip trace observations suggests that differences in dislocation substructure evolution, stress environment, and the presence of image forces close to a free surface could influence the measurement of CRSS values.

2. Dislocation content from differential aperture X-ray peak streak analysis

The subsurface dislocation content in a Ti-5Al-2.5Sn (wt.%) uniaxial tension sample deformed at ambient temperature was assessed using peak streak analysis of micro-Laue diffraction patterns collected non-destructively by differential aperture X-ray microscopy (DAXM) and transmission electron microscopy (TEM) from the same volume of material. To determine whether the mostly near-screw dislocation content observed in the TEM foil can be identified by a (nominally pure) edge dislocation-based analysis of the streaked diffraction peaks in the red circle from a DAXM voxel (red

sphere in figure on next page) that is close to the TEM foil location was analyzed. The major streak direction in all three analyzed peaks are only consistent with $\mathbf{a}_3$ dislocations on basal planes, which are the predominant dislocations found in the TEM analysis. The critical observation is that although the peak streak analysis model is based on an edge dislocation assumption, the analysis successfully determines the Burgers vectors of the dominant dislocations although the dislocations are predominantly screw in character. Despite the fact that the majority dislocation content is correctly identified by the streak analysis, significant other dislocation content observed in the TEM foil was not clearly identified, *i.e.*, neither the prismatic nor basal $\mathbf{a}_1$ dislocation content resulted in identifiable streaked peaks. Expanding this analysis to include the orientation gradient with neighboring voxels, involving use of the Frank-Bilby equation, enables the density of GNDs on each slip system to be determined spatially, which is the subject of papers in preparation.

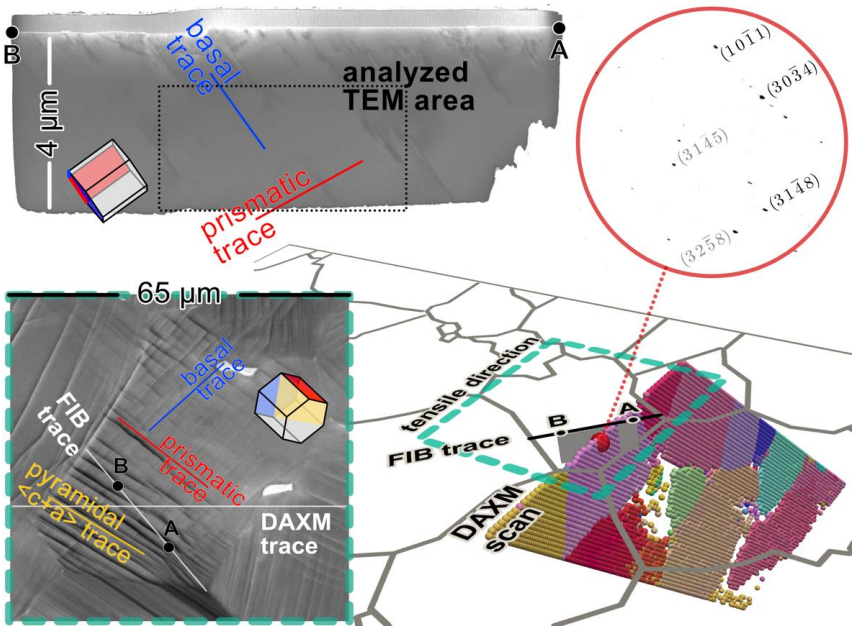

3. Insights into dislocation slip accommodation across grain boundaries

Slip transfer across grain boundaries is commonly observed in relation to slip traces such as those shown in the top left image on the next page. Because the slip planes associated with these correlated traces are not coplanar, understanding of how slip transfer takes place through the boundary is investigated using atomic force microscopy (AFM), electron channeling contrast imaging (ECCI), and serial sectioning. Cases where one slip system is accommodated by a single system in the neighboring grain (left column figures on the next page) have been compared to the situation where the single system is accommodated by two distinct slip systems in the neighboring grain (right column figures on the next page).

To assess the shear in the two distinct slip system case, AFM was used to determine the total shear in all of the slip bands meeting at the boundaries and, in turn, the total residual Burgers vector remaining within the boundary. In all cases of double slip accommodation, the experimentally observed activity corresponds with the calculated minimization of the residual Burgers vector between slip systems 1 and 2 in the receiving grain (blue minimum on the lower right hand side plot). Similar calculations of the optimum shear transmission show that in experimentally observed single slip accommodation (such as in the left column), the activity expected on any secondary slip system is either minimal or zero, which was observed in the majority of the cases examined. These results conclusively show that the primary motivating factor in shear accommodation at grain boundaries is the minimization of the residual Burgers vector.

Nevertheless, this assessment does not explain how the shear is accommodated when the corresponding slip plane intersections at the grain boundary do not meet at common lines below the surface. Also, it is not clear if the free surface in typical '2-D' studies influences the observation of slip transfer. A secondary electron image showing the traces of two prism <a> slip systems meeting at common points on the grain boundary is shown in the left hand side top figure. An ECC image of the same area after removing approximately 5 µm is shown in the left hand side middle image. While

the spacing between the slip bands in the respective grains remains the same, the distance between each slip band intersection with the grain boundary is displaced by ~7 µm. Detailed ECCI analysis in the area within the red box in the left hand side middle image indicates that the two slip systems remain correlated by cross slip onto a secondary slip plane. In this particular case, a pyramidal <a> slip system (indicated by small arrows in lower left hand side image), carries the slip from the intersection point of the prism <a> slip system in the upper grain to merge with the primary slip system in the lower grain. In all such cases, the secondary accommodating slip system has the same Burgers vector as the primary accommodating slip system. However, these secondary accommodating systems typically have significantly higher CRSS (i.e. the primary prism <a> slip is much easier to activate than the secondary pyramidal <a> slip). This observation suggests that the surface indeed influences the observation of slip transfer. This analysis also confirms that the critical factor in accommodating slip is the minimization of the residual Burgers vector, and that the dislocations accommodating the slip transfer can have Burgers vectors locally active on secondary planes in order to accomplish slip transfer.

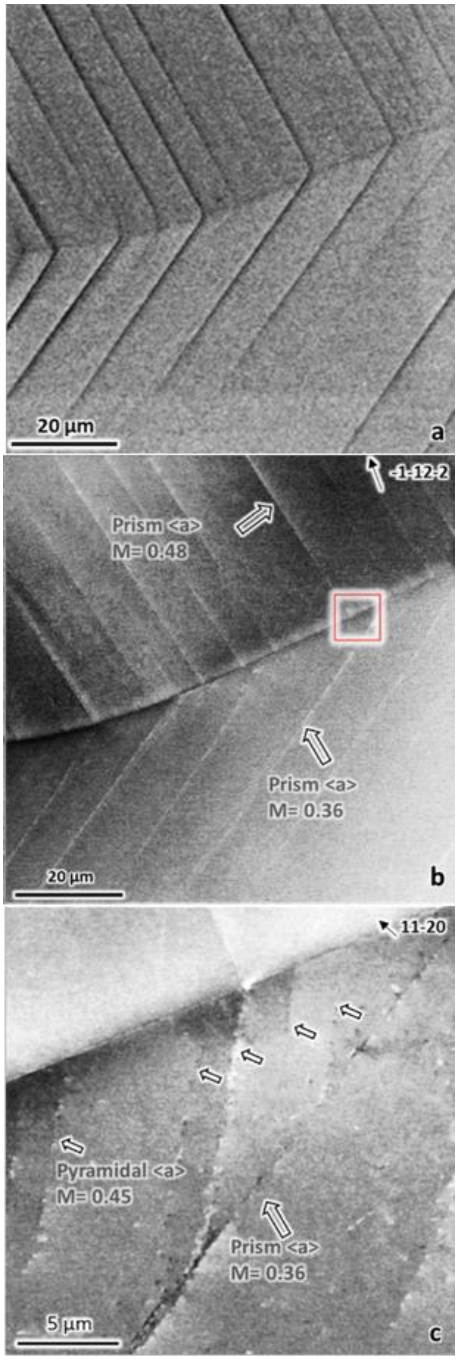

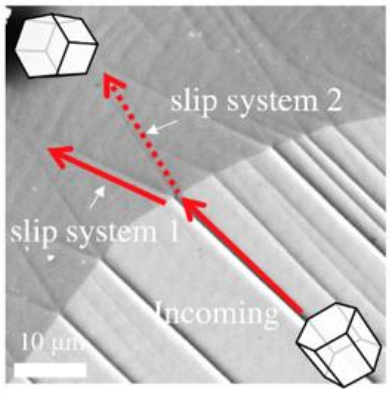

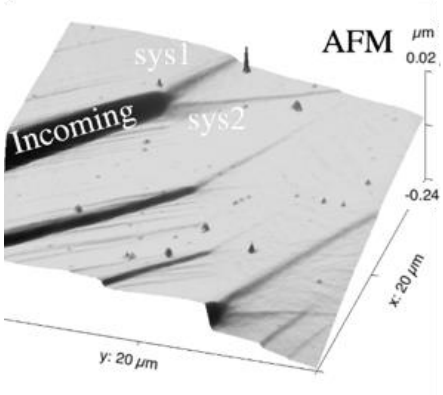

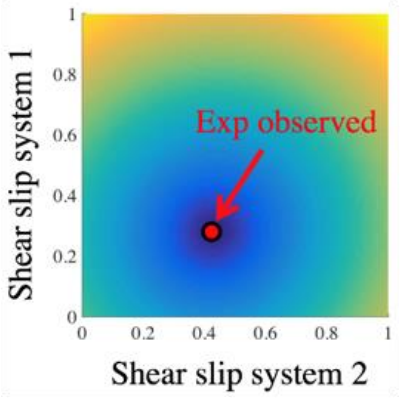

Future Plans

Crystal plasticity simulations of the experimentally characterized microstructures examined in this work are guiding the development of better modeling approaches that are necessary to establish a paradigm in which the physical processes responsible for damage nucleation in polycrystals can be simulated. Continuing efforts to distinguish between surface and bulk deformation phenomena, and how this influences modeling, will be a primary focus of future work.

References

1. Chakraborty, A., Zhang, C., Balachandran, S., Bieler, T. R., & Eisenlohr, P., *Acta Mat.*, submitted.
2. Bieler, T. R., Alizadeh, R., Peña-Ortega, M., & Llorca, J. (2019). *Int. J. Plasticity*, *118*, 269–290.
3. Haouala, S., Bieler, T. R., Segurado, J., Llorca, J., *Int. J. Plasticity*, under revision.

Publications (2017-2019)

Ballor, J., Ikeda, M., Kautz, E. J., Boehlert, C. J., & Devaraj, A. (2019). Composition-dependent microstructure-property relationships of Fe and Al modified Ti-12Cr (wt.%). *JOM, 71*(7), 2321–2330.

Bieler, T. R., Alizadeh, R., Peña-Ortega, M., & Llorca, J. (2019). An analysis of (the lack of) slip transfer between near-cube oriented grains in pure Al. *Int. J. Plasticity, 118*, 269–290.

Chakraborty, A., Zhang, C., Balachandran, S., Bieler, T. R., & Eisenlohr, P. (2019). Assessment of surface and bulk-dominated methodologies to measure critical resolved shear stresses in hexagonal materials. *Acta Mater.*, submitted.

Dunlap, B. E., Ruggles, T. J., Fullwood, D. T., Jackson, B., & Crimp, M. A. (2018). Comparison of dislocation characterization by electron channeling contrast imaging and cross-correlation electron backscattered diffraction. *Ultramicroscopy*, *184*, 125–133.

Dunlap, B. E., Ruggles, T. J., Fullwood, D. T., & Crimp, M. A. (2017). Comparison of dislocation mapping using electron channeling contrast imaging and cross-correlation electron backscattered diffraction. *Microscopy and Microanalysis*, *23*(S1), 546–547.

Han, S., Eisenlohr, P., & Crimp, M. A. (2018). ECCI based characterization of dislocation shear in polycrystalline arrays during heterogeneous deformation of commercially pure titanium. *Mater. Charact.*, *142*, 504–514.

Haouala, S., Bieler, T. R., Segurado, J., Llorca, J., Effect of slip transmission at grain boundaries in a copper bicrystal, *Int. J. Plasticity*, under revision.

Khademi, V., Ikeda, M., Hernandez-Escobar, D., & Boehlert, C. J. (2019). The Elevated-Temperature Strength Enhancement of a Low-Cost Beta Titanium Alloy Through Thermomechanically-Induced Phase Transformation. *JOM*, Vol. 71 Issue 9, DOI: 10.1007/s11837-019-03598-2, in press.

Ruggles, T. J., Yoo, Y. S. J., Dunlap, B. E., Crimp, M. A., & Kacher, J. (2019). Correlating results from high resolution EBSD with TEM- and ECCI-based dislocation microscopy: approaching single dislocation sensitivity via noise reduction. *Ultramicroscopy*, in press.

Zhang, C., Balachandran, S., Eisenlohr, P., Crimp, M. A., Boehlert, C. J., Xu, R., et al. (2018). Comparison of dislocation content measured with transmission electron microscopy and micro-Laue diffraction based streak analysis. *Scripta Mater.*, *144*, 74–77.

Zhang, C., Bieler, T. R., & Eisenlohr, P. (2018). Exploring the accuracy limits of lattice strain quantification with synthetic diffraction data. *Scripta Mater.*, *154*, 127–130.

Zheng, Z., Eisenlohr, P., Bieler, T. R., Pagan, D. C., & Dunne, F. P. E. (2019). Heterogeneous internal strain evolution in commercial purity titanium due to anisotropic coefficients of thermal expansion. *JOM*, in press.

Nanomechanics and Nanometallurgy of Boundaries

Brad L. Boyce, Khalid Hattar, Stephen Foiles (now retired), Remi Dingreville, Ryan Sills, Sandia National Laboratories

Program Scope

In the deformation, fatigue, creep, and irradiation response of metals, grain boundaries play a complex mediating role. The current program focuses not only on the fundamental role of structural and chemical defects on boundary stability, but also the interplay with mechanical and irradiation-induced degradation mechanisms. The seemingly unusual GB-driven evolution of nanocrystalline metals has led to a rethinking of the fundamental role of boundary mechanisms for all materials and grain sizes. There is a recognition that GBs are not static barriers with constant character, but their structure and corresponding properties necessarily evolve with deformation.[1] Shear coupling, the phenomenon by which external shear stress drives GBs to undergo some ratio of sliding and normal migration, has been well established as one mechanical mechanism for evolution. Just in the past few years, top researchers have begun to speculate that boundary migration (microstructural evolution) and shear coupling are mechanistically connected for "all boundaries under all conditions".[2] However, how this proposed mechanism applies to imperfect GBs is still an open question. Our core hypothesis is that the presence and evolution of defects within grain boundaries alter the GB behavior in response to thermal, irradiation, and/or mechanical driving forces. We seek to understand how evolving boundary structure & chemistry governs the mechanical, thermal, and irradiation response.

Recent Progress

a. Thermal response of grain boundaries. Our project contributes to the fundamental understanding of the influence of boundary character on its thermal response, connecting the macroscopic and atomic perspectives, in both pure systems and in alloys. In recent years, the nanocrystalline community has focused heavily on the role of solute to lower the thermodynamic driving force for GB motion. Our specific interest has been in understanding the convoluted contributions that solute plays in lowering the driving force while simultaneously providing kinetic pinning points, especially in the context of heterogeneous GB properties. An interesting effect emerges in immiscible NC alloys due to the interconnected roles of GB segregation and bulk alloy phase separation. Based on a combination of phase field diffuse interface model and in-situ TEM annealing experiments in nanocrystalline Pt-Au, we have examined grain growth dynamics in immiscible NC alloys, where both GB solute segregation and bulk phase separation act in conjunction.[3] While segregation provides the intended role of lowering the energetic cost of the GBs, the accompanying phase separation can also play a kinetic role in simultaneously stabilizing the GBs via Zener pinning. Corresponding phase field[3] and molecular dynamics models[4] are useful to elaborate the relative roles of segregation vs phase separation. Generally, in systems with low GB segregation, precipitation of solute-rich domains and associated Zener pinning effects lead to sluggish grain growth rates. In contrast, GB solute segregation plays a more dominant role as the heat of segregation increases in comparison with the bulk heat of

mixing. Finally, associated atomistic models and experimental observations have shown that solute segregation to GBs is not uniform: there is compositional heterogeneity across different boundary types, and even *within* an individual GB.[4, 5] This heterogeneous segregation is related to the structural differences in GBs such as differences in excess free volume; the departures from mean-field behavior are critical since not all boundaries are stabilized uniformly leading to the possibility of a percolating network of unstable boundaries and subsequent abnormal grain growth.

b. Mechanical response of GBs. In addition to the thermal driving forces such as those described in the preceding section, our team places an emphasis on the connection of boundary character to mechanical response, especially beyond yield strength where boundary behavior affects properties such as toughness, fatigue resistance, and wear behavior. In-situ characterization allows direct observation of the dynamic boundary-scale processes which occur in such scenarios. Utilizing a Hysitron in-situ TEM picoindenter, modified to be capable of fatigue frequencies up to 300 Hz, the microstructural evolution of nanostructured thin film tensile is observed. Evidence of localized deformation and grain growth within 150 nm of the crack tip was observed by both standard imaging and Automated Crystal Orientation Mapping (ACOM). Complementary studies using molecular dynamics simulation[6] and in-situ synchrotron x-ray diffraction[7,8] provided additional details on the fatigue-induced microstructural evolution process.

In-situ observations are complemented by interrupted and post-mortem ex-situ experiments. The Pt-Au alloy, discussed in the preceding section, was studied with regard to mechanical stability. This system was identified by our group not only because of the ability to undergo solute segregation and enhanced boundary stability, but also because it is the most noble binary alloy thereby mitigating the kinetic effects of oxygen-uptake which confounds other studies of nanocrystalline stability. Perhaps the most surprising result was the effect that the Au stabilization played in improving the wear resistance under low contact stresses. While our work and others had previously shown that nanocrystalline metals are susceptible to wear-induced grain growth with concomitant increase in frictional behavior and loss in wear resistance, this stabilized alloy exhibited a substantially lower wear rate, orders of magnitude below any previous reports for metals – nanocrystalline or otherwise, as shown in Figure 1.[9] In fact, the hemispherical sapphire counterface used in this study exhibited much higher wear rates than the Pt-Au. Not only does the Pt-Au system have surprising wear resistance, but also displays novel toughening mechanisms. Using a combination of in-situ tensile experiments and complementary molecular dynamics simulations, we have shown that inhomogeneous chemical

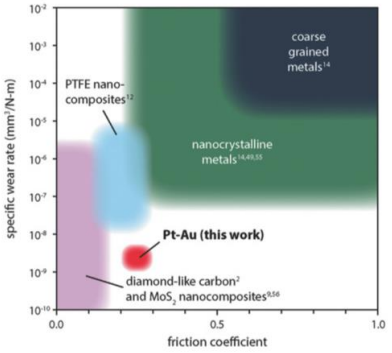

Figure 1. Ashby wear-friction map showing the low wear rate of Pt-Au attributed to the resistance to wear-induced grain growth and the subsequent tribocatalytic formation of diamond-like carbon surface films[9].

segregation to the GB can lead to a new toughening mechanism termed compositional crack arrest.[10]

Irradiation response of boundaries. Similar to grain-boundary mediated mechanical deformation, GBs have been shown to absorb irradiation-induced crystal defects such as dislocation loops and bubbles as a function of grain size.[11] This behavior is magnified in the nanocrystalline regime and is generally attributed to the high density of GBs with excess free volume necessary to accommodate such defects.[12] Our group's ability to observe in-situ ion irradiation has indicated that *within* the nanocrystalline regime defect absorption is not always enhanced by decreasing grain size. The stability of these sessile defects observed in small, 20–40 nm, grains is the proposed primary mechanism for the lack of grain-size dependence on defect absorption in the nanocrystalline regime.[13] The notion of a plateau or peak in grain-size dependent irradiation-induced defect accommodation parallels the observed Hall-Petch breakdown in yield strength, and our own group's observation of a plateau in fatigue resistance in the nanocrystalline regime, albeit with different mechanistic explanations.

Future Plans

Building off prior research, we recognize that there are outstanding questions regarding boundary response in thermal, mechanical, and irradiation environments. A fundamental question regards the mechanisms by which structural and chemical features of the grain boundary influence boundary dynamics. Many established and even recent thermodynamic models for boundary migration are mean field theories which ascribe the same characteristics to each GB.[14-17] Early works to understand boundary dynamics often attempted to employ a single scalar parameter such as misorientation angle. More recent and sophisticated concepts such as the fundamental zone representation[18] and interfacial stiffness[19] still focus on the 'macroscopic' character of the GB. However, these approaches appear to be at odds with the recognition that a given macroscopic GB configuration does not necessarily have a single structural arrangement: there are a multiplicity of nearly-degenerate metastable structural states which can be relaxed (or excited) with a low energy barrier.[20,21] Moreover, each nearly energetically equivalent configuration can contain distinct defect or solute arrangements and will interact differently with both applied stimuli and nearby defects.

Our core hypothesis that underpins this research is that **the presence and evolution of defects within grain boundaries alter the GB behavior in response to thermal, irradiation, and/or mechanical driving forces.** Here, 'defects' can be structural defects such as disconnections or chemical defects such as inhomogeneous solute or boundary precipitates. This thesis follows from our prior work which focused on the effects of heterogeneous GB character on properties ranging from solute segregation to mobility to interfacial toughness. This macroscopic viewpoint is still relevant as it governs the arrangement of GB defects and solute that can be supported during evolution, but as our previous work has shown it is not alone a sufficient descriptor. Moving forward, we augment the macroscopic GB perspective with the notion that both structural defects and chemical heterogeneities *within* a particular GB are largely responsible for the behavior. The objective of the project is to understand the intertwined roles

of macroscopic character and boundary defects on migration dynamics, while also demonstrating control over these processes under various driving forces. We are pursuing two related lines of questioning:

(1) The fundamental understanding of boundary behavior associated with the character, defects, and local composition in response to thermal, irradiation, and monotonic/cyclic mechanical driving forces. *A key sub-hypothesis for this section is that both defects within boundaries and near boundaries alter the local response of the boundaries to external stimuli.* A corollary is that macroscopic boundary character is not only important because it establishes mean field parameters such as energy and excess free volume, but also because it dictates what types of defects are supported and how they influence the boundary behavior.

(2) The network effects of boundary type and triple junction distributions on response to both isolated and combined environments. *A key sub-hypothesis is that chemically-graded boundary networks can be tailored to evolve into a self-stabilized configuration which resists evolution in combined thermal, mechanical, and irradiation environments.* A related question in this regard is the synergistic or antagonistic effects of superimposed environments: e.g. will evolution driven by one stimulus disrupt or enable incipient response to a second stimulus?

Acknowledgement: Sandia National Laboratories is a multimission laboratory managed and operated by National Technology and Engineering Solutions of Sandia, LLC., a wholly owned subsidiary of Honeywell International, Inc., for the U.S. Department of Energy's National Nuclear Security Administration under contract DE-NA-0003525.

References

1. Panzarino, J.F., Z. Pan, and T.J. Rupert, Acta Materialia, 2016. 120: p. 1-13.
2. Thomas, S.L., et al., Nature communications, 2017. 8(1): p. 1764.
3. Abdeljawad, F., et al., Acta Materialia, 2017. 126: p. 528-539.
4. O'Brien, C., et al., Journal of materials science, 2018. 53(4): p. 2911-2927.
5. Dingreville, R. and S. Berbenni, Acta Materialia, 2016. 104: p. 237-249.
6. Foiles, S.M., et al., Modelling and Simulation in Materials Science and Engineering, 2018.
7. Furnish, T., et al., Journal of Materials Science, 2017. 52(1): p. 46-59.
8. Furnish, T.A., et al., Scripta Materialia, 2018. 143: p. 15-19.
9. Curry, J.F., et al., Advanced Materials, 2018. 30(32): p. 1802026.
10. Heckman, N.M., et al., Nanoscale, 2018. 10(45): p. 21231-21243.
11. Barr, C.M., et al., JOM: p. 1-12.
12. Zarnas, P.D., R. Dingreville, and J. Qu, Computational Materials Science, 2018. 144: p. 99-112.
13. Barr, C.M., et al., Applied Physics Letters, 2018. 112(18): p. 181903.
14. Weissmüller, J., Nanostructured Materials, 1993. 3(1-6): p. 261-272.
15. Chookajorn, T., H.A. Murdoch, and C.A. Schuh, Science, 2012. 337(6097): p. 951-954.
16. Abdeljawad, F. and S.M. Foiles, Acta Materialia, 2015. 101: p. 159-171.
17. Saber, M., et al., Journal of applied physics, 2013. 113(6): p. 063515.
18. Homer, E.R., S. Patala, and J.L. Priedeman, Scientific reports, 2015. 5: p. 15476.
19. Abdeljawad, F., et al., Acta Materialia, 2018. 158: p. 440-453.
20. Han, J., V. Vitek, and D.J. Srolovitz, Acta Materialia, 2016. 104: p. 259-273.
21. Frolov, T., et al., Acta Materialia, 2018. 159: p. 123-134.

Publications
Past 24 months

1. C.J. O'Brien, C.M. Barr, P.M. Price, K. Hattar, S.M. Foiles, "Grain Boundary Phase Transformations in PtAu and Relevance to Thermal Stabilization of Bulk Nanocrystalline Metals." *Journal of Materials Science*, 2018.
2. C.M. Barr, N. Li, B.L. Boyce, K. Hattar, "Examining the influence of grain size on radiation tolerance in the nanocrystalline regime." *Applied Physics Letters*, 2018.
3. T.A. Furnish, D.C. Bufford, F. Ren, A. Mehta, K. Hattar, B.L. Boyce, "Evidence that abnormal grain growth precedes fatigue crack initiation in nanocrystalline Ni-Fe." *Scripta Materialia*, 2018
4. J.F. Curry, T.F. Babuska, T.A. Furnish, P. Lu, D.P. Adams, A.B. Kustas, B.L. Nation, M.T. Dugger, M. Chandross, B.G. Clark, B.L. Boyce, C.A. Schuh, N. Argibay, "Achieving Ultralow Wear with Stable Nanocrystalline Metals." *Advanced Materials*, 2018.
5. F. Abdeljawad, S.M. Foiles, A.P. Moore, A.R. Hinkle, C.M. Barr, N.M. Heckman, K. Hattar, B.L. Boyce, "The role of the interface stiffness tensor on grain boundary dynamics", *Acta Materialia*, 2018.
6. N.M. Heckman, S.M. Foiles, C.J. O'Brien, M. Chandross, C.M. Barr, N. Argibay, K. Hattar, P. Lu, D.P. Adams, B.L. Boyce, "New nanoscale toughening mechanisms mitigate embrittlement in binary nanocrystalline alloys", *Nanoscale*, 2018.
7. S.M. Foiles, F. Abdeljawad, A. Moore, B.L. Boyce, "Fatigue-driven acceleration of abnormal grain growth in nanocrystalline wires", *Modeling and Simulation in Materials Science and Engineering*, 2019.
8. C.M. Barr, O. El-Atwani, D. Kaoumi, K. Hattar, "Interplay Between Grain Boundaries and Radiation Damage", *JOM*, 2019.
9. X. Zhang, K. Hattar, Y. Chen, L. Shao, J. Li, C. Sun, K. Yu, N. Li, M.L. Taheri, H. Wang, J. Wang, M. Nastasi, "Radiation damage in nanostructured materials." *Progress in Materials Science*, 2018.
10. G.S. Jawaharram, P.M. Price, C.M. Barr, K. Hattar, R.S. Averback, and S.J. Dillon. "High temperature irradiation induced creep in Ag nanopillars measured via in situ transmission electron microscopy." *Scripta Materialia*, 2018.
11. J.A. Hinks, F. Hibberd, K. Hattar, A. Ilinov, D.C. Bufford, F. Djurabekova, G. Greaves, A. Kuronen, S.E. Donnelly, and K. Nordlund. "Effects of crystallographic and geometric orientation on ion beam sputtering of gold nanorods." *Scientific reports* 8, no. 1 (2018): 512.
12. J.D. Schuler, C.M. Barr, N.M. Heckman, G. Copeland, B.L. Boyce, K. Hattar, T.J. Rupert, "In situ high-cycle fatigue reveals the importance of grain boundary structure in nanocrystalline Cu-Zr", *JOM*, 2019.
13. P. Lu, F. Abdeljawad, M. Rodriguez, M. Chandross, D.P. Adams, B.L. Boyce, B.G. Clark, N. Argibay, "On the thermal stability and grain boundary segregation in nanocrystalline PtAu alloys", *Materialia*, 2019.
14. O.K. Donaldson, K. Hattar, T. Kaub, G.B. Thompson, and J.R. Trelewicz. "Solute stabilization of nanocrystalline tungsten against abnormal grain growth." *Journal of Materials Research*, 2018.

15. S.J. Dillon, D. C. Bufford, Q. S. Jawaharram, X. Liu, C. Lear, K. Hattar, R.S. Averback, "Irradiation-induced creep in metallic nanolaminates characterized by In situ TEM pillar nanocompression," *Journal of Nuclear Materials*, 2017.
16. D.C. Bufford, C.M. Barr, B. Wang, K. Hattar, “Application of in situ TEM to investigate irradiation creep in nanocrystalline Zr”, *JOM*, accepted for publication, 2019.

Effect of gradient architectures on the strength, deformation, and failure of nanoglasses

Paulo Branicio, University of Southern California

Program Scope

Metallic nanoglasses (NG), amorphous metallic alloys with a nanostructure, display an unusual set of mechanical properties. They derive from bulk metallic glasses (BMG) and inherit their high yield strength and absence of dislocation plasticity. In contrast with BMG, NG have the ability to deform plastically and exhibit tunable ductility, dictated by the length scale of their nanostructure. NG are promising materials for the design of components for medical implants, sporting equipment, and nuclear energy devices. To this point their mechanical properties have been discussed as a function of particle size, where they display a trade-off between strength and ductility, with large ductility achieved, as the nanostructure is refined, at the cost of lower strength. A limited compromise between strength and ductility has been demonstrated by the PI's group for a heterogeneous structure constructed combining two length scales in the same nanostructure. A promising new concept leverage on the combination of dissimilar particle sizes to generate a seamless gradient nanoglass (GNG) structure. The concept is inspired by developments on gradient nanostructured materials, which have been shown to generate materials with a unique and unexpected combination of mechanical properties originating from the synergy of dissimilar length scale behaviors. GNG suggest an unexplored path to induce novel mechanical properties that could potentially enable combinations of strength and ductility unachievable by other heterogeneous MG and NG structures.

Recent Progress

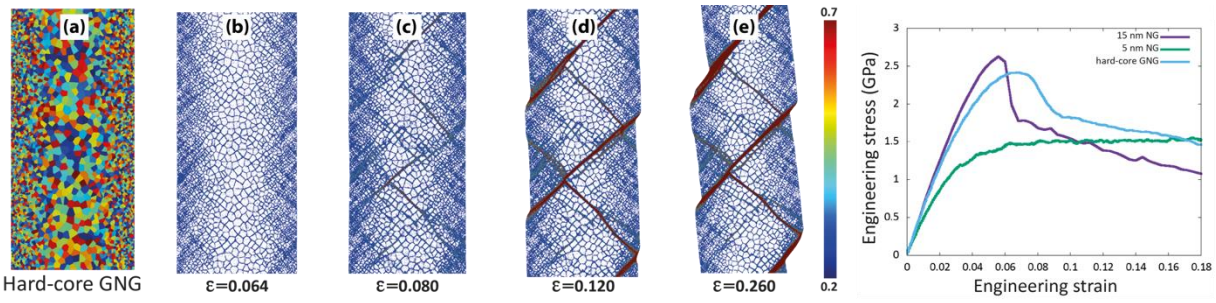

Preliminary Mechanical behavior of GNG with double gradient size from 3 to 15 nm. The hard-core region of the structure has average 15 nm particle size. (a) Color indicates different grains in the double gradient GNG. (b)-(f) Deformation profiles with color indicating the local van Mises strain. (f) Engineering stress-strain curves for tensile loading.

Future Plans

This project focuses on the design, generation, and characterization of the mechanical properties of GNG employing high-end parallel molecular dynamics (MD) simulations, visualization, and data analytics. We will perform large-scale MD simulations to describe the structure and mechanical behavior of GNG structures and data analysis to clarify the underlying mechanisms controlling their mechanical response.

The objective is to develop a comprehensive atomistic to nanoscale understanding of the deformation and failure of GNG to further the description of deformation mechanisms in the general class of gradient nanostructured materials. In particular, the PI will investigate how the presence of a seamless particle size gradient in a NG influence the expected particle-size-dependent glass-glass-interface activities. If it is capable of enhancing the delocalization of deformation of large particle size regions and constrain early deformation, consequently augmenting the strength, of small particle size regions, allowing the generation of structures exceeding the currently achievable strength-to-ductility relationship of BMG and NG. The outcomes of this research are expected to provide a framework for the generation of GNG, shed light on the effect of gradient design on the mechanical properties of heterogeneous amorphous materials, and advance the field of gradient functional materials.

Thermal Activation in Dislocation Dynamics of Face-Centered Cubic Metals

Wei Cai, Stanford University

Program Scope

Dislocation dynamics controls plastic deformation, mechanical strength, and failure of crystalline materials. It also governs fatigue resistance under cyclic loading, creep resistance at elevated-temperature, and radiation resistance for reactor applications. Thermally activated dislocation processes play a critical role in the strain hardening and dislocation patterning behavior of crystals, but are still not well understood. Cross slip and removal of Lomer-Cottrell (LC) junctions are two important thermally activated processes in pure Face-Centered Cubic (FCC) metals. Many fundamental questions regarding these processes still remain open, and our proposed research seeks to provide answers. This project will use dislocation dynamics (DD) simulations and atomistic simulations with advanced sampling techniques to determine the fundamental mechanisms of cross slip and LC junction removal processes and their consequence on strain hardening.

Recent Progress

The newly developed sub-cycling integrator for ParaDiS and its implementation on GPU has led to an orders-of-magnitude increase of computational efficiency in work hardening simulation of single crystals. This allows us to probe the deformation behaviors of bulk Cu with simulation cell size of $(15\ \mu m)^3$ over an appreciable range of plastic strain in which the work hardening rate can be reliably extracted (Fig. 1a) using a single GPU for several weeks (something that used to require hundreds of CPUs over several months). We found that while the flow stress depends on the strain rate, the strain hardening rate seems not sensitive to the strain rate, and our predicted strain hardening rate at 10^2-10^3 s^{-1} is in good agreement with the experimental measurements under the quasi-static loading condition (Fig. 1a).

The new DD capability provides us with a valuable tool to understand how the dislocation microstructure control the rate of strain hardening [1]. For the first time, we found that for [001] loading) the dislocation network consists of links whose length satisfy an *exponential distribution* (Fig. 1b). This fundamental finding has later been confirmed by other groups using both DD simulations and molecular dynamics (MD)

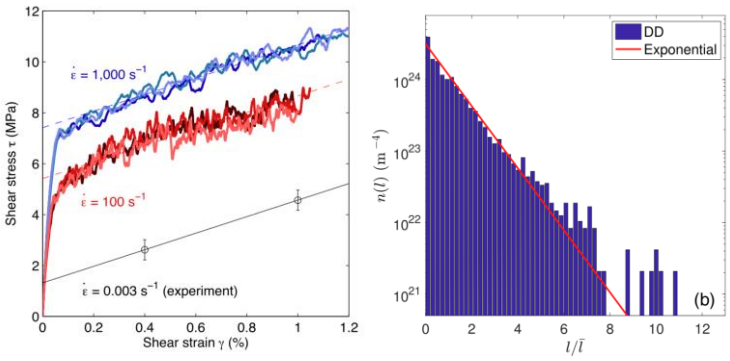

Figure 1. (a) Shear stress-strain curves of single crystal Cu deformed along [001] axis. Thick curves are DD predictions at two different strain rates. Thin solid line is extracted from experimental data [1]. (b) Dislocation link length distribution $n(L)$ from a DDD simulation snapshot at 0.87% shear strain.

simulations. The exponential distribution of link lengths is fully characterized by two variables: the total dislocation density ρ, and the nondimensional parameter $\varphi \equiv N^2/\rho^3$, where N is the number of dislocation lines per unit volume. While the density ρ describes the total amount of dislocations in the material volume, the nondimensional parameter φ describes how they are arranged. We believe the parameter φ is an important microstructural information that should be kept in the coarse-grained continuum theory of crystal plasticity based on dislocation fields.

We have now performed a large number of DD strain hardening simulations on single crystal Cu for >100 loading orientations in the stereographic triangle (Fig. 2). This is the first time that the strain hardening rate is systematically predicted over such a wide range of orientations. The predictions show that the strain hardening rate remain high over a much wider angular range of loading orientations near the [001] orientation, than over the [111] or the [011] orientation. The strain hardening rate is rather weak around the [011] orientation. We have further confirmed that exponential distribution of dislocation link lengths, remains true for all of these loading conditions, as long as the dislocation links on different slip systems are considered separately.

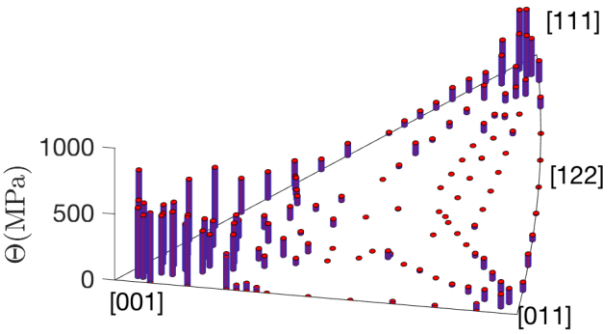

Figure 2. Strain hardening rate predicted by DDD simulations for single-crystal Cu at 10^3 s^{-1}. Each rod in the stereographic triangle corresponds to a different loading direction.

Future Plans

We plan to incorporate the dislocation cross slip rate model constructed based on atomistic simulations into our DD model and use it to predict the effect of thermally activated processes on the temperature/strain rate effects on strain hardening. We will also perform molecular dynamics (MD) simulations of cross slip to reveal any finite temperature effects possibly missed by zero-temperature energy barrier calculations.

We plan to develop a systematic approach to obtain crystal plasticity models using machine learning tools and the large amount of data produced by our DDD simulations. We will address the fundamental questions of what essential microstructural information (beyond dislocation densities) needs to be retained in a continuum theory of crystal plasticity, and what are the equations of motion for the microstructural parameters that are consistent with explicit DDD simulations.

We plan to enable a one-to-one comparison between DDD simulations and experimental measurements on FCC single crystals under identical conditions, by applying the same loading histories in DDD simulations as measured experimentally. This will be accomplished through a collaborative effort with Prof. KT Ramesh's group at Johns Hopkins University. Ramesh's group

have performed Kolsky bar shock compression experiments on several single crystal Cu samples along the [001] directions. This opportunity of establishing the first quantitative, direct comparison between dislocation-based simulations and stress-strain measurements, which is critically needed by the scientific community. We expect that a tremendous amount would be learned on the fundamentals of crystal plasticity once such a comparison is made.

We plan to quantitatively compare the DD against MD simulations under identical size and loading rates, for both stress-strain curves and dislocation microstructure evolution. The purpose of this comparison is to identify the key physical mechanisms (lacking in existing DD simulations) that causes significant discrepancies between DD and MD predictions. PI Cai is part of an LC Grand Challenge team of Lawrence Livermore National Laboratory (LLNL), which have access to the large-scale computing resources to produce the MD simulations needed for this comparison.

References

1. R. B. Sills, N. Bertin, A. Aghaei, W. Cai, "Dislocation networks and the microstructural origin of strain hardening", Phys. Rev. Lett. 121, 085501 (2018).

Publications

1. Y. Wang, X. Zhang, W. Cai, "Spherical harmonics method for computing the image stress due to a spherical void", J. Mech. Phys. Solids, 126, 151 (2019).
2. M. Kiani, Y. Wang, N. Bertin, W. Cai, W. Gu, "Strengthening Mechanism of a Single Precipitate in a Metallic Nanocube", Nano Lett. 19, 255 (2019).
3. D. M. Barnett, W. Cai, "Properties of the Eshelby Tensor and Existence of the Equivalent Ellipsoidal Inclusion Solution", J. Mech. Phys. Solids, 121, 71 (2018).
4. R. B. Sills, N. Bertin, A. Aghaei, W. Cai, "Dislocation networks and the microstructural origin of strain hardening", Phys. Rev. Lett. 121, 085501 (2018).
5. N. Bertin, W. Cai, "Energy of periodic discrete dislocation networks", J. Mech. Phys. Solids, 121, 133 (2018).
6. Sh. Akhondzadeh, R. B. Sills, S. Papanicolaou, E. Van der Giessen, W. Cai, "Geometrically projected discrete dislocation dynamics", Model. Simul. Mater. Sci. Eng., 26, 065011 (2018).
7. N. Bertin, V. Glavas, D. Datta, W. Cai, "A spectral approach for discrete dislocation dynamics simulations of nanoindentation", Model. Simul. Mater. Sci. Eng., 26, 055004 (2018).
8. J. Wang, Y. Wang, W. Cai, J. Li, Z. Zhang, S. X. Mao, "Discrete shear band plasticity through dislocation activities in body-centered cubic tungsten nanowires", Sci. Rep., 8, 4574 (2018).

9. R. B. Sills, W. Cai, “Free Energy Change of a Dislocation Due to a Cottrell Atmosphere”, Philos. Mag. 98, 1491 (2018).
10. N. Bertin, W. Cai, “Computation of virtual X-ray diffraction patterns from discrete dislocation structures”, Comput. Mater. Sci., 146, 268 (2018).

Multi-Scale Study of the Role of Microstructure in the Deformation Behavior of Hexagonal Materials

Laurent Capolungo, Los Alamos National Laboratory

Program Scope

Twinning and martensitic transformations accommodate strain during plastic deformation of HCP materials via the formation and growth of reoriented/transformed 3D domains. The kinetics of propagation of these domains is controlled by the intrinsic mobility of the facets/interfacial defects separating them from the host phase, by the internal stresses acting as driving forces for transformations to occur, and by the presence of local defects which can either impede or favor the propagation process. The material's science community, surprisingly, has focused on twin and martensitic domain morphology and interface mobility mostly from a 2D perspective. Our program addresses the full 3D character of transformed domains. Leveraging atomic and micron-scales characterization techniques in combination with both simulation and analysis tools, this program aims at unraveling the nature of interfacial defects, at correlating their intrinsic properties (mobilities, metastable states) and their environment (local stress state and defect content) to the kinetics of microstructure evolutions. The goal being to understand which dominant local microstructure features and associated thermodynamic landscape most affects the activation of these rare events (i.e. twin and martensitic transformation) that induce drastic and sudden changes in the microstructure and mechanical response.

Recent Progress

This section focuses on advances made in: characterizing the 3D shape of twins, characterizing the structure of 3D defects/facets mediating twin transformation, studying the migration of these facets, quantifying the stress state near twinned microstructures and, analyzing the effect of twin/defect interactions on twinning. In what follows the η_1, k_1 and λ, directions will denote the direction of shear, twin plane normal and direction perpendicular to both η_1 and k_1, respectively (see Figure 1).

To reveal the 3D shape of twin domains, sections of Mg samples were prepared to compare the size of twin domains along its width, length and thickness [1]. The statistical analysis of EBSD maps led to critically important new observation: (1) Twin growth is anisotropic with faster propagation along the lateral λ direction followed by the η_1 and k_1 directions, in that order; (2) The common description of twins as elliptical domains is thus far too idealized as twins are irregular in shape; (3) The observed twin morphology may result from the intrinsic mobility of facets bounding twin domains and/or from the distribution of driving forces acting on those. These 3 complementary aspects of twinning have been studied in parallel.

TEM characterization accompanied with simulations using Generalized discrete defect dynamics (GD^3), and Molecular Dynamics (MD) were performed to relate 3D twin growth to interfacial defects bounding twin domains [2-4]. The first objective was to identify by means of TEM complemented by MD, the nature of defects bounding twin domains. As shown in Figure 1, for the first time, we identified all likely facets bounding $(10\bar{1}2)$ twins in Mg and $(10\bar{1}1)$ twins in Ti [4]. This study is critical as a rigorous understanding of the kinetics of twinning can only begin by characterizing the defects that mediate the transformation.

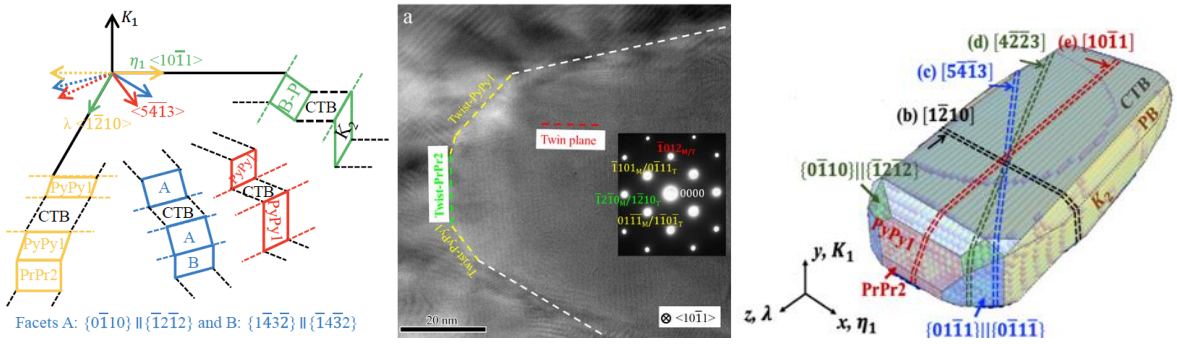

Figure 1: (Left) Reconstructed 3D twin domain showing all facets identified by HRTEM. (Middle) HRTEM micrograph of $\{\bar{1}012\}$ twin boundaries viewed along a $<10\bar{1}1>$ direction. (Center) Twin tip, comprised of Twist-PyPy1 $((\bar{1}101)_M//(0\bar{1}11)_T$ and $(01\bar{1}\bar{1})_M//(1\bar{1}0\bar{1})_T)$ and Twist-PrPr2 $((\bar{1}2\bar{1}0)_M//(1\bar{2}10)_T)$ facets. (Right) MD simulations of a 21×8×41 nm^3 3D $(\bar{1}012)$ twin under 1 GPa twinning shear stress associated with twinning at 100 K [4].

MD-based study revealed, consistently with experimental observations, that migration along the lateral side is the fastest (see Figure 1). It was also found that, as a function of orientation and stress, facets can adopt several different equilibrium and non-equilibrium configurations with strikingly different mobilities. In parallel, the driving forces acting on the twin domains were also quantified. Using X-ray diffraction and the differential aperture microscopy technique (Advanced Photon Source), we revealed that the heterogeneity in the driving forces acting on twin domains is far larger than previously thought [5]. These findings motivate the need for high fidelity models that accurately predict the relative kinetics of twinning and quantify the associated internal stress state evolution.

Finally, the potential roles of domain/domain interactions (DDI) on transformation kinetics was preliminarily assessed. High-pressure X-ray synchrotron experiments (Advanced Photon Source) shows that the presence of twins prior to high pressure loading significantly decreases the critical pressure triggering martensitic transformation; thereby revealing an unknown correlation between twinning and α-to-ω phase transformation. Second, EBSD analysis of deformed Mg microstructures revealed that twin transmission across grain boundaries accelerates growth at the twin/grain boundary junction thereby further contributing to the development of these complex 3D twinned topologies [6]. Modeling of the process, albeit considering static configurations, showed that the local driving force at twin/grain boundary junctions increases when twin transmission occurs; thereby rationalizing the observations.

Future Plans

In the next 3 years, focus will be placed on the study of domain/domain interactions (DDI) *which are hypothesized to play a dominant role on the kinetics of formation of complex 3D hierarchical microstructure.* 4 types of interactions will be studied in Mg and Ti (see Figure 2): (a) a twin domain interacting with another twin in the host crystal and sharing a common zone axis, (b) a twin interacting with another twin with different zone axis within the host crystal, (c) a twin interacting with another twin across a grain boundary and (d) a twin domain interacting with an ω domain.

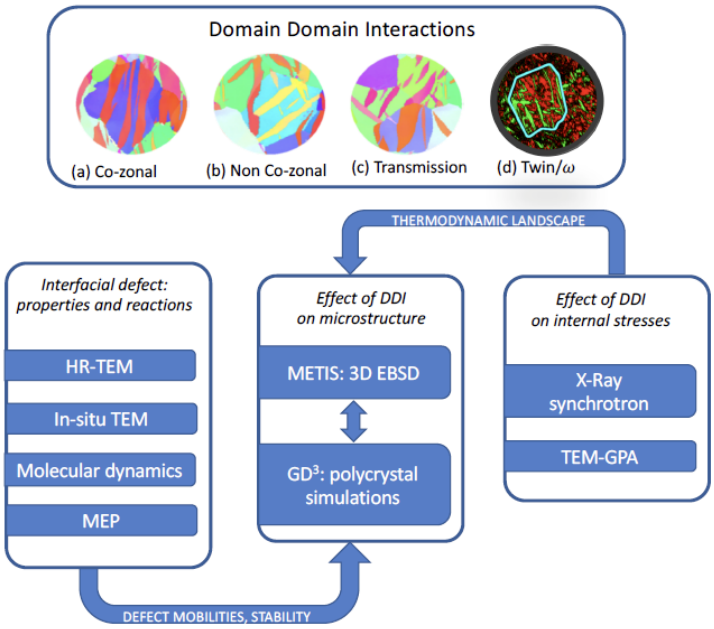

Figure 9: Structure of the program

Acronyms: TEM: Transmission electron microscopy, MEP: Minimum Energy Pathway search methods, GPA: Geometrical Phase analysis, EBSD: Electron Back Scattering Diffraction

From the microstructure viewpoint alone, and drawing parallels from dislocation mechanics, one expects DDIs to have a significant impact on the mechanical response of HCP metals. Remarkably though, our understanding of DDI remains particularly superficial; the processes leading to the formation of 3D hierarchical microstructures are not understood. Conceptually different but not necessarily exclusive views can be considered. First, one could foresee DDI as resulting from the simultaneous and uncorrelated nucleation of domains that will interact in the short range as they grow. Opposite to this, one could postulate that the statistics and geometry of DDI are controlled by long-range elastic strain fields associated with the presence of forming domains. In this view, the formation and growth of a twin in a crystal would condition the nucleation, growth and transmission of other twins. Commonly to these two viewpoints lies the question of the role of DDI on twin growth: Are the kinetics of growth of connected twin domains

largely different from those of isolated domains? How is the 3D path of interacting domains affected by short and long-range interactions between domains?

Testing the leading hypothesis and addressing the aforementioned subsidiary questions entails that: (i) interfacial defect motion and stability be studied in the presence and in absence of other defects, (ii) the internal stress field in the presence and in absence of interactions be quantified and, (iii) the net effects of short and long-range domain interactions be quantified simultaneously. The project will be structured around these 3 topics. (i) will be mainly performed with transmission electron microscopy and with atomistic simulations. This work will provide guidance to GD^3 (e.g. interfacial defect reactions, facet junction mobility etc.). The second task focuses on the quantification of the stress state in regions in which DDI occurs. In-situ X-ray synchrotron experiments and TEM-GPA characterization will be performed to this end. Interpretation of these measures will allow for a validation of the GD^3 framework as well as assess the effect of short-range interactions between twin facets and other twin facets/ω phase facets on stress relaxation. Finally, in the third task, both the effects of short and long-range DDI will be studied at the polycrystal length scale. This task will rely on the use and extension of both GD^3 and of METIS-3D (code for statistical analysis of 3D EBSD microstructure). The overall metric for success will be measured by our ability to, via the use of GD^3, reproduce the statistical measures of 3D microstructures gathered using 3D EBSD data.

References

[1] Y. Liu, P.Z. Tang, M.Y. Gong, R.J. McCabe, J. Wang, C.N. Tomé, Three dimensional character of {10-12} deformation twin in Mg, Nat Commun (2019) (Accepted for publications).
[2] M. Gong, V. Taupin, L. Capolungo, The kinetics of growth of twins: 3d perspectives, (in preparation) (2019).
[3] D. Spearot, L. Capolungo, V. Taupin, Structure and Kinetics Three-Dimensional Defects on the {10-12} Twin Boundary in Magnesium: Atomistic and Phase-field Simulations, J Mech Phys Solids (2019) submitted.
[4] S. Wang, M.Y. Gong, R.J. McCabe, L. Capolungo, J. Wang, C.N. Tomé, Characterizing facets in {10-12} twin boundaries at the atomic scale in three dimensions, Nat Mater (2019) (Under review).
[5] M.A. Kumar, B. Clausen, L. Capolungo, R.J. McCabe, W. Liu, J.Z. Tischler, C.N. Tome, Deformation twinning and grain partitioning in a hexagonal close-packed magnesium alloy, Nat Commun 9 (2018).
[6] M.A. Kumar, L. Capolungo, R.J. McCabe, C.N. Tomé, Characterizing the role of adjoining twins at grain boundaries in hexagonal close packed materials, Sci Rep-Uk 9(1) (2019) 3846.

Publications:

M. Arul Kumar, I.J. Beyerlein, **C.N. Tomé**, "A measure of plastic anisotropy for hexagonal close packed metals: application to alloying effects on the formability of Mg", J of Alloys and Compounds 695 (2017) 1488-97.

M. Arul Kumar, I.J. Beyerlein, R.A. Lebensohn, **C.N. Tomé,** "Modeling the effect of neighboring grains on twin growth in HCP polycrystals", Modeling and Sim in Mats Sc and Engineering 25 (2017) 064007 (25pp).

M. Arul Kumar, I.J. Beyerlein, R.A. Lebensohn, **C.N. Tomé**, "Role of alloying elements on twin growth and twin transmission in magnesium alloys", Materials Sc and Engineering A706 (2017) 295-303.

M. Arul Kumar, I.J. Beyerlein, R.A. Lebensohn, **C.N. Tomé**, "Modeling the effect of alloying elements in magnesium on deformation twin characteristics", in: K. Solanki, D. Orlov, A. Singh, N. Neelameggham (Eds.), Magnesium Technology 2017, The minerals, metals and materials series, Springer, 2017, pp. 159-165.

I.J. Beyerlein, **M. Arul Kumar**, "The stochastic nature of deformation twinning: Application to HCP metals", chapter in "Handbook of Materials Modeling. Volume 1 Methods: Theory and Modeling", edited by Wanda Andreoni and Sidney Tip.

A. Kumar, **M. Arul Kumar**, I.J. Beyerlein, "First-principles study of crystallographic slip modes in ω-Zr", Scientific Reports **7** (2017) 893.

Y. Liu, N. Li, **M. Arul Kumar**, S. Pathak, J. Wang, **R.J. McCabe**, N.A. Mara, **C.N. Tomé**, "Experimentally quantifying critical stresses associated with basal slip and twinning in magnesium using micro-pillars", Acta Materialia 135 (2017) 411-421.

H. Wang, **L. Capolungo, B. Clausen, C.N. Tomé**, "A crystal plasticity model based on transition state theory", Intl J of Plasticity 93 (2017) 251-268**.**

M. Arul Kumar, M. Wroński, **R.J. McCabe, L. Capolungo**, K. Wierzbanowski, **C.N. Tomé**, "Role of microstructure on twin nucleation and growth in HCP titanium: a statistical study", Acta Materialia 148 (2018) 123-132.

M. Arul Kumar, B. Clausen, L. Capolungo, R.J. McCabe, W. Liu, J. Tischler, **C.N. Tomé**, "Deformation twinning and grain partitioning in a HCP magnesium alloy", Nature Communications 9 (2018) 4761.

M. Arul Kumar, M. Gong, I.J. Beyerlein, J. Wang, **C. N. Tomé**, "Role of local stresses on co-zone twin-twin junction formation in HCP magnesium", Acta Materialia 168 (2019) 353-36.

M. Arul Kumar, L. Capolungo, R.J. McCabe, C. N. Tomé, "Characterizing the role of adjoining twins at grain boundaries in hexagonal close packed materials", Scientific Reports 9 (2019) 3846

M. Arul Kumar, B. Leu, P. Rottmann, L. Ma, I.J. Beyerlein, "Characterization of staggered twin formation in HCP magnesium", in: V. Joshi, D. Orlov, N. Neelameggham (Eds.), Magnesium Technology 2019, The minerals, metals and materials series, Springer, 2019.

L. Capolungo, V. Taupin, "Generalized discrete defect dynamics", Materials Theory 3 (2019) 2.

M. Y. Gong, G. Liu, J. Wang, **L. Capolungo, C.N. Tomé**, "Atomistic simulations of interaction between basal <a> dislocations and 3-dimensional twins in Mg", Acta Materialia 155 (2018) 187-198**.**

R. LeSar, **L. Capolungo**, "Handbook of Materials Modeling. Volume 1 Methods: Theory and Modeling Chapter", Springer 2018.

E. Martinez, L. Capolungo, C.N. Tomé, "Atomistic analysis of the twin stability and growth in alpha-Ti", Physical Review Materials 2 (2018) 08603.

C. Pradalier, PA Juan, **R.J. McCabe, L. Capolungo**, "A Graph Theory-Based Automated Twin Recognition Technique for Electron Backscatter Diffraction Analysis", Integrating Materials and Manufacturing Innovation 7 (2018) 12-27.

D.E. Spearot, **L. Capolungo, C.N. Tomé**, "Shear driven motion of Mg (10-12) twin boundaries via disconnection terrace nucleation, growth and coalescence", Phys Rev Materials 3 (2019) 053606.

C.N. Tomé, I.J. Beyerlein, **R.J. McCabe**, J. Wang, "Multiscale Statistical Study of Twinning in HCP Metals", Chapter 9 of "Integrated Computational Materials Engineering (ICME) for Metals: Concepts and Case Studies", edited by M.F. Horstemeyer, (2018) J. Wiley & Sons (pp. 283-336).

M. Wroński, **M. Arul Kumar, L. Capolungo, R.J. McCabe**, K. Wierzbanowski, **C.N. Tomé**, "Deformation behavior of HCP titanium alloy: experiment and crystal plasticity modeling", Mats Science and Engineering A724 (2018) 289-297.

Y. Liu, P.Z. Tang, M.Y. Gong, **R.J. McCabe**, J. Wang, **C.N. Tomé**, "Three-dimensional character of $\{10\bar{1}2\}$ deformation twin in Mg", Nature Communications (2019) accepted for publication.

Molecular Design of Hybrid Films with Unusual Mechanical Properties

Professor Reinhold H. Dauskardt
Department of Materials Science and Engineering, Stanford University
Stanford, CA 94305 – 4034, Email: dauskardt@stanford.edu

Program Scope

Our research is focused on fundamental studies related to the molecular design, synthesis, characterization and modeling of molecular-reinforced hybrid glass films for superior mechanical and fracture properties. Molecular-reinforced hybrid glass films exhibit unique electro-optical properties while maintaining excellent thermal stability. They have important technological application for emerging nanoscience and energy technologies including anti-reflective and ultra-barrier layers in photovoltaics and display technologies. However, they are often inherently brittle in nature, do not adhere well to adjacent substrates, and exhibit poor mechanical properties.

Our research brings together a unique combination of internationally recognized thin-film processing and mechanical characterization capabilities coupled with computational modeling that we have pioneered to study hybrid films. Composition and molecular structure are characterized using high resolution X-ray, electron, optical and nuclear spectroscopy. Mechanical properties are studied using acoustic, nanoindentation, force modulated AFM, and thin-film adhesion and cohesion techniques we have pioneered for thin-film structures. We leverage computational modeling capabilities that allow us to understand the complex molecular structure, free volume, cohesive and elastic properties of hybrid molecular materials. This has enabled the molecular design, synthesis, characterization and modeling of hybrid films for superior mechanical and fracture properties.

Recent Progress

Controlling Elastic Stiffness of Hybrid Glasses with Precursor Geometry: Designing hybrid glasses to maintain high levels of mechanical strength and stiffness while keeping low density remains as a significant challenge that can ultimately limit the integration and use of these materials in emerging device technologies including dielectrics in microelectronics, antireflective (AR) coatings, protective coatings in flexible electronics, and molecular sieves for biosensing.[1-5] To address this challenge, we introduced in our previous program the *hyperconnected* hybrid network architectures as a new design strategy to improve the stiffness of these materials.[6] Hyperconnected network architectures, wherein the connectivity of a silicon atom within the network extends beyond its chemical coordination number of four, results in exceptional mechanical properties in that the stiffness can reach up to three times higher than that of fully dense silica. However, the most recent results we have indicate that not only hyperconnectivity but also the *molecular geometry* of the precursors chosen to generate the networks plays a role in

increasing stiffness.

We simulated several hyperconnected hybrid networks derived from a range of precursors to identify the effects of different geometrical features these precursors have on the resulting mechanical properties. While short carbon bridge length and molecular symmetry in a precursor are among the features that can lead to an increase in network stiffness, we also found that *molecular planarity* is the most effective feature that plays a significant role in increasing elastic properties. Compared to the hyperconnected networks derived from acylic precursors such as flexible silane, those generated with cyclic precursors having a more planar orientation of atoms therefore result in significantly improved bulk modulus values. **Fig. 1a** shows the bulk moduli of hyperconnected networks with cyclic precursors having different degrees of molecular planarity. The ones with the highest molecular planarity, 1,3,5-benzene and 1,2,4-cyclopentadiene, lead to the highest stiffness values achieved.

An important implication of the use of cyclic planar precursors is that when the carbon bridge length of the cyclic precursor is short, molecular planarity decreases due to the steric hinderance effects, leading to a reduced bulk modulus value as shown with the 1,2,3-cyclopropane network. This leads to the great advantage of increasing stiffness while decreasing density, since high molecular planarity in a cyclic precursor is only achieved when the carbon bridge length is sufficiently long, as in the case of 1,3,5-benzene and 1,2,4-cyclopentadine networks, both having higher stiffness but much lower density than the 1,2,3-cyclopropane network.

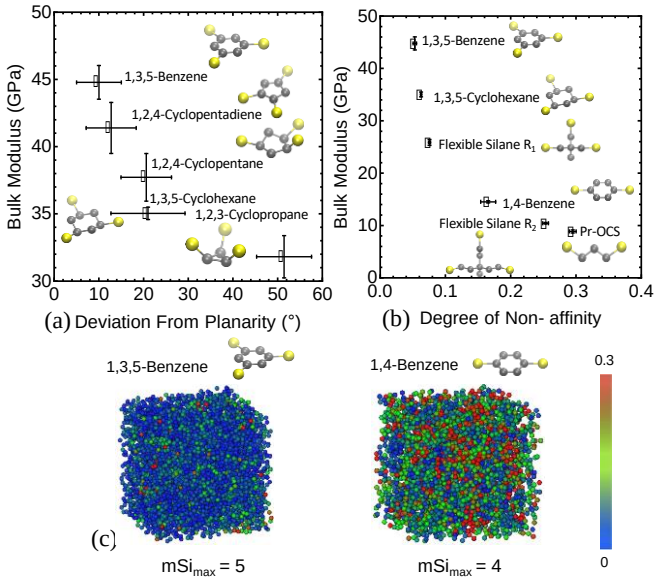

Figure 1: (**a**) The degree planarity of several cyclic precursors and its effects on the resulting mechanical properties. Deviation from planarity quantifies how planar each molecule is. A smaller amount of deviation corresponds to higher molecular planarity. (**b**) Degree of non-affine deformations correlate with bulk modulus for several different hybrid glass networks. **(c)** Comparison of the degree of non-affine deformations in 1,3,5-benzene and 1,4-benzene networks, emphasizing the role of hyperconnectivity in 1,3,5-benzene network as a topological constraint in decreasing non-affinity and increasing stiffness.

Controlling Local Deformation Mechanisms with Network Connectivity and Precursor Geometry: We also explored the combined effect of precursor geometry and network connectivity on the molecular level in the form of geometrical and topological constraints, which in return reflect on bulk mechanical properties by reinforcing structural rigidity. We

calculated the degree of non-affine deformations in these networks, which corresponds to a degree of deviation of the local deformation field from the macroscopic deformation field applied.[7] Geometrical and topological constraints in the network act to decrease these deviations in the local deformation field, which increases overall network stiffness. **Fig. 1b,** and **c** show the degree of non-affinity and bulk modulus values for several hyperconnected and also traditionally bridged networks formed by different precursors. As can be seen, there is a correlation between stiffness and degree of non-affine deformations in hybrid glass networks, which is controlled by the network connectivity and precursor geometry. While similar trends can be found in literature for different types of network structures ranging from elastic and polymeric networks to cytoskeleton,[8-10] this has never been shown for hybrid glass networks of our interest before. Non-affine deformation analysis therefore not only validates the effectiveness of precursor geometry as a new fundamental structural property for the design of hybrid glasses materials with exceptional mechanical properties, but also serves as a new predictive metric for the stiffness of these materials that is ultimately controlled by precursor geometry and network connectivity.

Design of Mechanically Ultrastiff Hybrid Materials: Exploiting both *hyperconnectivity* and *precursor geometry* to generate *ultrastiff* hybrid materials in light of our aforementioned results will lead to unprecedented combinations of stiffness and density of these materials. **Fig. 2a** shows the results we obtained for the bulk modulus and density of hyperconnected networks with cyclic precursors, together with two new networks derived from 1,2,5,6-pentalene and 1,4,6,9-naphthalene precursors. Both of these precursors have high molecular planarity, as well as having a *maximum network connectivity of six*, going beyond the maximum network connectivity of five we used in our previous model hybrid glasses. The networks derived from 1,2,5,6-pentalene and 1,4,6,9-naphthalene are both stiffer than the 1,3,5-benzene network, which set the highest stiffness value we achieved previously, while maintaining a comparable density.

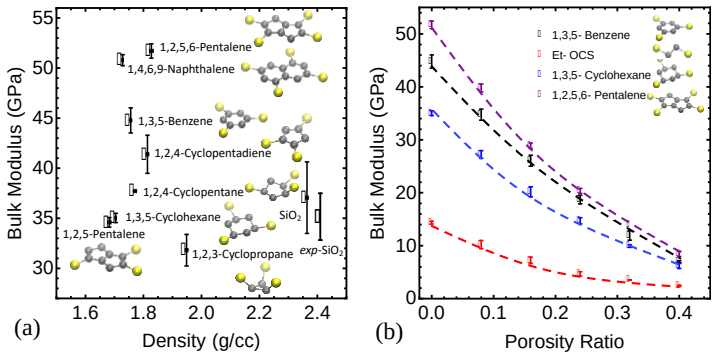

Figure 2: (a) The predicted bulk modulus, *K*, as a function of the predicted mass density, ρ, for model organosilicate glasses with various cyclic precursors. The experimental (square) and simulated values for amorphous SiO_2 are shown for comparison. **(b)** Hybrid glass networks with nanoporosity at porosity levels increasing from 0%, 8%, 16%, 32% to 40%. Porous glasses with ultrastiff matrices obtained with 1,2,5,6-pentalene and 1,3,5-benzene lead to the highest bulk moduli at all porosity levels.

Importantly, an immediate use of such ultrastiff hybrids is the design of nanoporous hybrid glasses with an ultrastiff matrix. While nanoporosity is an important structural parameter that controls material properties such as dielectric constant, it severely degrades the

mechanical properties (**Fig. 4a**). However, our new design strategy to generate ultrastiff hybrid glass materials significantly enhances the elastic properties of nanoporous glasses compared to a state-of-the-art nanoporous ethylene-bridged glass as shown in **Fig. 2b**.

Future Plans

We will continue our research to develop hybrid films with improved mechanical and fracture properties. Specifically, we will continue to pioneer molecular design criteria to control the mechanical properties. By leveraging our atmospheric plasma deposition capabilities, we will synthesize hybrid materials with controlled molecular architectures and precursor geometry to further calibrate our computational models and develop hybrids with well-controlled degrees of elastic asymmetry and exceptional mechanical properties. Furthermore, we will develop new computational strategies to design new nanoporous hybrid glasses with controlled pore surface chemistry to expand our design space towards even lower density hybrids with exceptional mechanical and fracture properties.

References

1. Volksen, W., Miller, R. D. & Dubois, G. Low dielectric constant materials. **Chem. Rev**. **110,** 56–110 (2009).
2. Volksen, W., Lionti, K., Magbitang, T. & Dubois, G. Hybrid low dielectric constant thin films for microelectronics. **Scr. Mate***r*. **74,** 19–24 (2014).
3. Hiller, J. A., Mendelsohn, J. D. & Rubner, M. F. Reversibly erasable nanoporous anti-reflection coatings from polyelectrolyte multilayers. **Nat. Mater**. **1,** 59–63 (2002).
4. Kresge, C. T., Leonowicz, M. E., Roth, W. J., Vartuli, J. C. & Beck, J. S. Ordered mesoporous molecular sieves synthesized by a liquid-crystal template mechanism. **Nature 359,** 710–712 (1992).
5. Dong, S., Zhao, Z. & Dauskardt, R. H. Dual Precursor Atmospheric Plasma Deposition of Transparent Bilayer Protective Coatings on Plastics. **ACS Appl. Mater. Interfaces 7,** 17929–17934 (2015).
6. J. A. Burg, M. S. Oliver, G. Dubois, and R. H. Dauskardt, “Hyperconnected Molecular Glass Network Architectures with Exceptional Elastic Properties,” **Nature Communications**, 2017.
7. K. I. Kilic, R. H. Dauskardt, “Nonaffine Deformations in ULK Dielectric Glasses” Proceedings of the IEEE IITC, Santa Clara, CA, 2018.
8. G. Buxton and N. Clarke, ““Bending to Stretching” Transition in Disordered Networks", **Physical Review Letters**, vol. 98, no. 23, 2007.
9. A. Basu, Q. Wen, X. Mao, T. Lubensky, P. Janmey and A. Yodh, "Nonaffine Displacements in Flexible Polymer Networks", **Macromolecules**, vol. 44, no. 6, pp. 1671-1679, 2011.
10. D. Head, A. Levine and F. MacKintosh, "Distinct regimes of elastic response and deformation modes of cross-linked cytoskeletal and semiflexible polymer networks", **Physical Review E**, vol. 68, no. 6, 2003.

Recent Publications

Under review:

1. Karsu I. Kilic and Reinhold H. Dauskardt,"Design of Ultrastiff Hybrid Glasses," **Advanced Functional Materials**, under review, 2019.

Published:

1. Y. Ding, S. Dong, F. Hilt, R.H. Dauskardt, "Open-Air Spray Plasma Deposited UV-Absorbing Nanocomposite Coatings", **Nanoscale**, vol. 10, pp. 14525-14533, 2018.

2. Y. Ding, Q. Xiao, R.H. Dauskardt, "Molecular design of confined organic network hybrids with controlled deformation rate sensitivity and moisture resistance", **Acta Materialia**, vol. 142, pp. 162-171, 2018.

3. Karsu I. Kilic and Reinhold H. Dauskardt, "Nonaffine Deformations in ULK Dielectric Glasses" Proceedings of the **IEEE IITC**, 2018.

4. Joseph A. Burg and Reinhold H Dauskardt, "The Effects of Terminal Groups on Elastic Asymmetries in Hybrid Molecular Materials," **Journal of Physical Chemistry B**, 2017.

5. Joseph A. Burg, Mark S. Oliver, Geraud Dubois, and Reinhold H. Dauskardt, "Hyperconnected Molecular Glass Network Architectures with Exceptional Elastic Properties," **Nature Communications**, 2017.

Improving radiation response of solid state interfaces via control of curvature

Michael J. Demkowicz, Kelvin Y. Xie

Texas A&M Engineering Experiment Station (TEES)

Program Scope

The goal of this project is to discover the effects of curvature on the radiation response of solid-state interfaces and explore strategies for elevating the radiation resistance of composite materials via control of interface curvature. Materials that are simultaneously resistant to numerous forms of radiation-induced degradation call for intricate, hierarchical microstructures composed of multiple, interpenetrating phases with high curved interfaces [1], such as those shown in Fig. 1. Yet the majority of previous studies dedicated to radiation response of interfaces have focused on nearly-flat interfaces, leaving the effect of interface curvature unexplored.

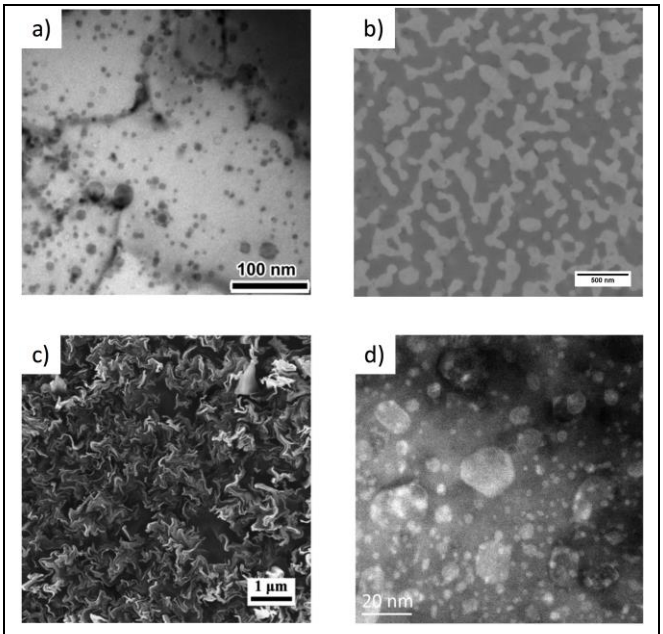

Fig. 1: Hierarchical materials with high curvature interfaces: a) oxide dispersion-strengthened (ODS) austenitic stainless steel [2], b) bicontinuous TaTi/ZrTi composite processed *via* solid metal dealloying (SMD) [3], c) *in situ* Cu-Nb microcomposite [4], d) radiation-induced, self-organized Cu-Nb-W composite [5].

This project integrates experiments and simulations to address three fundamental, scientific hypotheses:

Hypothesis A: The efficiency with which interfaces absorb radiation-induced point defects increases with interface curvature. Thus, composites with nano-curved interfaces (radii of curvature below 100nm) are more radiation resistant than composites with an equal volumetric density of flat interfaces.

Hypothesis B: Interface curvature provides additional nucleation sites for radiation-induced voids and precipitates on the concave (positive curvature) side of a curved interface. This factor influences the asymmetric growth of voids and precipitates at heterophase interfaces, impacting the degradation of interfacial cohesion under irradiation.

Hypothesis C: Radiation-induced voids and impurity precipitates increase the thermal stability of curved interfaces by reducing curvature-driven mass transport along them.

Underlying these hypotheses is the recognition that curvature changes the atomic-level structure of interfaces by introducing defects that may not be present in flat interfaces, such as facet junctions or disconnections. We expect these defects to influence interface radiation response in the manner articulated in our hypotheses. To assess our scientific hypotheses, we organize our work into three integrated research tasks (IRTs):

IRT 1: response of curved interfaces to vacancies and interstitials

IRT 2: implanted impurities and their effect on thermal stability of curved interfaces

IRT 3: radiation resistance of metal composites with highly curved interfaces

IRTs 1 and 2 rely on model materials specially-synthesized using physical vapor deposition (PVD) and lithography. By contrast, IRT 3 compares the radiation response of a variety of different composites that contain complex networks of nano-curved interfaces—such as those shown in Fig. 1—to the radiation response of PVD multilayer composites with an equal volumetric density of flat interfaces.

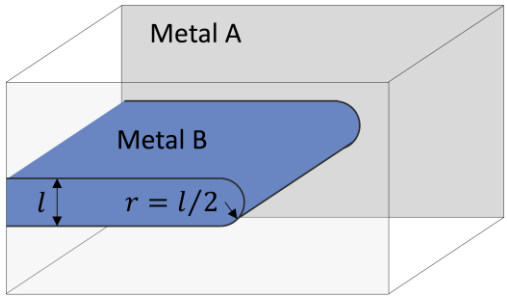

Fig. 2: A single layer of metal B terminating along a straight edge within a matrix of metal A. Upon annealing, the termination edge developed a mean curvature of $\kappa = \frac{1}{r} = \frac{2}{l}$.

The model materials investigated in IRTs 1 and 2 are two-element, A-B thin film composites consisting of a layer of element A sandwiched between two layers of element B. Both B layers are continuous across the entire area of the film. The A layer, however, terminates along a straight edge within the composite, as illustrated in Fig. 2. We use lithographic methods to create this terminated layer structure [6]. Upon careful annealing, the edge of the terminated layer develops a rounded interface with mean curvature approximately equal to the 2/t, where t is the thickness of the layer. Thus, by controlling t, we control the curvature of the edge along which A terminates, allowing us to systematically explore the effect of curvature on radiation response. To assess the effect of curvature on interfaces with differing misfit strains, we investigate two series of A-B element pairs: Cu-FCC pairs, where A=Cu and B=Ir, Ag, or Pb, and Cu-BCC pairs, where A=Cu and B=V, Mo, or Nb. Samples of all compositions will be irradiated/implanted using ion accelerators and examined using quantitative transmission electron microscopy techniques. Atomistic models will be constructed to interpret the response of these samples in terms of atomic-level interface structure.

Recent Progress

Our focus during FY1 of this project has been on three tasks:

Task 1: Perfecting methods for synthesizing the model materials to be used in IRTs 1 and 2. We have used the deposition and lithography equipment at TAMU's AggieFab to create Nb-Cu-Nb trilayers, where the middle (Cu) layer terminates along a straight edge. The Nb layers are ~500nm thick and the Cu layer is ~100nm thick. This task required optimization of the deposition conditions to minimize impurity content (especially O), as measured by XPS, as well as film quality. We have also perfected our methods for sectioning and imaging the resulting samples and performing controlled anneals on them. Our success in this effort positions us to begin performing investigations on thermal stability (IRT 2) and irradiation experiments (IRT 1) in the fall of 2019.

Task 2: Acquiring and characterizing interatomic potentials for all the Cu-FCC and Cu-BCC pairs to be investigated in IRTs 1 and 2. We have collected all of the available EAM interatomic potentials for the Cu-FCC and Cu-BCC pairs to be investigated as part of IRTs 1 and 2. By calculating physical properties such as elastic constants, lattice parameters, cohesive energies, vacancy and interstitial formation energies, and heats of mixing, we have validated the accuracy

of these potentials. As expected, no EAM potential was found for the Cu-Ir binary system. We have therefore developed this potential ourselves, completing the set of potentials needed for our project. Our success in this task positions us to perform one-to-one comparisons between simulations and experiments to be performed as part of IRTs 1 and 2.

Cu and Ir are phase separating metals with minimal solid solubility and no stable intermetallic compounds. Therefore, we constructed our EAM Cu-Ir potential by fitting to cohesive energies and lattice parameters of hypothetical Cu-Ir crystals, including DO_{22} Cu_3Ir, DO_{22} $CuIr_3$, $L2_1$ Cu_3Ir, $L2_1$ $CuIr_3$, $L1_1$ CuIr, $L1_0$ CuIr, and B2 CuIr. The fitting data also include the formation enthalpies of Cu_xIr_{1-x} quasirandom solid solutions. All these quantities are obtained using first-principles, density-functional theory (DFT) calculations. A manuscript describing the resulting potential is currently in preparation.

Task 3: Investigating the helium implantation response of two composites types under IRT 3: a Ta/Ti in situ composite made by annealing a vapor deposited TaTi solid solution and Cu/W composites made by spinodal decomposition by high- temperature PVD. Under IRT 3, we have investigated two metal composites containing complex, interpenetrating microstructures with curved interfaces. One of them was an *in situ* Ta/Ti composite formed via phase separation of a TaTi solid solution under annealing. This sample was already available to us from another project. The sample was implanted with helium (He) impurities using the ion implanters at the CINT user facility at LANL. This work was made possible through the success of a CINT rapid access proposal, which we submitted in the fall of 2018. We then used TEM to investigate the size, number density, and distribution of He bubbles in the as-deposited TaTi single-phase alloy and a Ta/Ti dual-phase nanocomposite.

Using defocus imaging, we found that bubbles had an average diameter of ~1.7 nm and number density of ~$4\times10^4/\mu m^2$. He bubbles were found to segregate preferentially to grain boundaries, as illustrated in Fig. 3. In the Ta/Ti nanocomposite, bubbles in the Ti(HCP)-rich phase were found to be are smaller and of higher number density (~1.2 nm, ~$12\times10^4/\mu m^2$) than those in the Ta(BCC)-rich phase (~3 nm, ~$2.4\times10^4/\mu m^2$) as well as in the single-phase alloy. These findings stand in contrast to previous investigations on FCC/BCC composites, where bubbles are always found to be smaller in the BCC phase. In the Ta/Ti composite, He bubbles were also observed to decorate phase boundaries. However, these bubbles were generally smaller than those on the grain boundaries. These findings represent the first investigation of He implantation response in BCC/HCP nanocomposites. They are currently under preparation for publication.

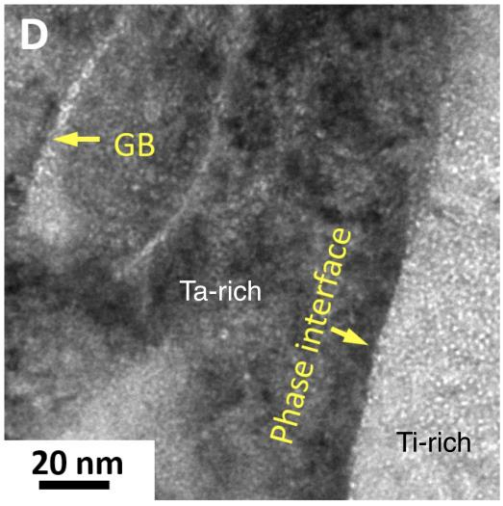

Fig. 3: Defocus TEM micrograph of He bubbles (bright) near a grain boundary (GB) and phase interface in a He-implanted *in situ* Ta-Ti nanocomposite.

Finally, through our CINT user project, we also created Cu-W nanocomposites formed by spinodal decomposition during high-temperature co-deposition. Several different deposition temperatures and deposition rates were used, giving rise

to different spinodally decomposed microstructure morphologies. These samples were implanted with He and the depth profiles of the implanted He were measured using nuclear reaction analysis (NRA). TEM imaging of the He-implanted microstructures has yet to be performed for these samples.

Future Plans

Our main goal in FY2 is to use the model materials created in the current FY to complete IRT 2, which is concerned with the effect of implanted impurities on thermal stability of curved interfaces. Completion of this work will enable us to verify or falsify science hypotheses B and C. The work to be completed includes:

- Anneal model materials over a range of times and temperatures and, based on the resulting microstructure evolution, determine the mobility of the heterophase interfaces in them.
- Repeat this investigation for samples that were implanted with He; assess the effect of interfacial He impurities on interface mobility and, therefore, high-temperature microstructure stability in composites with highly curved interfaces.
- Using precession electron diffraction (PED), determine the crystallographic character of the heterophase interfaces in our model materials; construct atomistic models that are faithful to the experimentally-determined interface character and use these models to investigage the effect of He impurities on interfacial mass transport.

Simultaneously, we will also continue to prepare for carrying out IRT 1 (which tests hypotheses A and B). Since this IRT requires model materials with very thin middle ("A") layers, we expect that we may have to make use of the high-performance PVD equipment available at the CINT facility at LANL.

References

[1] *Basic research needs for future nuclear energy*. US Department of Energy, Office of Science, 2017.

[2] K. Suresh, M. Nagini, R. Vijay, M. Ramakrishna, R.C. Gundakaram, A.V. Reddy, G. Sundararajan. *Microstructural studies of oxide dispersion strengthened austenitic steels*, Mater. Des. **110** (2016) 519-525.

[3] I. McCue, M.J. Demkowicz. *Alloy Design Criteria for Solid Metal Dealloying of Thin Films*, JOM **69** (2017) 2199-2205.

[4] L.P. Deng, K. Han, K.T. Hartwig, T.M. Siegrist, L.Y. Dong, Z.Y. Sun, X.F. Yang, Q. Liu. *Hardness, electrical resistivity, and modeling of in situ Cu-Nb microcomposites*, J. Alloy. Compd. **602** (2014) 331-338.

[5] X. Zhang, J.G. Wen, P. Bellon, R.S. Averback. *Irradiation-induced selective precipitation in Cu-Nb-W alloys: An approach towards coarsening resistance*, Acta Mater. **61** (2013) 2004-2015.

[6] M.G. Ramezani, M.J. Demkowicz, G. Feng, M.P. Rutner. *Joining of physical vapor-deposited metal nano-layered composites*, Scr. Mater. **139** (2017) 114-118.

Publications

[1] S. Xiang, I. McCue, D. Yadav, Y.Q. Wang, J.K. Baldwin, M.J. Demkowicz, K.Y. Xie. *Transmission electron microscopy characterization of helium bubbles in a Ta-Ti alloy and a Ta/Ti nanocomposite*, **in preparation** (2019).

[2] T. Duong, T. Duong, M.J. Demkowicz. An embedded-atom method potential for the Cu-Ir binary system, **in preparation** (2019).

Continuum dislocation dynamics modeling of self-organized dislocation structures in metals

Anter El-Azab, School of Materials Engineering, Purdue University

Program Scope

This project aims to provide a first-principles understanding of the collective aspects of dislocation dynamics that lead to dislocation patterning in deforming FCC metals. Of primary interest are the early stages of dislocation pattern formation. The fundamental role of spatial and temporal dislocation correlations in dislocation self-organization, collective dislocation mobility, and short range reactions under deformation are being investigated within the recently developed continuum dislocation dynamics framework [1]. The enhanced framework is being used to predict the patterning of dislocations in Cu and other FCC metals as a function of strain rate and crystallographic orientation. To capture the underlying science of deformation mechanisms on mesoscopic length scales and enable direct comparisons with deformation measurements, continuum dislocation dynamics simulations will be extended to volumes on the order of 15μm – 25μm on edge and strains up to 4-5%. These simulations will provide a new level of predictions for comparison with *in situ* and *ex situ* Transmission Electron Microscopy (TEM), Electron Backscattering Diffraction (EBSD), and direct and absolute model validation with 3D Dark Field X-Ray Microscopy (DFXM) and both polychromatic and scanning-monochromatic 3D X-Ray Microscopy (3DXM) experiments using focused synchrotron x-ray beams.

Recent Progress

We extended continuum dislocation dynamics (CDD) framework to model dislocation junction reactions formation. In CDD, dislocations are represented by density fields the evolution of which is governed by transport-reaction type equations. These equations are solved concurrently with crystal mechanics equations using the eigenstrain approach [1,2]. Several types of dislocation reactions are to be considered: the annihilation process within the same slip system, collinear annihilation, and glissile and sessile junction reactions. Together with cross slip, these processes represent the physics to be incorporated into dislocation dynamics models of patterning. The reactions processes and cross slip lead to the appearance of so-called network terms in the transport reaction equations governing the dislocation densities. These network terms can be constructed within the transport-reaction systems by subtracting the reacting dislocation density vector from each reacting slip system and adding to the same density to the product slip system (for glissile junction) or forming immobile densities (in the case of sessile junctions). In the case of annihilation, no product is formed. In previous models, junction reactions were typically accounted for by adding Taylor hardening terms as resistive stress

components in CDD models [2]. Unlike the explicit treatment of reactions into the governing equations, such resistive stresses result in slowing down the motion of dislocations with no change in the dislocation densities.

We have established energy-based criteria for junction reactions in terms of dislocation vector densities and the corresponding Burgers vectors. The criteria can be used for all kinds of junction reactions, both glissile and sessile. When junctions are formed, the total energy will be reduced. An important aspect of the generalized junction formation criterion developed here is that it depends on both the Burgers vectors and line directions of the reacting species. The line direction dependence distinguishes this criterion from Frank's [3], which depends only on Burgers vectors, and it delineates the range of orientations in which junctions form (central, yellow regions in Fig. 1 from those for forest cutting. The orientation dependence of dislocation line calculated by this energy criterion shows that it's easier to form glissile junction and Lomer-Cotrell junction than Hirth junction. The network term of junction reactions has been carefully formulated in terms of dislocation vector densities. It is a function of the reacting dislocation densities together with a junction reaction rate, which can be derived by discrete dislocation dynamics (DDD). A simple test is shown in Fig. 2 in which a glissile junction (blue bundle) has formed as a result of reaction between dislocations on two slip systems (red and green). The results show that enhanced CDD framework is able to capture the change of dislocation network due to reactions: dislocations on two collinear slip systems annihilate when they are in opposite directions; glissile junction formed on the new slip system behaves like Frank-Read source generating new dislocation loops; and sessile Lomer-Cottrell and Hirth junctions stop at the intersection of the two slip planes. These results are consistent with the existing discrete dislocation dynamics (DDD) simulations.

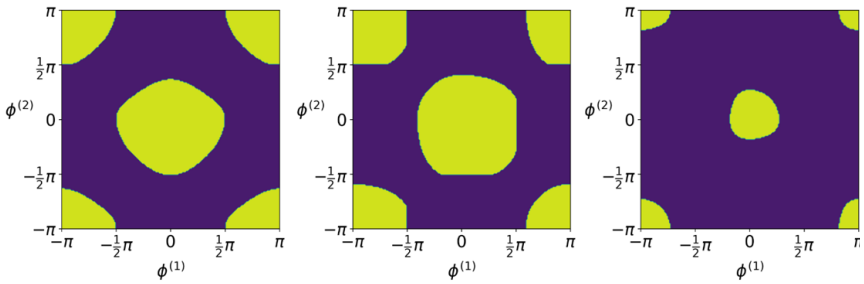

Fig. 1: Orientation map for the junction reactions through the energy-based criterion developed under the current project. From left to right: glissile, Lomer-Cottrell, and Hirth, respectively.

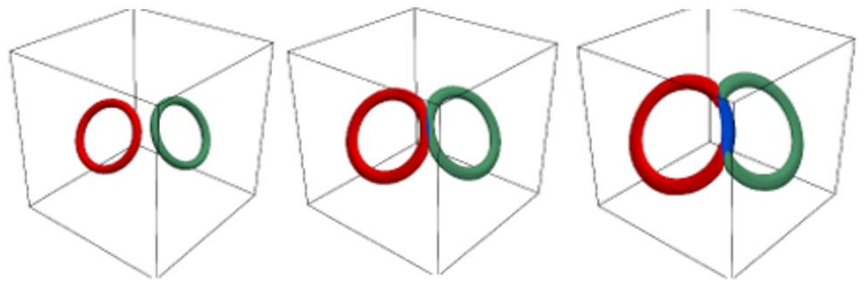

Fig. 2: A sequence of snapshots illustrating the formation of glissile junction (blue) due to reactions between coplanar systems (red and green dislocation bundles).

The junction implementation approach discussed above has been implemented in our CDD code via an operator splitting scheme in which both the transport (glide motion) and reactions of dislocations were treated in a staggered fashion. Simulation of collective dislocation dynamics has been started with simulation domains consisting of a large number of dislocation loop bundles on each slip system. The initial results are very promising and show that our approach predicts the dislocation patterns and hardening behavior of crystals as originally hypothesized. Figs. 3 and 4 provide sample results for the stress-strain curve, dislocation density evolution, and dislocation pattern, respectively. In this implementation, only glissile junction formation is included in the continuum dislocation dynamics equations while the sessile locks are substituted for by Taylor type hardening terms. The stress-strain behavior shown in Fig. 3 (left panel) for Cu single crystal loaded at a constant rate along the [001] direction shows less-than-optimal hardening rate beyond the initial yielding. While this can be adjusted by adjusting the Taylor hardening coefficients compensating for the sessile junctions, we plan to remove those terms completely in favor of an explicit representation of sessile junctions in the next simulations. Fig. 3 shows also the total dislocation density evolution corresponding to the stress-strain curves. The results are consistent with DDD simulations at the same conditions. The dislocation density for the individual slip systems is shown in Fig. 4, corresponding to the short simulation ending at 1.2% strain in Fig. 3. The density evolution is non-smooth as should be at the level of resolution considered in our mesoscale simulation. This non-smoothness is due to the random dislocation reactions and cross slip taking place within the dislocation systems. It is noted that the density on the slip systems

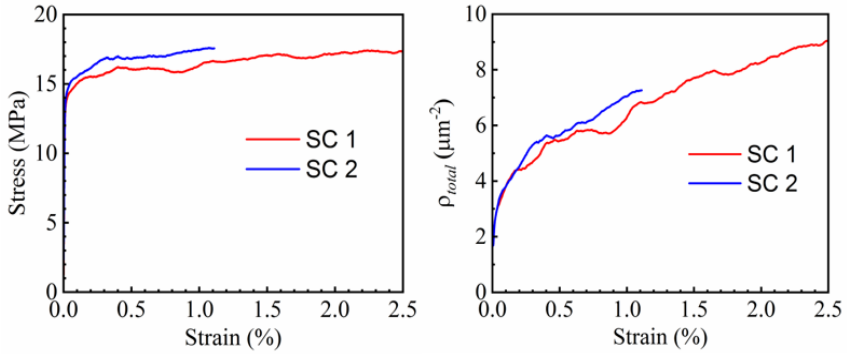

Fig. 3: Stress-strain curve and dislocation density evolution for two simulation conditions, SC1 and SC2 differing slightly Taylor coefficients.

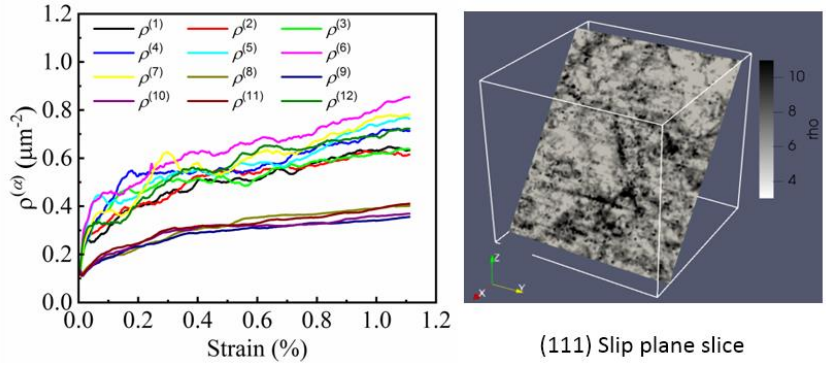

Fig. 4. Dislocation pattern at 0.8% strain shown on a (111) plane within the simulated volume. This volume is approximately 5 micron on the edge. The figure shows the beginning of cell formation.

perpendicular to the loading axis are also evolving, albeit slowly, due to the reactions, cross slip, as well as the 3D nature of the internal stress field. The right panel shows a slice of the dislocation density over a (111) plane showing the beginning of dislocation patterning. It is clear that our model is able to predict the initial formation of dislocation cell structure characteristic of [001] loading.

We are currently completing the testing for the sessile lock formation and destruction, investigating the orientation dependence of stress-strain behavior and patterns in preparation for comparison with experiments.

Future Plans

In next year we will:

- Finalize the dislocation correlation calculations.
- Finalize the simulation of coarse grained junction reactions using discrete dislocation dynamics simulations.
- Implement the dislocation correlations and short range interactions in continuum dislocation dynamics code.
- Complete the predictions of dislocation patterns and comparison with experiments.

References

[1] S. Xia, J. Belak, and A. El-Azab, The discrete-continuum connection in dislocation dynamics: I. Time coarse graining of cross slip, Modelling and Simulation in Materials Science and Engineering, 24 (2016) 075007.

[2] T. Hochrainer, Thermodynamically consistent continuum dislocation dynamics, Journal of the Mechanics and Physics of Solids, 88 (2016) 12-22.

[3] J. Hirth and J. Lothe, Theory of Dislocations, John Wiley & Sons, 1982.

Publications

Three papers fully supported by this project and three partially supported papers are being finalized.

Fundamental Mechanisms Controlling Dislocation-Obstacle Interactions in Metals and Alloys

[*]David T. Fullwood, [*]Eric R. Homer and [+]Robert H. Wagoner

[*]Mechanical Engineering Department, Brigham Young University, Provo UT 84602, USA, dfullwood@byu.edu
[+]Department of Material Science and Engineering, Ohio State University, 2041 College Rd, Columbus OH 43210, USA

Program Scope

Despite various advances in modeling the behavior of dislocations at the meso-scale, the accurate prediction of bulk dislocation evolution at the sub-grain level remains a challenge. This project seeks to test the hypothesis that bulk (meso-scale) grain boundary (GB) / dislocation interactions can be predicted using simple geometrical considerations of the relevant slip systems, and/or other local microstructural characteristics; furthermore, the backstresses associated with the resultant geometrically necessary dislocations (GNDs), when added to single crystal hardening behavior, produce the resultant polycrystalline deformation response. The hypothesis is explored via a combined modeling and experimental approach.

Cross-correlation EBSD is used to map actual GND content in order to compare simulated predictions with experimental measurements. The study focuses particularly on grain boundaries, where GND buildup often occurs. Furthermore, MD simulations of dislocation / GB interactions across a wide number of GB types are used to inform the selection of transmissivity factor, and test the hypothesis at the atomistic and nano-level.

The hypothesized and uncovered mechanisms are captured and tested via a super-dislocation (SD) model, based upon crystal plasticity, and incorporating meso-scale elastic dislocation interactions.

Recent Progress

The key questions that have recently been investigated by the team are: i) What is the obstacle stress associated with a particular GB type? ii) How does that obstacle stress influence the distribution of GNDs near the GB? and iii) How does the resultant backstress from the GND distribution contribute to overall hardening?

The first question was tackled directly using an MD approach. MD simulations of dislocation / GB interactions were carried out on more than 33 different FCC Ni bicrystals, each subjected to four different loading conditions to induce incident dislocation / GB interactions in 132 unique configurations. The resulting simulations produced 189 dislocation / GB interactions. Each interaction was analyzed to determine properties that affected the likelihood of transmission, reflection, or absorption of the dislocation at the GB of interest. Properties included the slip system of the incident dislocation, resolved shear stresses associated with the interaction, and geometric factors including transmissivity [1] and dislocation content left behind in the GB (residual Burgers vector, RBV) following a transmission event [2]. Each simulation cell consists of ~500,000 atoms and has a configuration designed such that applied uniaxial loads, cause nucleation of dislocations at a sharp notch, which then propagate into the GB. Figure 1 shows two separate dislocations as they interact with the GB; one transmits through while the other reflects back. The associated resolved shear stresses for the respective incident slip system are also shown in Fig. 1.

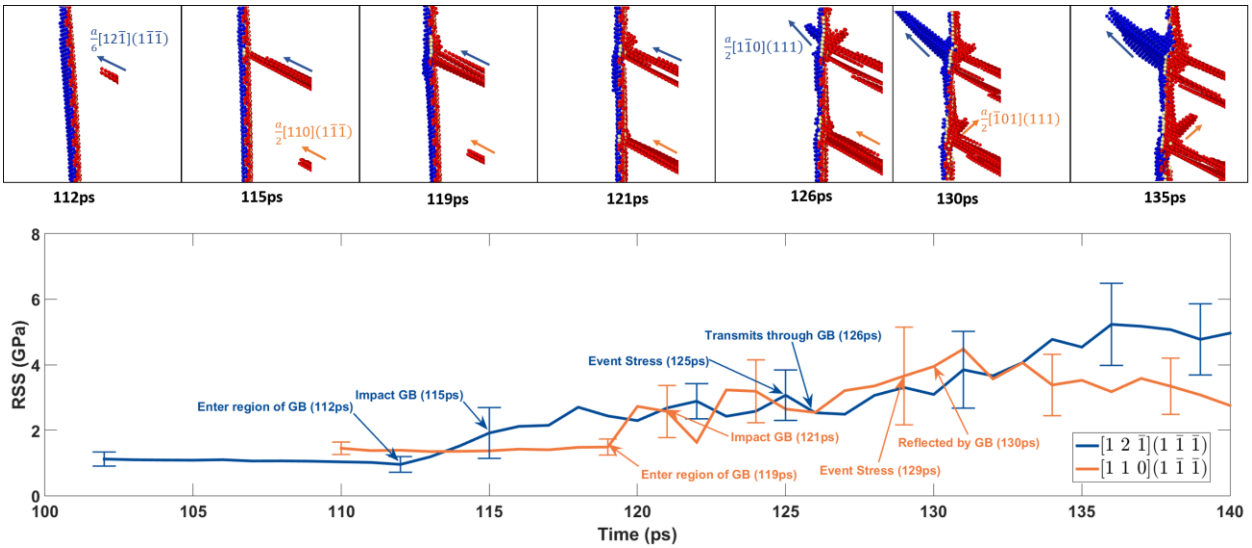

Fig. 1 Snapshots of the simulation of the [100] Tilt Σ25a bicrystal. Two dislocations of the same slip plane but different slip directions impact the GB at different locations and at different times. The first dislocation (blue) transmits while the second dislocation (orange) reflects. The resolved shear stress associated with each event is shown beneath the snapshots and are labelled accordingly.

Analysis of all 189 simulated interactions confirms the ability to predict the slip system of a transmitted dislocation using the common geometric criteria of transmissivity and residual Burgers vector. Transmissivity factor predicts the slip system for transmission with reasonable accuracy and predicts the slip plane of the transmitted dislocation with even higher accuracy. For the majority of transmitted dislocations, the transmissivity value is within 20% of the maximum possible value for the given dislocation-GB interaction. RBV predicts the slip direction for transmission well.

The MD results also provide insight into the type of interaction observed, though these insights were more difficult to extract. There was a surprising lack of correlation between any of the geometric factors and resolved shear stress and whether a dislocation transmitted through, was absorbed by, or reflected back from a GB. Transmission frequency decreased with increasing disorientation angle. Reflection of dislocations occurred more frequently at twist GBs than tilt GBs while the opposite is true of transmission. Both twist and tilt GBs were equally likely to absorb dislocations. Partial dislocations are more likely to transmit than full dislocations. Twist GBs appear to have an energy barrier to transmission; below GB energies of ~950 mJ/m^2, transmission is exclusively observed and above this value transmission is not observed.

Machine learning was required to find complex combinations of geometric properties, such as the minimum residual Burgers vector (RBV) and the disorientation angle between the two grains, to determine whether dislocations would transmit through or be absorbed by a GB; the machine learning model can correctly predict transmission 75.5% of the time and correctly predict absorption 77% of the time. Reflection is not effectively predicted in this study.

The first and second question mentioned above were also combined in an empirical study of how GND buildup correlates with GB type in both BCC Ta and FCC nickel. The key question to be answered is whether GBs with higher predicted obstacle strength (presumed to correlate with lower transmissivity) tend to associate with higher GND buildup. The resultant observations enable a focused study on GBs of particular interest, as well as highlighting the particular obstacle interaction mechanisms that contribute to kinematic hardening and other backstress-enabled phenomena.

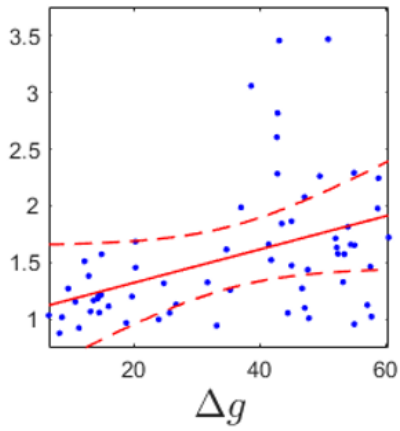

Fig. 2 Correlation between GB GND density, as a multiple of mean grain GND density, and GB misorientation

Both tantalum oligocrystals and polycrystals displayed a weak, albeit significant, statistical link between GB character (including various transmissivity factors) and increased GND density. Figure 2 illustrates the relationship for GB misorientation and GND buildup in the neighborhood of the GBs.

These Ta polycrystal results also reflect the observations made for three nickel superalloys, using high resolution digital image correlation (HRDIC). Figure 3 shows an inverse pole figure, a shear strain map and the profile of shear along a single slip band in the RR1000 alloy. As can be seen, there is a strain gradient from the middle area of the grain towards the grain boundaries at each end of the slip band. This is typical for several hundred slip bands investigated.

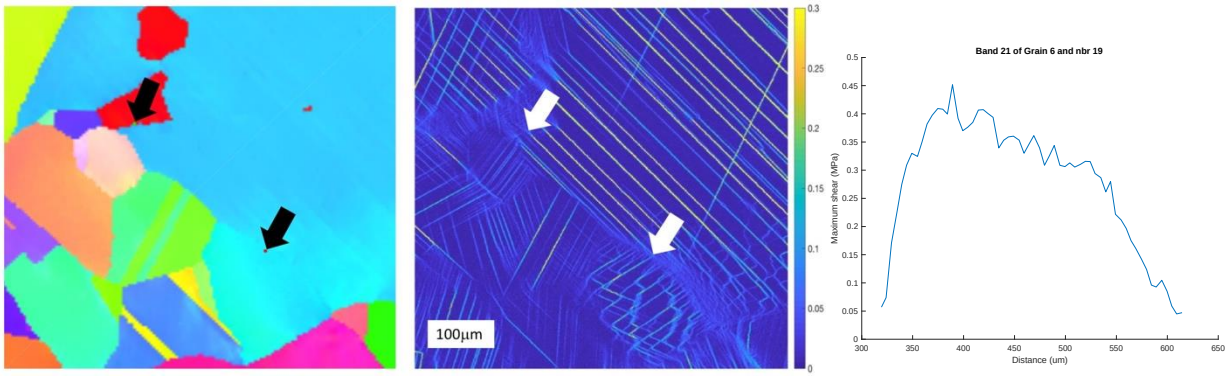

Fig. 3 - Inverse pole figure for segment of RR1000 coarse precipitate sample (left), map of maximum shear (middle) and profile of maximum shear along indicated band.

If the shear gradient is treated as a pileup of edge dislocations (a view that is supported by the local orientation gradients – see the IPF figure), then the dislocation spacing and resultant backstress can be calculated for the dislocation closest to the grain boundary. No significant correlations were observed between the distribution of pileup stresses and various GB transmissivity factors and other metrics of GB character. The combined experimental and MD studies present two potential ideas for further study: i) the obstacle stress associated with a particular GB is only weakly related to its character (or related in a very complex / stochastic manner); and/or ii) the GND buildup associated with a boundary is dominated by the local incompatibility requirements, with actual level of obstacle stress playing a secondary role. Clarification of the magnitude of the influence exerted by the competing phenomena is underway.

The third question, relating to the relationship between GND distributions and hardening rates was investigated using the Ta oligocrystals, for which full 3D information was available to model. Both the CPFEM and SD model capture the approximately correct stress-strain curve; however, the SD model uses inferred single crystal hardening parameters plus backstress relating to GND distributions (Fig. 4). The difference between SD and SD* (the same model, without backstress) illustrates the magnitude of hardening that is contributed by the backstress. Consistent with macroscopic backstress studies, the backstress dominates early in the deformation, and the SSD hardening contributes more later on.

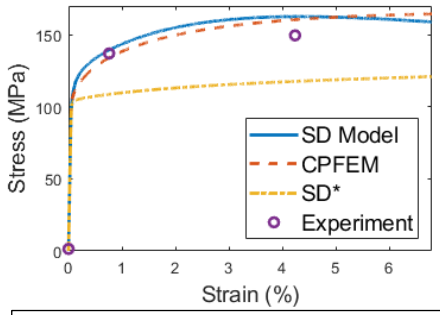

Fig. 4 Measured and modeled engineering stress vs strain for Ta oligocrystal #3. SD and CPFEM use inferred single crystal and best fit polycrystal hardening parameters, respectively; SD* is the same as SD, but without backstress

Future Plans

The next stage of the MD work, currently under way, is focused on examining resolved shear stresses associated with transmission and their correlation with a limited set of geometric parameters. The approach employs the concurrent atomistic-continuum method to simulate larger bicrystals to improve the fidelity of the stress measurements associated with the dislocation / GB interactions. The goal is to gain a better understanding of obstacle stresses required for the SD model to accurately predict dislocation / GB interactions.

Two combined HREBSD / HRDIC studies are underway (on Ta and Ni) to confirm the relationships between local hardening rates and GND distributions, as a more sensitive indicator of the role of backstress in sub-grain level deformation. The Ni experiment will take place in collaboration with the University of Manchester to test several stages of loading and unloading in a pure nickel sample, with combined HREBSD / HRDIC, to further highlight local backstress behavior.

The SD model originally used a column-selection method and Hirth's equation (suitable parallel edge-edge interaction in one grain only) to calculate interactions between GNDs. A new version will be based on computing and representing the full GND content in each element by Nye's Tensor, and incorporating the full remote stress field (from all GNDs) in the backstress via Zbib's method [3]. This addresses the most serious, perennial concern of reviewers that only edge-edge slip was incorporated in SD, a single slip system at a time. Furthermore, the column method introduced instabilities in back stress, requiring it to be incorporated as a friction stress (always opposing the applied stress), rather than a more accurate and more correct signed stress that can hinder or assist the applied stress. This will also be addressed at the same time.

References

[1] Z. Shen, R.H. Wagoner, W.A.T. Clark, Dislocation and grain boundary interactions in metals, Acta Metall. 36(12) (1988) 3231-3242.
[2] W.Z. Abuzaid, M.D. Sangid, J.D. Carroll, H. Sehitoglu, J. Lambros, Slip transfer and plastic strain accumulation across grain boundaries in Hastelloy X, Journal Of The Mechanics And Physics Of Solids 60(6) (2012) 1201-1220.
[3] H.M. Zbib, M. Rhee, J.P. Hirth, On plastic deformation and the dynamics of 3D dislocations, International Journal of Mechanical Sciences 40(2-3) (1998) 113-127.

Publications since 2017 retreat:

1. Hyuk Jong Bong, Hojun Lim, Myoung - Gyu Lee, David Fullwood, Eric Homer and R. H. Wagoner, An RVE Procedure for Micromechanical Prediction of Mechanical Behavior of Dual-phase Steel, Materials Science and Engineering A, 695 (2017), 101-111
2. Richard Wyman, David Fullwood, Robert Wagoner, Eric Homer, Variability of non-Schmid effects in grain boundary dislocation nucleation criteria, Acta Materialia, 124C (2017) 588-597
3. Landon Hansen, Brian Jackson, David Fullwood, Stuart I. Wright, Marc de Graef, Eric Homer, Robert Wagoner, Influence of Noise Generating Factors on Cross Correlation EBSD Measurement of GNDs, Microscopy and Microanalysis, in press, 23 (2017), Issue 3, 460-471
4. W. Gan, H.J. Bong, H. Lim, R. Boger, F. Barlat, R.H. Wagoner. Mechanism of the Bauschinger effect in Al-Ge-Si alloys, Materials Science and Engineering A 684 (2017) 353-372
5. Brian Jackson, David Fullwood, Jordan Christensen, and Stuart Wright, Resolving pseudosymmetry in gamma-TiAl using cross correlation electron backscatter diffraction with dynamically simulated reference patterns, Journal of Applied Crystalography, 51 (2018), 655-669
6. Travis M. Rampton, Stuart I. Wright, Michael P. Miles, Eric R. Homer, Robert H. Wagoner, David T. Fullwood, Improved Twin Detection via Tracking of Individual Kikuchi Band Intensity of EBSD Patterns, Ultramicroscopy, 185 (2018), 5-14
7. Bret E. Dunlap, Timothy J. Ruggles, David T. Fullwood, Brian Jackson, Martin A. Crimp, Comparison of Dislocation Characterization By Electron Channeling Contrast Imaging and Cross-Correlation Electron Backscattered Diffraction, Ultramicroscopy, 184A (2018), 125-133
8. Bret E. Dunlap, Timothy J. Ruggles, David T. Fullwood, Martin A. Crimp, Comparison of Dislocation Mapping Using Electron Channeling Contrast Imaging and Cross-Correlation Electron Backscattered Diffraction, Microscopy and Microanalysis 23 (2017) suppl 1, 546-547
9. Adams, DW, DT Fullwood, RH Wagoner, and ER Homer (2019). Atomistic survey of grain boundary-dislocation inter- actions in FCC nickel. Computational Materials Science 164, 171-185
10. Homer, ER (2019). High-throughput simulations for insight into grain boundary structure-property relationships and other complex microstructural phenomena. Computational Materials Science 161, 244-254
11. Greg C. Randall, Kameron R. Hansen, Brian Jackson, David T. Fullwood, Lower-bound Dislocation Density Mapping in Microcoined Tantalum using High-Resolution Electron Backscatter Diffraction, Materials Characterization, 153 (2019), 318-327

The Role of Anisotropy on the Self-Organization of Gas Bubble Superlattice

J. Gan[1], Y. Zhang[1], C. Sun[1], Y. Gao[1], C. Jiang[1], L. He[1], D. Sprouster[2], S. Gill[2], M. Topsakal[2], L. Ecker[2]

[1]Idaho National Laboratory, [2]Brookhaven National Laboratory

Program Scope

Three-dimensionally ordered nanostructures have many potential applications and irradiation is a useful tool for creating them. Gas bubble superlattice (GBS) and void superlattice are the two important ordered nanostructures of great scientific interest. The objective of this project is to understand the fundamental mechanisms controlling the self-organization of these patterned structures, to aid the development of novel materials with novel properties and for applications in conditions involving irradiation. Although both types of superlattices were investigated extensively in the past, a consensus on the formation mechanisms is yet to be achieved. Moreover, the recent discovery of incoherent face-centered-cubic (fcc) Xe bubble lattice in body-centered-cubic (bcc) U-Mo (Fig.1) challenges the widely accepted coherency between superlattices and matrices. A complete mechanistic understanding of bubble lattice self-organization will have a large impact to materials science and nuclear technology advancement. This project takes an integrated experimental and computational approach. The focus is placed on the self-organization mechanisms of nanostructures under irradiation. The factors that dictate the self-organization, including materials properties and irradiation conditions, will be identified to assist new material development. The studies center on two appealing self-organization hypotheses proposed in the literature: *anisotropic elastic interaction* between voids or bubbles and *anisotropy diffusion* such as one-dimensional (1D) self-interstitial atoms (SIA) diffusion. In the past two years, the role of 1D SIA diffusion has been elucidated by coupling atomistic modeling and inert gas-ion implantation experiments using metals such as bcc Mo and W, with the former being elastically anisotropic while the latter isotropic. Following the theory proposed in our previous work, the effects of irradiation condition on the formation and the properties of GBSs are discerned experimentally. Efforts have also been made to investigate the fundamental interaction between inert gas and metal matrices, and GBS stabilities under irradiation and annealing. The research outcomes from the Phase-I studies suggest the possibility of developing a unified theory for both void superlattices and GBS, and for various types of inert gases and matrix materials.

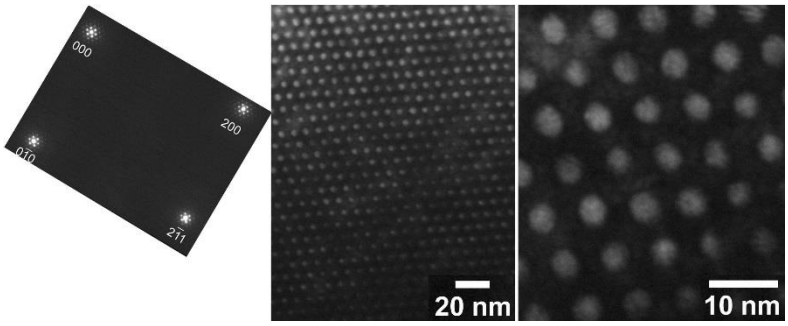

Fig. 1 TEM select area diffraction at zone [011] of bcc U-Mo showing satellite spots from Xe bubble superlattice (left). Bright field images of Xe bubble superlattice at low (center) and high (right) magnification.

Recent Progress

By coupling the non-destructive synchrotron beam analysis and TEM characterization with modeling, full information regarding GBS including bubble size, distance, pressure and chemistry can be achieved. Effects of helium implantation parameter on He GBS formation are evaluated using small angle x-ray scattering (SAXS) analysis. X-ray Absorption Spectroscopy (XAS) measurements at the SRX beamline of the NSLS-II were employed to determine the structure of the Kr and Xe gas atoms in the irradiated U-Mo fuel reference sample. Results show that the fission gas atoms are under intense pressure (~1.5 - 2.0 GPa) with crystalline spectra consistent with an FCC structure, indicating the Xe/Kr bubbles in neutron irradiated U-Mo are actually in solid state in FCC crystal form at room temperature. Figure 2 shows the results of the SAXS and XAS measurements for this project.

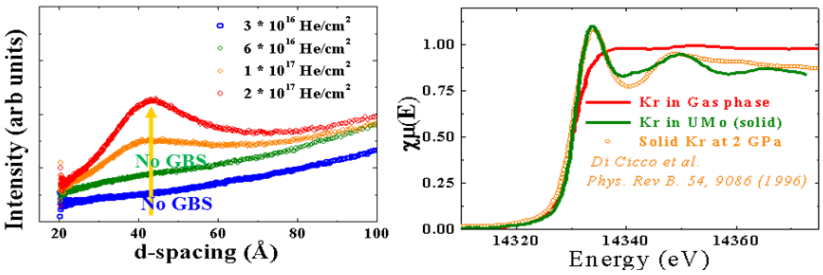

Fig. 2 Synchrotron beam SAXS data for Mo irradiated with He ions at 300 ℃ (left) and XAS data from the SRX of NSLS-II showing solid state of Kr in Xe/Kr bubble superlattice in irradiated U-Mo reference sample.

Besides He GBS formation in Mo, W and Fe, GBS with Ne, Ar and Kr are also investigated, as shown in Figure 3. Ne GBS formed from TEM in-situ irradiation at 300 °C to a dose of 10 at.%Ne with an average bubble size of ~ 1.5 nm and bubble lattice constant ~ 5.1 nm, similar to that of He GBS in Mo. Argon GBS formation in Fe from TEM in-situ irradiation at room temperature was identified at 3.5×10^{16} Ar/cm^2. The degree of ordering was further improved at 7.3×10^{16} Ar/cm^2, with an average bubble size of ~ 1.8 nm and a GBS lattice constant of ~ 6.4 nm. TEM in-situ irradiation of Mo with 300 keV Kr ions at 300 °C revealed Kr bubble presence at 1.6 at.%Kr, a slightly aligned Kr bubbles at 4.0 at.%Kr and disordered random bubbles at 9.0 at.%Kr with increased bubble size. Kr GBS was not identified under this irradiation condition. An experiment with two-step TEM in-situ Kr ion irradiation at 300 °C was also carried out using the IVEM at ANL. Mo was irradiated in Step-1 with 300 keV Kr to ~ 3 at.%Kr, where Kr bubbles are randomly distributed, followed by Step-2 irradiation with 1.0 MeV Kr ions (mostly transmitted) to 2.5 dpa, where the evidence of slightly ordering of Kr GBS can be identified. Comparing to He GBS, the difficulty with ion irradiation experiment for Kr and Xe GBS formation indicates the formation mechanism could change with these large gas ions since the binding energy with vacancy is significantly higher and role of elasticity anisotropic on the GBS formation may become important. It is expected that these difference in comparison to that of small gas ions are important and may eventually attribute to the different bubble superlattice structure from the matrix of host material such as an fcc GBS on a bcc host material.

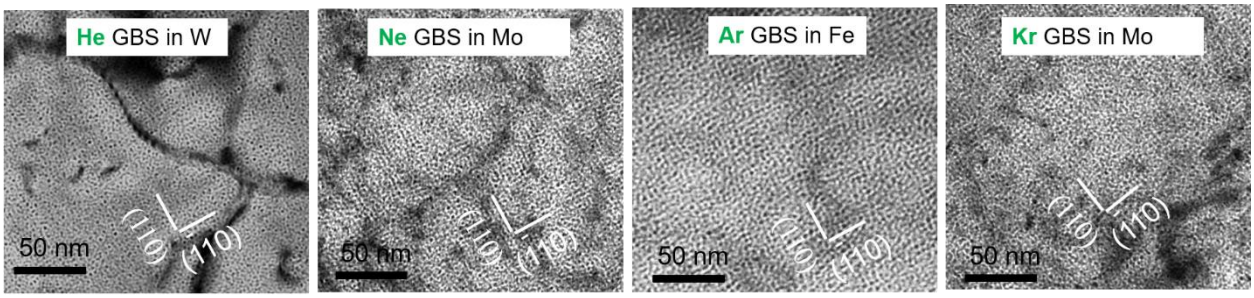

Fig.3 TEM bright field images reveal the development of noble gas bubble superlattice in bcc metals. The role of elastic anisotropy and SIA diffusion anisotropy is elucidated.

According to our newly developed theory, superlattices form by superposition of symmetrical concentration waves that develop at the critical point when the uniform concentration field becomes unstable. This implies that the formation process of superlattices will experience three stages at finite temperatures. Before the instability occurs, the voids or bubbles distribute randomly because no perturbation waves are stable. Upon the occurrence of instability, symmetrical waves start to develop. Due to stochastic effects, they do not develop at the same time. A planar ordering will appear due to the wave that develops first. Eventually, all symmetrical waves will develop, and their superposition leads to a three-dimensional superlattice. Such a three-stage formation process has been observed in both Atomic Kinetic Monte Carlo (AKMC) simulations and He ion implantation experiments in bcc Mo. Such observations prove that indeed superlattices form by symmetrical waves that develop at the instability point. It was found that the formation of gas bubble superlattice depends on specific irradiation conditions, specifically temperature, fluence and flux. The ratio of bubble superlattice constant to bubble diameter falls between 2 and 5, and it requires relatively lower irradiation temperature with higher He appm/dpa ratio.

In addition, synchrotron based multi-modal imaging (Figure 4) studies of Kr irradiated single crystal W was performed at HXN beamline at NSLS II to elucidate structural changes (lattice distortion and strain) using nanodiffraction and elemental changes using X-ray fluorescence (XRF). Single crystal tungsten was Kr irradiated at energy of 1.8 MeV to a fluence of 2.25×10^{17} ions/cm^2 in the Ion Beam Lab at Sandia National Laboratories. Python based data analysis scripts were developed to extract local strain variability from variations in the length of the reciprocal-lattice vector relative to the mean.

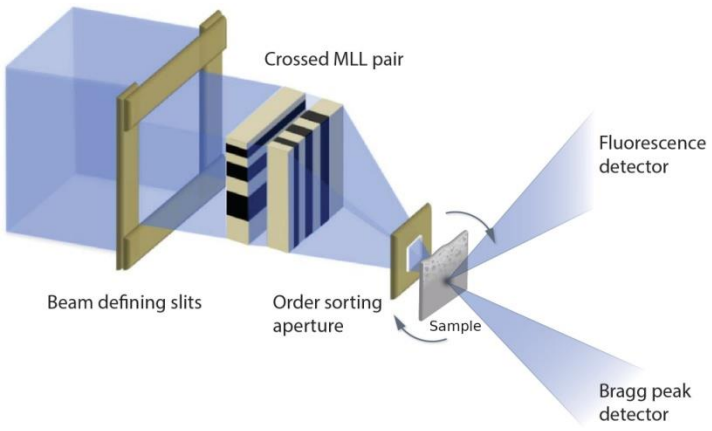

Fig. 4 Schematic showing multi-modal imaging set-up at HXN beamline, NSLS II for simultaneous XRF and nanodiffraction mapping of Kr irradiated single crystal W.

X-ray based nano-diffraction was used to study structural changes in the tungsten matrix. It was observed that as the probe moves from unirradiated W region to Kr irradiated W region the diffraction peak intensity changes from a sharp well defined peak to diffuse diffraction intensity. Such change in diffraction intensity clearly indicates the changes in microstructure after Kr irradiation, where W matrix changes from highly crystalline character (single crystal) in pristine matrix to distorted crystalline region. Such deviation from single crystal character can be attributed to presence of radiation induced defects. High densities of such radiation-induced defects as observed in this study result in significant strain in the surrounding matrix.

Following the rate theory framework used to predict the characteristic length scales, the recombination rate between vacancies and self-interstitial atoms (SIAs) is derived in the discrete lattice space. It is found that the appearance of perturbation reduces the recombination rate. More importantly, such a reduction becomes anisotropic when interstitials diffuse anisotropically. Because the growth rates of perturbation waves are proportional to the negative of recombination rates, the wave directions associated with the most reduction in recombination will be favored over others to grow. This allows for theoretical predictions of superlattice symmetry by numerically calculating the reduction of recombination rate due to perturbations and anisotropic diffusion. As such, the physical connection between anisotropic interstitial diffusion and superlattice symmetry is established. Moreover, this demonstrates the rate theory framework is capable to predict both superlattice parameter and structure. For one-dimensional interstitial diffusion along the [111] direction, all wave directions in the (111) plane are favored equally, indicating random void distribution when projected in the [111] direction. For one dimensional interstitial diffusion along the [111] and [-111] directions, a single wave vector [0 1 -1] is favored, indicating (01-1) planar ordering. All <110> waves are favored when interstitials diffuse one-dimensionally along all <111> directions, indicating a bcc superlattice. The predictions are confirmed by AKMC simulations.

Extensive density functional theory (DFT) calculations have been performed to predict the energetics, site preference, and migration barriers of noble gas atoms (He, Ne, Ar, and Kr) in transition metals with a bcc crystal structure. Interestingly, while He consistently prefers tetrahedral sites over octahedral sites in all bcc transition metals, Ne, Ar, and Kr prefer octahedral sites in group 5B (V, Nb, and Ta) and tetrahedral sites in group 6B (Cr, Mo, and W) and 8B (Fe) metals. Our results further reveal strong correlations between the formation energy of a noble gas atom and the charge density of the host matrix. Specifically, the formation energy increases with the atomic size of the gas atom and the charge density at the site for the gas atom to be located. As shown in Figure 5, bigger gas atoms and higher charge densities lead to more perturbation in the local electron density due to the repulsion between the inert gas atom and a charge field; accordingly the bubble formation energy will be higher. The information on gas-metal interaction is critical for extending the understanding of void superlattice to GBS.

The high gas interstitial formation energy leads to strong binding between gas atoms and vacancies or voids. DFT calculations show that inert gas atoms have strong affinities to

vacancies or voids, indicating a strong tendency to precipitate into bubbles. The binding becomes stronger with increase gas atom size in a given metal. With sufficiently high gas to vacancy ratio in a gas-vacancy cluster, the presence of gas atoms can effectively suppress recombination of vacancies and SIAs and stabilize vacancy clusters, i.e., voids. This suggests strong driving forces, particularly for Xe, to form stable gas bubbles under irradiation. Moreover, since the lower temperature bound for superlattice formation is governed by the recombination limit, this implies that GBS can form at lower temperatures that void superlattice do.

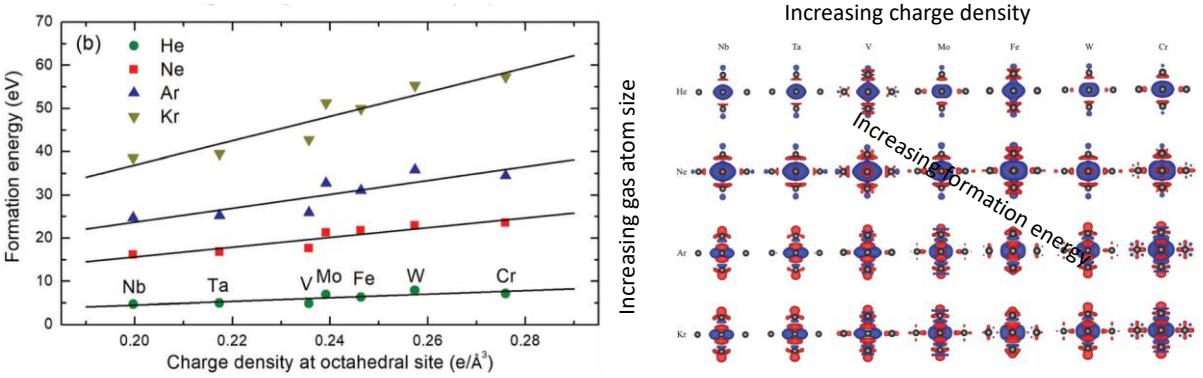

Fig. 5 Formation energies of inert gas atoms at the octahedral site in various bcc metals (left) and the corresponding variation in local electron density: > 0.5 eV/A3 in red and < - 0.5 eV/A3 in blue (right).

TEM in-situ 16 keV He ion implantation at -100 °C, 25 °C and 100 °C up to 7 at.%He revealed GBS with corresponding homologous temperatures of 0.096, 0.17 and 0.21, respectively. Since Fe is elastically anisotropic with isotropic SIA diffusion, it suggests that the anisotropic 1D diffusion of individual SIA may not be the necessary condition for GBS formation. MD simulations show that small SIA clusters with more than five SIAs diffuse anisotropically along <111> in pure Fe. Therefore, anisotropic diffusion of small SIA clusters may play an important role on GBS formation in Fe. The formation of He GBS in Fe at relatively low irradiation temperature (T_m = 0.096) inspired interest for further investigation. Vacancy mobility is quite low at this temperature and it is below the typical low temperature limit ($0.15T_m$) for He GBS formation. SIA clusters and loops in bcc Fe have very low migration barriers and they diffuse actively at low temperatures. Because the loops migration along their burgers vector direction anisotropically, the role of SIA loop migration on GBS formation needs to be investigated to extend the current theories for GBS formation.

Future Plans

Based on the knowledge learned from Phase-1 studies, several key science questions are raised. (1) *Can a unified theory be developed for both void lattice and GBS?* (2) *What is the role of small SIA cluster on GBS formation?* (3) *What is the effect of crystal structure and alloying addition on GBS formation?* According to the diffusion anisotropy hypothesis, the ordering is

determined by SIA or SIA cluster diffusion anisotropy, not directly related to crystal structure and alloy composition. It is hypothesized that current theory developed based on results in bcc metals can be generalized into other crystal structures in metals and alloys. (4) *What is the role of elastic anisotropic property on the formation of GBS with heavy inert gas atoms, such as Kr and Xe?* It is hypothesized that the role of elastic anisotropy on GBS formation is gas atom size dependent and it becomes important at large gas atoms.

These questions will be answered in our Phase-2 studies. Coupled modeling and experiments will be carried out to investigate: 1) the effect of gas atoms in thermodynamics and kinetics of point defects and how they affect defect self-organization, for the purpose of unifying void superlattices and GBS; 2) the configurations and migrations of SIA clusters/loops in both fcc and bcc metals, as well as their effects on superlattice formation; 3) the effects of bubble internal pressure on bubble-bubble interaction and on bubble ordering; and 4) the possibility of modifying defect properties via alloying for the purpose of controlling defect self-organization.

References

1. J. Gan, D.D. Keiser, D. M. Wachs, A. B. Robinson, B. D. Miller, J. of Nuclear Materials, 396, 234-239 (2010).
2. D. A. Terentyev, L. Malerba, and M. Hou, Physical Review B, 75, 104108 (2007).
3. A. Di Cicco, Physical Review B, v54, n13, 9086 (1996).
4. J. Reinitz, Nature 482, 464 (2012).
5. N. M. Ghoniem, D. Walgraef, and S. J. Zinkle, Journal of Computer-Aided Materials Design 8, 1 (2001).
6. R.W. Harrison, G. Greaves, J.A. Hinks & S.E. Donnelly, Scientific Report 7, 7724 (2017).
7. C. H. Woo and W. Frank, J. Nuclear Materials 137, 7 (1985).
8. T. T. Hlatshwayo, J. H. O'Connell, V. A. Skuratov, M. Msimanga, R. J. Kuhudzai, E. G. Njoroge1 and J. B. Malherbe, J. Phys. D: Appl. Phys. 48, 465306 (2015).
9. W. L. Gong, L. M. Wang and R. C. Ewing, J. Appl. Phys. 84, 4204 (1998).

Publications (Aug. 2017 – July 2019)

(1) C. Sun, D. Sprouster, K. Hatter, L.E. Ecker, L. He, Y. Gao, Y. Zhang, J. Gan, "Formation of tetragonal gas bubble superlattice in bulk molybdenum under helium ion implantation", Scripta Materialia, 149 (2018) 26-30.

(2) C. Jiang, Y. Zhang, Y. Gao, J. Gan. "Ab initio theory of noble gas atoms in bcc transition metals", Phys. Chem. Chem. Phys., 20 (2018) 17048.

(3) Y. Gao, Y. Zhang, D. Schwen, C. Jiang, C. Sun, J. Gan & X. Bai, "Theoretical prediction and atomic kinetic Monte Carlo simulations of void superlattice self-organization under irradiation", Scientific Report (2018) 8:6629.

(4) J. Gan, C. Sun, L. He, Y. Zhang, C. Jiang, Y. Gao. "Thermal stability of helium bubble superlattice under TEM in-situ heating", J. Nucl. Mater. 505 (2018) 207-211.

(5) Y. Gao, Y. Zhang, C. Jiang, J. Gan & D. Schwen, “Formation and Self-organization of Void Superlattice under Irradiation: a Phase Field Study”, Materialia, 1 (2018) 78-88.

(6) D.J. Sprouster, C. Sun, Y. Zhang, S.N. Chodankar, J. Gan, L.E. Ecker, “Irradiation-dependent Helium Gas Bubble Superlattice in Tungsten”, Scientific Report (2019) 9:2277.

(7) Y. Gao, Y. Zhang, D. Schwen, C. Jiang, J. Gan, “Bifurcation and Pattern Symmetry Selection in Reaction-Diffusion Systems with Kinetic Anisotropy”, Scientific Report (2019) 9:7835.

Multiscale Mechanical Properties and Alloy Design

Easo P. George,[1,2] Albina Borisevich,[1] Ying Yang[1]

[1]Oak Ridge National Laboratory, Materials Science and Technology Division, Oak Ridge, TN 37831;
[2]University of Tennessee, Department of Materials Science and Engineering, Knoxville, TN 37996

Program Scope

High-entropy alloys (HEAs) and medium-entropy alloys (MEAs) occupy the centers of multicomponent phase diagrams; that is, they comprise multiple principal elements in relatively high concentrations. Some of these alloys are highly malleable and can be thermomechanically processed to yield single-phase microstructures with FCC [1] or BCC [2] crystal structures. Additionally, a few HEAs [3,4] are also able to overcome the vexing strength-toughness tradeoff [5]. Therefore, they can be the bases for next-generation, damage-tolerant, ultrastrong materials [6]. To that end, our goal is to understand the fundamental factors that govern phase stability and mechanical behavior of HEAs/MEAs. Additionally, we are interested in applying that knowledge to control the behavior and properties of precipitate-strengthened alloys whose matrices are HEAs/MEAs. We investigate model alloys whose compositions are designed to address specific questions about the role of fundamental physical properties (e.g. elastic moduli, planar fault energies) and mechanisms (e.g. twinning, phase transformations, precipitation) on strength and ductility. Careful thermomechanical processing is employed to control microstructure, followed by mechanical testing and analyses using a variety of techniques including neutron diffraction, advanced electron microscopy, and atom probe tomography. MD simulations as well as first principles calculations are used to interpret the experimental results. We expect that insights from our work will produce broad scientific principles for the design of an important new class of structural materials based on HEAs/MEAs. Since the last PI meeting, new co-PIs Albina Borisevich and Ying Yang have replaced the previous co-PIs Hongbin Bei, Yanfei Gao, James Morris and Yury Osetskiy. Here we describe our most recent work on multiphase HEAs.

Recent progress

Prior research on HEAs found that there are at least two ways to simultaneously increase the strength and ductility of HEAs. The first is to dynamically introduce nanoscale interfaces during deformation, e.g. by twinning [3] or phase transformation [7]. This results in enhanced work hardening and postponed necking. An example of transformation induced plasticity (TRIP) enhancing the strength and ductility of certain FCC alloys is shown in Fig. 1 (red curves), where the dashed curve represents the stress-strain behavior of a Fe-Mn-Co-Cr alloy that does not undergo TRIP whereas the solid line represents a Fe-Mn-Co-Cr variant that does undergo TRIP [7]. In this case, the TRIP effect is due to a deformation-induced FCC→HCP phase transformation. A second approach is to introduce a large volume fraction of nanoprecipitates in a FCC matrix, which leads to strengthening and ductilization by microband-induced plasticity. A successful

example of that approach is also shown in Fig. 1 (blue curves) where the dashed curve represents the stress-strain behavior of a Fe-Mn-Ni alloy without nanoprecipitates and the solid curve that of a Fe-Mn-Ni alloy with nanoprecipitates [8].

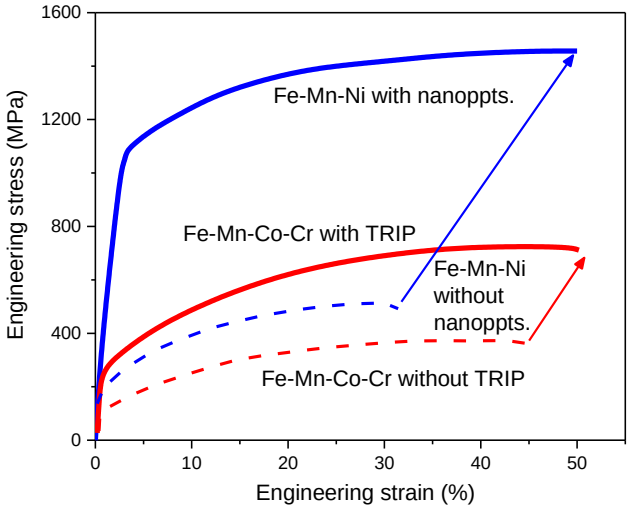

Fig. 1 Simultaneous improvement of strength and ductility of HEAs via TRIP [7] and formation of nanoprecipitates [8].

As discussed in a recent review paper [9], in order to obtain significant improvements in the mechanical properties of HEAs/MEAs, multiple strengthening mechanisms such as twinning, TRIP and nano-precipitation need to be simultaneously activated. Consistent with this, our recent work focuses on developing a new alloy design strategy that can take advantage of both nanoprecipitates and TRIP in the same alloy. To achieve our goal, we need to carefully design the matrix and precipitates, as schematically shown in Fig. 2. Although the name "FCC HEAs" implies our alloys have the FCC structure, that need not be their most stable structure. On the contrary, we purposefully designed the FCC phase to be metastable at room temperature, so that it can undergo a phase transformation during subsequent deformation. In addition, we want the transformation from the metastable to its thermodynamically stable state to occur in a diffusionless manner (*a la* the shear transformation leading to martensite). Given these limitations, we realized that phases such as sigma and equilibrium ferrite (which have a favorable thermodynamic driving force) would not qualify as suitable strengthening phases as they need significant diffusion to occur. Therefore, we designed a matrix composition that would readily undergo a martensitic transformation under constraint-free conditions. As for the nanoprecipitates, we wanted them to serve two functions: one, to strengthen the matrix (in the usual precipitate-hardening way) and second to impede the FCC to martensite phase transformation that would otherwise occur during cooling. The strengthening role of precipitates is straightforward and has been utilized many times before. What is novel in our approach is the use of nanoprecipitates to delay the thermodynamically favorable phase transformation until stress is applied, resulting in deformation-induced phase transformation and, in turn, TRIP.

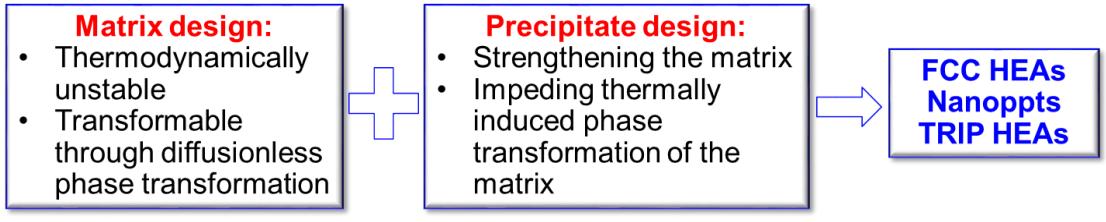

Fig. 2 Design approach for new FCC HEAs that take advantage of both nanoprecipitate and TRIP effects.

Following this strategy, we designed a medium-entropy Fe-Ni-Al-Ti alloy. In this alloy, Fe and Ni are the major elements in the MEA matrix and Al, Ti are the nanoprecipitate formers. With the aid of computational thermodynamics, we calculated the phase amounts in this alloy as a function of temperature (Fig. 3a) and the chemical composition of the matrix as a function of temperature (Fig. 3b). Between 925 and 1240 °C, the alloy is single-phase FCC. At temperatures of 925 °C and below, $L1_2$ precipitates form in the FCC matrix. Although the dashed line shows that bcc_eq (ferrite) becomes stable at temperatures below 625 °C, as a practical matter it is very difficult to form ferrite due to sluggish kinetics. Based on these predicted phase equilibria, we chose a solutionizing temperature of 1100 °C followed by an aging temperature of 700 °C to form ~25 mol% of the $L1_2$ nanoprecipitates in our alloy. Upon formation of the precipitates, which are rich in Ni, Al and Ti, their concentrations in the FCC matrix were reduced to ~23 at %, ~3.5 at %, and ~0.5 at %, respectively (Fig. 3b). Although the FCC structure of this composition is metastable

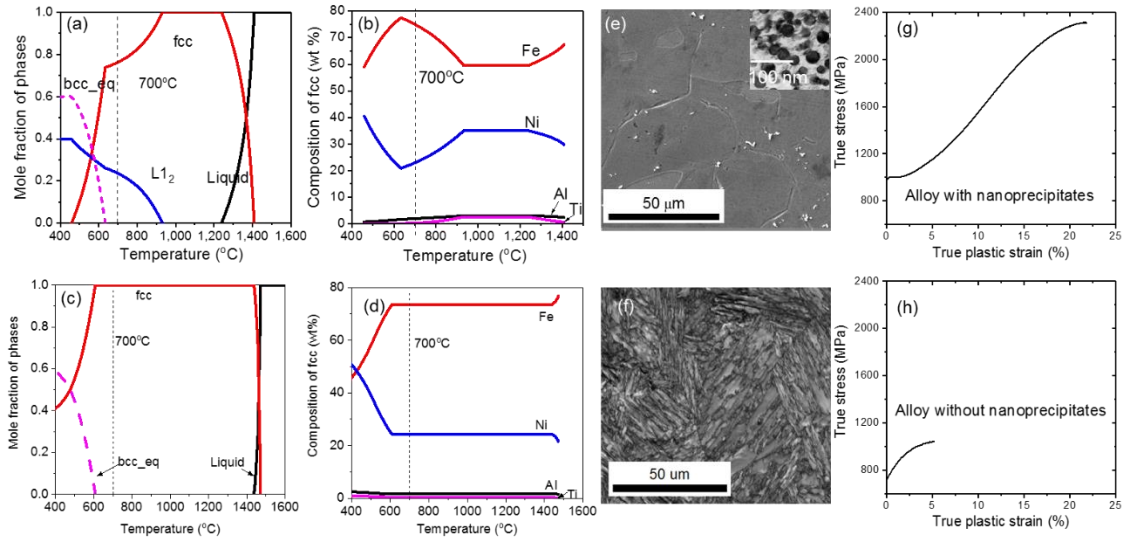

Fig. 3 (a-b) Calculated phase amount and matrix composition vs temperature for the alloy with nanoprecipitates. (c-d) Calculated phase amount and matrix composition vs temperature for the alloy without precipitates and having the same composition as the matrix of the two-phase alloy. (e) SEM-BSE image after 700 °C aging showing equiaxed austenite grains with a small amount of lenticular BCC regions in the alloy containing nanoprecipitates. (f) SEM-BSE image after 700 °C aging showing fully martensitic lath structure in the alloy without nanoprecipitates. (g-h) Room-temperature true stress-strain curves of the precipitate-containing and precipitate-free alloys.

relative to the bcc_eq (ferrite phase), the FCC→BCC_eq ferrite is not our target phase transformation as it requires diffusion. Rather, what is attractive about this composition is that it exhibits a strong tendency for the diffusionless FCC→BCC (martensite) transformation [10] which is also thermodynamically favorable. To validate this, an alloy having the matrix composition of the afore-mentioned precipitate-strengthened alloy (after aging at 700 °C) was made using the same synthesis and processing routes. Our calculations had indicated that no $L1_2$ precipitates should form in this matrix alloy (Fig. 3c), so its composition should remain the same at all temperatures (Fig. 3d), assuming that bcc_eq (ferrite) does not form. The two alloys, one with nanoprecipitates and the other without, but both having the same matrix composition were

investigated. The alloy with nanoprecipitates has a primarily equiaxed austenite (FCC) structure containing a few isolated lenticular (BCC) regions (Fig. 3e), where the inset shows the nanoprecipitates in the matrix. The other alloy, without nanoprecipitates, has a completely transformed martensitic lath structure (Fig. 3f). Clearly, the nanoprecipitates in the former alloy impeded the martensitic transformation, resulting in mostly retained austenite in the microstructure. To investigate the effects of nanoprecipitates on mechanical behavior, room-temperature tensile tests were performed on the two alloys (with and without nanoprecipitates). Examples of true stress-strain curves are shown in Fig. 3g and 3h. The yield strength, ultimate tensile strength, and uniform plastic elongation of the precipitate containing alloy are all significantly higher than those of the alloy without precipitates. In fact, the strength-ductility combination of the precipitate-containing alloy places it near the top of the strongest structural alloys designed to date. The combination of high strength and ductility in our alloy is a result of hardening from the nanoprecipitates as well as deformation-induced transformation of the metastable FCC matrix to BCC martensite.

Future Plans

The alloy design strategy introduced here is just a start because it can be further refined, for example, by tuning the precipitate distribution (size, spacing, volume fraction), grain size, the degree of cold work and recovery, and the thermodynamic driving force for phase transformation. Our future plans call for understanding how these variables affect the phase transformation and mechanical behaviors in the newly developed FCC MEAs in which both nanoprecipitates and TRIP effects are utilized to attain ultrahigh strength with good ductility.

References

1 Gali, Aravind & George, Easo P. Tensile properties of high-and medium-entropy alloys. *Intermetallics* **39**, 74-78 (2013).

2 Senkov, ON & Semiatin, SL. Microstructure and properties of a refractory high-entropy alloy after cold working. *Journal of Alloys and Compounds* **649**, 1110-1123 (2015).

3 Gludovatz, Bernd, Hohenwarter, Anton, Catoor, Dhiraj, Chang, Edwin H, George, Easo P & Ritchie, Robert O. A fracture-resistant high-entropy alloy for cryogenic applications. *Science* **345**, 1153-1158 (2014).

4 Gludovatz, Bernd, Hohenwarter, Anton, Thurston, Keli VS, Bei, Hongbin, Wu, Zhenggang, George, Easo P & Ritchie, Robert O. Exceptional damage-tolerance of a medium-entropy alloy CrCoNi at cryogenic temperatures. *Nature communications* **7**, 10602 (2016).

5 Ritchie, Robert O. The conflicts between strength and toughness. *Nature materials* **10**, 817 (2011).

6 Morris Jr, JW. Maraging steels: Making steel strong and cheap. *Nature materials* **16**, 787 (2017).

7 Li, Zhiming, Pradeep, Konda Gokuldoss, Deng, Yun, Raabe, Dierk & Tasan, Cemal Cem. Metastable high-entropy dual-phase alloys overcome the strength–ductility trade-off. *Nature* **534**, 227 (2016).

8 Yang, T, Zhao, YL, Tong, Y, Jiao, ZB, Wei, J, Cai, JX, Han, XD, Chen, D, Hu, A, Kai, JJ, Lu, K, Liu, Y & Liu, CT. Multicomponent intermetallic nanoparticles and superb mechanical behaviors of complex alloys. *Science* **362**, 933-937 (2018).
9 George, Easo P, Raabe, Dierk & Ritchie, Robert O. High-entropy alloys. *Nature Reviews Materials*, 1 (2019).
10 Kaufman, Larry & Cohen, Morris. The martensitic transformation in the iron-nickel system. *JOM* **8**, 1393-1401 (1956).

Publications (since last PI meeting)

K.V.S. Thurston, B. Gludovatz, Q. Yu, G. Laplanche, E.P. George, R.O. Ritchie, Temperature and load-ratio dependent fatigue-crack growth in the CrMnFeCoNi high-entropy alloy, *J. Alloys Cmpd*. **794**, 525-533 (2019).

N. Gao, D.H. Lu, Y.Y. Zhao, X.W. Liu, G.H. Liu, Y. Wu, G. Liu, Z.T. Fan, Z.P. Lu, E.P. George, Strengthening of a CrMnFeCoNi high-entropy alloy by carbide precipitation, *J. Alloys Cmpd*. **792**, 1028-1035 (2019).

K.V.S. Thurston, A. Hohenwarter, G. Laplanche, E.P. George, B. Gludovatz, R.O. Ritchie, On the onset of deformation twinning in the CrMnFeCoNi high-entropy alloy using a novel tensile specimen geometry, *Intermetallics* **110**, 106469 (2019).

Q. Ding, F. Xiaoqian, D. Chen, H. Bei, B. Gludovatz, J. Li, Z. Zhang, E.P. George, Q. Yu, T. Zhu, R.O. Ritchie, Real-time nanoscale observation of deformation mechanisms in CrCoNi-based medium- to high-entropy alloys at cryogenic temperatures, *Materials Today* **25**, 21-27 (2019).

W. Guo, Z. Pei, X. Sang, J.D. Poplawsky, S. Bruschi, J. Qu, D. Raabe, H. Bei, Shape-preserving machining produces gradient nanolaminate medium entropy alloys with high strain hardening capability, *Acta Mater*. **170**, 176-186 (2019).

Zongrui Pei, Rui Li, Jian-Feng Nie and James R Morris, First-principles study of the solute segregation in twin boundaries in Mg and possible descriptors for mechanical properties, *Mater. Design* **165**, 107574 (2019).

P. Shower, J.R. Morris, D. Shin, B. Radhakrishnan, L. Allard and A. Shyam, Temperature-dependent stability of θ'-Al_2Cu precipitates investigated with phase field theory and experiments, *Materialia* **5**, 100185 (2019).

P. Grammatikopoulos, D.J. Bacon, Yu.N. Osetsky, Simulation of the interaction between an edge dislocation and <111> interstitial dislocation loops in α-iron, *Radiation Effects and Defects in Solids*, **174**, 329-339 (2019).

Y.N. Osetsky, G.M. Pharr, J.R. Morris, Two modes of screw dislocation glide in fcc single-phase concentrated alloys, *Acta Mater*. **164**, 741-748 (2019).

C.E. Slone, J. Miao, E.P. George, M.J. Mills, Achieving ultra-high strength and ductility in equiatomic CrCoNi with partially recrystallized microstructures, *Acta Mater*. **165**, 496-507 (2019).

X.W. Liu, G. Laplanche, A. Kostka, S.G. Fries, J. Pfetzing-Micklich, G. Liu, E.P. George, Columnar to equiaxed transition and grain refinement of cast CrCoNi medium-entropy alloy by microalloying with titanium and carbon, *J. Alloys Cmpd*. **775**, 1068-1076 (2019).

H. Dobbelstein, E.L. Gurevich, E.P. George, A. Ostendorf, G. Laplanche, Laser metal deposition of compositionally graded TiZrNbTa refractory high-entropy alloys using elemental powder blends, *Additive Manufacturing*, **25**, 252-262 (2019).

L.J. Santodonato, R.R. Unocic, H. Bei, P.K. Liaw, J.R. Morris, Predictive multiphase evolution in Al-containing high-entropy alloys, *Nat. Commun*. **9**, 4520 (2018).

K. Jin, Y. Xia, M. Crespillo, H. Xue, Y. Zhang, Y.F. Gao, H. Bei, Quantifying early stage irradiation damage from nanoindentation pop-in tests, *Scr. Mater*. **157**, 49-53 (2018).

T. Liu, Y. F. Gao, H. Bei, K. An, In situ neutron diffraction study on tensile deformation behavior of carbon-strengthened CoCrFeMnNi high-entropy alloys at room and elevated temperatures, *J. Mater. Res*. **33**, 3192-3203 (2018).

Z. Wu, W. Guo, K. Jin, J.D. Poplawsky, Y.F. Gao, H. Bei, Enhanced strength and ductility of a tungsten-doped CoCrNi medium-entropy alloy, *J. Mater. Res*. **33**, 3301-3309 (2018).

C.E. Slone, S. Chakraborty, J. Miao, E.P. George, M.J. Mills, S.R. Niezgoda, Influence of deformation induced nanoscale twinning and FCC-HCP transformation on hardening and texture development in medium-entropy CrCoNi alloy, *Acta Mater*. **158**, 38-52 (2018).

G. Laplanche, S. Berglund, C. Reinhart, A. Kostka, F. Fox, E.P. George, Phase stability and kinetics of σ-phase precipitation in CrMnFeCoNi high-entropy alloys, *Acta Mater*. **161**, 338-351 (2018).

H. Dobbelstein, E.L. Gurevich, E.P. George, A. Ostendorf, G. Laplanche, Laser metal deposition of a refractory TiZrNbHfTa high-entropy alloy *Additive Manufacturing* **24**, 386-390 (2018).

Z. Wu, M.C. Troparevsky, Y.F. Gao, J.R. Morris, G.M. Stocks, H. Bei, Phase stability, physical properties and strengthening mechanisms of concentrated solid solution alloys, *Curr. Opin. Solid State Mater. Sci*. **21**, 267-284 (2017).

J.H. Lee, Y.F. Gao, A.F. Bower, H.T. Xu, G.M. Pharr, Stiffness of frictional contact of dissimilar elastic solids, *J. Mech. Phys. Sol*. **112**, 318-333 (2018).

W.D. Li, P.K. Liaw, Y.F. Gao, Fracture resistance of high entropy alloys: a review, *Intermetallics* **99**, 69-83 (2018).

T.K. Liu, Z. Wu, A.D. Stoica, Q. Xie, W. Wu, Y.F. Gao, H. Bei, K. An, Twinning-mediated work hardening and texture evolution in CrCoFeMnNi high entropy alloys at cryogenic temperature, *Mater. Des*. **131**, 419-427 (2017).

K.E. Nygren, K.M. Bertsch, S. Wang, H. Bei, A. Nagao, I.M. Robertson, Hydrogen embrittlement in compositionally complex FeNiCoCrMn FCC solid solution alloy, *Curr. Opin. Solid State Mater. Sci*. **22**, 1-7 (2018).

Y. Zou, L. Zhang, Y. Li, H. Wang, J. Liu, P. K. Liaw, H. Bei, Z. Zhang, Improvement of mechanical behaviors of a superlight Mg-Li base alloy by duplex phases and fine precipitates, *J. Alloys Compd*. **735**, 2625-2633 (2018).

Z. Wang, H. Bei, I. Baker, Microband induced plasticity and the temperature dependence of the mechanical properties of a carbon-doped FeNiMnAlCr high entropy alloy, *Mater. Charact*. **139**, 373-381 (2018).

W. Guo, Y. Meng, X. Zhang, V. Bedekard, H. Bei, S. Hyde, Q. Guo, G.B. Thompson, R. Shivpuri, J.-M, Zuo, J.D. Poplawsky, Extremely hard amorphous-crystalline hybrid steel surface produced by deformation induced cementite amorphization, *Acta Mater*. **152**, 107-118 (2018).

G. Laplanche, J. Bonneville, C. Varvenne, W.A. Curtin, E.P. George, Thermal activation parameters of plastic flow reveal deformation mechanisms in the CrMnFeCoNi high-entropy alloy, *Acta Mater*. **143**, 257-264 (2018).

G. Laplanche, P. Gadaud, C. Barsch, K. Demtroder, C. Reinhart, J. Schreuer, E.P. George, Elastic moduli and thermal expansion coefficients of medium-entropy subsystems of the CrMnFeCoNi high-entropy alloy, *J. Alloys Cmpd*. 746, 244-255 (2018).

H.L. Jia, X. Xie, L. Zhao, J.F. Wang, Y.F. Gao, K.A. Dahmen, W.D. Li, P.K. Liaw, C.L. Ma, Effects of similar-element-substitution on the glass-forming ability and mechanical behaviors of Ti-Cu-Zr-Pd bulk metallic glasses, *J. Mater. Res. Tech*. **7**, 261-269 (2018).

Z. Wu, S.A. David, Z. Feng, H. Bei, Weldability of a high entropy CrMnFeCoNi alloy, *Scr. Mater.* **124**, 81-85 (2016).

Z. Wu, Y.F. Gao, H. Bei, Thermal activation mechanisms and Labusch-type strengthening analysis for a family of high-entropy and equiatomic solid-solution alloys, *Acta Mater.*, **120**, 108-119 (2016).

W. Zhang, Y.F. Gao, Y.Z. Xia, H. Bei, Indentation Schmid factor and incipient plasticity by nanoindentation pop-in tests in hexagonal close-packed single crystals, *Acta Mater*. **134**, 53-65 (2017).

Shijun Zhao, Yuri Osetsky and Yanwen Zhang, Atomic-scale dynamics of edge dislocations in Ni and concentrated solid solution NiFe alloys, *J. Alloys Comp.*, **701** 1003-1008 (2017).

C.C. Yu, J.P. Chu, H.L. Jia, Y.L. Shen, Y.F. Gao, P.K. Liaw, Y. Yokoyama, "Influence of thin-film metallic glass coating on fatigue behavior of bulk metallic glass: experiments and finite element modeling," *Mater. Sci. Eng. A* **692**, 146-155 (2017).

O. Schneeweiss, M. Friak, M. Dudova, D. Holex, M. Sob, D. Kriegner, V. Holy, P. Beran, E.P. George, J. Neugebauer, A. Dlouhy, "Magnetic properties of the CrMnFeCoNi high-entropy alloy," *Phys. Rev.* B, **96**, 014437 (2017).

Solute/Twin boundary interaction as a new atomic-scale mechanism for Dynamic Strain Aging

Maryam Ghazisaeidi (PI) and Michael Mills (co PI), Ohio State University

Program Scope

Twinning is an important mechanism during the plastic deformation of materials with hexagonal close-packed (hcp) structures. Strength and formability are among critical properties of this family of structural materials that can be tailored by controlling the twin nucleation and growth. In this project, we investigate the effect of different alloying elements on twin nucleation and growth in hcp alloys and the corresponding impacts on the plastic deformation of these materials. We previously employed density functional theory (DFT) to obtain a complete picture of thermodynamics and kinetics associated with the segregation of oxygen (O) interstitials to the (10-12) twin boundaries in titanium (Ti) [1]. Our results predicted strong driving force as well as enhanced diffusivity of oxygen atoms near the twin boundary, facilitating the segregation of oxygen to the twin boundary. The enhanced diffusion of O to the twin boundary and subsequent pinning of the boundary results in serrated flow- similar behavior to dynamics strain aging (DSA). Here, we study the role of interstitial solutes on the twin growth and subsequently DSA. We develop a framework to predict equilibrium concentration of segregated solutes and strengthening due to solute-twin interactions at given strain rate and temperature conditions. Without using any fitting parameters and based on first-principles inputs, our model predicts the occurrence of stress drop due to the solute/twin pinning at the experimental strain-rate and temperature conditions. Experimental characterization is also being performed to identify the possibility of DSA due twinning in Ti alloys.

Recent Progress

Figure 1 shows the change in additional strengthening versus strain rate due to the oxygen segregation to the twin boundary in Ti. The responsible mechanism for the change in additional strengthening arises from the competition between solute diffusion to the twin boundaries and the twin

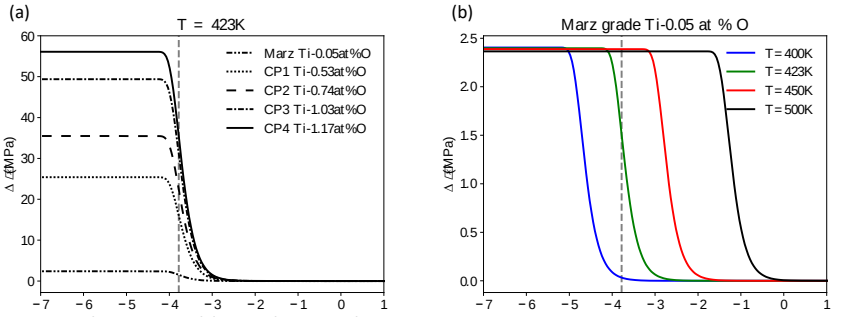

Figure 1: Change in additional strengthening versus strain rate at various temperatures and initial oxygen content in Ti. (a) shows the prediction of present model at T=423K for different oxygen contents and (b) shows the strength prediction at various temperatures for Ti-0.05at% O. Dashed lines show the experimental strain rate reported in Akhtar [2].

growth rate. At low strain rates, where twin growth is slow, the boundary experiences an additional pinning stress exerted by the segregated solutes. Upon increasing the strain rate to a critical value, the strength will drop to zero, indicating that the twin growth rate is not faster than solute diffusion and the boundary can escape the segregated solutes. Increasing the temperature also results in higher solute diffusion rates requiring the comparatively higher growth rate for solutes to trap the moving boundary. Similar to the dislocation pinning by solutes, twin growth impediment through solute segregation also causes the stress flow instability, thereby occurrence of DSA. Our predictions are in agreement with available experimental evidence by Akhtar [2] where serrated flow was identified in Ti-0.05 at pct O with an active (10-12) twinning deformation mode. This mechanism is further explored by experimental efforts.

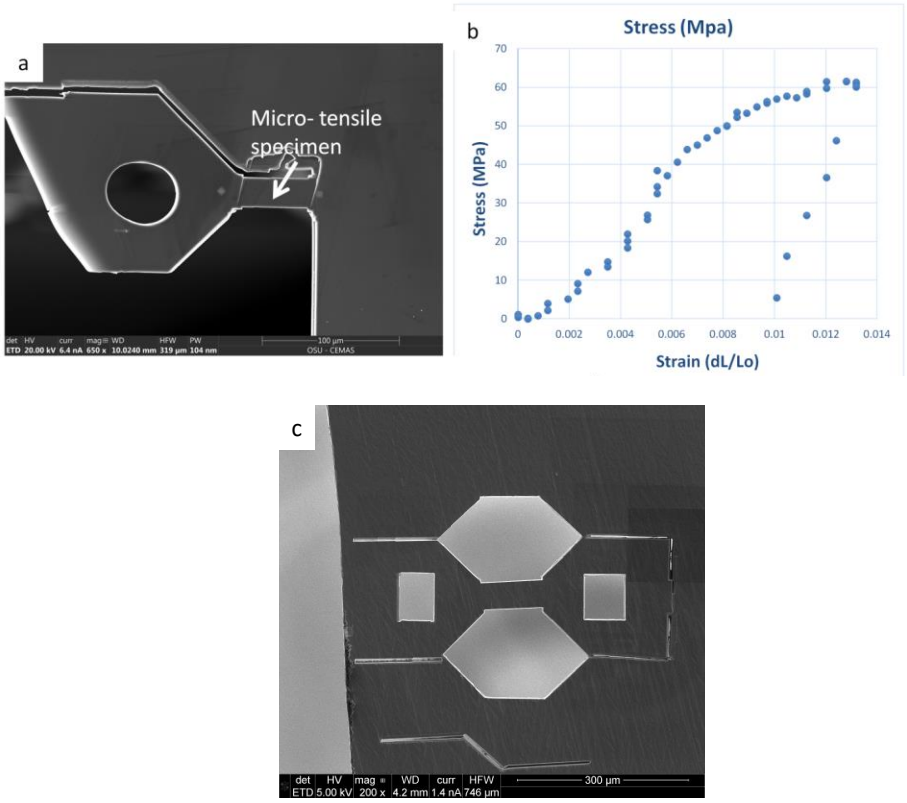

Figure 2: In-situ micro-tensile testing of single crystal pure Ti sample: (a) scanning electron microscope image of micro-tensile sample prepared sing FIB, (b) stress-strain curve for micro-tensile testing on single crystal pure Ti at room temperature and (c)

To investigate the serrated flow as a result of solute/twin interactions, in-situ micro-tensile testing of single crystal Ti oriented favorably for activation of twins are going to be performed. Ti samples with various oxygen concentrations are prepared for testing at ambient and elevated temperatures. Figure 2(a) shows the specimen prepared using focus ion beam (FIB) with the corresponding dimensions. The stress-strain curve obtained from this sample using micro-tensile testing at room temperature is shown in Figure 2(b). Samples for elevated temperature testing which typically require larger sizes are prepared as shown in Figure 2(c). Currently, we are developing high resolution strain mapping for micro-tensile testing to study the strain localization associated with plastic deformation.

Future Plans:

We developed a model to predict the solute strengthening resulting from interstitial solute segregation to the twin boundaries that can cause DSA. Our goal is to extend the model to incorporate the effect of substitutional solutes which transport via vacancy-mediated diffusion mechanism on the twin boundary segregation. We also perform DFT calculations to compute binding energy, vacancy formation energy/entropy and transition barrier energies for the solute/vacancy jumps within hcp alloys. We use these values as input to the developed model to particularly investigate the effect of rare earth elements on twin growth in Mg alloys leading to DSA. Experimental works will be also performed on this class of alloys.

References:

1. "Oxygen Diffusion Near (10-12) Twin Boundary in Titanium" M. S. Hooshmand, C. Niu, D. R. Trinkle and M. Ghazisaeidi, *Acta Mater* (156) pp 11-19 (2018) .

2. Basal slip and twinning in alpha-titanium single crystals. A. Akhtar, Metall Trans. A 6(5):1105, 1975

List of Publications:

3. "Atomistic modeling of dislocation interactions with twin boundaries in Ti " M. S. Hooshmand, M. J. Mills and M. Ghazisaeidi *Modelling Simul. Mater. Sci*. Eng. 25(4) 045003 (2017).
4. "Oxygen Diffusion Near (10-12) Twin Boundary in Titanium" M. S. Hooshmand, C. Niu, D. R. Trinkle and M. Ghazisaeidi, *Acta Mater* (156) pp 11-19 (2018) .
5. "An integrated experimental and computational study of diffusion and atomic mobility of the aluminum-magnesium system" Wei Zhong, M. S. Hooshmand, Maryam Ghazisaeidi, Wolfgang Windl, Ji-Cheng Zhao, *under review*
6. Solute/Twin boundary interaction as a new atomic-scale mechanism for Dynamic Strain Aging. M. S. Hooshmand and M. Ghazisaeidi, *under review*

A Fundamental Study on the Link between Mechanical Properties and Atomic-level Microstructure in Nano-sized Metallic Glasses

Julia R. Greer, Principal Investigator, California Institute of Technology

Program Scope

This project seeks to gain a fundamental understanding on the effects of atomic-level microstructure in metallic glasses on its strength, stiffness, and viscoelastic properties, via state-of-the-art nanofabrication techniques, *in-situ* nano- mechanical experiments, micro- structural analysis, and atomistic simulations. Our previous works have been dedicated to investigate the effects of deposition technique (i.e. electrodeposition and sputtering) and post-processing (i.e. thermal annealing and irradiation) on the microstructure and mechanical properties of the material. The main objective of the proposed work is to understand the effect of room temperature physical aging on the mechanical properties and the atomic-level microstructure of sputtered Zr-Ni-Al metallic glass. Uniaxial pillar compression experiments demonstrate a new property: age- induced strengthening. Molecular dynamics simulations are performed to quantify the short range order, free volume distribution and mechanical properties of the metallic glass at various microstructural states. These efforts help elucidate the link between mechanical properties and atomic-level microstructure in amorphous metals.

Recent Progress

Sputtered metallic glasses (MGs) represent a unique class of materials because their non-periodic atomic arrangements are far from equilibrium. This microstructure gives rise to their exceptional mechanical properties; for example, experiments and simulations of deformation of small-scale sputtered Zr-based MGs demonstrate their exceptional compressive and tensile strengths in excess of 1 GPa and exceptional tensile ductility of ~150% [1].

We report a new property that emerges in sputtered metallic glasses: age-induced strengthening. We measured compressive strengths of cylinders with diameters between 300 nm to 1.1 μm carved from a 5 μm-thick sputtered Zr-Ni-Al thin film that was aged in a nitrogen environment for three years. Nanomechanical experiments revealed that the aged samples had a stiffness of 91 ± 4 GPa and a yield strength of 2.7 ± 0.2 GPa for all cylinder sizes, which represents a nearly 50% increase in yield strength and a 31% increase in the elastic modulus compared to equivalently-sized as-sputtered samples. We also observed nano-size-induced failure suppression: samples with diameters below 600 nm deformed smoothly and non-catastrophically; those with larger diameters deformed via a series of observable and detectable shear bands that propagated to the surfaces. Molecular dynamics (MD) simulations of uniaxial

compression of chemically equivalent Zr-Ni-Al MG nanowires revealed that the underlying physics of enhanced strengths involves the evolution of local disorder that can be quantified in the number of five-fold atomic bonds. The average amount of five-fold bonding increased systematically with energetic relaxation and the maximum compressive stress.

Experiments and simulations in this work demonstrate that sputtered metallic glasses strengthen by 50% when solely aged for three years, i.e. without any accompanying annealing or mechanical treatment, which originates from atomic-level microstructural relaxation in these materials. This provides a useful foundation for simple design of advanced materials whose mechanical properties can be predicted and prescribed a priori using physical principles of atomic-level relaxation.

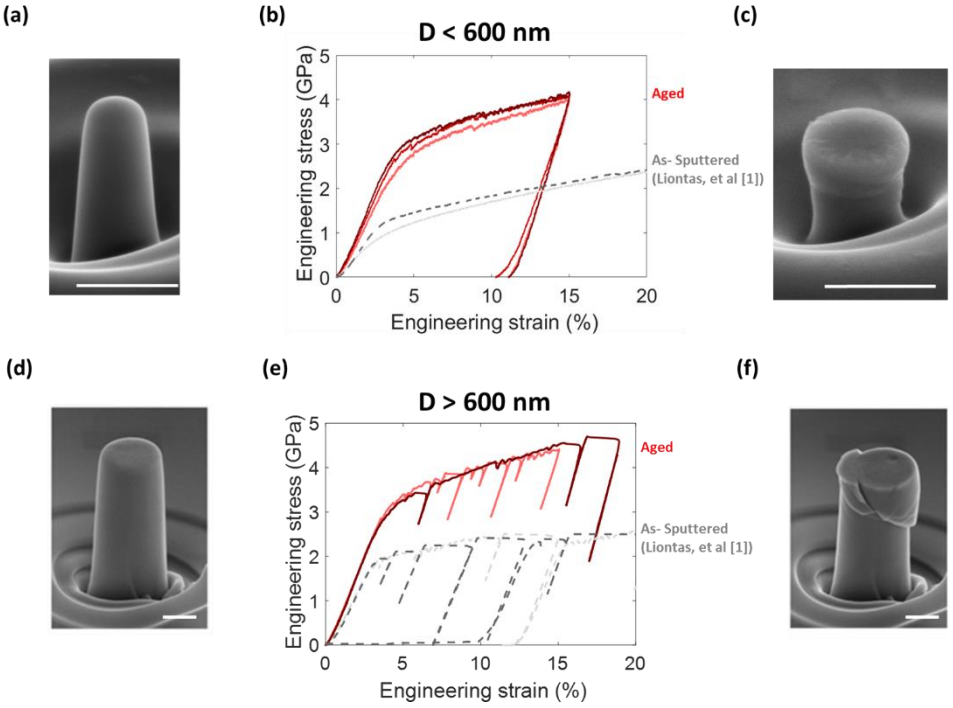

Figure 1: Uniaxial pillar compression experiments of RT aged Zr-Ni-Al, including **(left)** SEM image before compression, **(center)** engineering stress-strain data (denoted in red), and **(right)** SEM image after compression. The data is grouped by pillar diameter (D) with diameters less than 600 nm in the top row, and diameters greater than 600 nm in the bottom row. All scale bars in the SEM images correspond to 500 nm. For reference, the engineering stress- strain data for as-sputtered Zr-Ni-Al is shown in grey.

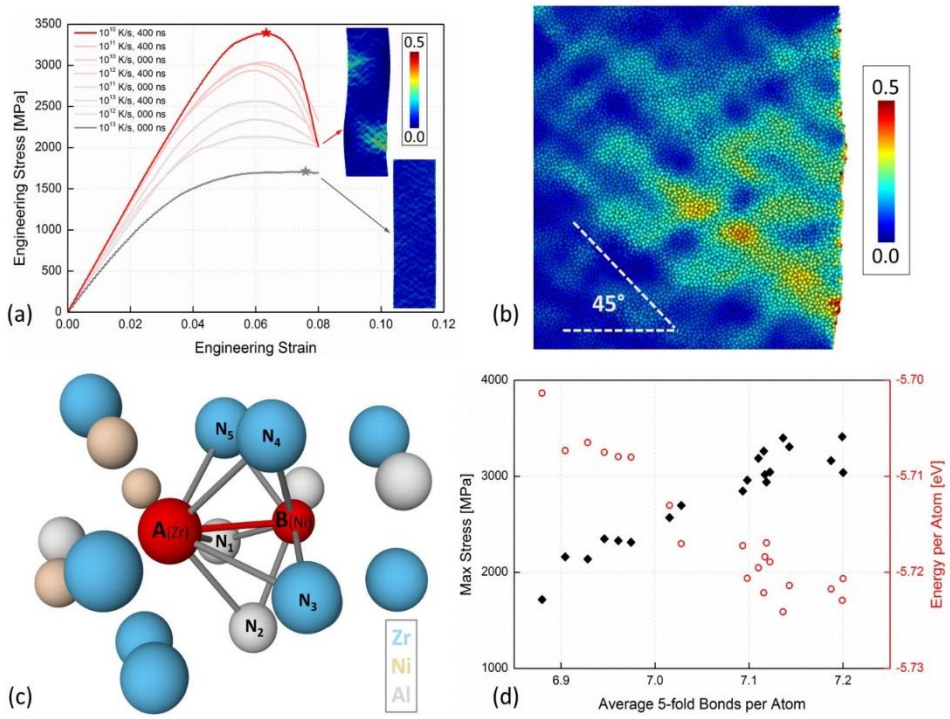

Figure 2: (a) Summarized stress vs. strain of simulated compression of a $Zr_{55}Ni_{25}Al_{20}$ nanowire. Red curve represents the upper stress boundary (lowest quench rate of 10^{10} K/s and longest anneal time of 400 ns); grey curve indicates the lower boundary on stress (highest quench rate of 10^{13} K/s and not annealed). Insets show deformed nanowires colored by atomic shear strain. (b) A close-up of the sample initially quenched at 10^{10} K/s and subsequently annealed for 400 ns at 0.8 shear strain. Shear planes nucleate from the surface and propagate into the wire at ~45° with respect to the nanowire axis. (c) A schematic cluster of atoms taken from the simulated MG. The two red atoms share 5 neighbors (indicated by grey bonds) and thus we classify their bond (the red bond) as a "5-fold bond". (d) Summary plot showing that the maximum compressive stress increases with the average number of 5-fold bonds while the average atomic energy decreases with the average number of 5-fold bonds.

Future Plans

To provide further insight into age-induced strengthening, we are performing dynamic mechanical analysis (DMA) on micro- and nano-sized cylindrical pillars to determine the viscoelastic properties of the Zr-Ni-Al metallic glass. At frequencies of 450Hz, we observe a peak in loss modulus of 61.5 GPa and 38.8 GPa for the aged and as- sputtered Zr-Ni-Al, respectively. We believe that this peak corresponds to the activation of hydrogen mobility within the Zr-Ni-Al host matrix. Hydrogen from ambient air became trapped in the interstitial sites of the Zr_4 tetrahedral structure and formed ZrH_x [2]. The formation of hydride from hydrogen and zirconium reduces its free energy and is energetically favorable [3]. Sputtering produces a thin film

which has large amounts of free volume and promotes the diffusion of hydrogen into the host matrix. Therefore, sputtering combined with zirconium's affinity for forming bonds with hydrogen greatly increases the chance of hydride formation in sputtered Zr-based metallic glass.

Future works will involve the use of nuclear reaction hydrogen depth profiling techniques to identify the depth of hydrogen implantation in sputtered Zr-Ni-Al metallic glass. A resonant nuclear reaction experiment will be performed where a tandem accelerator is used to bombard the metallic glass specimen with nitrogen-15. At the resonance energy (6.38 MeV), the yield of the characteristic gamma radiation (4.43 MeV) will be proportional to the number of hydrogen atoms at the surface of the sample. When the energy of nitrogen-15 is increased, the surface hydrogen is no longer detected because the energy lies above the resonance. As the nitrogen-15 loses energy while passing through the sample, it reaches the resonance energy at a characteristic depth. Thus, the yield of gamma ray is proportional to the hydrogen content at this depth. In this experiment, the hydrogen concentration profile can be determined by measuring the gamma ray yield versus the energy of the nitrogen-15. This study will isolate the effect of the hydrogen resonance so that the response from metallic glass can be clearly decoupled from that of hydrogen. Furthermore, this work opens the door for further investigation into the effect of hydride on the microstructure and mechanical properties of sputtered metallic glass.

References

[1] R. Liontas, M. Jafary-Zadeh, Q. Zeng, Y. W. Zhang, W. L. Mao, J. R. Greer "Substantial tensile ductility in sputtered Zr-Ni-Al nano-sized metallic glass" ***Acta Mater.* 118,** 270-285 (2016)

[2] M. Christensen, W. Wolf, C. Freeman, E. Wimmer, R. B. Adamson, L. Hallstadius, P. E. Cantonwine and E. V. Mader "H in α-Zr and in zirconium hydrides: solubility, effect on dimensional changes, and the role of defects" ***J Phys.: Condens. Matter* 27**, 025402 (2015)

[3] N. Eliaz, and D. Eliezer, "Overview of hydrogen interaction with amorphous alloys" ***Adv. Perform. Mater.* 6,** 5–31 (1999)

Publications

1. R. L. Thompson, Y. Wang, and J.R. Greer "Irradiation enhances strength and deformability of nano-architected metallic glass" ***Adv. Eng. Mater.* 20** 1701055 1-11 (2018)

2. R. Liontas, and J. R. Greer "3D nano-architected metallic glass: Size effect suppresses catastrophic failure" ***Acta Mater.* 133**, 393-407 (2017)

Understanding extreme strength and plasticity in nanotwinned Ni-Mo-W alloys

Kevin J. Hemker, Departments of Mechanical Engineering and Materials Science & Engineering, Johns Hopkins University

Program Scope

This study involves a multi-scale experimental effort to elucidate the underlying mechanisms that govern the mechanical response of nanotwinned Ni-Mo-W alloys [1-3]. Grounded by the extensive literature that exists for nanotwinned Cu [4-14], we hypothesize that the interplay between hard and soft slip systems, interactions of dislocations with CTBs, and detwinning all play a role. The specific goals being pursued in the present study are to: (i) Identify the active deformation mechanisms that underpin the ultrahigh strength and anisotropic plasticity in nanotwinned Ni-Mo-W alloys with post mortem and in situ electron microscopy. (ii) Quantify the role of that coherent twin boundary (CTB) orientation and resolved shear stresses play in determining the mechanical response of nanotwinned Ni-Mo-W via in situ micropillar compression. (iii) Employ nanoscale orientation and strain mapping to quantify nanotwinned structures and the mesoscale accumulation of stresses through automated computer orientation mapping (ACOM). (iv) Elucidate how variations in alloy and processing parameters affect nanotwinning in Ni alloys through combinatorial variations in alloy content. The program is designed to enhance the synthesis of nanotwinned Ni-Mo-W alloys and to elucidate the mechanisms that underpin their unusual suite of physical and mechanical properties.

Recent Progress

The deposition of nanotwinned $Ni_{83.6}Mo_{14}W_{2.4}$ alloys has been shown to yield thin films with a favorable suite of properties [1,2]. Combinatorial sputtering allowed us to expand upon that study, produce a compositional spread of $Ni_{85}Mo_{15-x}W_x$, alloys and investigate their physical and mechanical properties as a function of alloy chemistry. A wide processing window for the formation of the desired nanotwinned microstructure was discovered; nanotwins were observed in all films and over a wide range of powers. The addition of Mo and W was found to decrease the coefficient of thermal expansion (CTE) and to provide a route for tailoring the CTE and its temperature dependence with precise compositional control (Fig. 1).

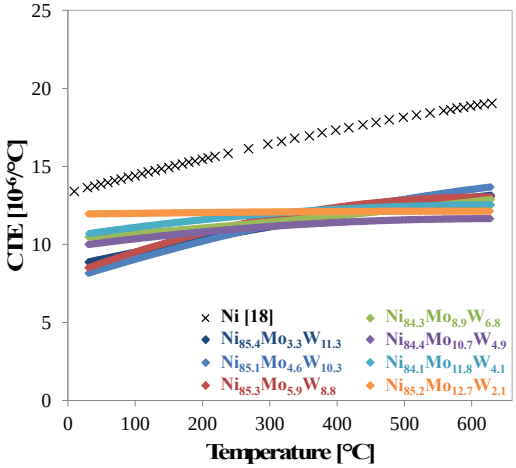

Fig. 1: CTE versus temperature for compositional spread of Ni-Mo-W alloys, with associated at.% compositions, compared to pure Ni [15].

Microscale mechanical testing was employed to measure the in-plane tensile properties, and ultrahigh ultimate tensile strengths approaching 3 GPa were measured. Heat treating the films for 1 hour at 400 and 600°C did not result in a change of the nanotwinned microstructure or the attendant tensile properties (Fig. 2). In situ micropillar experiments of the films demonstrated compressive strengths of 3-4 GPa and extremely localized plasticity. FIB lift-out was employed to prepare TEM foils of the deformed micropillars, and post mortem examination of a highly deformed micropillars revealed the formation of localized shear bands with intense regions of crystallization and the formation of nanocrystalline grains, see for example Fig. 3. The columnar nanotwinned grains are visible in the regions marked with red stars and SAED patterns of these regions resulted in the patterns shown in Fig. 3(b). Regions of intense shear are located between the nanotwinned regions and were found to be nanocrystalline as shown in Figs. 3(a) and 3(c). The nanotwins and the formation of nanocrystalline grains were also captured in ACOM orientation maps of these samples. Techniques for preparing lift-out specimens of a series of micropillars with various amounts of plastic deformation have been developed to document the earlier stages of shear band formation.

A visit to UCSB and collaborative exchange with the Gianola group resulted in the preparation of push-to-pull microtensile in situ samples from nanotwinned Ni-Mo-W films. Load frame malfunctions postponed the first round of in situ TSEM experiments but follow up visits are scheduled.

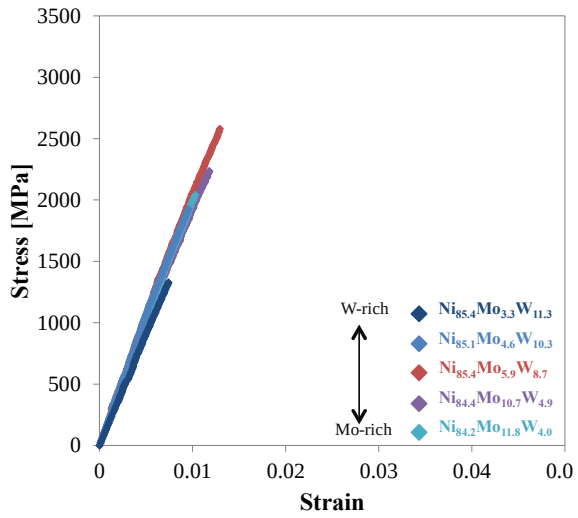

Fig. 2: Tensile stress-strain response for a subset of films heat treated for 1 hour at 400°C in 10^{-6} Torr vacuum showing linear-elastic behavior. No changes in the microstructure or the mechanical properties are observed in films heat treated at 400°C or 600°C but annealing at 1,000°C results in 10% tensile ductility.

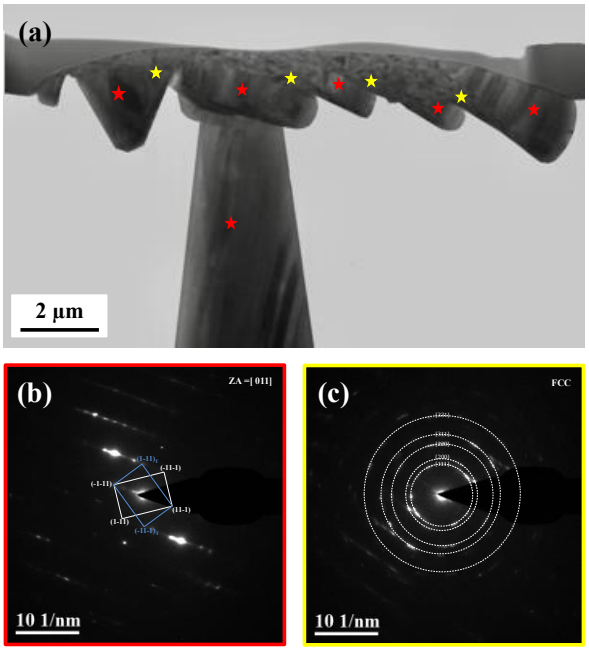

Fig. 3: (a) Cross-sectional TEM lift-out of a deformed micropillar thinned to electron transparent with inset before thinning and re-deposition. SAED patterns were taken in the starred regions with (b) the nanotwinned (red) and (c) the nanocrystalline (yellow) microstructures.

Collaborations with Drs. Khalid Hattar and Brad Boyce have also paved the way for in situ TEM observations of shear band formation and dislocation–twin boundary interactions at CINT.

Future Plans

The next stage of this investigation will focus on electron microscopy studies. Post mortem lift out and TEM observations of micropillars of various compositions and microstructural orientations will be conducted to determine their effect on the nanotwin microstructure and the formation of intense shear bands at various stages of plastic deformation. Evidence for dislocation-CTB interactions, de-twinning and dynamic crystallization will be documented and used to explain the onset of highly localized plasticity. The SEM-based micropillar compression tests conducted at JHU will be expanded by varying the loading direction with respect to the CTBs. TEM in situ experiments will be conducted at CINT by Dr. Mo-Rigen He in collaboration with Drs. Brad Boyce and Khalid Hattar. Finally, collaborations with Professor Daniel Gianola and his group at UCSB will enable in situ transmission-SEM (TSEM) experiments that will complement the in situ TEM experiments to be undertaken at CINT.

References

1. Sim, G.-D., J.A. Krogstad, K.M. Reddy, K.Y. Xie, G.M. Valentino, T.P. Weihs, and K.J. Hemker, *Nanotwinned metal MEMS films with unprecedented strength and stability,* Science Advances, **3** (2017) e1700685.
2. Sim, G.-D., J.A. Krogstad, K.Y. Xie, S. Dasgupta, G.M. Valentino, T.P. Weihs, and K.J. Hemker, *Tailoring the mechanical properties of sputter deposited nanotwinned nickel-molybdenum-tungsten films,* Acta Materialia, **144** (2018) 216-225.
3. Emigh, M.G. , McAuliffe, R.D., Chen, C. Mabon, J.C., Weihs, T.P., Hemker, K.J. Shoemaker, D.P., Krogstad, J.A., *Influence of a nanotwinned, nanocrystalline microstructure on aging of a Ni-25Mo-8Cr superalloy,* Acta Materialia **156** (2018) 411-419.
4. Lu, L., Y. Shen, X. Chen, L. Qian, and K. Lu, *Ultrahigh strength and high electrical conductivity in copper,* Science, **304** (2004) 422-426.
5. Anderoglu, O., A. Misra, H. Wang, and X. Zhang, *Thermal stability of sputtered Cu films with nanoscale growth twins,* Journal of Applied Physics, **103** (2008) 094322.
6. Shen, Y., L. Lu, Q. Lu, Z. Jin, and K. Lu, *Tensile properties of copper with nano-scale twins,* Scripta Materialia, **52** (2005) 989-994.
7. Dao, M., L. Lu, Y. Shen, and S. Suresh, *Strength, strain-rate sensitivity and ductility of copper with nanoscale twins.* Acta Materialia, **54** (2006) 5421-5432.
8. Lu, L., X. Chen, X. Huang, and K. Lu, *Revealing the maximum strength in nanotwinned copper,* Science, **323** (2009) 607-610.
9. Li, X., Y. Wei, L. Lu, K. Lu, and H. Gao, *Dislocation nucleation governed softening and maximum strength in nano-twinned metals,* Nature, **464** (2010) 877-880.

10. You, Z., X. Li, L. Gui, Q. Lu, T. Zhu, H. Gao, and L. Lu, *Plastic anisotropy and associated deformation mechanisms in nanotwinned metals.* Acta Materialia, **61**(2013) 217-227.
11. Jang, D., X. Li, H. Gao, and J.R. Greer, *Deformation mechanisms in nanotwinned metal nanopillars.* Nature nanotechnology, **7** (2012) 594-601.
12. Beyerlein, I.J., X. Zhang, and A. Misra, *Growth twins and deformation twins in metals,* Annual Review of Materials Research, **44** (2014) 329-363.
13. Liu, Y., N. Li, D. Bufford, J. Lee, J. Wang, H. Wang, and X. Zhang, *In situ nanoindentation studies on detwinning and work hardening in nanotwinned monolithic metals,* JOM, **68**(2016) 127-135.
14. Lu, K., L. Lu, and S. Suresh, *Strengthening materials by engineering coherent internal boundaries at the nanoscale.* Science, **324** (2009) 349-352.
15. Pavlovic, A., V.S. Babu, and M.S. Seehra, *High-temperature thermal expansion of binary alloys of Ni with Cr, Mo and Re: a comparison with molecular dynamics simulations,* Journal of Physics: Condensed Matter, **8** (1996) 3139.

Publications Supported by this BES Grant

David Raciti, Liang Cao, Kenneth JT Livi, Paul F Rottmann, Xin Tang, Chenyang Li, Zachary Hicks, Kit H Bowen, Kevin J Hemker, Tim Mueller, Chao Wang. "Low-Overpotential Electro-reduction of Carbon Monoxide Using Copper Nanowires", *ACS Catalysis* **7** (2017) 4467-4472.

L Cao, D Raciti, C Li, KJT Livi, PF Rottmann, KJ Hemker, T Mueller, C Wang. "Mechanistic Insights for Low-Overpotential Electroreduction of CO2 to CO on Copper Nanowires", *ACS Catalysis* **7** (2017) 8578-8587.

Paul F Rottmann, Kevin J Hemker. "Twin formation during thermal annealing of nanocrystalline copper films", *Scripta Materialia* **141** (2017) 76-79.

Paul F Rottmann, Kevin J Hemker. "Experimental quantification of mechanically induced boundary migration in nanocrystalline copper films", *Acta Materialia* **140** (2017) 46-55.

Paul R Rottmann, Kevin J Hemker, "Nanoscale elastic strain mapping of polycrystalline Materials", *Materials Research Letters, **6*** (2018) 249-254.

GD Sim, JA Krogstad, KY Xie, S Dasgupta, GM Valentino, TP Weihs, KJ Hemker. "Tailoring the mechanical properties of sputter deposited nanotwinned nickel-molybdenum-tungsten films", *Acta Materialia* **144** (2018) 216-225.

Paul R Rottmann, Kevin J Hemker, "Nanoscale elastic strain mapping of polycrystalline Materials", *Materials Research Letters, **6*** (2018) 249-254.

Computational and Experimental Investigation of Cryogenic Grain Boundary Motion for Enhanced Mechanical Properties

Eric R. Homer
Department of Mechanical Engineering, Brigham Young University, Provo, UT, 84602
eric.homer@byu.edu

Program Scope

The major goal of the project is to determine the feasibility of cryogenic processing to obtain enhanced mechanical properties by influencing the microstructural network of grain boundaries (GBs). GBs have a significant influence on numerous material properties, including strength and ductility. Thermomechanical processing frequently modifies these material properties by altering GB networks through the motion of GBs. This processing is facilitated by the thermally activated motion of large populations of GBs, making it difficult to control the resulting microstructure. In contrast, at cryogenic temperatures, coarsening has been measured in a subset of select GBs (Brons et al., 2014; Zhang, Weertman, & Eastman, 2005). This difference in GBs that could be mobile at cryogenic temperatures presents a transformational opportunity to create different microstructural networks that have enhanced strength and ductility.

The specific goals and tasks associated with the project during the past funding period, ending July 2019, were to (i) observe and measure cryogenic GB mobilities and mechanisms, (ii) identify crystallographic trends of cryogenically mobile GBs, and (iii) determine cryogenic processing-structure-property relationships. The work combined simulations, which were used to investigate the atomic mechanisms that could enable cryogenic GB migration, with experiments, executed through collaborations designed to provide evidence of the phenomena.

Recent Progress

Origins of cryogenic GB migration: ordered atomic migration mechanisms

One of the primary goals of the past funding period was to understand what mechanisms could enable boundary migration at cryogenic temperatures and what could be the origin of the non-thermally activated inverse temperature dependence. Two publications in particular provided unique insight, one examining Σ3 GBs (Priedeman, Olmsted, & Homer, 2017), and another examining Σ7 and Σ9 GBs (Bair & Homer, 2019).

In these works, atomic motions of the highly mobile, non-thermally activated GBs revealed ordered migration patterns. Each atom in the GB had a specific motion to undergo as determined by its position in the structure. For the Σ3 GBs, each atomic plane moved in a direction consistent with a Shockley partial dislocation (as illustrated in Fig. 1a), and in some cases had very small activation energies (as low as 0.009 eV). The Σ7 and Σ9 GBs also had specific slip direction, but these were not consistent with known dislocation directions. A

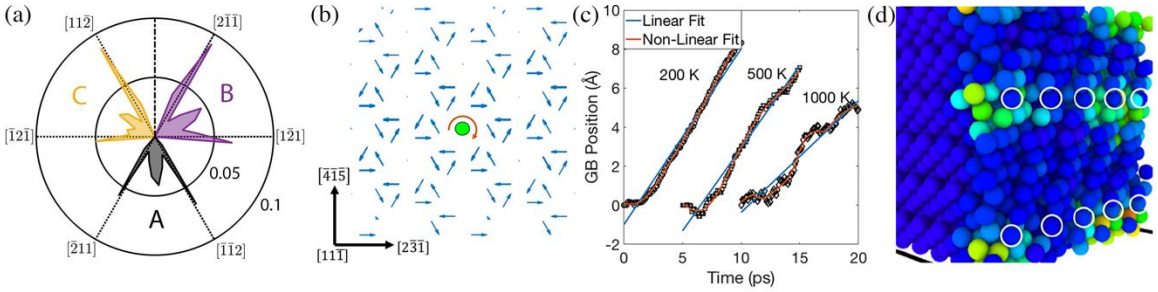

Figure 1. (a) Slip vector distribution separated out by atomic planes for migration of a Σ3 GB. (b) Slip vector plot showing atom motions in a Σ7 GB (111) plane. (c) GB Position vs Time for several temperatures, showing stick-slip stagnation at higher temperatures. (d) Migration of a Σ7 GB with atoms colored by slip vector magnitude and CSL atoms circled in white.

possible explanation for the inverse temperature dependence, even seen in random walk simulations, was given as dislocation drag it is also known to exhibit inverse temperature dependence (Al'shitz & Indenbom, 1975). Additional examination showed that CSL atoms, common to both lattices, could act as pinning sites to slow a GB as it migrates. The ordered slip around a CSL atom (c.f. Fig. 1b) is frustrated at higher temperatures; stick-slip like behavior is observed at higher temperatures (c.f. Fig. 1c), with the GB stopping and starting around CSL atom sites (c.f. Fig. 1d).

In short, one strong conclusion from the works of Priedeman et al. (2017) and Bair & Homer (2019), is that the ordered atomic motions are integral to both the high mobility, that would enable migration at cryogenic temperatures, and appear to be the source of the non-thermally activated temperature-dependence of the mobility.

Role of GB crystallography and structure

Another primary goal of the past funding period was to identify trends in GB structure that influence migration at cryogenic temperatures. The works of Priedeman et al. (2017) and Bair & Homer (2019) were informative on crystallographic character while Rosenbrock, Homer, Csányi, & Hart (2017) provided insight into atomic structure.

The Σ3 GBs showed clear dependence on the crystallography with similar boundary plane orientations exhibiting similar mobility behaviors (Priedeman et al., 2017). In the Σ7 and Σ9 GBs, interesting trends in the crystallography regarding the transition from one mobility type to another were observed. While the crystallography of these GBs did not directly point to which GB exhibited specific mobility types, the temperature at which they transitioned to different mobility types was clearly dependent upon the crystallography (Bair & Homer, 2019).

Since crystallography only acts as a constraint on GB character (Han, Vitek, & Srolovitz, 2016), the properties of a GB are controlled by the atomic structure. To this end, machine learning of GB atomic structure-property relationships was carried out using a new tool called smooth overlap of atomic positions (SOAP) developed by Bartok et al. (2013). Using this tool to describe the atomic structure of GBs, Rosenbrock et al. (2017) predicted the mobility type of a

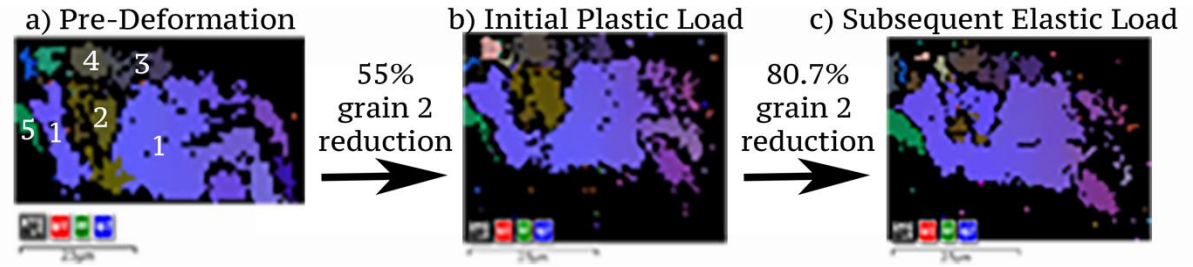

Figure 2. Micromechanical loading at cryogenic temperatures showing stress-driven grain growth under elastic and plastic deformation.

GB with 74.3 ± 2.7 % accuracy. In short, the machine learning algorithm was able to predict a dynamic GB property (mobility) based solely on the static atomic structure of the GB. More importantly, with no a priori knowledge of defect structures, the machine identified several well-known defects (e.g. a partial dislocation, and a pair of full dislocations arranged according to the Read-Shockley low angle GB structure). The presence or absence of these defects was correlated with the tendency for a GB to exhibit thermally activated or non-thermally activated GB migration.

In summary, crystallographic trends demonstrate strong influence on some, but not all, characteristics of GB mobility. Most importantly, there appears to be some influence on the transition between different mobility types. In addition, machine learning discovered important atomic structures correlated with specific types of mobility that may facilitate the ordered atomic motions of cryogenic mobility.

Experiments and collaborations

Experimental work in a collaboration with Peter Hosemann at the University of California, Berkeley has demonstrated stress-driven grain growth at cryogenic temperatures using in situ micromechanical loading and real time electron backscatter diffraction (Frazer et al., 2019). Equal channel angular pressed (ECAP) copper was milled into micro pillars and then subjected to a series of elastic and plastic deformations. While maintained at cryogenic temperatures, one grain in particular (grain 2 in Fig. 2) has an area reduction of 55% following the initial plastic load. A subsequent elastic load causes further reduction to 80% of its original size. The boundary most involved with this migration is a low-angle GB. These results provide direct evidence of stress-driven grain growth at cryogenic temperatures, whereas previous ex-situ examinations demonstrated coarsening after cryogenic loading, but samples were not maintained at cryogenic temperatures between deformation and characterization (Brons et al., 2014; Zhang et al., 2005).

In other collaboration work with Greg Thompson at the University of Alabama, Cu grains were sputter deposited with a high fraction of Σ3 GBs (a GB predicted by simulations to exhibit non-thermally activated mobility). In-situ mechanical loading in the TEM induced grain growth and grain refinement as well as the emission of dislocations from boundaries as characterized by precession electron diffraction (PED).

In summary, these efforts demonstrate stress-driven grain growth at cryogenic temperatures and the potential for cryogenic processing to cause microstructural evolution in a subset of GBs.

Future Plans

The project was just renewed, starting August 2019. The planned work builds on the previous demonstrations that (i) ordered atomic motions, with low activation energies, are central to cryogenic mobility, and (ii) additional thermal energy only serves to frustrate the coordinated movements, leading to a non-thermally activated inverse temperature dependence on GB mobility.

In the next period, we seek to understand how these ordered motions can be leveraged for ideal processing conditions and in materials responsive to the treatment. Thus, the planned work seeks to test three hypotheses related to the complexities of different materials, multiplicity of GB structures, and alloying/solute elements. Specifically, the project will (i) investigate how the ordered atomic motions vary between interatomic potentials and whether they can be reconciled using classical models of migration, (ii) determine if variations in atomic structure at GBs influences the ordered migrations that facilitate cryogenic mobility, and (iii) determine to what extent solute atoms can be accommodated without interrupting the ordered atomic motions.

As part of the renewal, Greg Thompson at the University of Alabama, will become an official collaborator on the project and will conduct in situ experiments to test predictions as to which materials will cryogenically coarsen and which will not, as affected by different GB types and varying solute content and types. Atomistic simulations will examine how ordered atomic motions are influenced by interatomic potential, multiplicity of GB structures, and solute atoms at or near the GB.

References

Al'shitz, V. A., & Indenbom, V. L. (1975). Dynamic dragging of dislocations. *Sov Phys-Usp*, *18*(1), 1–20.

Bartók, A. P., Kondor, R., & Csányi, G. (2013). On representing chemical environments. *Physical Review B*, *87*(18), 184115. http://doi.org/10.1103/PhysRevB.87.184115

Brons, J. G., Hardwick, J. A., Padilla, H. A., II, Hattar, K., Thompson, G. B., & Boyce, B. L. (2014). The role of copper twin boundaries in cryogenic indentation-induced grain growth. *Materials Science & Engineering A*, *592*, 182–188. http://doi.org/10.1016/j.msea.2013.11.005

Han, J., Vitek, V., & Srolovitz, D. J. (2016). Grain-boundary metastability and its statistical properties. *Acta Materialia*, *104*, 259–273. http://doi.org/10.1016/j.actamat.2015.11.035

Zhang, K., Weertman, J. R., & Eastman, J. A. (2005). Rapid stress-driven grain coarsening in nanocrystalline Cu at ambient and cryogenic temperatures. *Applied Physics Letters*, *87*(6), 061921. http://doi.org/10.1063/1.2008377

Publications

Priedeman, J. L., Olmsted, D. L., & Homer, E. R. (2017). The role of crystallography and the mechanisms associated with migration of incoherent twin grain boundaries. *Acta Materialia*, *131*, 553–563. http://doi.org/10.1016/j.actamat.2017.04.016

Rosenbrock, C. W., Homer, E. R., Csányi, G., & Hart, G. L. W. (2017). Discovering the building blocks of atomic systems using machine learning: application to grain boundaries. *Npj Computational Materials*, *3*(1), 29. http://doi.org/10.1038/s41524-017-0027-x

Zhang, Y. B., Budai, J. D., Tischler, J. Z., Liu, W., Xu, R., Homer, E. R., Godfrey, A., and Juul Jensen, D. (2017). Boundary migration in a 3D deformed microstructure inside an opaque sample. *Scientific Reports*, 7, 4423. https://doi.org/10.1038/s41598-017-04087-9.

Priedeman, J. L., Rosenbrock, C. W., Johnson, O. K., and Homer, E. R. (2018). Quantifying and connecting atomic and crystallographic grain boundary structure using local environment representation and dimensionality reduction techniques. *Acta Materialia*, 161, 431. https://doi.org/10.1016/j.actamat.2018.09.011.

Bair, J. L., & Homer, E. R. (2019). Antithermal Mobility in Σ7 and Σ9 Grain Boundaries Caused by Stick-Slip Stagnation of Ordered Atomic Motions about Coincidence Site Lattice Atoms. *Acta Materialia*, *162*, 10–18. http://doi.org/10.1016/j.actamat.2018.09.033

Homer, E. R. (2019). High-throughput simulations for insight into grain boundary structure-property relationships and other complex microstructural phenomena. *Computational Materials Science*, 161, 244. https://doi.org/10.1016/j.commatsci.2019.01.041.

Homer, E. R., Hensley, D., Rosenbrock, C. W., Nguyen A., and Hart, G. L. W. (2019). Machine-learning informed representations for grain boundary structures. *Frontiers in Materials*, 6, 168. http://dx.doi.org/10.3389/fmats.2019.00168.

Frazer, D., Bair, J. L., Homer, E. R., and Hosemann, P. (2019). Cryogenic stress-driven grain growth observed via microcompression with in situ electron backscatter diffraction. *Acta Materialia*, Submitted.

Fundamental Study of Fatigue Crack Initiation at Grain and Twin Boundaries in Austenitic Stainless Steel

Josh Kacher, Georgia Institute of Technology

Program Scope

The overarching goal of this project is to understand the dislocation-based mechanisms driving fatigue crack initiation at grain and twin boundaries. The hypothesis of the work is that dislocation structures equivalent to persistent slip bands (PSBs) form in the boundaries, leading to local stress concentrations and fatigue crack initiation. The sub-goals associated with this work include:

- Understanding the evolution of the dynamic stress state and dislocation density surrounding PSB/grain boundary interactions. This will require the development of new techniques that couple high resolution electron backscatter diffraction (HREBSD) with *in situ* scanning electron microscopy (SEM) deformation.

- Uncover the mechanisms by which dislocations are accommodated in grain and twin boundaries during fatigue. The proposed approach here is to conduct *in situ* transmission electron microscopy (TEM) deformation experiments on fatigued samples.

- Establish correlations between microstructure, deformation accommodation, and crack initiation across time and length scales.

This work primarily focuses on understanding fatigue crack initiation in austenitic stainless steels, though fatigue in high purity Al samples is also being investigated as the grain boundary morphology can be directly accessed via liquid Ga embrittlement.

Recent Progress

Current research has focused on developing the *in situ* TEM deformation experiments, applying the Ga embrittlement approach for investigating grain boundary morphology evolution during cyclic loading, and correlating TEM and EBSD dislocation density measurements. Main progress points include:

- Resolving the evolving geometrically necessary dislocation (GND) density as a function of fatigue loading in stainless steel by EBSD.

- Tracking grain boundary morphology in high purity Al as a function of cycles loaded during fatigue testing.

- Directly correlating TEM-based dislocation density measurements with high resolution EBSD-based measurements.

1. Resolving the evolving GND density as a function of fatigue

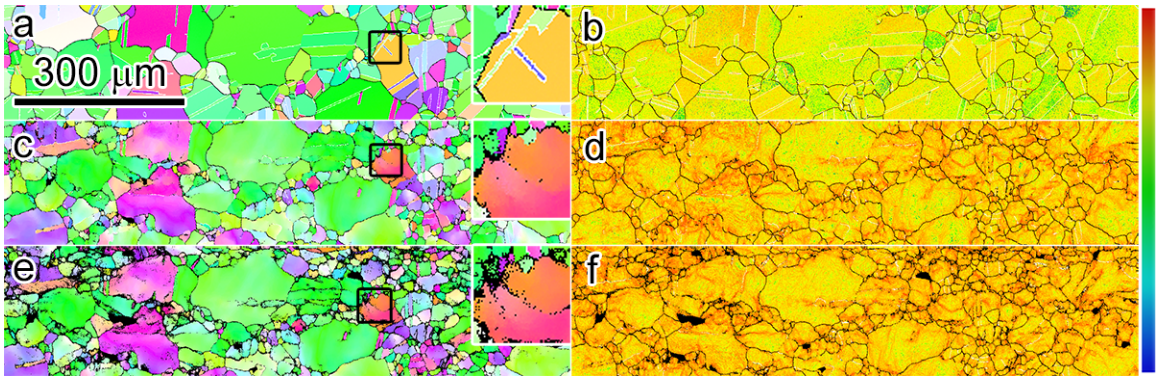

Figure 1. EBSD-based analysis of effect of fatigue loading on microstructure in stainless steel 316L at 0 (a-b), 100 (c-d), and 1,000 (e-f) cycles. a, c, and d show the orientation map, inset shows twins disappearing in the boxed region. b, d, and f show the log-based GND density map. Legend goes from 10^{12} to $10^{15.5}$ m^{-2}.

EBSD provides a statistical tool to evaluate microstructure evolution, including changes in GND density, as a function of loading conditions [1]. As microstructure characteristics such as grain boundary character, twin distribution, and grain size are evaluated on the same grid as GND density, correlations between features of interest and dislocation accumulation are straightforward to establish. Figure 1 shows the microstructure of a polished stainless steel 316L sample in its annealed state, after 100 cycles, and after 1,000 cycles during a stress-controlled tension-tension fatigue test (σ_{max} = 450 MPa, R = 0.1). As can be seen from the similarity between Figure 1d and f, the GND density reaches a saturation level after 100 cycles and increases only slowly after that. The dislocation accumulation is most pronounced in clusters of smaller grains, with the most pronounced levels occurring near grain boundaries. Interestingly, the thinnest annealing twins, prevalent in the as-annealed condition, were seen to be unstable during fatigue loading. One example of a twin disappearing is highlighted in Figure 1. Figure 2 shows a twin partially disappearing after 100 cycles. As can be seen, the twin has fractured via secondary twin formation mechanisms. Ongoing efforts are currently investigating the detwinning mechanisms and their potential influence on damage localization as well as determining when the GND density saturates.

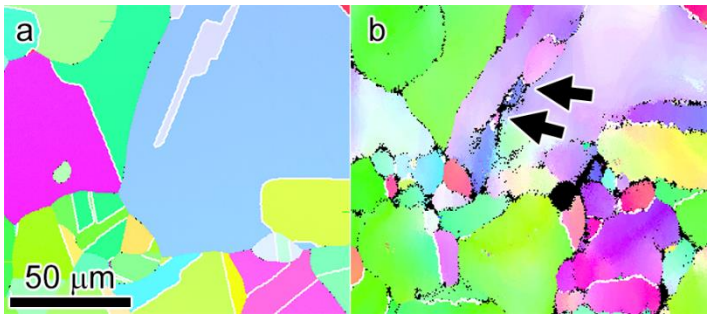

Figure 2. Detwinning mechanism seen during cyclic loading. a) Orientation map showing twin in the annealed sample. b) Orientation map from same grain after 100 cycles. Arrows indicate secondary twin boundaries formed within the original twin.

2. Grain boundary morphological evolution of high purity Al

In order to investigate grain boundary morphology changes during cyclic loading, fatigued high purity Al samples were embrittled and fractured using liquid Ga, exposing the grain boundary

state. This work was motivated by reports in the literature that show that higher stress amplitudes during cyclic loading increase the likelihood of fatigue crack initiation at grain boundaries rather than at intragranular defects [2, 3]. We investigated how the morphology of boundaries change at different stages of low cycle fatigue. We also analyzed the associated dislocation structures by TEM to investigate any correlation between grain boundary ledge formation and dislocation cell structure formation.

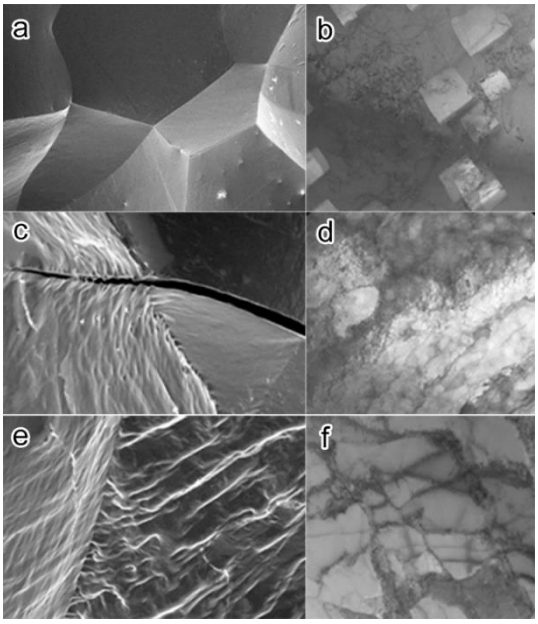

Figure 3. SEM images of grain boundaries and TEM images of dislocations after fatigue loading after 1 cycle (a-b), 100 cycles(c-d), and 1,000 cycles (e-f).

Figure 3 shows an overview of the results so far taken from a low cycle fatigue tests (fatigue life ~5,000 cycles), with samples investigated after 1, 100, and 1,000 cycles. The images show an increase in ledge formation at triple junctions and grain faces, with the initial state after 1 cycle still relatively pristine. Similarly, the images show the development of a well-defined dislocation cell structure with increasing number of loading cycles. Over the course of the next year, we plan on investigating how the ledge formation evolves as a function of loading conditions under both high and low cycle conditions and relate the findings to fatigue crack formation in Al samples.

3. Correlating TEM and EBSD-based dislocation density measurements

High resolution electron backscatter diffraction (HREBSD), an SEM-based diffraction technique, may be used to measure the lattice distortion of a crystalline material and to infer the geometrically necessary dislocation (GND) content. However, the extent to which EBSD-based measurements accurately represent the GND state of the material is still under debate. One of the key technical challenges of this research project is the ability to reliably measure the geometrically necessary dislocation (GND) density using high resolution EBSD. To assess the accuracy of our measurements, we directly compared EBSD-based GND measurements with TEM measurements in 302 stainless steel (Fig. 4). We incorporated recent advances to the GND density calculation algorithms developed by Timothy Ruggles at NASA that take into account uneven distributions in noise levels to refine the measurements. Dislocation densities of individual slip systems were calculated using an energy minimization approach (shown in Fig. 4d-e) [4]. As can be seen in the

figure, dislocation systems characterized in the TEM can be directly identified in the EBSD-based GND maps. Especially exciting, we found that the Burgers vector and slip plane was also correctly identified in the EBSD-based GND density maps.

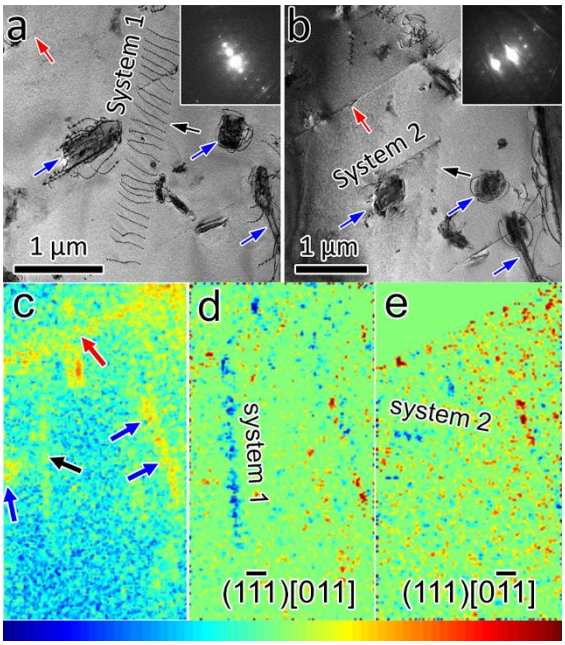

Figure 4. Comparison between EBSD and TEM-based dislocation characterization. a-b) TEM bright field images of two dislocation systems (marked by black arrows) near a twin boundary (marked by red arrow). c) Log scale GND map of same region, colored arrows indicate same locations as are shown in (a-b). Legend is 10^{13} to 10^{15} m^{-2}. d-e) Log scale GND density resolved onto different slip systems showing System 1 and System 2 with system labeled in each figure. Dislocation systems appear as blue. Legend is -5^{13} to 5^{13} m^{-2} (sign corresponds to sign of Burgers vector.

Future Plans

Future plans will focus on 1) better understanding the interactions of dislocation at twin boundaries in fatigued samples via *in situ* TEM deformation, 2) Correlating fatigue crack formation sites with microstructure features of interest via EBSD at interrupted stages of deformation, and 3) understanding the influence of loading conditions on grain boundary morphology evolution during cyclic loading of high purity Al. A key part of this will be *in situ* TEM testing of thin samples extracted from bulk samples after they have undergone cyclic loading to better understand how deformation structures influence dislocation/grain boundary and dislocation/twin boundary interactions.

References

1. Yoo, Y.S.J., et al., *Relating microstructure to defect behavior in AA6061 using a combined computational and multiscale electron microscopy approach.* Acta Materialia, 2019. **174**: p. 81-91.
2. Fougeres, R., *Early stages of fatigue damage in aluminium and aluminium alloys.* Journal de Physique IV Colloque, 1993. **03**(C7): p. C7-669-C7-678.
3. Li, P., N.J. Marchand, and B. Ilschner, *Crack initiation mechanisms in low cycle fatigue of aluminium alloy 7075 T6.* Materials Science and Engineering: A, 1989. **119**: p. 41-50.
4. Ruggles, T.J., D.T. Fullwood, and J.W. Kysar, *Resolving geometrically necessary dislocation density onto individual dislocation types using EBSD-based continuum dislocation microscopy.* International Journal of Plasticity, 2016. **76**: p. 231-243.

Publications

None

WastePD: Center for Performance and Design of Nuclear Waste Forms and Containers

Gerald S. Frankel,[1*] Jincheng Du,[2] Stephane Gin,[3] Seong H. Kim,[4] Jie Lian,[5] Jenifer S. Locke,[1] Gregory B. Olson,[6] Joseph V. Ryan,[7] John R. Scully,[8] Chris D. Taylor,[1] John D. Vienna,[7] Jianwei Wang,[9] Wolfgang Windl[1]

*[1]Ohio State University (**lead institution**); [2]University of North Texas; [3]Commissariat à l'énergie atomique et aux énergies alternatives (CEA), France; [4]Pennsylvania State University; [5]Rensselaer Polytechnic Institute; [6]QuesTek Innovations LLC; [7]Pacific Northwest National Laboratory; [8]University of Virginia; [9]Louisiana State University*

The goal of WastePD is to develop the science underlying material degradation to allow performance prediction over long periods. Such knowledge will also support the design of new materials for nuclear waste forms and containers with improved performance. The approaches for design and long-term performance prediction of glass, ceramics and metals, are currently empirical, i.e. based on correlations, experience, and intuition. The WastePD has established a new framework, called SEDMAT (Science of Environmental Degradation of Materials), for developing theory-based predictive models of materials degradation. This approach has been used to unify the modeling of degradation across the three materials classes studied by WastePD. SEDMAT 1.x activities have focused on improvements in the state-of-the-art models. Most of the activities of WastePD have been in SEDMAT 2.x (**Figure 1**) by developing relevant calculable parameters and utilizing them along with machine learning to generate predictive models accounting for distinct degradation mechanisms. The nature of this approach allows for continual advances in understanding and modeling (hence 2.x). The ultimate goal is SEDMAT 3.x, which will combine multiscale, multiphysics models that accurately describe the details of each of the controlling mechanisms and chemical/physical interactions controlling the degradation process.

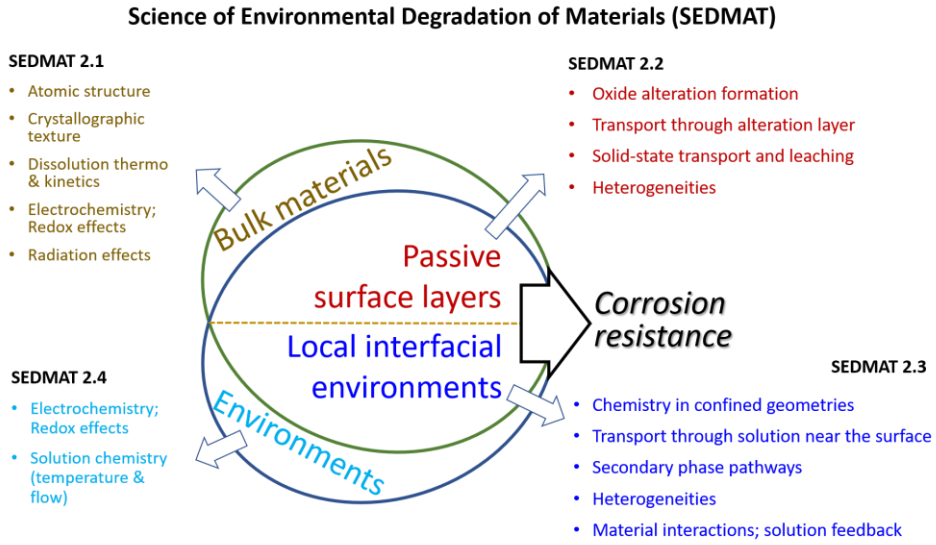

***Figure 1** The framework of SEDMAT 2.x.*

This poster will describe the development of SEDMAT as well as experimental activities to support the modeling and to develop better understanding of the physical phenomena. The **Glass Thrust** is studying the alteration layer formed on a model nuclear waste glass called International Simple Glass (ISG) in corrosive environments using isotope exchange experiments, flash freezing and cryo preparation of samples for APT, residual stress assessment, and modeling by molecular dynamics and reactive force field methods (**Figure 2**). The **Ceramic Thrust** is studying model compounds such as iodoapatite, hollandite, perovskite, pyrochlore and wollastonite. The effects of environmental parameters such as pH and temperature were investigated. Artificial neural networks (ANNs) were used to predict crystal structures suitable for waste storage (**Figure 3**). Passivation layers were modeled and characterized. The **Metals Thrust** is focusing on high entropy alloys and showed remarkable corrosion resistance for an alloy containing many elements expected to provide corrosion resistance and for alloys with few such elements. A new framework for pitting corrosion has been developed and validated with artificial 1D pits. Approaches to calculate metal-metal and metal-oxide bond strength in complex alloys and oxides, respectively, as well as chloride-metal interactions have been developed (**Figure 4**). The interactions of metals and glass or ceramics during corrosion in contact have been investigated, and acceleration of glass and ceramic corrosion with protection of the stainless-steel metal was observed.

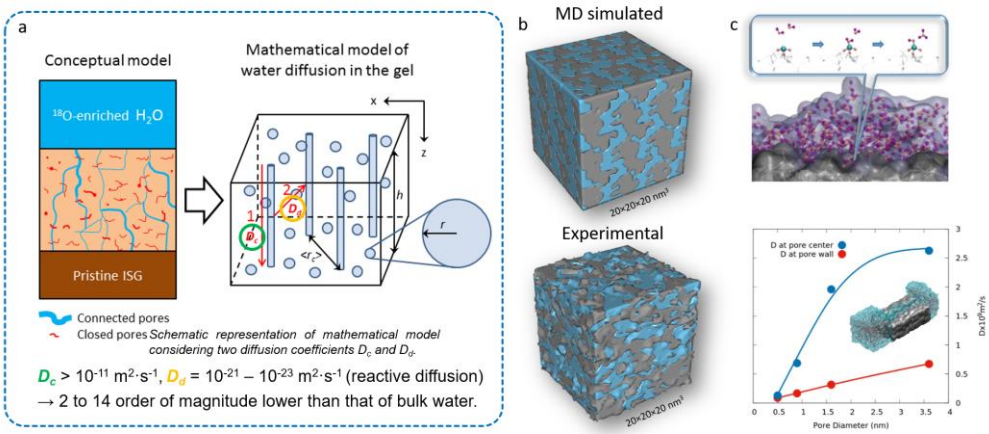

Figure 2 *a) New models of water diffusion in the glass alteration layer (gel). b) The gel structure obtained by MD simulation and cryo-APT. c) Reactions at the water-glass interfaces for bulk or porous silica glasses from reactive potential based MD simulations, and water diffusion coefficient difference in confined geometry: at the center and close to the wall in cylindrical pores of silica from MD simulations.*

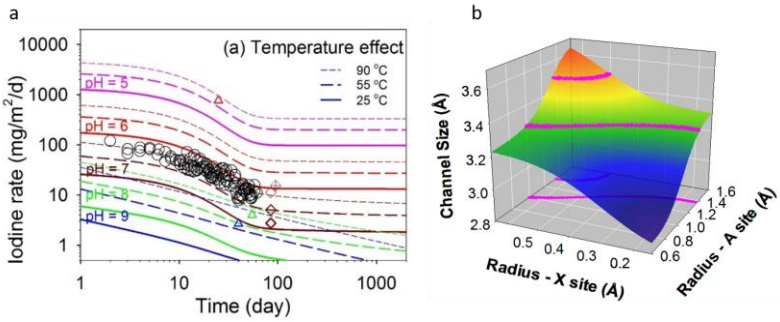

Figure 3 *a) Prediction of iodine release rate as a function of time at different pHs and temperature. b) Prediction of cell parameters for ceramic waste forms by machine learning.*

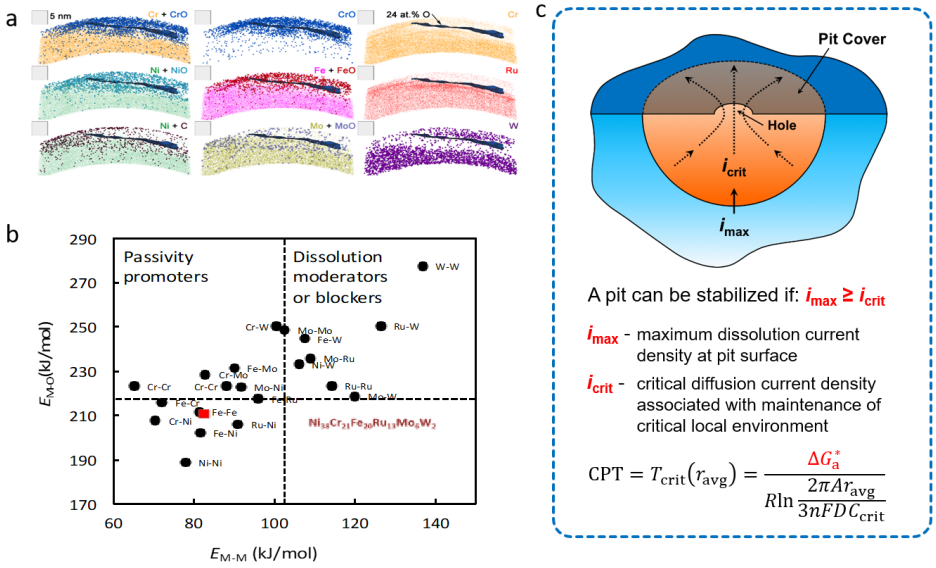

Figure 4 *a) the oxide layer of WastePD* corrosion resistant *HEA revealed by APT. b)* Marcus plot for HEA type alloys without Hubbard-U correction for electronic correlation effects. Assumes a corundum structure for M-O and *FCC* structure for M-M bond strength. *c) new pitting theory to define calculable metrics.*

Elucidating Grain Growth in Thermo-Magnetic Processed Materials by Transfer Learning and Reinforcement Learning

A. Krause, University of Florida (Lead Principal Investigator)
J. Harley, University of Florida (Principal Investigator)
M. Tonks, University of Florida (Principal Investigator)
M. Kesler, Oak Ridge National Laboratory (Principal Investigator)

The goal of the proposed work is to combine deep, model-based reinforcement learning and transfer learning to elucidate one of the most fundamental, yet poorly understood, mechanisms in materials science: *abnormal grain growth*. **We hypothesize that abnormal grain growth is the result of highly anisotropic grain boundary character *networks*, where a unique combination of neighboring grain boundaries incentivize accelerated growth.** We will test this hypothesis with an anisotropic mesoscale grain growth model that incorporates the complexity of grain boundary character and energy anisotropy. Rather than rely on heuristics to define the grain growth behavior, we will *teach* the mesoscale grain growth model how to simulate grain growth. This is accomplished by integrating experimental microstructure data with model-based machine learning strategies. A machine learning approach is necessary for us to capture the high combinatorial, highly complex space of grain boundary character in a grain growth model. **The developed anisotropic mesoscale grain growth model will be a new tool for exploring the microstructural features and processing parameters critical to inducing and sustaining or inhibiting abnormal grain growth.** This project addresses two of DOE's main topic areas: (1) synthesis science including nucleation, growth and restructuring of hierarchical materials and (2) behavior of properties and processes in extreme environments, particularly temperature and magnetic fields. This goal will be accomplished by our team's unique expertise, which encompasses grain boundary characterization (**Krause**), machine learning methods (**Harley**), mesoscale grain growth modeling (**Tonks**), and thermomagnetic materials processing (**Ludtka**).

This project will be divided into three tasks, summarized in Fig. 1, using alumina as a model material due to its high anisotropy:

1. Use machine learning methods to identify the physical descriptors of 3D microstructural data collected at different periods of grain growth. The samples will be made with both traditional powder processing and a thermo-magnetic process to create a wide array of grain topologies and crystallographic textures.
2. Apply transfer and reinforcement learning to train the anisotropic mesoscale grain growth model, where the machine learning agents will adjust the simulations to reach the physical descriptors previously identified for each growth period in Task 1.
3. Validate the developed model by conducting a grain growth study using a non-destructive characterization method and directly comparing the results to simulations. We will then test our hypothesis using the validated anisotropic mesoscale grain growth model with simulated microstructures where we control the character anisotropy of neighboring grain boundaries.

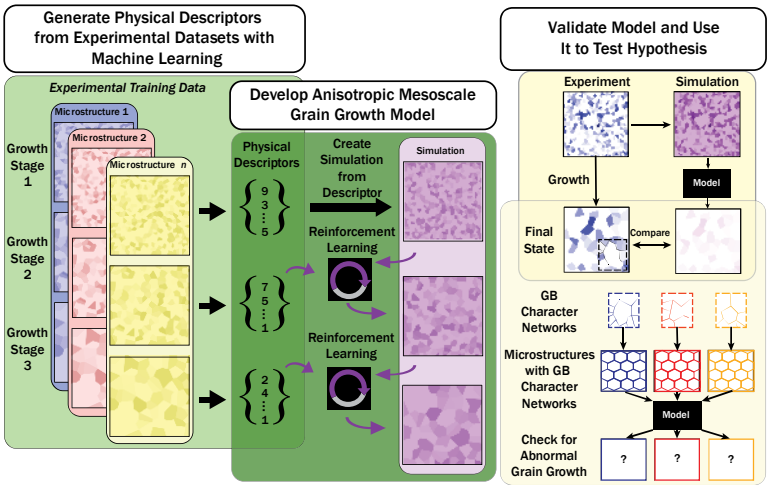

Figure 1: Overview of project tasks planned to test hypothesis.

The anisotropic mesoscale grain growth model will provide mechanistic insight into grain growth that would otherwise be inaccessible from experiments and isotropic grain growth models. These insights could inspire new processing designs that either promote or avoid these grain boundary character networks to control abnormal grain growth.

Dynamic, robust, radiation-resistant ceramics: harnessing thermodynamic and kinetic driving forces

Jessica A. Krogstad
Department of Materials Science and Engineering
University of Illinois, Urbana-Champaign

Program Scope

The *overarching objective* of this project is to establish a class of structural ceramics with enhanced radiation tolerance based on a dynamic microstructure by harnessing the synergistic effects of radiation enhanced diffusion, capillarity and thermally induced mass transport on microstructural evolution. Specifically, we aim to quantify changes in mass transport behavior that may influence the microstructural evolution of ionic/covalent ceramic materials subjected to irradiation. Currently, we are focused on quantifying the interactions between irradiation induced defects and microstructural features such as grain boundaries, pores or free surfaces. This has also given rise to an emphasis in understanding how those same defects interact with each other near these features, or as a function of irradiation conditions (temperature, flux, ion energy).

Recent Progress

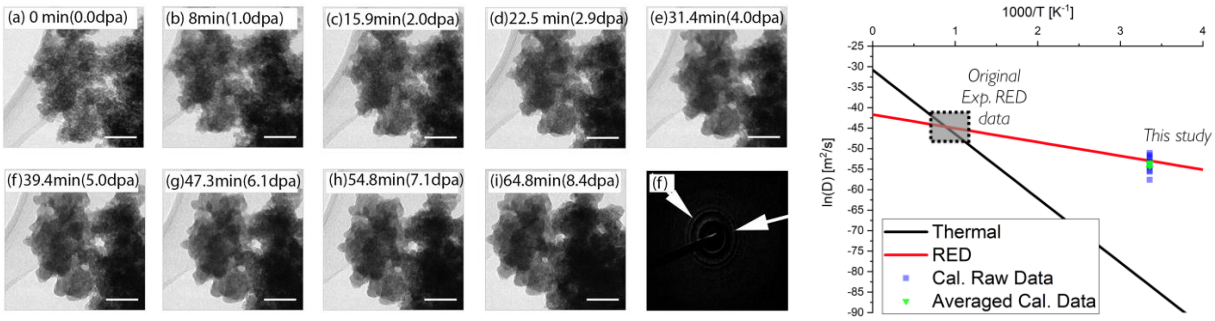

Figure 1 – Representative Frames at varies times during in-situ ion irradiation of CeOx particles at room temperature. Scale bar on each image is 50 nm. The extracted diffusivity data are plotted on the right and compared to thermally activated diffusion (black) and literature values of radiation enhanced diffusion at higher temperatures (red).

The increased point defect population arising from irradiation damage may lead to the phenomenon of radiation enhanced diffusion (RED). RED may accelerate the rate of phase or microstructural evolution of a material subject to irradiation, making it key in understanding, predicting and designing radiation tolerant microstructures. However, quantifying RED for ceramic systems is both onerous and complicated due to the complexity of the crystal, and therefore defect, chemistries. As a result, RED behavior has, to date, only been experimentally determined for three ceramic systems [1-3]. By adapting a simple two body sintering model, we have leveraged *in situ* observations of nanoparticles subject to ion irradiation to extract RED coefficients quite efficiently. For example, **Figure 1** depicts a representative series of images collected during an *in situ* irradiation experiment conducted in the I^3TEM at Sandia National

Laboratories, wherein the agglomerate of ceria (CeO_2) nanoparticles densify at room temperature with increasing ion damage. This approach does involve a number of important assumptions about the dominant diffusion mode, but by adjusting the initial particle size or temperature we may be able to probe the transition between sink limited and recombination limited regimes of RED.

As we establish a quantitative baseline for RED behavior in our ceramic systems of interest (CeO_2 and YSZ), we aim to use this insight to better understand the evolution of presintered ceramic bodies. Numerous reports have demonstrated the nanocrystalline ceramics have improved radiation tolerance (fewer residual defects) but they suffer from irradiation assisted grain growth, which not only reduces the sink density of the grain boundaries but also may lead to increased residual stress and microcracking, e.g. [4-5]. Pores may also serve as efficient defect sinks while providing a unique combination of compliance and grain boundary pinning centers. However, the exact interactions between the pores, radiation induced defects and the overall microstructural evolution are not well understood. For example, Figure 2 includes bright field images from two nearly identical scandia-stabilized zirconia nanocrystalline ceramics, which were densified via SPS then annealed to introduce a fine, well dispersed array of nanopores. In (a) and (b) the annealing step resulted in an average grain size of 30-34nm, while the sample in (c) was annealed until the average grain size was approximately 120nm. Both specimens were then irradiated *ex situ* under the same beam at room temperature. The finer grain size ceramic experienced no apparent grain growth during irradiation, while the larger grain—yet still nanograined—ceramic experienced measurable grain growth and densification during irradiation. Observations of fully dense nanocrystalline ceramics across a similar range of grain sizes all showed grain growth, suggesting that the pores and the distribution thereof play an important role in defect accommodation.

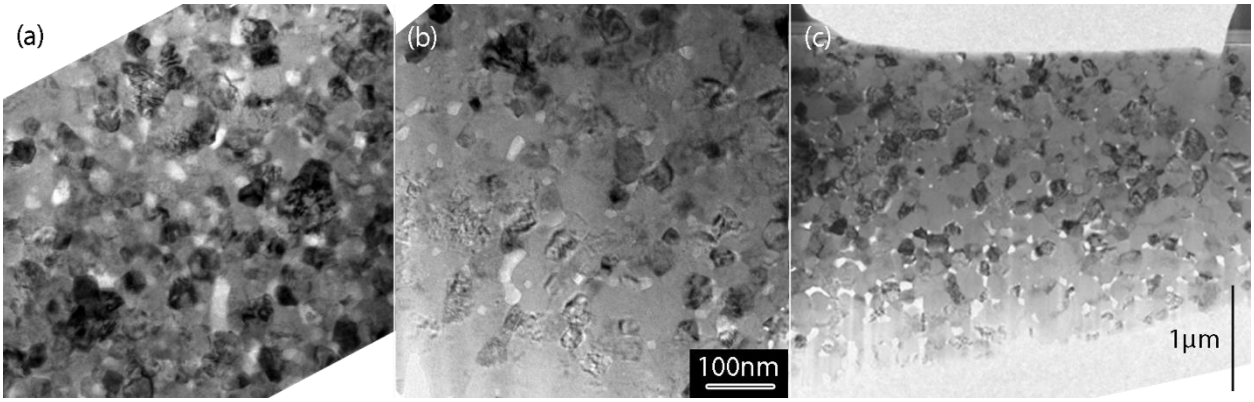

Figure 2 – Bright field TEM images of a nanocrystalline Sc-doped zirconia (8.4mol%Sc_2O_3-ZrO_2) densified via SPS, then heat treated to introduce a fine dispersion of pores and tailor the grain size and irradiated with 2.8MeV Au to a fluence of 1×10^{15} ions/cm^2. (a) Within 1µm of the top surface of the irradiated pellet of ScZ with an average grain size of 32.9±1.3nm post irradiation. (b) More than 4µm (below the max damage layer) into the depth of the same irradiated ScZ pellet where the grain size is approximately 34.3±1.1nm. (c) Overview of a FIB lamella from a pellet of the same composition but with a starting grain size of approximately 120nm. Modest growth to an average grain size of 132nm and reduction in porosity is observed in the irradiated region.

The initial microstructure (grain size, porosity, chemical heterogeneities, etc) are all expected to contribute to the radiation tolerance of a ceramic—the irradiation conditions may also have a significant influence on the type, mobility and distribution of the defects. The 2.8MeV Au ions used in the previously described experiments generate point defects through ballistic interactions or nuclear stopping behavior. These point defects interact with each other and microstructural features—contributing to the RED effects and the microstructural evolution behavior. Higher energy ions shifts the nature of ion interactions towards electronic stopping behavior and therefore the nature, population and behavior of the generated defects. As such, we have undertaken a series of *ex situ* irradiation experiments using a 45MeV Au ion beam on both polycrystalline 3YSZ and single crystal 10YSZ. Under these conditions, point defects are generated and are apparently mobile enough to arrange themselves into an ordered array as evident from the superlattice reflections apparent in SADP shown in Figure 3(b). The same superlattice reflections are absent deeper into the ceramic pellet. These specific superlattice reflections are characteristic of C-type oxides, e.g. Y_2O_3. Raman spectroscopy has confirmed the increased defect population, but has not yet been quantified, while XPS indicates unexpected changes in the oxidation state of the zirconium cations. We do not yet understand how the defects have sufficient mobility to organize, yet do not coalesce/annihilate. However, such defect ordering may lead to unique functionality if the defect structure is sufficiently stable.

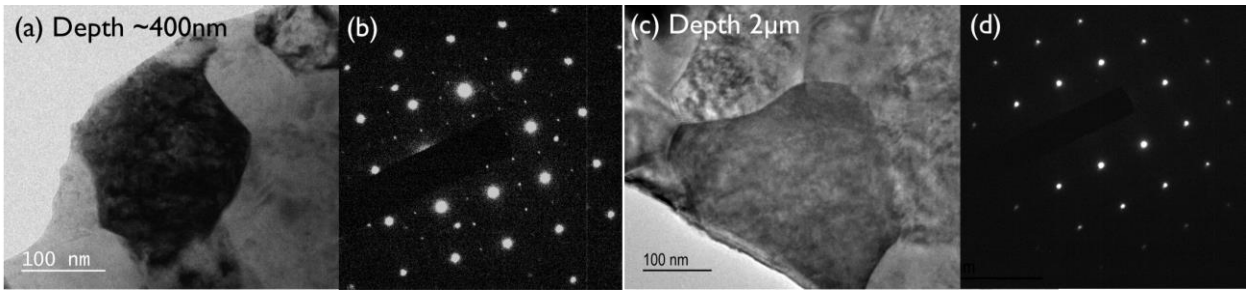

Figure 3 – 3YSZ irradiated with 45MeV Au to a fluence of 1×10^{15} ions/cm^2. (a) Bright field image collected near the surface of the irradiated pellet. (b) Selected area diffraction pattern (SADP) collected from the dark grain in (a) oriented to the [100] zone axis. An array of superlattice reflections are apparent between the fundamental reflections. (c) Bright field image collected approximately 2μm below the surface of the irradiated pellet. (d) SADP in the same zone axis and no forbidden reflections are found between the fundamental reflections.

Future Plans

These results have established several interesting, and in some cases unanticipated lines of investigation which require additional experiments and analysis to establish mechanistic understanding of the observed phenomenon. Specifically, we plan to undertake a systematic investigation of the relationship between nanoparticle size/temperature and RED to both understand the limitations of this approach while still extracting critical insight on the transition between the different RED regimes. We have yet to make the direct connection between the RED studies and the microstructural evolution of presintered ceramics. However, we anticipate that additional characterization of the irradiated nanocrystalline/nanoporous ceramics, specifically

with respect to the chemical heterogeneity before, during and after irradiation, will clarify critical differences between free surfaces and embedded interfaces and how they influence RED and therefore microstructural evolution. Continued collaboration with researchers at Los Alamos National Laboratory and Argonne National Laboratory will provide an opportunity to explore the relationship between porosity and microstructural evolution under irradiation in a different ceramic system, specific in amorphous and crystalline pyrochlores. Finally, we aim to continue pursuing the effect of large thermal gradients on the mobility and transport of irradiation induced defects.

References

[1] Van Sambeek, Andrew I., Robert S. Averback, C. P. Flynn, M. H. Yang, and W. Jaeger. "Radiation enhanced diffusion in MgO." *Journal of applied physics* 83, no. 12 (1998): 7576-7584.

[2] Han, Xiaochun, and Brent J. Heuser. "Radiation enhanced diffusion of Nd in UO2." *Journal of Nuclear Materials* 466 (2015): 588-596.

[3] Pappas, Harrison K., Brent J. Heuser, and Melissa M. Strehle. "Measurement of radiation-enhanced diffusion of La in single crystal thin film CeO2." *Journal of Nuclear Materials* 405, no. 2 (2010): 118-125.

[4] Dey, Sanchita, John W. Drazin, Yongqiang Wang, James A. Valdez, Terry G. Holesinger, Blas P. Uberuaga, and Ricardo HR Castro. "Radiation tolerance of nanocrystalline ceramics: insights from Yttria Stabilized Zirconia." *Scientific reports* 5 (2015): 7746.

[5] Dey, Sanchita, John Mardinly, Yongqiang Wang, James A. Valdez, Terry G. Holesinger, Blas P. Uberuaga, Jeff J. Ditto, John W. Drazin, and Ricardo HR Castro. "Irradiation-induced grain growth and defect evolution in nanocrystalline zirconia with doped grain boundaries." *Physical Chemistry Chemical Physics* 18, no. 25 (2016): 16921-16929.

Publications

C.S. Smith, N. Madden, **J.A. Krogstad**. "Variation in Densification Behavior of Ionic Conducting Ceramics Processed via Spark Plasma Sintering." (2019) *Under review. J. Am. Ceram Soc.*

N. Madden, S. A. Briggs, T. J. Boyle, D. Perales, J. Kolar-Guitterez, J. M. Sears, D. T. Yonemoto, E. Sivonxay, K. Hattar[a*], J.A. Krogstad. "Radiation Induced Sintering Phenomena in Fluorite-based ceramic nanoparticles." (2019) *In preparation.*

N. Madden, E. Lang, S. Murray, D. Shoemaker, J.P. Allain, K. Hattar, J.A. Krogstad. "Defect ordering in yttria stabilized zirconia under 45 MeV ion irradiation." (2019) *In preparation.*

Mechanical Properties of Metals at the Micrometer Scale in Different Environments

Seok-Woo Lee, University of Connecticut

Program Scope

Mechanical properties of metals at the micrometer scale are different from those of bulk metals because the plasticity is controlled by the intermittent operation of individual dislocation sources instead of the continuous and collective evolution of dislocation structures. Also, dislocation multiplication is limited at the micrometer scale because dislocations are easily annihilated at the free surface. Temperature usually significantly affects mechanical properties of metals, but its influence on the metal plasticity at the micrometer scale is not well understood. Ductile-to-brittle transition (DBT) is often observed in body-centered-cubic (BCC) metals. At a low temperature, the low mobility of screw dislocation cannot accommodate the imposed strain rate, leading to DBT. Because source-controlled plasticity at the micrometer scale works differently from bulk-scale plasticity, DBT is also expected to occur differently at the micrometer scale. Sample dimension, dislocation cross-slip, and dislocation mobility are the important factors in DBT processes in BCC metals. Many fundamental questions regarding these processes still remain open, and our proposed research seeks to provide answers. This project will use in-situ cryogenic micromechanical testing system, line dislocation dynamics simulations, and atomistic simulations to unveil fundamental mechanisms of source-controlled plasticity at a low temperature and their consequence on DBT.

Recent Progress

Over the last one year, we have made the significant progress in understanding source-controlled plasticity in BCC metals at a low temperature. In experimental side, we performed micro-tensile test on [0 0 1] niobium micropillar with 2 μm in thickness at 298, 100, and 56 K, and confirmed the presence of DBT. Also, we conducted the atomistic simulation on BCC nanopillar with a single screw dislocation and confirmed that a cross-slip is strongly suppressed at a low temperature.

(a) Ductile-to-Brittle Transition Driven by Dislocation Starvation

In-situ cryogenic micromechanical testing revealed that [0 0 1] niobium micropillar becomes significantly brittle at a low temperature (100 and 56 K), compared to room temperature (298 K) (Figure 1). Fractography clearly shows the brittle fracture surface for samples tested at a low temperature but the ductile fracture surface for samples tested at room temperature. Room temperature sample shows the presence of a large number of fine curvy slip bands, while low temperature samples shows straight slip bands, some of which have the large slip steps. Transmission electron microscopy showed that low temperature samples contain almost no dislocation after fracture. At the “same” strain, room temperature samples contain an extremely high dislocation density, suggesting that dislocation multiplication occurs actively at room temperature. At a low temperature, dislocation cross-slip does not seem to occur due to the insufficient thermal energy. As a result, a dislocation could keep a simple shape, be annihilated at the free surface, and have a low chance to develop a complex network structure. Once all mobile dislocations are annihilated at the free surface, a sample is not able to accommodate the imposed plastic strain rate, and brittle fracture occurs. At bulk scale, DBT occurs due to the low mobility

of screw dislocation, but at the micrometer scale, DBT could occur due to the lack of mobile dislocations. We term this process '*Ductile-to-brittle transition driven by dislocation starvation*'.

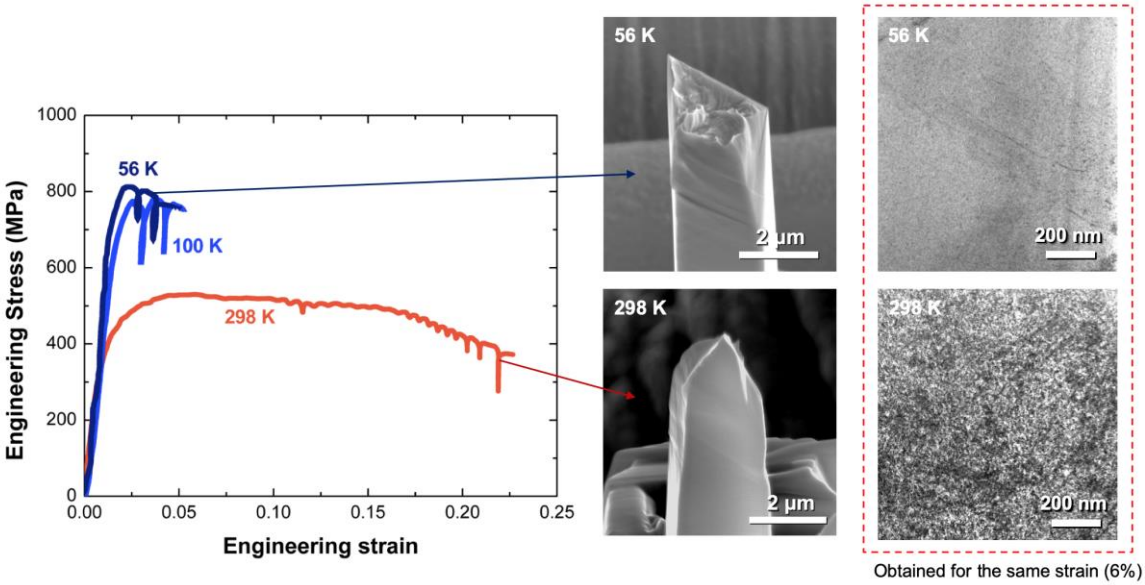

Figure 1. Engineering stress-strain curves at 298, 100 and 56K (left); Scanning electron microscope images of fractured samples (middle); Bright-field transmission electron microscope images. Note that two TEM images are obtained at the same total strain (~6%).

(b) Temperature-dependent behavior of a single screw dislocation in BCC nanopillars

Atomistic simulations were done on [0 0 1] niobium (Nb) and molybdenum (Mo) nanopillar that contains a single screw dislocation. Simulation results show that cross-slip is suppressed at a low temperature, resulting in the smooth motion of dislocation. Above a critical temperature of cross-slip (Nb: 200K and Mo: 500K), localized cross-slips occur vigorous on the screw dislocation (Figure 2). These results suggest that the dynamic evolution of complex dislocation structure could be shown above a critical temperature of cross-slip, leading to significant dislocation multiplication. This result agrees with our experimental observation in (a).

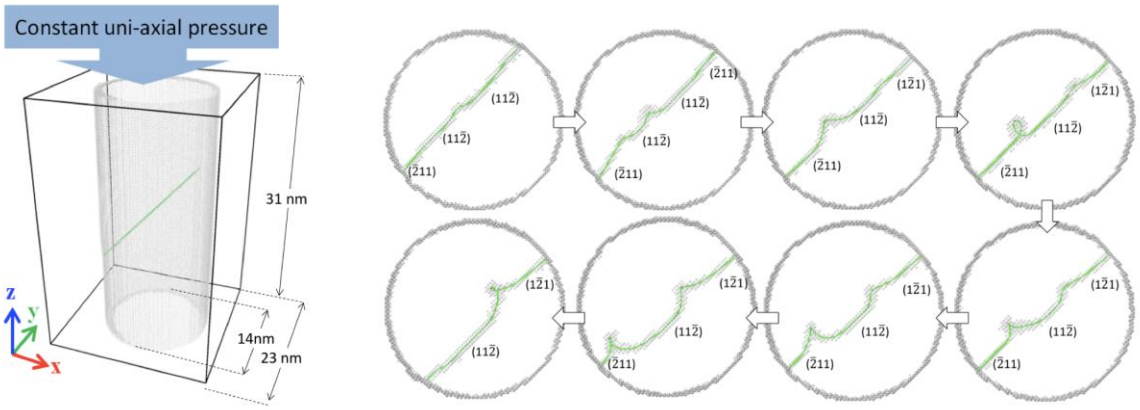

Figure 2. Simulation set-up (left); Dynamic evolution of screw dislocation structure due to the localized cross-slip event (Nb, T=250 K),

In this computational study, we also obtained the critical stress for self-multiplication as a function of temperature. This was motivated by Weinberger and Cai's work that calculated the critical stress for self-multiplication as a function of sample dimension for Mo [1]. Here, we identified the three distinct regimes of critical stress for self-multiplication with temperature. We found that the dynamics of cross-slipped segments plays an important role in determination of these three regimes.

Future Plans

We plan to introduce the different amount of dislocations by pre-straining a bulk Nb crystal (10% and 20%). Because dislocation starvation induces brittle fracture, the presence of more mobile dislocations at the initial condition would allow the more plastic strain before fracture. Too many dislocations may induce the brittle fracture due to dislocation locking. So, we expect that there is an optimum dislocation density to bring out the highest ductility at a given low temperature and at a given micrometer-scale dimension.

We also plan to investigate a BCC metal with different Peierls stress. Dislocation mobility is still an important factor to control the DBT process as well as dislocation cross-slip. To compare with Nb data (low Peierls stress), BCC tungsten (W) or Mo (high Peierl stress) will be investigated. The influence of Peierls stress on DBT at the micrometer scale will be understood.

We will also develop a line dislocation dynamics simulation of bcc crystals and investigate the role of dislocation mobility and cross-slip in evolution of dislocation structures at a low temperature. The goal is to identify how dislocation density decreases or increases with a different combination of dislocation mobility and cross-slip probability. This work will allow us to gain a fundamental understanding of dislocation plasticity of bcc metals at the micrometer scale and at a low temperature.

References

1. Christopher R. Weinberger, Wei Cai, *Proceedings of National Academy of Sciences*, **23**, 14304-14307 (2008).

Publications

1. Gyuho Song, Seok-Woo Lee, **"**Effect of temperature on surface-controlled dislocation multiplication in body-centered-cubic metal micropillars**,"** *Computational Materials Science* **168**, 172-179 (2019)

Multi-scale Modeling of Shear Banding in Metallic Glasses

PI: Lin Li The University of Alabama

Program Scope

Metallic glasses (MGs) possess amorphous structures with inherent heterogeneity at the nanoscale, which has profound impacts on glass dynamics and mechanical properties. The goal of this research is to develop a fundamental understanding of the heterogeneity in monolithic MGs, and the correlation of such heterogeneity with MG deformation, specifically focusing on the shear banding process, using integrated multi-scale simulations and developing a multi-scale model. Over the past two years, we explore the dynamic heterogeneity of the elementary deformation processes using atomistic simulations, focusing on the shear transformation characteristics and the structural evolution at the atomic scale in response to external stimuli. In addition, we experimentally validate the nanoscale heterogeneity and its connection with atomic packing configurations in MGs using atomic force microscopy (AFM). These nanoscale features will inform a developed mesoscale shear transformation zone (STZ) dynamics model, simulating the organization of STZs into shear-band patterns and linking with MG mechanical properties measured at large scales. The outcome could allow for a materials-by-design approach for developing MGs with enhanced mechanical performance (e.g., ductility and fracture toughness) via controlling and deploying the inherent MG heterogeneity.

Recent Progress

The evolution of atomic configuration in an elementary thermally-activated deformation process. The understanding of structural evolution in response to external forces in amorphous materials remains incomplete due to the complexity of their structure. As such, various complex phenomena in amorphous materials have been interpreted using the concept of the potential energy landscape (PEL) [1-2]. In this work, the evolution of atomic configuration in an elementary thermally-activated deformation process is investigated in a Cu64Zr36 model metallic glass system with different cooling histories spanning five orders of magnitude. We probe the reconfiguration of the short-range order clusters [3] at key states, i.e., initial, saddle and final on the PEL, as shown in **Fig. 1**. Very interestingly, a universal short-ranged order state is found

Figure 1 Schematic PEL for an MG and representative atomic reconfiguration at the initial, saddle and final states during the elementary process on PEL.

for the central atoms at the saddle states (ref to **Fig. 2**), which is invariant with respect cooling history, and more importantly, analogous to a special form of melts, referred as configurationally molten state (CMS), with the effective temperature hundreds of degrees above the glass transition temperature Tg. The local melting at the saddle states renders the atomic structures at the final states only weakly dependent on the initial states, implying the decoupling of the activation and relaxation stages of the elementary process. The localized CMS model at the saddle states sheds light on the physics of elementary processes in the PEL, the resultant decoupling of the elementary process could greatly simplify the dynamics of glass inherent structure evolution, and may apply to postulates of the glass rejuvenation route via thermomechanical protocols. This work is in collaboration with Dr. Jun Ding, Professor Rob Ritchie at Lawrence Berkley National Laboratory (LBNL) and Prof. Egami at Oak Ridge National Lab (ORNL).

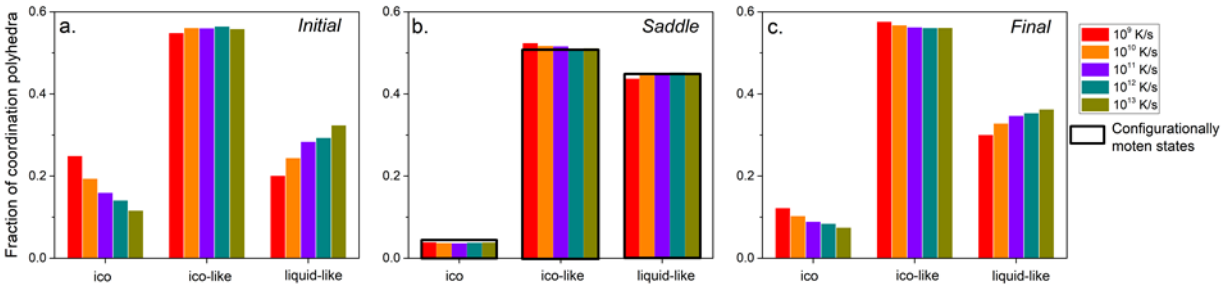

Figure 2 The distribution of three groups of characteristic coordination polyhedra, including icosahedral, icosahedral-like, and liquid-like types, around the central triggered atoms of MG configurations quenched from various cooling rates, at the (a) initial, (b) saddle and (c) final state, respectively, upon thermal excitation.

Transformation characteristics of the elementary deformation process. The mechanical deformation of MGs is postulated to originate from an elementary process called shear transformation zones (STZs). However, the precise identification of the STZ remains elusive, different experiments and simulations show a large variety of STZ sizes, from few atoms to several hundred. Here we develop a novel method to identify the STZ by a machine learning outlier detection algorithm. We employ the Activation-Relaxation Technique (ARTn) [4] to simulate thermal activation in amorphous solids, creating necessary raw atomistic

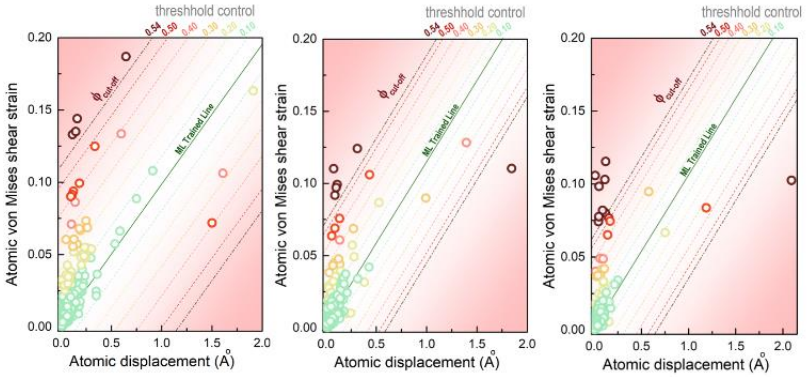

Figure 3 The automation process of the LinearRANSAC machine learning algorithm identifies the outlier atoms of each individual event. (a) –(c) represent three representative independent events in a model Cu64Zr36 MG cooled by 10^{11} K/s.

simulation events data to identify the critical atoms that have gone through a shear transformation. The STZs of each critical event can be detected by a linear based outlier detection algorithm as demonstrated **in Fig 3**. In this algorithm, a residual threshold parameter needs to be first determined by a double slope stopping convergence criteria while conducting the parameter sweep of the number of local atoms with respect to the residual threshold. We use this method to successfully identify STZ in a Cu64Zr36 metallic glass system with three cooling rates. The average number of atoms in the identified STZs is less than 10 atoms, consistent with the physics-based studies by Fan et al [5]. The average values of the various transformation quantities in the identified STZs match the widely-used characteristic values of an STZ during the thermally-activated process. Moreover, this method is robust to a wide range of training data of Activation-Relaxation techniques (ART) simulations so that it can be applied to different systems of amorphous solids. This method has been implemented in our open-source software ART_data_analyzer.

Nanoscale mechanical heterogeneity in MGs. Motivated by the impact of the nanoscale feature on the modulating MG flow [6], we study the chemical effect on tuning the nanoscale mechanical heterogeneity of a representative Cu-Zr-Al metallic glass (MG) system using a combined experimental and modeling approach. The amplitude-modulation dynamic atomic force microscopy (AM-AFM) is employed to measure the local mechanical response, revealing a reduction of nanoscale spatial heterogeneity in the local viscoelastic response after introducing Al into the $Cu_{50}Zr_{50}$ MG, as shown in **Fig 4.** With the assistance of atomistic simulations (i.e., molecular dynamics), the change of such nanoscale heterogeneity is related to the variation of local atomic structures upon Al alloying. The addition of Al increases the population of the short-range ordered icosahedral clusters, enhancing their connection to form a uniform network and thus reducing the structural heterogeneity at the nanoscale. In contrast, the $Cu_{50}Zr_{50}$ MG exhibits less icosahedral clusters, which tend to aggregate and disperse in space, resulting in a larger correlation length of the icosahedral order. This insight provides a fundamental understanding of the role of the nanoscale heterogeneity on the remarkable performance difference in the uniform monolithic MGs. This discovery could further facilitate tailoring the MG properties with selective modulation of chemical composition.

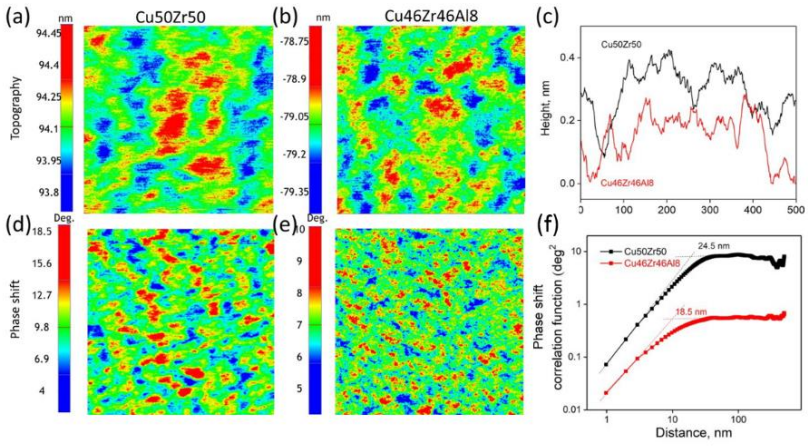

Figure 4 AFM results of Cu50Zr50 vs. Cu46Zr46Al8 MGs (a)-(b) the height image with root-mean-square (RMS) roughness less than 1 nm, confirmed by (c) height profile. (d)-(e) the phase shift images, reflecting the variation of nanoscale viscoelastic heterogeneity. (f) The calculated autocorrelation function of phase shifts, quantifying the variation of spatial heterogeneity.

Future Plans

In the coming year, we will focus on experimental validation of the model prediction on nanoscale heterogeneity tuning the deformation behaviors of MGs. Specifically, atomic force microscopy will be used to characterize the evolution of nanoscale inelastic heterogeneity in the MG thin films successfully fabricated via different sputtering conditions and chemical compositions. The mechanical responses will be measured using nanoindentation, focusing on shear banding, intermittent dynamics, and slip avalanches. The experimental results will be used to calibrate the multi-scale model and validate the model prediction on the critical spatial correlation condition that controls shear banding and ductility of MGs. In addition, we are collaborating with LBNL where the four-dimensional scanning transmission electron microscopy is used for the type, size, distribution, and volume fraction of atomic ordering at nano-scale, unveiling the structural mechanisms of nanoscale heterogeneity in MGs.

References

[1] P. G. Debenedetti & F. H. Stillinger. Supercooled liquids and the glass transition, Nature, 410, 259, (2001)

[2] D. J. Wales. A microscopic basis for the global appearance of energy landscapes, Science, 293, 2067, (2001).

[3] Y. Q. Cheng & E. Ma, Atomic-level structure and structure–property relationship in metallic glasses, Prog. Mater. Sci., 56, 379-473 (2011).

[4] H. Kallel, N. Mousseau & F. Schiettekatte, Evolution of the potential-energy surface of amorphous silicon, Phys. Rev. Lett., 105, 045503, (2010)

[5] Y. Fan, T. Iwashita, & T. Egami, How thermally activated deformation starts in metallic glass, Nat. Commun., 5, 5083, (2014)

[6] J.C.Qiao, et al., Structural heterogeneities and mechanical behavior of amorphous alloys, Prog. Mater. Sci., 104, 250-329 (2019).

Publications

[1] Wang N, Ding J, Yan F, Asta M, Ritchie RO, Li L, Spatial correlation of elastic heterogeneity tunes the deformation behaviors of metallic glasses, npj Computational Materials, 19, 2018

[2] Wang N, Ding J, Lou P, Liu YH, Li L, Yan F, Chemical Variation Induced Nanoscale Spatial Heterogeneity in Metallic Glasses, Materials Research Letter, 6, 2018

[3] Li L, Homer ER, Shear transformation zone dynamics modeling of deformation in metallic glasses, Handbook of Materials Modeling, Second Edition, edited by Yip S, Andreoni W, Springer, 2018

[4] Tian L, Li L, Ding J, Mousseau N, ART_data_analyzer: a python package that automates parallelized computation in a user workflow for studying the kinetics and dynamic evolution of materials, Software X, 9, 2019, P 238.

[5] Wang N, Tian L, Asta M, Ritchie RO, Egami TK, Li L, Ding J, Local flash melting at the saddle states of beta relaxation in Cu64Zr36 metallic glasses (submitted)

[6] Tian L, Yue F, Li L, Identifying the flow defects in amorphous solids by activation and relaxation techniques and machine learning outlier detection methods (submitted).

Low Temperature Cyclic Deformation Behavior of Ultrafine-grained Pure Magnesium

Qizhen Li, Washington State University

Program Scope

Grain refinement of magnesium (Mg) is an appealing processing technique to overcome the material's relatively low ductility caused by the material's HCP structure and limited slip systems [1-3]. This project aims at exploring the cyclic mechanical properties of ultrafine-grained pure Mg at low temperatures and uncovering the corresponding fundamental fatigue deformation mechanisms. The research aims will be accomplished through fatigue testing and microstructure characterization of the specimens. The research results will reveal the detailed activities of dislocations, twins, and grain boundaries in the specimens at the studied temperatures and cyclic loading conditions and will be able to provide new insight on the low temperature fatigue deformation mechanisms. The underlying understanding of the mechanisms will greatly contribute to the research community and allow the broader practical applications of this type of material.

Recent Progress

Two different microstructures were obtained to represent ultrafine grained samples (Mg^{FG}) with average grain size of ~10 μm and coarse grained samples (Mg^{CG}) with average grain size of ~ 40 μm. Both types of samples were mechanically tested under 25°C, 0°C, -30°C, and -60°C through static tensile testing and fatigue testing. Static tensile testing results were used to obtain the ultimate tensile strength (σ_{UTS}) for both types of samples as shown in Figure 1. σ_{UTS} increases with the decrease of temperature for coarse grained samples, while it first decreases then increases for ultrafine grained samples. For each testing

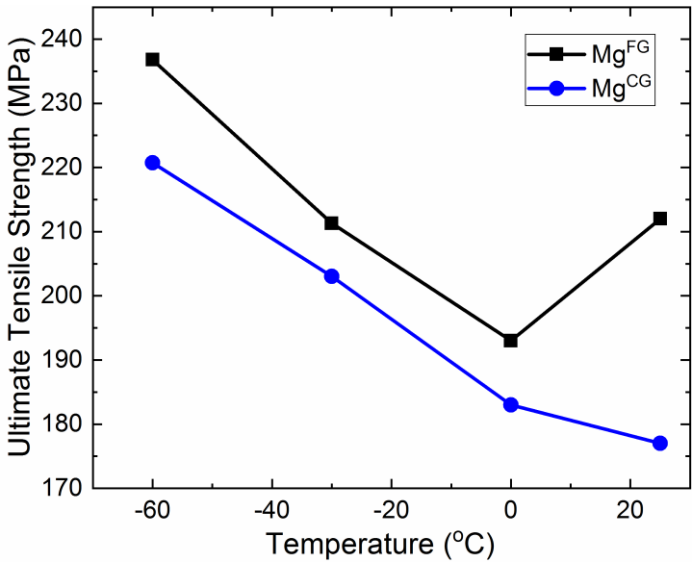

Figure 1. Ultimate tensile strengths for ultrafine grained samples and coarse grained samples under the testing temperatures of 25°C, 0°C, -30°C, and -60°C.

temperature, σ_{UTS} for ultrafine grained samples is higher than that for coarse grained samples. At room temperature, σ_{UTS} for Mg^{FG} is about 20% larger than that for Mg^{CG}. With the decrease of testing temperature, the difference in σ_{UTS} for Mg^{FG} and Mg^{CG} first becomes smaller and then slightly increases.

The σ_{UTS} data served as a base for the selection of stress ranges used for fatigue testing. For the testing temperatures of 25°C and 0°C, fatigue testing was performed for a range of stress ranges until a runout occurs. For the testing temperatures of -30°C and -60°C, fatigue testing was conducted under the stress conditions of $\frac{\sigma_{max}}{\sigma_{UTS}}$ = 0.8 and 0.9 for both types of samples (Note: σ_{max} is maximum stress). The following Figure 2 provides a summary of the fatigue testing results. In Figure 2, solid lines with filled symbols are used to represent the results for ultrafine grained samples, while dashed lines with open symbols are for coarse grained samples. In addition, the same line color and symbol color are used for each testing temperature. The results show that Mg^{FG} samples have longer fatigue lives than Mg^{CG} samples for each testing temperature. Fatigue lives for Mg^{FG} samples decreases when the testing temperature decreases from 25°C to 0°C.

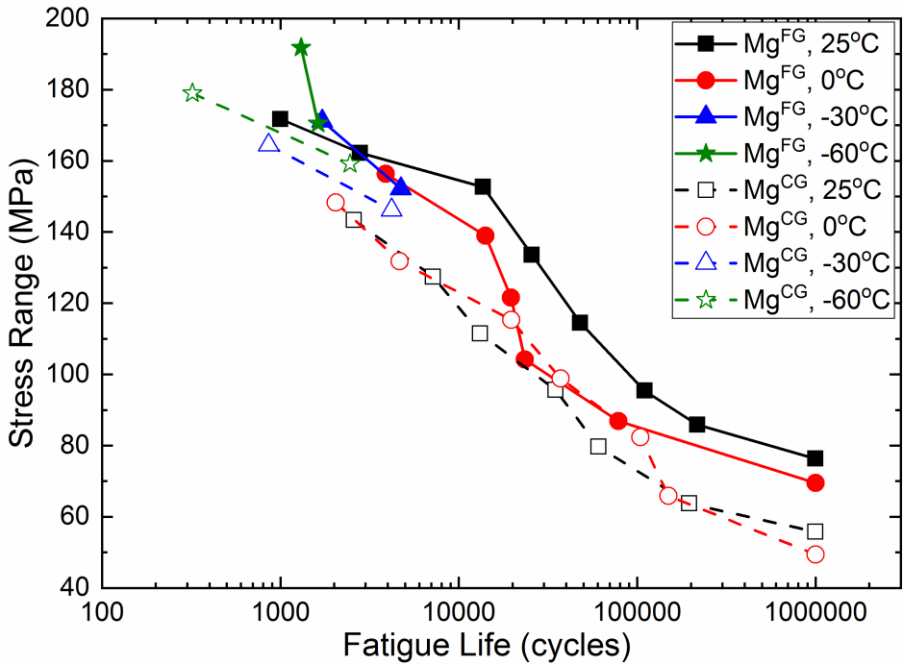

Figure 2. Fatigue life for Mg^{FG} and Mg^{CG} samples at different stress ranges for the testing temperatures of 25°C, 0°C, -30°C, and -60°C.

Fractured surfaces of the tested samples were observed under scanning electron microscope (SEM). Figure 3 presents some SEM images of fractured surfaces of Mg^{FG} samples tested at 25°C (i.e. Figure 3(a) and (b)) and 0°C (i.e. Figure 3(c)) respectively and that of Mg^{CG} samples tested at 25°C (i.e. Figure 3(d)). In Figure 3(a), the top edge is right below one side surface of the sample. The low magnification image shows both a pretty flat region close to the top and a rough region towards the sample inside. The flat region corresponds to the zone for fatigue crack initiation and stable propagation, while the rough region corresponds to the zone for unstable crack propagation and final rupture. The SEM observation showed that the Mg^{FG}

sample tested at 25°C possessed the larger flat region than the Mg^{CG} sample tested at 25°C, while the Mg^{FG} sample tested at 0°C possessed a slightly smaller flat region than the Mg^{CG} sample tested at 25°C. High magnification images for these samples show that the flat zone is composed of fatigue striations. The formation of striations was due to the twinning-detwinning process during fatigue testing. The images also shows that each grain had multiple parallel twins. Cracks were transgranular or intergranular, and they were along grain boundaries or twin boundaries. Figure 3(b-d) also shows that the striation spacing for the Mg^{FG} sample tested at 25°C is similar to that for the Mg^{FG} sample tested at 0°C, while the striation spacing for the Mg^{CG} sample tested at 25°C is much larger than those for the Mg^{FG} samples tested at 25°C and 0°C. This indicates that the striation spacing is correlated to the samples' grain sizes and the samples with larger grain sizes would have coarser striations.

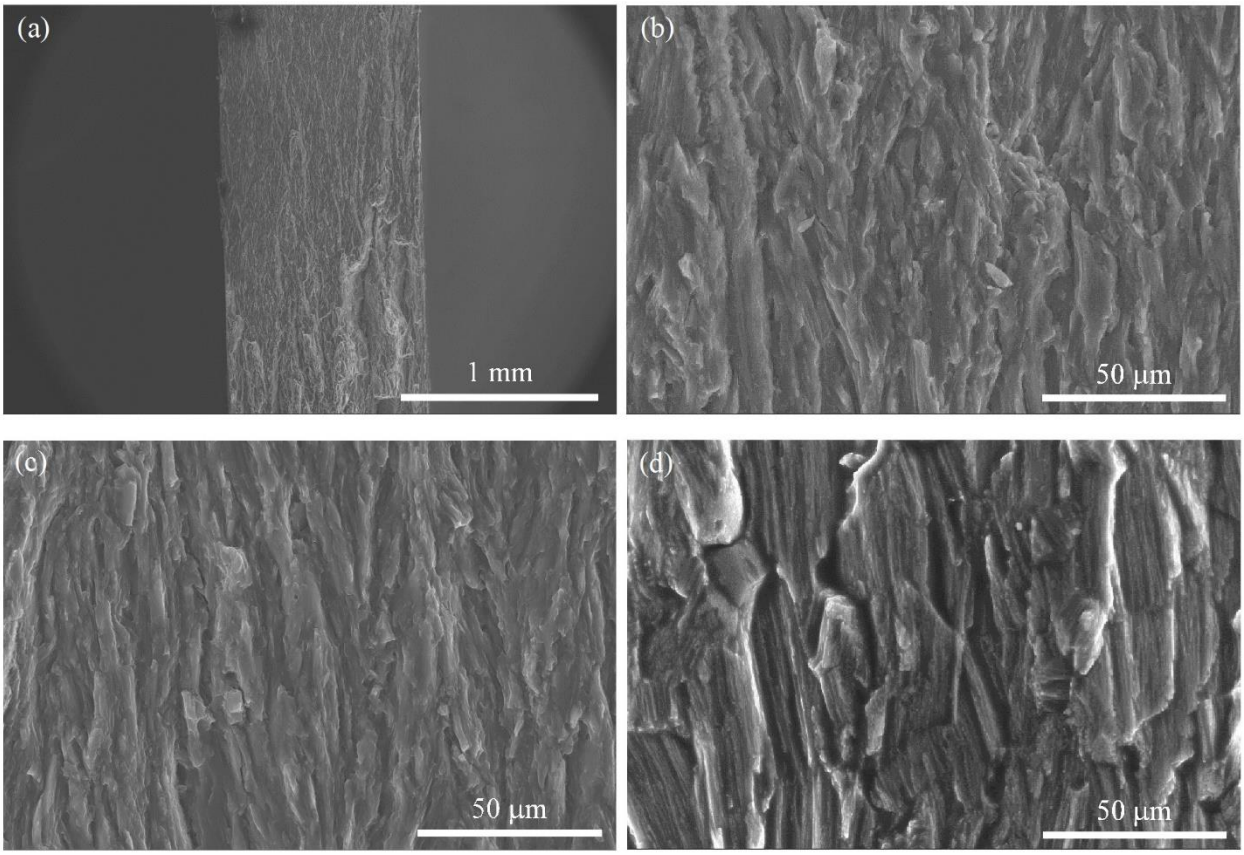

Figure 3. SEM micrographs of fractured sample surfaces after fatigue testing at $\sigma_{max}/\sigma_{UTS} = 0.6$. (a) Low magnification image of Mg^{FG} sample tested at room temperature, (b) high magnification image of Mg^{FG} sample tested at room temperature, (c) high magnification image of Mg^{FG} sample tested at 0°C, and (d) high magnification image of Mg^{CG} sample tested at room temperature.

Future Plans

- Continuing to perform fatigue testing under different stress ranges at -30°C and -60°C for magnesium with coarse grains until a runout occurs.

- Continuing to perform fatigue testing under different stress ranges at -30^{o}C and -60^{o}C for magnesium with ultrafine grains until a runout occurs.
- Continuing to observe fracture surfaces of the tested samples through SEM.
- Observing deformation mechanisms and twins/dislocations of the tested samples through EBSD.
- Investigating deformation mechanisms and twins/dislocations of the tested samples through TEM.
- Analyzing the results for paper publication in national and international journals and disseminating research results in national and international conferences.

References

[1] M.T. Perez-Prado, J.A. del Valle, O.A. Ruano, Grain refinement of MG-Al-Zn alloys via accumulative roll bonding, Scripta Materialia 51, 2004, pp. 1093

[2] Y. Yoshida, K. Arai, S. Itoh, S. Kamado, Y. Kojima, Realization of high strength and high ductility for AZ61 magnesium alloy by severe warm working, Science and Technology of Advanced Materials 6, 2005, pp. 185

[3] W.M. Gan, M.Y. Zheng, H. Chang, X.J.Wang, X.G. Qiao, K.Wu, B. Schwebke, H.G. Brokmeier, Microstructure and tensile property of the ECAPed pure magnesium, Journal of Alloys and Compounds 470, 2009, pp. 256

Publications

1. Q. Li, X. Jiao, Recrystallization mechanism and activation energies of ultrafine grained magnesium during annealing processing, Materialia, 2019, 100188
2. D. Hou, Y. Zhu, Q. Li, T. Liu, H. Wen, The effect of {10-12} twinning on the deformation behavior of AZ31 magnesium alloy, Materials Science and Engineering A 746 (2019) 314-321
3. Q. Li, X. Jiao, Exploration of Equal Channel Angular Pressing Routes for Efficiently Achieving Microstructure Refinement in Magnesium, Materials Science and Engineering A 733 (2018) 179-189
4. D. Hou, Q. Li, H. Wen, Study of reversible motion of 10-12 tensile twin boundaries in a magnesium alloy during strain path changes, Materials Letters 231 (2018) 84-86
5. X. Li, J. Zhang, D. Hou, Q. Li, Compressive deformation and fracture behaviors of AZ31 magnesium alloys with equiaxed grains or bimodal grains, Materials Science and Engineering: A 729 (2018) 466-476

6. Invited talk, Q. Li, Recrystallization activation energies in ultrafine grained magnesium during annealing, the Collaborative Conference on Materials Research (CCMR) 2019, Gyeonggi Goyang/Seoul, Korea, June 3-7, 2019
7. Invited talk, Q. Li, Evolution of Heterogeneous Microstructure of Equal Channel Angular Pressed Magnesium, 2019 TMS Annual Meeting & Exhibition, March 10-14, 2019, San Antonio, Texas
8. Q. Li, etc., Fracture behavior of magnesium at low temperatures under cyclic loading conditions, under preparation
9. Q. Li, etc., Effect of temperature on twinning and dislocation in magnesium under fatigue loading, under preparation

Title: Influence of 3D heterophase interface structure on deformation physics

N.A. Mara, University of Minnesota, Twin Cities (Principal Investigator)
I.J. Beyerlein, University of California, Santa Barbara, (Co-Principal Investigator)

Abstract: Detailed work into the defect-interface interactions enabling the enhanced mechanical behavior of two-phase or multiphase materials have only begun to investigate the rich parameter space of heterophase interface character, morphology, and chemistry. To date, heterophase interfaces are generally regarded as two dimensional (2D), and chemically and structurally abrupt. Yet for decades, studies have pointed to the enormous influence that the properties of the interface in the out-of-plane dimension can have on strength and mechanical behavior.

In this proposal, we aim to understand defect-interface interactions by pioneering basic research on *3D interfaces*. 3D interfaces are heterophase interfaces that extend out of plane into the two crystals on either side and are chemically, crystallographically, and/or topologically divergent, in up to three dimensions, from both crystals they join. Such interfaces influence not only the unit processes of single dislocations that can be understood at the atomic scale, but also mechanical behavior at the scales of a few to tens of dislocations and the resulting bulk behavior. Very rarely are interfaces found in nature perfectly 2D over distances more than a nanometer or two. The goal of this program is to systematically develop an understanding on how 3D interfaces can affect mechanical response. The types of 3D interfaces studied will encompass those containing chemical gradients and/or boundary curvature (of relevance to particle-strengthened materials, irradiated materials, lamellar composites, and more).

For 3D interface effects, the scientific issues that need to be addressed concern attaining a multiscale understanding of defect physics from the unit process encompassing the alterations in the dislocation core as it reacts with an interface to the collective process of impinging dislocation arrays that transform the interface structure to collective processes of multiple slip interactions. Each process is expected to be profoundly altered by varying the chemical composition and structure of the 3D interface. In this program, we will converge the program's synthesis, measurement, and modeling efforts to elucidate basic, controllable structural variables of the 3D interface that affect structural material performance. The materials containing interfaces will be synthesized via physical vapor deposition, a process by which the composition and/or structure may be systematically varied in the out-of-plane direction. Microstructural characterization will consist of a suite of techniques that addresses structure at the atomic level (TEM, Atom Probe), as well as mesoscales (X-ray, neutron reflectometry). Mechanical behavior will be investigated at length scales ranging from atomic-level dislocation-interface interactions (in-situ TEM) to micro scales (in-situ SEM and ex-situ nanomechanical testing). A combination of atomic-scale simulation and mesoscale phase field modeling will be employed to simulate dislocation interactions with the 3D interfaces we synthesize. The calculations together will aim to uncover fundamental mechanistic details underlying the dislocation reactions, to extract the

energies and critical stresses associated with them, and to relate them to the morphology and chemistry of the 3D interfaces.

This project was started in 2019

Taming Martensitic Transformations by Defect Engineering

Principal Investigators: Profs. Michael J. Mills, Peter M. Anderson, and Yunzhi Wang.
The Ohio State University, Department of Materials Science and Engineering

Program Scope

Shape memory alloys (SMAs) are an important class of materials whose functionality and performance are controlled by martensitic transformations (MT). This special type of phase transformation generates a change in crystal structure in response to external fields such as temperature and stress so that sensing and actuation can be realized simultaneously. However, the autocatalytic nature of MTs often produces a large hysteresis in stress–strain (SS) response. Two consequences for SMA actuators are low efficiency (less than 1%) and difficulty in precise position control of position or load. Obviously this SS behavior is completely opposite to the hysteresis-free and linear super-elastic properties desired for many advanced applications and serves as a key motivation in this program. The primary goal of this program is to seek new design strategies to regulate the autocatalytic MTs and render them smooth and continuous. The approach is to use defect engineering and nanotemplating to tame MTs both spatially and temporally. A key hypothesis is that MTs can be tamed by introducing stress and/or composition modulations at the nanoscale. These features must have a broad distribution of potency (or strength) for nucleating martensite and confining the spatial extent of its growth, so that the MTs take places continuously over a large temperature or stress range.

Experimental testing and characterization, theoretical analysis, and computer simulations will be used at multiple-scales to study the potency of various extended defects that induce distortions and concentration non-uniformities. Experiments will focus on NiTi and NiTiHf SMAs and provide: (1) detailed, multiscale characterization following large deformation; (2) constant-load thermal cycling and static annealing to validate competing hypotheses regarding austenite grain reorientation; (3) irradiation of TEM thin foils with Ni, Ti, and Hf ions using remarkable capabilities at CINT/Sandia that enable in situ characterization of defects and tensile testing; and (4) irradiation and thermal heat treatment of TEM thin foils to create/enhance nanoscale compositional modulations, followed by in situ tensile testing. Informed by the experimentally-characterized defect structures, the theoretical modeling and computer simulation efforts will focus on: (1) Theoretical analysis of defect generation during B2-B19' and B2-B19 MT cycling in NiTi and NiTiHf, respectively; (2) Phase field simulations of microstructural evolution, stress-strain, and volume fraction-temperature curves in SMA systems with defect "nanotemplates" – including dense dislocation networks, substructures, nanodomains of amorphous phase, Frank-loops, voids, and concentration non-uniformities; (3) thermo-mechanical simulations of aggregates of crystalline domains that are informed by smaller-scale phase field simulations and used to compare to macroscopic thermo-mechanical response; and (4) Validation at multiple scales.

This hypothesis-driven and intimately integrated experimental and computational program will create tremendous opportunities to explore uncharted territories of internal defect structure design and to engineer smarter microstructures for unprecedented properties of SMAs.

Recent Progress

<u>Effect of nano-precipitates on martensitic transformations (MTs)</u>

Experimental and modeling efforts were conducted to quantify the effect of nano precipitates on MTs in two high-temperature SMAs: Ni(Ti,Hf) and (Ni,Au)Ti. We have (1) developed a fundamental understanding of the inherent microstructure-property relationships in these SMAs, including the mutual interactions among precipitates, MTs and plastic deformation by dislocations, and (2) developed computational models that capture these structure-property relationships and provide novel insights into the important transformation and plasticity mechanisms that govern their behavior.

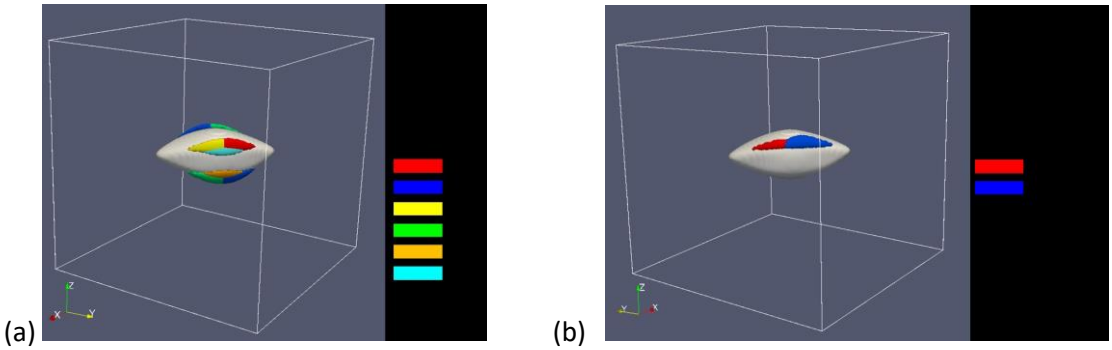

Fig. 1. (a) Elastic interaction energy plot between an H-phase precipitate and a martensite single variant (unit: -0.07 J/mm^3 or -0.588 KJ/mol); (b) Elastic interaction energy plot between an H-phase precipitate and a martensite nucleus (unit: -0.04 J/mm^3 or -0.3191 KJ/mol).

Similar to any other stress-carrying defects, the stress fields associated with coherent precipitates affect MTs. This was investigated through the calculation of the elastic interaction energy between the H-phase precipitates in Ni(Ti,Hf) and a nucleating martensitic particle (either single variant or an internally twinned particle, as shown respectively in Figs. 1 (a) and (b)). Due to the symmetry breaking during the B2 to B19' transformation in the NiTiHf alloy, there are twelve correspondence variants of martensite and 24 twinning modes among them. The plot shows the most preferred martensite variant and 24 twinning modes and the lowest elastic interaction energy is ~ -0.07 J/mm3 (~ -0.58 KJ/mol) for a single-variant particle and ~ -0.04 J/mm3 (~ -0.3191 KJ/mol) for an internally twinned particle.

Transformation-Induced Nanoscale Patterning of Defect Structures

We employed a coupled experiment-simulation approach to study the origin of dislocation patterning in 50.7 at.% Ni-Ti shape memory alloys. Earlier work subjected microcrystals to uniaxial compression at room temperature in order to study the formation of *a*[0-10]/(10-1) dislocation loops ~10 nm in size that were arrayed in high densities along (-110) planes (Fig. 2). The striking arrays and in particular the slip system could not be explained by the macroscopic compression, which favored a different slip system. This motivated the development of a new approach to study the coupling of phase transformations and plasticity at the nm-scale of individual martensite laths. The method – called the Phase Field-Crystal Plasticity (PF-CP) method – employs an explicit, large-deformation finite element solver that

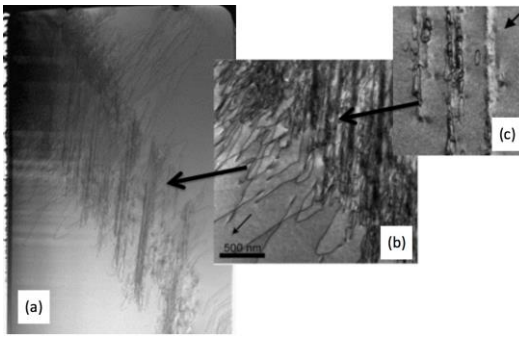

Fig. 2. (a) macro band of dislocations generated in a 50.7 at%Ni-Ti micron-scale crystal subjected to uniaxial compression. Insets show (b) dislocation arrays and (c) loops within arrays.

incorporates the phase field formalism for the B2-B19' phase transformation, crystal plasticity on slip systems in the B2 phase, and anisotropic thermo-elastic deformation. This was achieved by developing a custom USER-Material subroutine within the commercial finite element code ABAQUS.

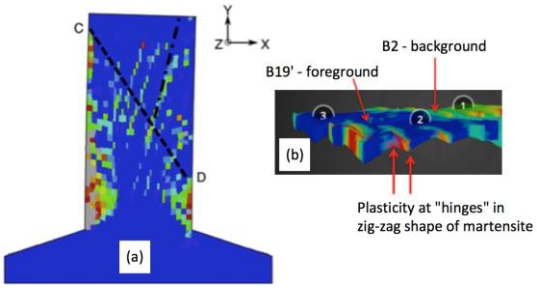

Fig. 3. Phase field-crystal plasticity simulation of a micropillar SMA sample under compressive loading, showing (a) striations of plasticity generated by a stress-induced martensite band and (b) a slice (~150 nm × ~150 nm × 1~5 nm) showing twinned martensite in the foreground and austenite in the background, with colors indicating plastic deformation along twin interfaces between martensite variants.

The results predicted the stress-induced B2-B19' transformation to initiate a band of B19' martensite within the microcrystal under compression, in remarkable similarity to the macro band observed in experiments (Fig. 3). Upon unloading, the simulations predicted linear striations of plastically deformed material, indicated by the colored segments in Fig. 3(a), that were left in the wake of a macroscopic martensitic band. The simulations were used to study the austenite-martensite interface at the finest (nm) scales, as it traveled across the sample at a significant fraction of the wave speed of the material. Fig. 3(b) shows the fidelity of the simulations, where the discrete zig-zag configuration of the martensitic (B19') state in the foreground gives way to the B2 state in the background. The color scheme records the profuse amount of plasticity associated with large deformation at the B2-B19' interface. These first-of-their-kind simulations were also used to study transformation-induced plasticity during thermal cycling. The results demonstrate that plasticity can shift critical temperatures for transformation, refine the scale of martensite, and even generate strain ratcheting during thermal cycling under a bias load.

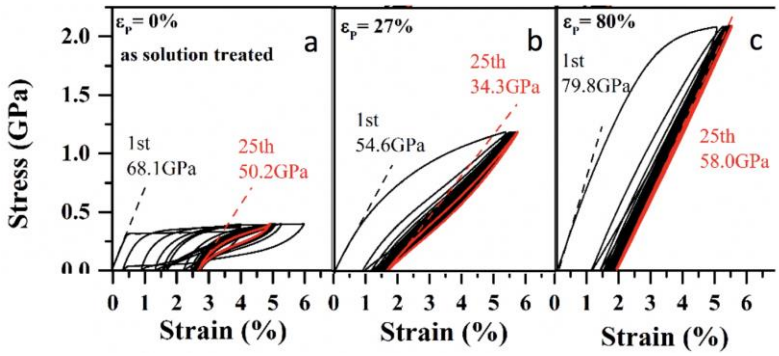

Fig. 4. Cyclic tensile tests on 50.2at%Ni-Ti as a function of plastic pre-strain (ε_P). Dramatically different behavior is observed in the initial cycle, and as a function of additional cycles. The pseudoelastic modulus has a minimum value at ε_P=25, a behavior indicative of a "strain glass" state for the M transformation.

Effect of Cold Rolling

The dramatic effect of cold rolling on the mechanical behavior of TiNi SMAs has been recognized for several decades, and examples of cyclic tensile tests after different pre-rolling strains are shown in Fig. 4. The source of this behavior stems from transformation-induced microstructural patterning. After cold-work, the sharp critical stress for normal MT disappears, indicating that the MT occurs over a wide range of stress values. Although this behavior is recognized and used in the "training" of SMAs, the mechanism underlying such an effect has remained a mystery. For instance, after 25 tensile cycles, a nearly perfectly linear pseudoelastic response with ultra-low modulus (34 GPa) is observed with little hysteresis. An hypothesis is that these attributes are expected for the "strain glass" state. This behavior is also affected by larger pre-strain (Fig. 4c), which increases the pseudoelastic modulus. This hypothesis is supported by recent high

resolution TEM results in which the local atomic structure of binary NiTi has been probed following cold rolling of 27%, where subsequent cycling dramatically reduces the pseudoelastic modulus condition. The selected area diffraction (SAD) pattern in Fig. 5 exhibits strong B2 reflections from the austenite and additional diffuse reflections. The fast Fourier transforms from several regions of a high resolution TEM image indicate variability from one region to the next, with intensities consistent with a B2 crystal changing to a pattern consistent with B19' martensite. Thus, in the 27% cold-rolled condition, these results indicate directly that retained martensite is present and it is confined to very localized, nanoscale regions.

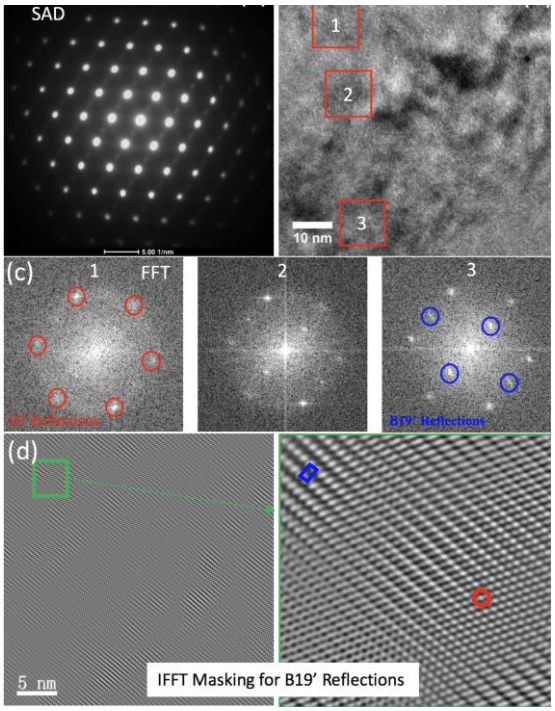

Fig. 5. SAD and HRTEM data along a <110>B2 zone axis for a 50.8Ni-Ti sample cold-rolled to 27%. Additional diffuse reflections can be attributed to a nanoscale, single variants of B19' residual martensite.

Future Plans

We will pursue four thrust areas for controlling and modeling the behavior of SMA systems that undergo reversible MTs. A graphical overview of the work is shown in Fig. 6. Binary NiTi and ternary NiTi-20Hf will be investigated. These alloy systems are selected for their different M crystal structures (monoclinic B19' for NiTi and orthorhombic B19 for NiTi-20Hf) and the proposed thrusts will for the first time explore differences in the response to extensive pre-deformation, annealing, and radiation effects. The activities will focus on SMAs having an initial austenitic structure although alloys with initial martensitic states will also be studied. Building upon the experimental and modeling techniques developed under the prior BES program, we will explore entirely new defect strain field/composition modulation routes to tame the B2-B19' and B2-B19 transformations. We will also study grain refinement and reorientation in austenite through transformation cycling and engineering special polycrystalline microstructures with primarily special Σ boundaries.

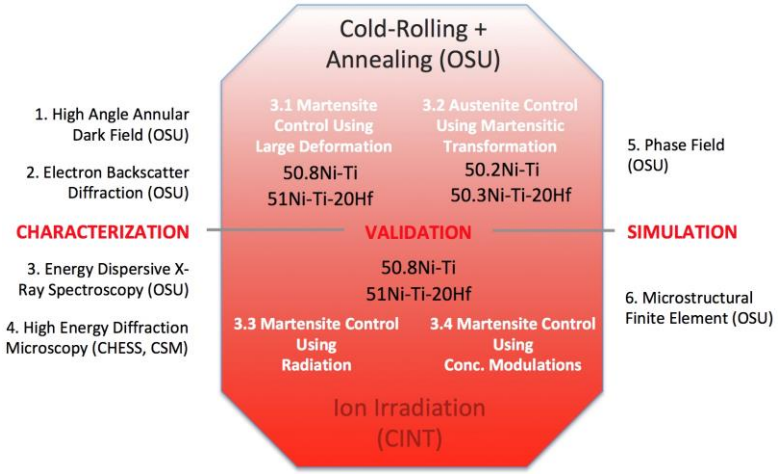

Fig. 6. Overview of the proposed effort showing the thrusts (3.1-3.4), key processing activities at OSU and CINT, alloy systems, and characterization and simulation techniques.

Publications

Kathryn Esham, *Precipitates and Nanoscale Templating of Martensite in Shape Memory Alloys*, MS Thesis, The Ohio State University (2017).

Y. Gao, S.A. Dregia, Y. Wang, "A universal symmetry criterion for the design of high performance ferroic materials", **Acta Materialia** 127 (2017), 438-449.

H. Paranjape, M.L. Bowers, M.J. Mills, P.M. Anderson, Mechanisms for phase transformation induced slip in shape memory alloy micro-crystals, **Acta Materialia** 132 (2017) 444-454.

J. Zhu, Y. Gao, D. Wang, T.Y. Zhang, Y. Wang, "Taming martensitic transformation via concentration modulation at nanoscale", **Acta Materialia** 130 (2017), 196-207.

Y. Gao, L. Casalena, M.L. Bowers, R.D. Noebe, M.J. Mills, Y. Wang, "An origin of functional fatigue of shape memory alloys", **Acta Materialia** 126 (2017), 389-400.

J. Zhu, H. Wu, D. Wang, Y. Gao, H. Wang, Y. Hao, R. Yang, T.Y. Zhang, Y. Wang, "Crystallographic analysis and phase field simulation of transformation plasticity in a multifunctional β-Ti alloy", **International Journal of Plasticity** 89 (2017), 110-129.

L. Casalena, G.S. Bigelow, Y. Gao, O. Benafan, R.D. Noebe, Y. Wang, M.J. Mills, "Mechanical Behavior and Microstructural Analysis of NiTi-40Au Shape Memory Alloys Exhibiting Work Output Above 400 °C," **Intermetallics** 86 (2017) 33-44.

L. Casalena, J.M. Sosa, D.R. Coughlin, F. Yang, X. Chen, H. Paranjape, Y.P. Gao, R.D. Noebe, G.S. Bigelow, D.J. Gaydosh, S.A. Padula, Y. Wang, P.M. Anderson, M.J. Mills, "Revealing Transformation and Deformation Mechanisms in NiTiHf and NiTiAu High Temperature Shape Memory Alloys Through Microstructural Investigations," **Microscopy and Microanalysis** 22 (S3), (2018) 1954-1955.

L. Casalena, Multimode=al Nanoscale Characterization of Transformation and Deformation Mechanisms in Several Ni-Ti Based Shape Memory Alloys, PhD Thesis, The Ohio State University (2017).

Q.L. Liang, D. Wang, J. Zhang, Y.C. Ji, X.D. Ding, Yu. Wang, X.B. Ren, Y. Wang, "Novel B19' Strain Glass with Large Recoverable Strain," ***Phys. Rew. Materials* 1**, 033608 (2017).

Y. Gao, Y.F. Zhang and Y. Wang, "Self-Organized Multi-Grain Patterning with Special Grain Boundaries Produced by Phase Transformation Cycling," ***Physical Review Materials* 2**, 073402 (2018).

Y. Gao and Y. Wang, "Hidden Pathway during FCC to BCC/BCT Transformations: Crystallographic Origin of Slip Martensite in Steels", ***Physical Review Materials* 2**, 09361 (2018).

J.M. Zhu, Y. Gao, D. Wang, J. Li, T.Y. Zhang, Y. Wang, "Rendering metals ultralow modulus and nearly hysteresis-free and linear super-elastic," ***Mater. Horiz.*** (2018) DOI: 10.1039/c8mh01141a.

P.P Paul, M. Fortman, H.M. Paranjape, P.M. Anderson, A.P. Stebner, L.C. Brinson, "Influence of Structure and Microstructure on Deformation Localization and Crack Growth in NiTi Shape Memory Alloys," Shape Memory And Superelasticity, **4,** 285-293 (2018).

D. Wang, Q.L. Liang, S.S. Zhao, P.Y. Zhao, L.S. Cui, Y. Wang, "Phase field simulations of martensitic transformation in pre-strained nanocomposite shape memory alloys," ***Acta Mater***. 164 (2019) 99-109.

Y. Gao, Y. Wang, Y.F. Zhang, “Deformation Pathway and Defect Generation in Crystals: A Combined Group Theory and Graph Theory Description,” ***IUCrJ*** (2019) 6. https://doi.org/10.1107/S2052252518017050.

A. N. Bucsek, L. Casalena, D. C. Pagan, P. P. Paul, Y. Chumlyakov, M. J. Mills, and A. P. Stebner, “Three-dimensional in situ characterization of phase transformation induced austenite grain refinement in nickel-titanium,” *Scr. Mater.*, vol. 162, (2019) 361–366.

J.Y. Zhang, Y.P. Gao, Y. Wang, W.Z. Zhang, “A generalized O-element approach for analyzing interface structures,” ***Acta Mater*****. 165** (2019) 508-519.

Plasticity of High-Strength Multiphase Metallic Composites

Amit Misra[1] (PI), Jian Wang[2] (co-PI), Jyoti Mazumder[1] (co-PI),

[1]University of Michigan, Ann Arbor; [2]University of Nebraska, Lincoln.

Program Scope

The goal of this research program is to elucidate the role of the microstructural scale, morphology and interphase boundary structure and crystallography in enabling plastic co-deformability in high-strength metallic composites containing disparate phases.

The proposed work aims to fill the gaps in knowledge in the fundamental understanding of plastic flow in metallic composites with soft/hard phases:

- Is plastic co-deformability favored as the interphase boundary spacing is reduced to nanoscale?

- Does the morphology (e.g., continuous vs degenerate lamellae or rods) of the hard phase influence plastic co-deformability?

- Can plastic co-deformability be achieved in composites with cubic/non-cubic phases?

- What is the role of the defect structure and crystallography of the interphase boundary in promoting plastic co-deformability?

Laser processed Al-Al_2Cu, Al-Al_2Cu-Si and Al-Si based eutectics are being used as model systems of metal-hard phase composites with a range of sizes, morphologies and interface crystallography. Nanoindentation, micro-compression, rolling, and *in situ* nanoindentation in scanning electron microscope (SEM) and transmission electron microscope (TEM) as well as high-resolution TEM characterization of defects are used to elucidate the mechanisms of nucleation and propagation of slip across interphase boundaries. The experimental research is conducted at University of Michigan with Prof. Mazumder leading the laser processing task and Prof. Misra leading the characterization task, while Prof. Wang at Nebraska leads the atomistic, meso-scale and crystal plasticity modeling task. Defect and interface-level properties obtained from atomistic modeling are used as input in the meso-scale model to compute strain hardening and local stress-strain response in a unit bi-crystal that are incorporated into the crystal plasticity finite element method to compute the macroscopic stress-strain response and compare with experimental measurements. The research will develop fundamental understanding of the microstructural design to enable ultra-strong metallic alloys (e.g., Al alloys with > 1 GPa strength levels) that exhibit significant plastic deformability at room temperature.

Recent Progress

The work in the last 2 years focused on testing the following hypotheses:

Hypothesis (i). Size: Reducing size may promote plastic co-deformability.

Hypothesis (ii). Interphase boundary crystallography and defect structure: Interfaces that act as efficient dislocation sources, either through easy slip transmission from soft to hard phase or

sites for glide dislocation nucleation by virtue of the defect structure, are more likely to promote plastic co-deformation.

Hypothesis (iii). Microstructural morphology: A bi-modal microstructure of a fine and relatively coarser composite may promote plastic co-deformability at high flow strengths.

Experimental and modeling results from the binary systems (Al-Al_2Cu) were used to test the first two hypotheses while ternary system (Al-Al_2Cu-Si) was used for the third hypothesis, and key findings are summarized below.

Effects of size and interface structures

- The interlamellar spacing (*l*) of Al-32.7 wt. %Cu eutectic alloy was refined to 30 nm using laser processing. A quantitative relationship was establish to correlate the interlamellar spacing with distance from solid-liquid interface and laser processing parameters such as power, spot size and scan speed.
- Compression tests on cylinders with height-to-diameter ratio of 2 and a range of diameters varying from 4 to 15 μm were conducted. As shown in Fig 1, the as-cast microstructures, with inter-lamellar spacing in the range of 500-700 μm, exhibited brittle behavior at low strengths. However, the laser refined eutectic microstructures of Al-Al_2Cu exhibited high strength and significant plasticity distributed uniformly across the sample, particularly at the finest inter-lamellar spacing of approximately 20 nm.

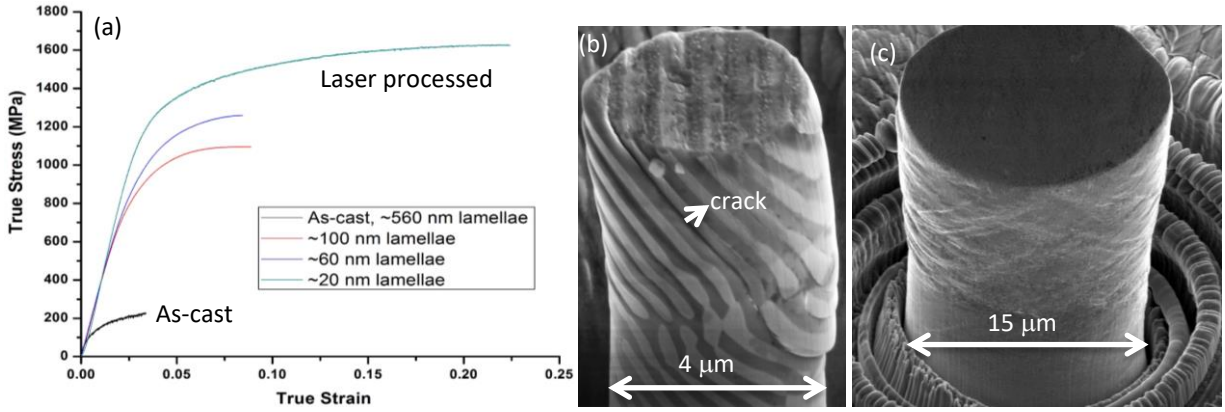

Fig. 1 (a) Stress-strain curves, in compression, of Al-Al_2Cu lamellar eutectics showing increasing strength and plasticity in the laser-processed microstructures compared to low strength and limited deformability in the coarse as-cast microstructure. SEM images of compressed samples show cracking in as-cast (b) and uniform deformation in nano-scale laser-processed eutectic (c).

- The orientation relationship between α-Al and θ-Al_2Cu phases in laser processed Al-Al_2Cu was measured from Kikuchi patterns obtained using electron backscattered diffraction (EBSD) and transmission-EBSD techniques. The characteristic orientation relationship (OR), $\{211\}_{Al2Cu}\|\{111\}_{Al}$ and $<120>_{Al2Cu}\|<110>_{Al}$, was observed independent of interlamellar spacing. This OR has two variants where, besides the two parallel planes, the variant I exhibits $(001)_{Al2Cu}\|\{001\}_{Al}$ and the variant II exhibits $(001)_{Al2Cu}\|\{111\}_{Al}$. Variant I prevails over

variant II in laser-processed α-Al and θ-Al_2Cu nano-laminates, and atomistic modeling indicates that this is due to the low energy interfaces associated with variant I, i.e., $\{211\}_{Al2Cu}||\{111\}_{Al}$ or $(001)_{Al2Cu}||\{001\}_{Al}$.

- Compared to deformation behaviors of microscale Al-Al_2Cu lamellar eutectics that exhibit brittle fracture of the intermetallic Al_2Cu phase, two unexpected deformation mechanisms – (i) localized shear on $\{011\}_{Al2Cu}$ planes, and (ii) faulted structure on $\{121\}_{Al2Cu}$ planes - were observed, for the first time, in the nanoscale θ-Al_2Cu layers through transmission electron microscopy. According to geometric analysis of slip systems across Al-Al_2Cu interface, the unexpected plasticity mechanisms were ascribed to slip continuity in Al-Al_2Cu eutectics associated with the orientation relationship and interface habit planes between α-Al and θ-Al_2Cu layers. The difference in shear mechanisms on the two planes, dislocation motion on $\{121\}_{Al2Cu}$ produces a planar fault but shear on $\{011\}_{Al2Cu}$ does not produce any fault, is attributed to low energy faulted structures associated with shear on $\{011\}_{Al2Cu}$ and $\{121\}_{Al2Cu}$ planes, as computed by first-principles DFT. First-principles DFT reveals that the faulted structure on $\{121\}_{Al2Cu}$ planes is associated with shearing $(\bar{1}21)_{Al2Cu}$ plane by a vector of $-1/6[311]_{Al2Cu}$. These findings reveal that crystallographic orientation relationships between metallic (soft) and intermetallic (hard) phases in nanoscale composite structures may lead to unusual deformation mechanisms and promote plastic co-deformation.

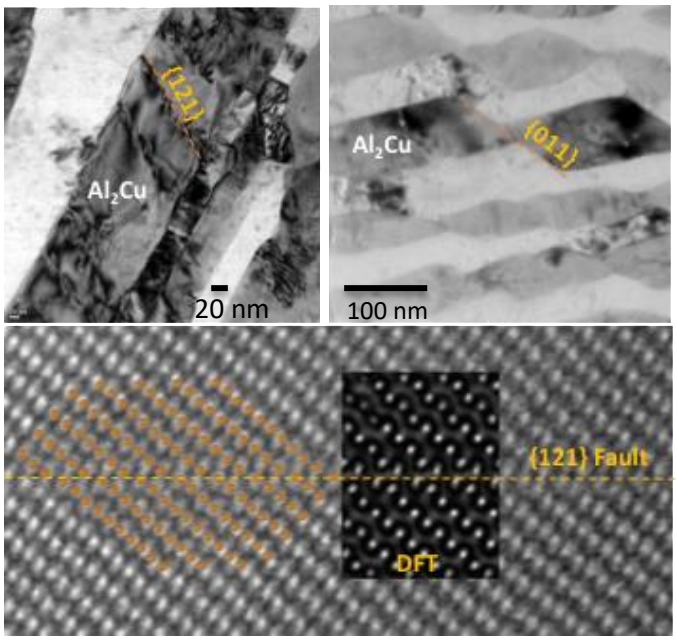

Fig. 2 (a) TEM image of multiple shear faults on $(121)_{Al2Cu}$ plane, (b) TEM image of multiple localized shears on $(011)_{Al2Cu}$ plane. Both deformation modes do not occur in monolithic Al_2Cu. (c) High-resolution Z-contrast image of a shear fault on $(121)_{Al2Cu}$ plane, viewed along $[101]_{Al2Cu}$, in deformed nanoscale laser-processed Al-Al_2Cu eutectic. The dark yellow dots denote Cu atoms and yellow dashed line indicates the shear plane. Simulated TEM image of DFT-computed relaxed fault structures of $(121)_{Al2Cu}$ plane, inserted in (c), indicates good match between experiment and density-functional-theory predictions and reveals a 1/6<311> shear.

- Taking nanoscale lamellar Al-Al_2Cu eutectic alloy as a model system, a mesoscale crystal plasticity (CP) model based on the confined layer slip (CLS) dislocation mechanism (referred to as CLS-CP) was developed to understand the buckling behavior under compression. In the CLS-CP model, buckling in Al_2Cu lamellae is constrained by the elastic-plastic deformation of Al lamellae. To capture the essential features of confined layer slip mechanism, plastic deformation in each lamella is the same through the layer thickness. The variation of elastic deformation through the layer thickness is captured through dividing each Al lamella into three

or more elements that have the same plastic deformation through the thickness. The CLS-CP model is able to predict mechanical properties of nano-scale lamellar soft/hard materials. The CLS-CP calculations reveal that critical compressive strain for buckling increases as layer thickness decreases, which agree with micro-pillar compression tests (Fig. 3).

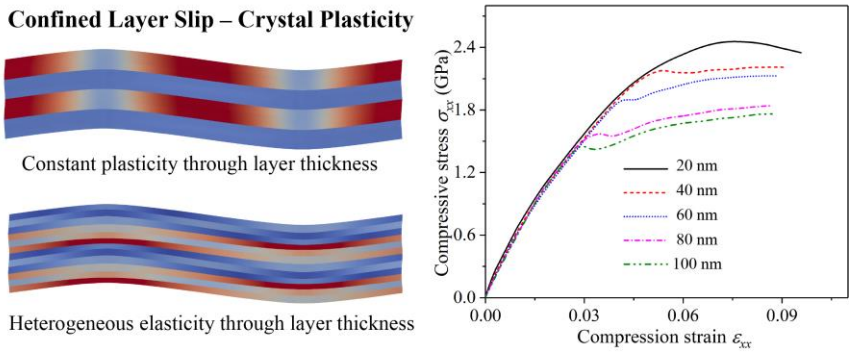

Fig. 3. CLS-CP model captures constant plasticity and heterogeneous elasticity through layer thickness, and predicts that critical compression strain corresponding to buckling increases as layer thickness decreases.

Effects of microstructure morphology

- In an $Al_{81}Cu_{13}Si_6$ ternary eutectic alloy, the extent of departure from equilibrium solidification (quantified by cooling rate) during laser processing determined the solidification microstructure, which was either a (i) ternary eutectic, or (ii) binary (Al-Al_2Cu)/ternary (Al-Al_2Cu-Si) bimodal eutectic, or (iii) dual-binary (Al-Al_2Cu)/Al-Si eutectic. This indicates that the laser processing can be used not just to refine but also control the morphology of the multiphase microstructures. Laser processing enables control of volume fraction and morphology and size of constituent phases that is not possible under equilibrium conditions so that microstructural states that give rise to unusual mechanical behavior can be accessed. The flow strength of bimodal eutectics can be changed by a factor of two as a result of differing fine eutectic volume fractions within the laser trace, and the highest strength is accompanied with enhanced plastic deformability. The mechanisms that enable continuity of plasticity across heterogeneous length-scales are being investigated.

Future Plans

New microstructure morphologies have been discovered in laser re-melted hypereutectic Al-Si alloys that will be used to test the hypothesis on microstructure morphology. Specifically, two kinds of microstructure will be explored. (i) Fully eutectic with interconnected nano-fibers of Si (≈ 50 nm diameter) that are internally nano-twinned thereby creating a hierarchy of defect length scales in a composite of disparate soft (Al) and hard (Si) phases: length scale associated with nanotwins in Si fibers and diameter, spacing and spatial arrangement of Si fibers in Al matrix. (ii) Primary Al dendrites containing a fine dispersion of Si precipitates embedded in a matrix of Al-Si eutectic as described in (i).

Publications (2017-2019)

1. J. Wang, Q. Zhou, A. Misra, P. Huang, F. Wang, and K. Xu, *Dislocation Interaction induced Structural Instability in Intermetallic Al_2Cu*, NPJ-Computational Materials, **3**, p 24 (2017).

2. J. Wang, Q. Zhou, S. Shao, A. Misra, *Strength and Plasticity of Nanolaminated Materials*, Materials Research Letters, **5**, p 1 (2017).

3. Q. Lei, B.P. Ramakrishnan, S. Wang, Y. Wang, J. Mazumder, A. Misra, *Structural refinement and nanomechanical response of laser remelted Al-Al_2Cu lamellar eutectic*, Materials Science and Engineering A, **706**, p 115 (2017).

4. B.P. Ramakrishnan, Q. Lei, A. Misra and J. Mazumder, *Effect of laser surface remelting on the microstructure and properties of Al-Al_2Cu-Si ternary eutectic alloy*, Scientific Reports (Nature Publishing Group), **7**, p 13468, (2017).

5. S. Shao, C. Zhou, A. Misra, J Wang, *Mesoscale Modeling of Dislocation-Interactions in Multilayered Materials*, In: Andreoni W., Yip S. (eds) Handbook of Materials Modeling. Springer, pp 1-30, (2018). https://doi.org/10.1007/978-3-319-42913-7_86-1

6. SJ Wang, G Liu, J Wang, A Misra, *Characteristic orientation relationships in nanoscale Al-Al_2Cu Eutectic*, Materials Characterization, **142**, p 170 (2018).

7. SJ Wang, G Liu, DY Xie, Q Lei, BP Ramakrishnan, J Mazumder, J Wang, A. Misra, *Plasticity of laser-processed nanoscale Al-Al_2Cu eutectic alloy*, Acta Materialia, **156**, p 52 (2018).

8. S. Shao, A, Misra, H. Huang, J. Wang, *Micro-scale modeling of interface-dominated mechanical behavior*, Journal Of Materials Science, **53**(8), p 5546-61, (2018).

9. GS Liu, MY Gong, DY Xie, J Wang, *Structures and Mechanical Properties of Al-Al_2Cu Interfaces*, JOM. The Minerals, Metals & Materials Society, **71**(4), 1200-1208 (2019).

10. GS Liu, D. Xie, S. Wang, A. Misra, J. Wang, *Mesoscale crystal plasticity modeling of nanoscale Al-Al_2Cu eutectic alloy*, International Journal of Plasticity, (2019), DOI: 10.1016/j.ijplas.2019.06.008.

11. I.J. Beyerlein, J Wang, *Interface-driven mechanisms in cubic/non-cubic nanolaminates at different scales*, MRS Bulletin **44** (1), 31-39 (2019)

12. MJ Buehler, A Misra, *Mechanical behavior of nanocomposites*, MRS Bulletin **44** (1), 19-24 (2019).

Fundamental Investigation of Grain Boundary Dislocation Mechanisms in Ultrafine Grained Metallic Films

Principal Investigators: Olivier Pierron[1], Josh Kacher[2] and Ting Zhu[1,2]
[1] Woodruff School of Mechanical Engineering
[2] School of Materials Science & Engineering
Georgia Institute of Technology, Atlanta, GA 30332

Program Scope

The overarching goal of this proposal is to acquire a fundamental understanding of dislocation mechanisms and grain boundary (GB) – dislocation interactions active in ultrafine grained (ufg) metallic films, and the extent to which they dictate plastic flow kinetics. The central hypothesis of the proposed research is that dislocation activity in ufg metallic films is mainly governed by GB characters and film-thickness-to-grain-size ratio (t/d). Our approach to study this hypothesis consists of a synergistic integration of *in situ* transmission electron microscopy (TEM) deformation experiments, microelectromechanical system (MEMS) based nanomechanical testing, and transition state theory based atomistic modeling, in order to provide a direct linkage between dislocation processes and their deformation kinetics. The objectives of the work are to:

1. Simultaneously identify the governing deformation mechanisms, obtain key details (such as character of the GBs where dislocation processes are observed), and measure the associated true activation volume V^* in ultrafine grained Au and Al thin films with different textures and t/d ratios, using a novel quantitative *in situ* TEM, MEMS-based nanomechanical testing technique.
2. Systematically investigate how the activation of the observed dislocation mechanisms vary as a function of GB characters and t/d ratios using the novel atomistic free-end nudged elastic band (NEB) method that overcomes the timescale limitation of molecular dynamics simulation.
3. Elucidate the role of GB characters, grain size, and film thickness in dislocation processes in ufg films using this integrated approach.

Recent Progress

1. Quantitative in situ TEM testing of <111> textured, 100-nm-thick Au polycrystalline specimens

Figure 1a shows a representative stress-strain curve from a monotonic test to failure of a 100-nm-thick Au specimen (see Figures 1c-f for SEM image and previous TKD characterization) tested with our newly acquired electrical biasing TEM holder operating our MEMS testers [1-3] inside a Tecnai F30 TEM (see Figure 1b). Both capacitive sensors are calibrated during the *in situ* TEM test. The curve does not start at origin: the specimen is pre-stressed due to the shrinking of the epoxy glue that is used to attach the large ends of the specimen to the MEMS device (see Figure 1d). This pre-stress can be measured by comparing the displacement in the load capacitive sensor before and after fracture of the specimen. The plastic strain to failure is approximately 4%. This technique can be used to perform *in situ* TEM stress and plastic strain measurements with good accuracy and precision.

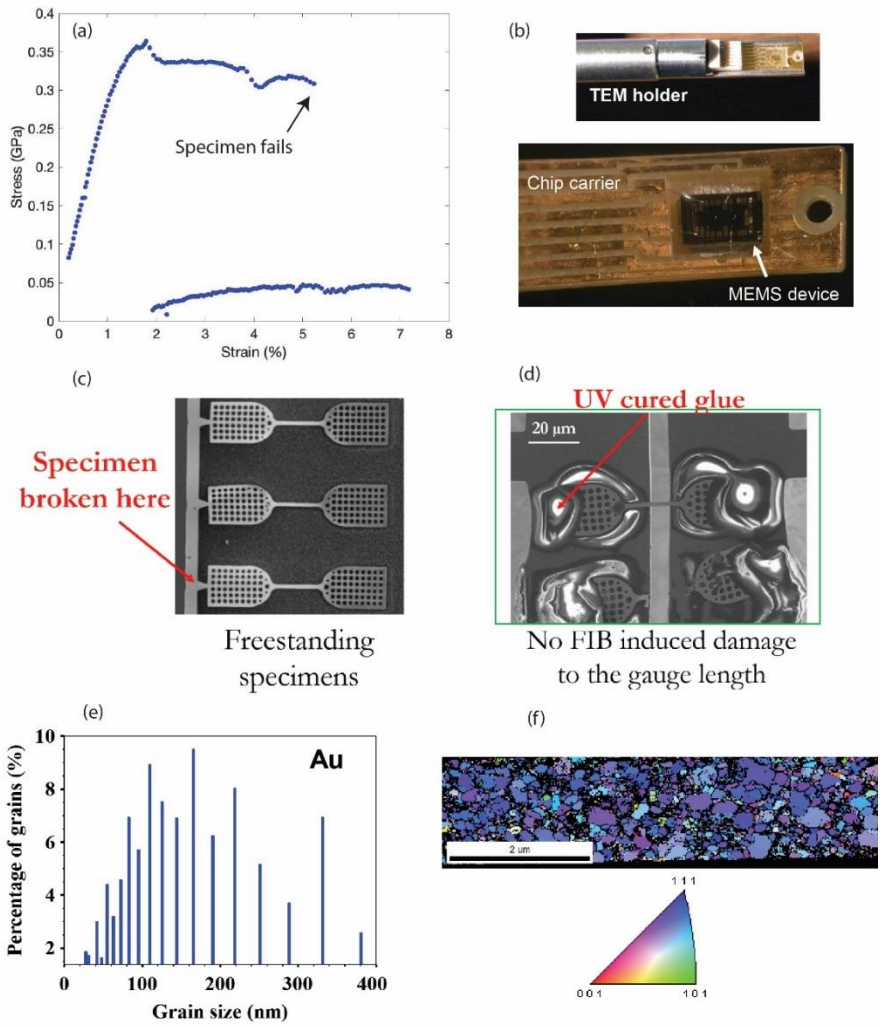

Figure 1. (a) Stress-strain curve of a 100-nm-thick Au specimen, measured with our (b) in situ TEM setup at GT (c) and (d) Au specimen before and after clamping onto MEMS device. (e) and (f) grain size distribution and TKD map of Au specimen.

Figure 2 shows a repeated stress relaxation test to measure true activation volume, using the new setup at Georgia Tech. These measurements are preferably performed at the onset of plastic deformation, i.e. prior to reaching the ultimate tensile strength, so that necking and the resulting non-uniform stress distribution along the specimen's gauge section has not occurred. The inherent stability of the MEMS device and the good precision in stress measurement (±2 MPa) coming from the low noise associated with capacitive sensing (<0.1 fF) enables good logarithmic fits of each stress relaxation segment (from which apparent activation volume, V_a, can be calculated). The true activation volume, V^*, can be calculated using [4]:

$$V^* = \sqrt{3}kT\frac{\ln\left(\dot{\sigma}_{i2}/\dot{\sigma}_{f1}\right)}{\Delta\sigma_{12}}$$

where $\Delta\sigma_{12}$ is the stress increase during reloading between relaxations 1 and 2, $\dot{\sigma}_{i2}$ is the stress decrease rate at the beginning of the second stress relaxation segment, and $\dot{\sigma}_{f1}$ is the stress decrease rate at the end of the first stress relaxation segment. From the three relaxation segments shown in Figure 2, V^* was measured to be 4 and 5 b^3, while V_a was in the 25-30 b^3 for each segment. Physically, V^* is proportional to the number of atoms involved in the thermally activated process

responsible for the dislocation overcoming a local barrier, and as such is considered a signature of that specific mechanism.

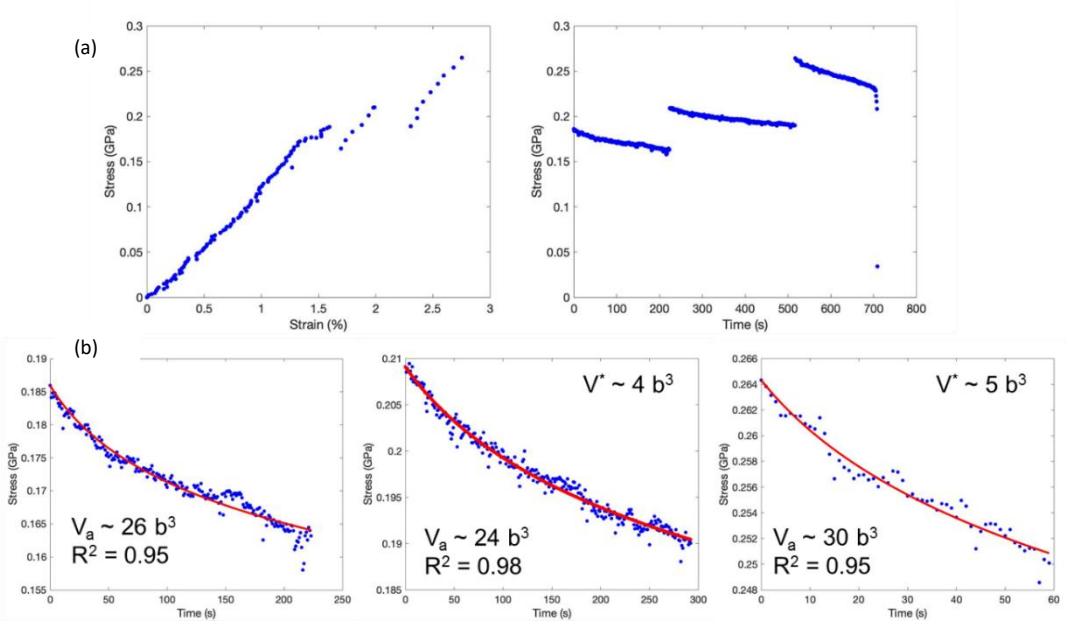

Figure 2. (a) Left: stress-strain curve for a multiple stress relaxation test, and right: corresponding stress vs time for the three successive relaxation segments. (b) stress vs time during each relaxation segment, with logarithmic fit, from which V_a and V^* can be obtained.

In situ TEM observations during or shortly after the activation volume measurements have mainly revealed trans-granular dislocation activities occurring in a few grains, with either grain boundary sources or internal sources. Figure 3 shows a typical example of a slip band along which dislocations travel (see red arrows). The dislocations nucleate at the bottom grain boundary (see large blue arrow in Fig 3). Previous *in situ* TEM observations of the same Au specimens had also revealed intergranular dislocation activities, especially in the presence of cracks (at larger applied strains) [3, 5].

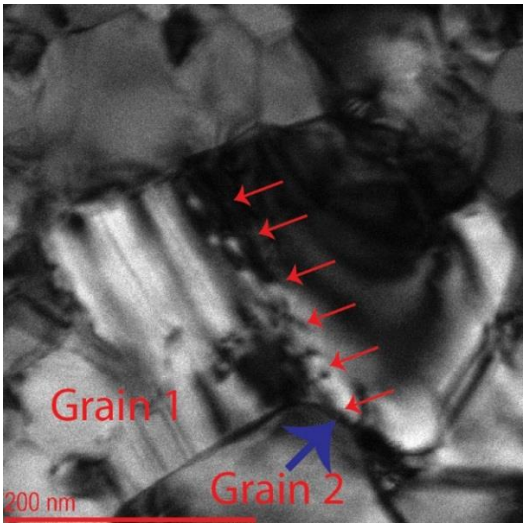

Figure 3. Snapshot from a TEM movie highlighting dislocations moving along a slip band (red arrows). The dislocations nucleate at the bottom curved grain boundary (blue arrow).

2. Atomistic modeling of grain boundary (GB)-mediated dislocation processes in polycrystalline Au films

Molecular dynamics (MD) simulations have been performed to investigate GB-mediated dislocation processes in a polycrystalline Au film under in-plane tension. MD results show that the dislocation nucleation from film surface and GB is the dominant plastic deformation mode during the initial yielding response. Further load increase results in dislocation interactions within grains, dislocation transmission across GBs, and GB migration. These MD results are generally consistent with our *in situ* TEM observations.

Figure 4 shows the representative MD results of GB-mediated dislocation processes. A polycrystalline Au film is constructed with a dominant <111> texture, similar to experimental samples (Fig. 4a). At the room temperature (300K) and under in-plane tension, the dominant dislocation slip systems in MD are illustrated in Figs. 4a & b. Figures 4c-f show several representative MD snapshots. It is seen that both high-angle GBs (HAGBs) and low-angle GBs (LAGBs) are present in the initial structure after sample relaxation by simulated annealing (Fig. 4c). As the applied load increases, the leading partial dislocations first nucleate from side surfaces of the film as well as from GBs; and these partials glide on the inclined {111} slip plane (as illustrated in Figs. 4a & b), dragging a long stacking fault ribbon behind (Fig. 4d). With increasing load, the trailing partials also nucleate from GBs, such that the leading and trailing partials move together as full dislocations (Fig. 4d). Glide of both leading partials and full dislocations is usually obstructed by GBs. Occasionally, the obstructed dislocation transmits across the GB; LAGBs can also migrate (Fig. 4e). These dislocation processes continue during the entire loading process (Fig. 4f).

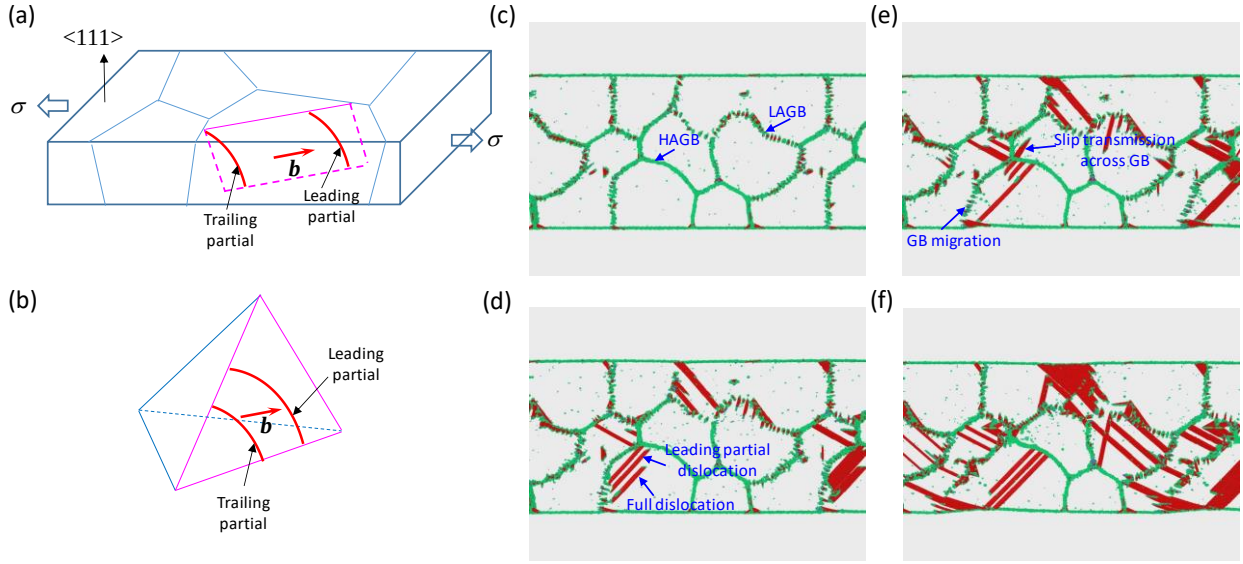

Figure 4. MD simulation result of GB-mediated dislocation processes in a polycrystalline Au film under tension. (a) Schematic of the film with a <111> texture and an average grain size of ~25 nm. (b) The dominant slip system of {111}<110> is indicated by the Thompson tetrahedron. (c-f) MD snapshots showing GB-mediated dislocation processes. For the clarity of visualization, atoms in the perfect lattice are removed; atoms on the surface and GB are colored in green; and atoms in the stacking fault in red.

Future Plans

Future plans include characterizing the nature of GBs where dislocation nucleation is observed, by performing TKD measurements on specimens prior to *in situ* TEM testing, in order to have maps similar to that shown in Fig. 1(f) to track location of dislocation activities during *in situ* TEM testing. The details of the GBs will serve as input for atomistic simulations. MD simulations along the line shown in Fig. 4 will be performed to compare with the detailed TEM characterization of GB-mediated dislocation processes. This will enable us to identify the candidate dislocation processes that are strength/rate controlling. Then atomistic reaction pathway simulations will be performed with the nudged elastic band method, so as to compute the activation energies and activation volumes associated with these unit processes. The results will be compared with our in situ stress relaxation measurements, in order to determine the GB-mediated dislocation processes that are strength/rate controlling.

References

1. Gupta, S. and O. Pierron, *A MEMS Tensile Testing Technique for Measuring True Activation Volume and Effective Stress in Nanocrystalline Ultrathin Microbeams.* Journal of Microelectromechanical Systems 2017. **26**(5): p. 1082-1092.
2. Gupta, S. and O.N. Pierron, *MEMS based nanomechanical testing method with independent electronic sensing of stress and strain.* Extreme Mechanics Letters, 2016. **8**: p. 167-176.
3. Hosseinian, E., M. Legros, and O.N. Pierron, *Quantifying and observing viscoplasticity at the nanoscale: highly localized deformation mechanisms in ultrathin nanocrystalline gold films.* Nanoscale, 2016. **8**(17): p. 9234-9244.
4. Martin, J.L., B. Lo Piccolo, T. Kruml, and J. Bonneville, *Characterization of thermally activated dislocation mechanisms using transient tests.* Materials Science and Engineering a-Structural Materials Properties Microstructure and Processing, 2002. **322**(1-2): p. 118-125.
5. Hosseinian, E., S. Gupta, O.N. Pierron, and M. Legros, *Size effects on intergranular crack growth mechanisms in ultrathin nanocrystalline gold free-standing films.* Acta Materialia, 2018. **143**: p. 77-87.

Publications

1. Kacher, J., T. Zhu, O. Pierron, and D.E. Spearot, *Integrating in situ TEM experiments and atomistic simulations for defect mechanics.* Current Opinion in Solid State and Materials Science, 2019. **23**(3): p. 117-128.
2. Bhowmick, S., H. Espinosa, K. Jungjohann, T. Pardoen, and O. Pierron, *Advanced microelectromechanical systems-based nanomechanical testing: Beyond stress and strain measurements.* MRS Bulletin, 2019. **44**(6): p. 487-493.

Nanomechanics: Friction and Elasticity in Nano-Objects

Elisa Riedo, NYU Tandon School of Engineering

Program Scope

The quest for materials with exceptional mechanical properties is the focus of major efforts since the beginning of civilization and sintering materials with a stiffness and hardness equal or superior to those of diamond is an ongoing challenge. In particular, for both scientific and technological reasons, the transformation of graphite into diamond remains one of the most fascinating and studied solid-to-solid phase transitions in materials science. Recently, several investigations revealed new and interesting phenomena related to phase changing 2D materials, highlighting the transformation of multi-layer graphene into a diamond-like structure. In particular, the PI and theoretical collaborators reported that under localized pressure, an atomically-thin graphene film grown on SiC(0001) behaves as a diamond-hard coating, exhibiting mechanical responses to nano-indentation superior to those of a diamond substrate.

The vision of this DoE research program is to investigate novel mechanical properties and phenomena in 2D materials with the overarching goal of defining a new basic understanding of mechanical behavior in nano and quantum systems. Here, we propose a research program aimed at developing a new basic understanding of the mechanical properties of 2D materials at the interface with solid substrates, with a focus on pressure induced phase-changing 2D materials, and 2D material-substrate interfaces.

Recent Progress

Very recently, atomic force microscopy experiments [1] developed in the PI's lab have shown that at room temperature, nanoindentation of an epitaxial graphene film supported and grown on SiC(0001) can induce, at pressures of about 1 GPa, **the formation of a new diamond-like phase with a stiffness much larger than the SiC substrate** (Fig. 1), and displaying **no residual indent (holes) upon large loads indentations with a diamond indenter**. Further **Å-Indentation** experiments performed with a diamond tip and comparing the stiffness of a film of CVD diamond and sapphire with 1L epi-graphene + BfL showed that the **stiffness of 1L+BfL epitaxial-graphene is larger than that one of diamond and sapphire (Fig. 1)**.

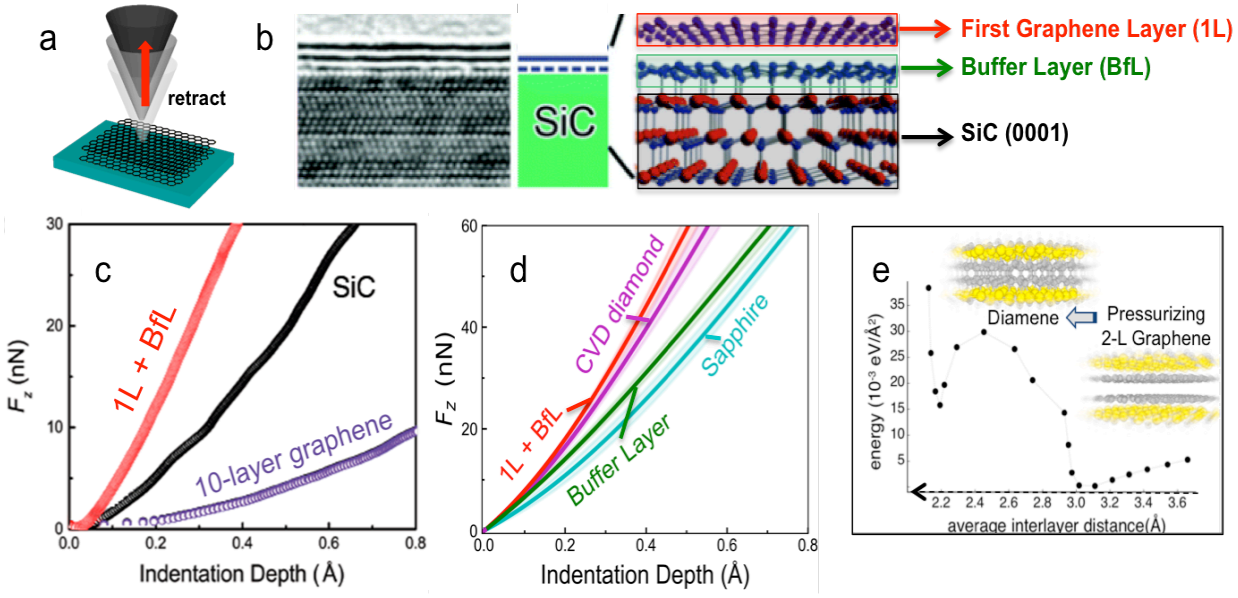

Fig. 1. Top panels, schematic illustration (a) and TEM images (b) of epitaxial graphene grown on SiC by Si sublimation at high temperatures. Bottom panels, experimental force vs. indentation curves of 1L+buffer layer graphene on SiC(0001), showing that that the stiffness of 1L+ BfL on SiC (red curves) is much larger than that one of the uncoated SiC substrate (black curve) (c), and larger than CVD diamond, bare buffer layer on SiC, and sapphire (d). (e) DFT simulation of the phase transformation process of 2-L graphene into ultra-hard diamene (grey-atoms are C-atoms and yellow-atoms are Si-atoms) [1].

To obtain the results described above here about the graphene-diamene phase transformation (and develop the here proposed research plan), the PI's group needed an indentation method to achieve sub-Å indentation depths in an atomically thin film supported by a rigid substrate, i.e. to measure the indentation stiffness of an epitaxial graphene film supported by a SiC substrate. This methodology, named Å-indentation [2], is a further development of modulated nanoindentation (MoNI), a method previously developed by the PI [3, 4]. While several AFM methods exist to obtain high-resolution imaging and mechanical measurements, they are mostly limited to soft materials and measurements of stiffness values below 100 GPa. On the other hand, a method allowing nanoscale imaging *in-situ* with nanoindentation for supported ultra-thin films having an elastic modulus of up to 1 TPa remain a challenge. During conventional nanoindentation measurements, the indentation depths are usually larger than 1 nm, which hinders the ability to study ultra-thin films (< 1, 10 nm) and 2D materials on rigid substrates, such as Si or SiC. Now, **by using diamond tips, extremely small amplitude oscillations (<< 1 Å) at high frequency, stiff cantilevers, and by acquiring the indentation curves in the unloading regime within 10s, the PI's group has shown how modulated Å-indentation enables non-destructive measurements of the contact stiffness and indentation modulus of ultra-thin (down to < 1 nm) ultra-stiff (up to 1 TPa) films, including CVD diamond films (~ 1 TPa stiffness), nanofilaments of ultra-stiff Q-Carbon** (Fig. 3) [5], **as well as the transverse modulus of 2D**

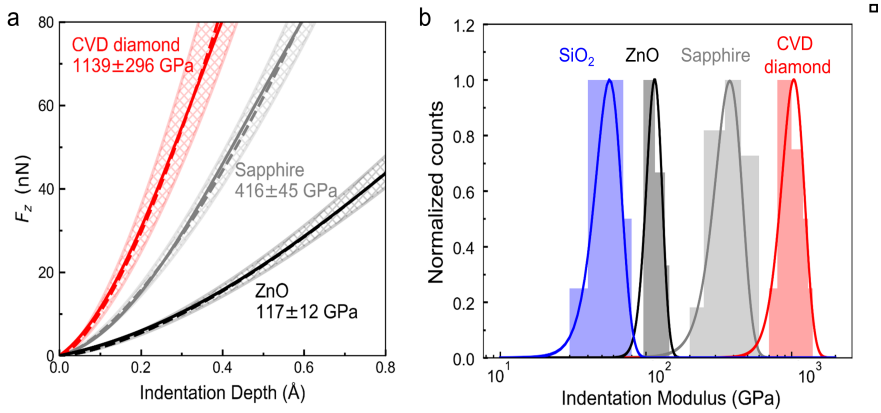

Fig. 2. (a) Experimental ÅI curves for ZnO (black solid line), sapphire (gray solid line), and CVD diamond (red solid line). The shaded areas correspond to one standard deviation from the mean. (b) Normalized distributions of indentation moduli for ZnO (115 ± 14 GPa), Sapphire (387 ± 81 GPa), CVD diamond (1005 ± 188 GPa) and SiO_2 (56 ± 11 GPa). Data are obtained by aggregate data for 15-30 experiments each.

materials [2] (Fig. 2 and 3). The analysis demonstrated that in presence of a good laboratory noise floor, the signal to noise ratio of ÅI implemented with an atomic force microscope and stiff cantilevers (diamond coated tips, 80 N/m) is such that a dynamic range of 80 dB — achievable with commercial Lock-in amplifiers — is sufficient to observe superior indentation curves having **indentation depths as small as 0.3 Å, and resolution in indentation < 0.05 Å, and in normal load < 0.5 nN**.

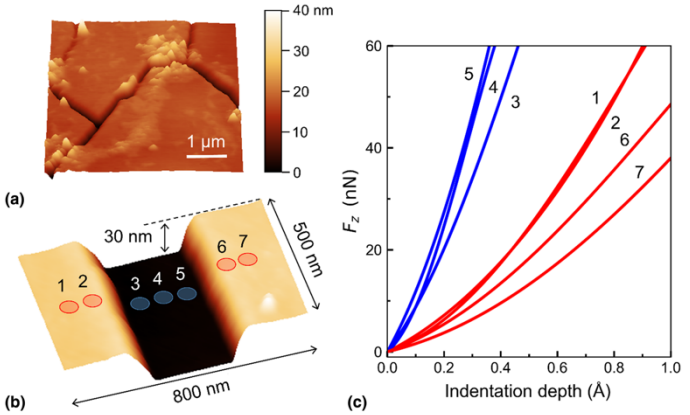

Figure 3. ÅI indentation of Q-carbon filaments. (a) AFM topography of Q-carbon filaments formed in amorphous carbon films. (b) AFM topography of a filament cross-section; markers indicate positions across the filament where indentation measurements are conducted. (c) ÅI curves measured on a Q-carbon filament and aC film. Blue and red lines are measurements performed on the Q-carbon filament and the surrounding aC film, respectively. Numbers refer to positions identified in (b).

An important step in the PI's previous research was the ability to identify the number of layers in the continuous films of epitaxial graphene on SiC, since the films contain a mixture of number of layer. Unfortunately, topographical images alone cannot identify the number of layers because of the complex morphology of the underneath SiC substrate. Furthermore, **it was crucial to be able to perform ÅI measurements in precise locations on the epitaxial graphene films with well know layers number**. Therefore, the PI **employed a fast and robust machine learning method, namely, a spectral clustering technique** [6, 7], to identify the number of layers in the different domains of a continuous epitaxial graphene film, and their spatial distribution. In particular, by means of atomic force microscopy the PI and collaborators were able to correlate the number of layers in epitaxial graphene on SiC and exfoliated graphene on SiO_2 with the frictional properties, indentation elasticity, and formation of ultra-stiff diamene layers (see Fig. 4) [7]. Through this

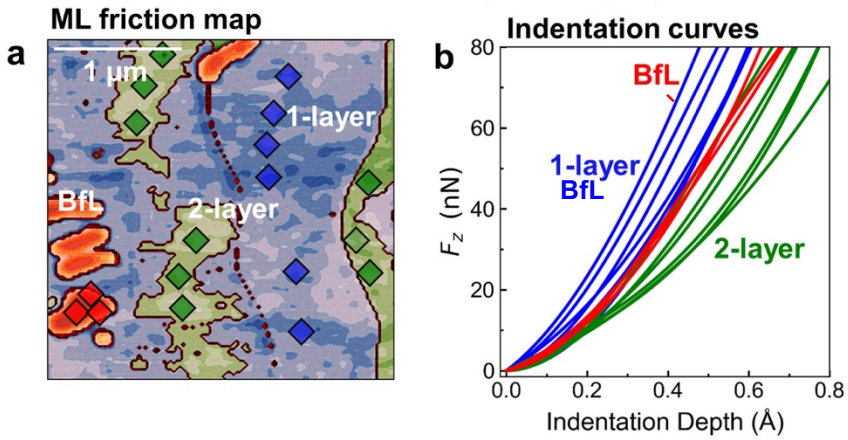

Fig. 4. Machine Learining (ML) and Å-indentation of few-layer epitaxial graphene. (a) ML analysis of an experimental friction map of epitaxial graphene surface. Markers indicate the positions where Å-indentation experiments are conducted. (b) Experimental indentation curves obtained in the positions indicated in (a) for the 1-layer +BfL (blue), 2-layer +BfL (green), and BfL (red) domains identified in the scan (a).

analysis, the PI and her group univocally demonstrated [7] that the formation of ultra-stiff diamene is obtained only in 1-layer plus buffer layer epitaxial graphene on SiC and that either the buffer layer alone, or thicker epitaxial graphene (2-layer plus buffer or more), as well as **exfoliated graphene films on SiO_2 for any number of layers do not exhibit the formation of this ultra-stiff phase in this range of pressures (up to 10 GPa)**.

Future Plans

The future research plan is focused at developing the basic knowledge and experimental tools for understanding pressure and strain induced phase transitions in 2D materials. In particular, we plan to investigate how structure, stacking, substrate interaction, defects, and number of layers impact the mechanical properties of phase changing 2D materials, and the phase transitions' diagrams.

References

[1] Y. Gao, T.F. Cao, F. Cellini, C. Berger, W.A. de Heer, E. Tosatti, E. Riedo, A. Bongiorno, Ultrahard carbon film from epitaxial two-layer graphene, Nature Nanotechnology, 13 (2018) 133-138.
[2] F. Cellini, Y. Gao, E. Riedo, Å-Indentation for non-destructive elastic moduli measurements of supported ultra-hard ultra-thin films and nanostructures, Scientific Reports, (2019), doi.org/10.1038/s41598-019-40636-0
[3] M. Lucas, W. Mai, R. Yang, Z.L. Wang, E. Riedo, Aspect Ratio Dependence of the Elastic Properties of ZnO Nanobelts, Nano Letters, 7 (2007) 1314-1317.
[4] 4. Y. Gao, S. Zhou, S. Kim, H.-C. Chiu, D. Nélias, C. Berger, W. de Heer, L. Polloni, R. Sordan, A. Bongiorno and E. Riedo, "Elastic coupling between layers in two-dimensional materials", Nature Materials 14, 714–721 (2015)
[5] J. Narayan, S. Gupta, A. Bhaumik, R. Sachan, F. Cellini, E. Riedo, Q-carbon harder than diamond, MRS Communications, 8 (2018) 428-436.
[6] U. von Luxburg, A tutorial on spectral clustering, Stat Comput, 17 (2007) 395-416.
[7] F. Cellini, F. Lavini, C. Berger, W.d. Heer, E. Riedo, Layer dependence of graphene-diamene phase transition in epitaxial and exfoliated few-layer graphene using machine learning, 2D Materials, (2019) doi.org/10.1088/2053-1583/ab1b9f.

Publications (2018-2019)
*** indicates Riedo contact author**

1. F. Cellini, Y. Gao, E. Riedo*, Å-Indentation for non-destructive elastic moduli measurements of supported ultra-hard ultra-thin films and nanostructures, **Scientific Reports,** (2019), doi.org/10.1038/s41598-019-40636-0
2. F. Cellini, F. Lavini, C. Berger, W.d. Heer, E. Riedo*, Layer dependence of graphene-diamene phase transition in epitaxial and exfoliated few-layer graphene using machine learning, **2D Materials**, (2019) doi.org/10.1088/2053-1583/ab1b9f.
3. Xiaorui Zheng, Annalisa Calò, Edoardo Albisetti, Xiangyu Liu, Abdullah Sanad M. Alharbi, Ghidewon Arefe, Xiaochi Liu, Martin Spieser, Won Jong Yoo, Takashi Taniguchi, Kenji Watanabe, Carmela Aruta, Alberto Ciarrocchi, Andras Kis, Brian S. Lee, Michal Lipson, James Hone, Davood Shahrjerdi, Elisa Riedo* "Patterning metal contacts on monolayer MoS_2 with vanishing Schottky barrier using thermal nanolithography", **Nature Electronics** (2019) 17–25 (2019) https://doi.org/10.1038/s41928-018-0191-0.
4. Filippo Cellini, Francesco Lavini, Tengfei Cao, Walt de Heer, Claire Berger, Angelo Bongiorno, Elisa Riedo*, "Epitaxial two-layer graphene under pressure: Diamene stiffer than Diamond" **FlatChem**, 10 8-13 (2018) doi.org/10.1016/j.flatc.2018.08.001
5. Y. Gao, T. Cao, F. Cellini, C. Berger, W. Heer, E. Tosatti, E. Riedo*, A. Bongiorno "Ultra-hard carbon film from epitaxial two-layer graphene" **Nature Nanotechnology** 13, 133–138 (2018), doi:10.1038/s41565-017-0023-9 (*Highlighted in several media and full article in Newsweek*)
6. Francesco Lavini, Annalisa Calò, Yang Gao, Edoardo Albisetti, Tai-De Li, Tengfei Cao, Guoqing Li, Linyou Cao, Carmela Aruta and Elisa Riedo* "Friction and work function oscillatory behavior for an even and odd number of layers in polycrystalline MoS_2" **Nanoscale** 10, 8304-8312 (2018), doi: 10.1039/C8NR00238J
7. J. Narayan, S. Gupta, A. Bhaumik, R. Sachan, F. Cellini, E. Riedo, "Q-carbon harder than diamond", **MRS Communications**, 1-9 (2018), https://doi.org/10.1557/mrc.2018.35
8. Edoardo Albisetti, Annalisa Calò, Martin Spieser, Armin W. Knoll, Elisa Riedo, Daniela Petti, "Stabilization and control of topological magnetic solitons via nanoscale patterning of the exchange bias", **Applied Physics Letters**, 113 (16), 162401 (2018) (Cover article) doi.org/10.1063/1.5047222
9. Edoardo Albisetti, Daniela Petti, Giacomo Sala, Raffaele Silvani, Silvia Tacchi, Simone Finizio, Sebastian Wintz, Annalisa Calò, Xiaorui Zheng, Jörg Raabe, Elisa Riedo, and Riccardo Bertacco, "Nanoscale spin-wave circuits based on engineered reconfigurable spin-textures", Nature **Communications Physics**, 1, 56 (2018) https://doi.org/10.1038/s42005-018-0056-x
10. E. Albisetti, D. Petti, Annalisa Calo, Xiaorui Zheng, R. Bertacco, E. Riedo*, "Thermal scanning probe lithography: from spintronics to biomedical applications", **Proc. SPIE** 10584, **Novel Patterning Technologies** 2018, 1058405 (2018); doi: 10.1117/12.2301253; https://doi.org/10.1117/12.2301253

Damage-Tolerant in Structural Materials

Robert O. Ritchie, Mark Asta and Andrew M. Minor

Lawrence Berkeley National Laboratory

Program Scope

The attainment of strength and toughness is a vital requirement for structural materials, although these properties are often mutually exclusive. Indeed, designing strong and tough materials has traditionally been a compromise between hardness *vs*. ductility. Here we examine strategies to solve this "conflict" in metallic alloys by focusing on the interplay between mechanisms that contribute to toughness, *i.e*., plasticity and crack-tip shielding, noting that these phenomena originate at very different length-scales. Our objective is to seek a fundamental understanding, at atomistic to macroscopic length-scales, of the scientific origins of damage-tolerance, specifically in multi-element metallic alloys. Our focus is currently on single-phase high-entropy alloys and metallic glasses, which can display exceptional damage tolerance, due to novel mechanisms that arise from their disordered structures. For metallic glasses, we have focused, on the existence of short and medium range ordering within the amorphous state, using numerical simulation and most recently state-of-the-art transmission electron microscopy, to discern its role in triggering shear-band formation, which we believe represents the fundamental origin of plasticity and toughness in these alloys. With respect to the damage-tolerance in face-centered cubic CrCoNi-based high-entropy alloys, we have coupled fracture mechanics measurements with *in situ* SEM and TEM testing to discern the synergy of dislocation and twinning mechanisms responsible for their properties. We are now also focusing on the role of short-range order in the CrCoNi-based alloys as well in body-centered cubic refractory high-entropy alloys which are intended for ultrahigh-temperature applications but are often plagued by severe brittleness. Our ultimate aim is to uncover the relationships between atomic-scale phenomena and the macroscopic mechanical behavior.

Recent Progress

Our current objectives are focused on the role of local chemical ordering in influencing the mechanical properties of bulk-metallic glasses (BMGs) and high-entropy alloys (HEAs).

Bulk-metallic glasses: An unlikely example of defeating the "strength *vs*. toughness conflict"[1] is BMGs. Being amorphous, BMGs display high strengths that can exceed ~1-2 GPa; they deform via shear bands, which can cause brittleness as a single shear band can lead to tensile failures at vanishingly small strains. However, multiple shear-band formation provides the basis for plasticity in these glassy alloys, and hence provides a means to developing toughness.[2] It is thus the key to making BMGs into structural materials, instead of simply "academic curiosities". Accordingly, we have sought the atomistic origins of such multiple shear banding in BMGs, initially using molecular dynamics (MD) simulations. On the premise that the glassy state in BMGs is not purely amorphous but can contain local short- to medium-range order (SRO/MRO) in the form of motifs of atoms with local icosahedral symmetry, certain motifs with less dense packing and less five-fold symmetry, termed geometrically unstable motifs or GUMs, may trigger the onset of shear banding due to their instability.[3,4] Indeed, the MD simulations show that clusters of GUMs initiate shear localization in BMGs; the further propagation of such shear bands is demonstrated to be accompanied by the breakdown of full icosahedral clusters as a structural signature.

Although the MD modeling is compelling,[3-6] *e.g.*, via simulations in $Cu_{46}Zr_{46}A_{l8}$ indicating that shear bands formed in the vicinity of a notch are coincident with the spatial distribution of local icosahedral order (Fig. 1),[7] experimental verification, that such local regions of GUMS can trigger shear banding to provide the fundamental essence of damage-tolerance in BMGs, is still lacking.

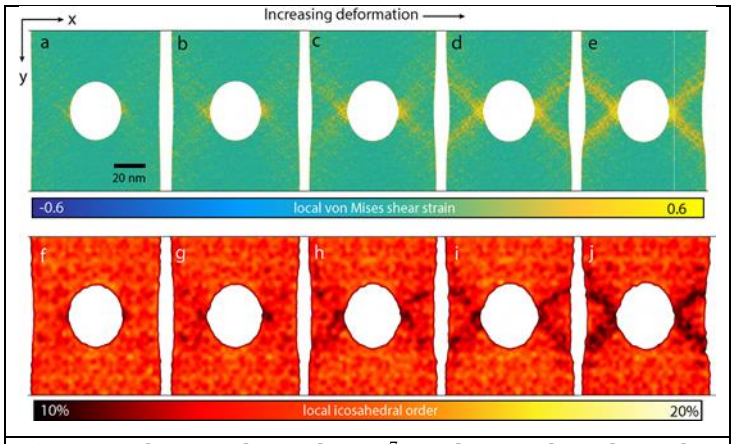

Fig. 1. Theoretical simulations[7] to discern the relationship between local icosahedral order and shear-band formation. Five frames of MD-simulated $Cu_{46}Zr_{46}A_{l8}$ at strains of 4, 5, 6, 7 and 8% respectively, under uniaxial tension. Color maps of (a-e) local Mises shear strain and (f-j) spatial distribution of local icosahedral order in coarse-graining scale, for such five frames.

As there has yet to be a direct observation of the initiation and propagation of individual defects in BMGs during deformation at the nanoscale, we have used *in situ* TEM nanobeam electron diffraction, with ultra-fast electron detectors, coupled with large-scale MD simulations (Fig. 1), to directly observe changes to the local atomic SRO/MRO during shear band formation in $Cu_{46}Zr_{46}Al_8$.[7] With a FIBed 80-90-nm thick sample containing a hole, pulled in tension in the TEAM 1 TEM, we observed a spatially resolved reduction in SRO/MRO prior to shear banding due to increased strain, which agrees with the MD simulations in Fig. 1, where a similar reduction in local order caused by shear transformation zone activation is seen.[7] We believe that this represents the first direct experimental evidence of the involvement of local ordering and plasticity in amorphous solids, an observation that serves as a direct link between the atomistic MD simulation and bulk mechanical properties in BMGs.

High Entropy Alloys: HEAs are a class of metallic alloys with multiple elements in nominally equal molar ratios that crystallize as concentrated solid solutions. Working on single-phase *fcc* CrCoNi-based alloys, in association with ORNL,[8-12] we found exceptional damage tolerance, with strengths >1 GPa and K_{JIc} toughness >200 MPa$\sqrt{m}$, properties which improve at low temperatures and approach the best on record. *In situ* straining experiments in an aberration-corrected TEM revealed a synergy of nanoscale deformation mechanisms,[10-12] resulting from their high lattice friction, yet low stacking fault energies (SFEs). In the stronger CrCoNi, a hierarchical twin network was formed with strength generated by dislocation arrest *at* twin and grain boundaries yet ductility created by rapid partial dislocation motion *along* boundaries.[11] Further *in situ* mechanistic studies, using cryo-TEM, revealed massive cross-slip at 93K, and a suite of plasticity mechanisms including the glide of partials/full dislocations, twinning, and multiple slip activated by dislocation/grain-boundary interactions (Fig. 2).[12] In such multi-principal element HEAs, SRO is to be expected, yet to date there is little evidence of this. We performed first-principles DFT-based Monte Carlo

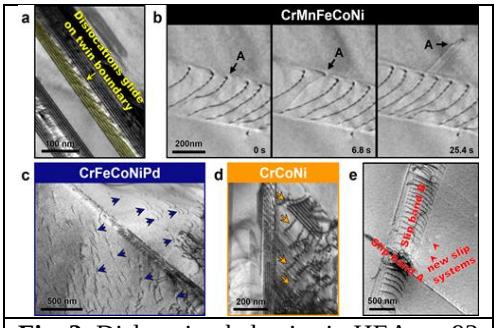

Fig. 2. Dislocation behavior in HEAs at 93 K. (a) Partials moving on twin boundaries in CrFeCoNiPd. (b) TEM images of cross-slip in CrMnFeCoNi. (c-d) Extensive cross-slip in CrFeCoNiPd and CrCoNi with individual cross-slip events marked by blue and orange arrows. (e) Interaction between different slip systems in CrFeCoNiPd.[12]

simulations on equimolar CrCoNi with several hundred atoms[13] and predicted that SRO would have a marked influence on SFEs and the relative energies of the *fcc* and *hcp* phases which governs TRIP and TWIP effects, parameters that are known to markedly affect the strength and deformation of CrCoNi-based HEAs. However, the role of SRO in HEAs remains an open issue because it has yet to be convincingly confirmed experimentally. In view of the fundamental importance of this issue, and its potential explanation of the truly exceptional mechanical properties of these alloys, this topic represents a major thrust of our proposed research for the next three years. It further presents the fascinating notion of being able to tune atomic order to achieve enhanced macroscale mechanical properties in these alloys.

Future Plans

As noted above, our primary objective is to use experiment, simulation and theory to identify the scientific principles underlying the attainment of damage tolerance in multiple-element alloys, with emphasis on the role of atomistic SRO in influencing their mechanical performance.

Metallic Glasses: Our hypotheses for generating damage-tolerance in metallic glasses has been to induce ductility through multiple shear banding; in light of this, atomistic simulations[3,4,14] suggest that such shear bands are induced by more loosely packed regions of SFO displaying lower degrees of icosahedral symmetry (GUMS). Indeed, our DFT and large-scale MD simulations have indicated that in various Cu_xZr_y glasses, 82% of the atoms undergoing shear transformations are actually GUMs; indeed, the instability of GUMS can specifically trigger shear transformations.

As there is little experimental evidence for this hypothesis, our intent is to provide such evidence, not only by quantifying the SRO for essentially macroscopic samples, but also to perform experiments in the TEM that explicitly link shear-band formation, and hence the origin of plasticity in BMGs, *directly* to regions of unstable short-range order (GUMs). Our goal is to establish quantitative structure-property relationships between GUMs and mechanical behavior, which can lead to an understanding of the fundamental origins of damage-tolerance in metallic glasses. To enable such direct experimental validation of the existence and role of structural SRO/MRO. To characterize these states in BMGs, we will induce GUMs locally through radiation in a He-ion microscope, and on loading the sample in the TEM will then employ a 4D-STEM technique[7,15] coupled with fast direct electron detectors (1,600 frames/sec) with an EELS spectrometer (Fig. 3) to generate a series of 2D diffraction patterns at each position, in order to relate the creation of a shear band to a local region of GUMs. We hope by these experiments to provide a fundamental description of the origin of the exceptional mechanical properties shown by certain metallic glasses and further present a means to enhance their damage-tolerance through the tuning of local atomic order.

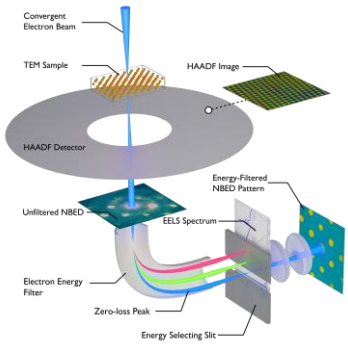

Fig. 3. Schematic illustration of the new energy-filtered 4D-STEM technique with an electron energy loss spectrometer to be used to characterize short- to medium-range order in BMGs.

***High-Entropy Alloys*:** Our main effort though will be focused on the topic of HEAs, specifically on two classes of alloys: the *fcc* CrCoNi-based alloys, which we have shown to have exceptional damage-tolerance at cryogenic temperatures,[8-12], and the far-less studied *bcc* refractory high-entropy alloys (RHEAs), which are intended for high-temperature use.[16,17] Our approach will be to continue to seek the fundamental, multiple-scale, origins of the damage-tolerance in these alloys

by: (i) conducting nonlinear-elastic fracture mechanics and R-curve methodologies to evaluate their fracture toughness as a function of temperature, (ii) characterizing the salient deformation mechanisms and fracture modes using *in situ* TEM and SEM experiments, (iii) continuing our Monte Carlo/MD simulations on CrCoNi alloys, and starting such simulations on RHEAs, to examine the role of local chemical SRO, specifically pertaining to its role in affecting dislocation mobility, which would radically influence mechanical behavior, and the interstitial formation energies, which would influence irradiation damage resistance, and (iv) using advanced TEM techniques to find direct experimental evidence of local chemical ordering or larger-scale clustering in these multiple principal element alloys, and to confirm our theoretical simulations in discerning how such local order affects mechanical behavior.

With respect to experimental determination of the role of SRO in CrCoNi alloys, we are using TEM imaging, with an in-column energy filter to remove inelastically scattered electrons, because ideally chemical SRO should exhibit a superlattice-like diffraction contrast. We have commenced these studies in CrCoNi; our preliminary results are shown Fig. 4 where indications of superlattice streaking are apparent in the annealed structures. We believe that this is an indication that the degree of SRO is increasing with annealing temperature and time, which corroborates our DFT-based Monte Carlo predictions.[13] Such experimental studies to verify the existence of SRO in HEAs together with identification of its effects on mechanical properties will be central feature of our research in this program over the next two years, from the perspective of discerning the fundamental atomistic origins that govern the mechanical properties, specifically the strength, tensile ductility and fracture toughness, of advanced multiple-element metallic alloys.

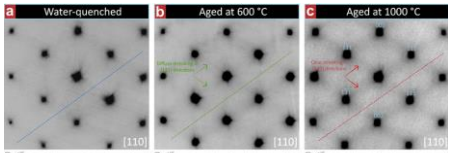

Fig. 4. Energy-filtered TEM studies of superlattice reflections to detect SRO in CrCoNi alloy, in the as-quenched (random), and aged (increased local order) conditions. Images show energy-filtered diffraction patterns, on the [110] zone. The quenched sample shows a regular *fcc* diffraction pattern; after annealing, extra superlattice streakings along {111} are visible.

References

1. Ritchie RO. *Nature Mater* 2101;**10**:817.
2. Demetriou MD, Launey ME, Garret G, Schramm, JP, *et al*. *Nature Mater* 2011;**10**;123.
3. Ding J, Ma E, Asta M, Ritchie RO. *Science Rep* 2015;**5**:17429.
4. Ding J, Asta M, Ritchie RO. *Phys Rev B* 2016;**93**:140204(R)
5. Hu YC, Guan PF, Li MZ, Liu CT, Bai HY, Wang WH. *Phys Rev B* 2016;**6793**:214202.
6. Zhao P, Li J, Hwang J, Wang Y. *Acta Mater* 2017;**134**:104.
7. Pekin, TC, Ding J, Gammer C, Ozdol VB, Ophus C, *et al. Nature Comm* 2019;**10**:2445.
8. Gludovatz B, Hohenwarter A, Cartoor D, Chang EH, *et al*. *Science* 2014;**345**:1153.
9. Gludovatz B, Hohenwarter A, Thurston KVS, Bei H, *et al*. *Nature Commun* 2016;**7**:10602.
10. Zhang ZJ, Mao MM, Wang J, Tian H, Gludovatz B, *et al*. *Nature Commun* 2015;**6**:10143.
11. Zhang Z, Sheng H, Wang Z, Gludovatz B, Zhang Z, *et al*. *Nature Commun* 2017;**8**,14390.
12. Ding Q, Fu X, Chen D, Bei H, Gludovatz B, Li J, *et al. Materials Today*, 2019;**25**:21.
13. Ding J, Yu Q, Asta M, Ritchie RO, *PNAS* 2018;**115**:8919.
14. Ding J, Patinet S, Falk ML, Cheng Y, Ma E, *PNAS* 2014;**111**:14052.
15. Pekin TC, Gammer C, Ciston J, Ophus C, Minor AM. *Scripta Mater* 2018;**146**:87.
16. Senkov ON, Semiatin SL. *J Alloys Cmpd* 2015;**649**:1110.
17. Dirras G, Lilensten L, Djemia P, Laurent-Brocq M, *et al*. *Mater Sci Eng A* 2016;**654**:30.

Publications

1. J. Ding, M. Asta, R.O. Ritchie, On the question of fractal packing structure in metallic glasses, *Proceedings of the National Academy of Sciences*, vol. 114 (32), Aug, 2017, pp. 8458-8463; doi.org/10.1073/pnas.1705723114.
2. K.V.S. Thurston, B. Gludovatz, A. Hohenwarter, G. Laplanche, E.P. George, R.O. Ritchie, Effect of temperature on the fatigue-crack growth behavior of the high-entropy Alloy CrMnFeCoNi, *Intermetallics*, vol. 88, Sept. 2017, pp. 65-72; doi.org/ 10.1016/j.intermet.2017.05.009.
3. N. Wang, J. Ding, F. Yan, M. Asta, R.O. Ritchie, L. Li, Spatial correlation of elastic heterogeneity tunes the deformation behavior of metallic glasses, *npj Computational Materials*, vol. 4, April 6, 2018, p. 19; doi.org /10.1038/s41524-018-0077-8.
4. T.C. Pekin, C. Gammer, J. Ciston, C. Ophus, A.M. Minor, *In situ* nanobeam electron diffraction strain mapping of planar slip in stainless steel, *Scripta Materialia*, vol. 146, 2018, pp. 87-90; doi.org/10.1016/j.scriptamat.2017.11.005.
5. C. Gammer, C. Ophus, T.C. Pekin, J. Eckert, A.M. Minor, Local nanoscale strain mapping of a metallic glass during *in situ* straining, *Applied Physics Letters*, vol. 112, 2018, pp. 171905; doi.org/10.1063/1.5025686.
6. R.P. Wilkerson, B. Gludovatz, J. Watts, A.P. Tomsia, G.E. Hilmas, R.O. Ritchie, A study of size effects in bioinspired, "nacre-like", metal-compliant-phase (nickel-alumina) coextruded ceramics, *Acta Materialia*, vol. 148, April 15, 2018, pp. 147-155; doi.org/ 10.1016/j.actamat.2018.01.046.
7. B. Wang, L. Luo, E. Guo, Y. Su, M. Wang, R.O. Ritchie, F. Y. Dong, L. Wang, J. J. Guo, H. Fu, Nanometer-scale gradient atomic packing structure surrounding soft spots in metallic glasses, *npj Computational Materials*, vol. 4, July 30, 2018, p. 41; doi.org/10.1038/s41524-018-0097-4.
8. J. Ding, Q. Yu, M. Asta, R.O. Ritchie, Tunable stacking fault energies by tailoring local chemical order in CrCoNi medium-entropy alloys, *Proceedings of the National Academy of Sciences*, vol. 115 (36), Sept. 4, 2018, pp. 8919-8924; doi.org/10.1073/pnas.1808660115.
9. J. Ding, M. Asta, R.O. Ritchie, Melts of CrCoNi-based high-entropy alloys: Atomic diffusion and electronic/atomic structure from *ab initio* simulation, *Applied Physics Letters*, vol. 113 (11), Sept. 10, 2018, p. 111902; doi.org/10.1063/1.5045216.
10. R.P. Wilkerson, B. Gludovatz, J. Ell, J. Watts, G.E. Hilmas, R.O. Ritchie, High-temperature damage-tolerance of coextruded, bioinspired ("nacre-like"), alumina/nickel compliant-phase ceramics, *Scripta Materialia*, vol. 158, Jan. 2019, pp. 110-115; doi.org/10.1016/j.scriptamat.2018.08.046.
11. A. Wat, J.I. Lee, C.W. Ryu, B. Gludovatz, J.Y. Kim, A.P. Tomsia, T. Ishikawa, J. Schmitz, A. Meyer, M. Alfreider, D. Kiener, E.S. Park, R.O. Ritchie, Bioinspired "nacre-like" alumina/bulk-metallic glass ceramics, *Nature Communications*, vol. 10, Feb. 2019, p. 961; doi.org/10.1038/s41467-019-08753-6.

12. Z. Li, S. Zhao, R.O. Ritchie, M.A. Meyers, Mechanical properties of high-entropy alloys with emphasis on face-centered cubic alloys, *Progress in Materials Science*, vol. 102, May 2019, pp. 296-345; doi.org/10.1016/j.pmatsci.2018.12.003.

13. Q. Ding, X. Fu, D. Chen, H. Bei, B. Gludovatz, J. Li, Z. Zhang, E.P. George, Q. Yu, T. Zhu, R.O. Ritchie, Real-time nanoscale observation of deformation mechanisms in CrCoNi-based medium/high-entropy alloys at cryogenic temperatures, *Materials Today*, vol. 25, May 2019, pp. 21-27; doi.org/10.1016/j.mattod.2019.03.001.

14. T.C. Pekin, J. Ding, C. Gammer, V.B. Ozdol, C. Ophus, M. Asta, R.O. Ritchie, A.M. Minor, Direct measurement of nanostructural change during *in situ* deformation of a bulk metallic glass, *Nature Communications*, vol. 10, June 4, 2019, p. 2445; doi.org/10.1038/s41467-019-10416-5.

15. L.S. Luo, B.B. Wang, F.Y. Dong, Y.Q. Su, E.Y. Guo, M.Y. Wang, L. Wang, J. X. Yu, R.O. Ritchie, J.J. Guo, H.Z. Fu, Structural origins for the generation of strength, ductility and toughness in bulk-metallic glasses using hydrogen microalloying, *Acta Materialia*, vol. 171, June 1, 2019, pp. 216-230; doi.org/10.1016/j.actamat.2019.04.022.

16. K.V.S. Thurston, B. Gludovatz, Q. Yu, G. Laplanche, E.P. George, R.O. Ritchie, Temperature and load-ratio dependent fatigue-crack growth in the CrMnFeCoNi high-entropy alloy, *Journal of Alloys and Compounds*, vol. 794, July 25, 2019, pp. 523-533; doi.org/10.1016/j.jallcom.2019.04.234.

17. K.V.S. Thurston, A. Hohenwarter, G. Laplanche, E.P. George, B. Gludovatz, R.O. Ritchie, On the onset of deformation twinning in the CrMnFeCoNi high-entropy alloy using a novel tensile Specimen geometry, *Intermetallics*, vol. 110, July 2019, p. 106469; doi.org/10.1016/j.intermet.2019.04012.

18. E.P. George, D. Raabe, R.O. Ritchie, High-entropy alloys, *Nature Reviews Materials*, 2019; doi.org/10.1038/s41578-019-0121-4.

Probing Fundamental Mechanisms of Plastic Deformation with High Energy X-rays

Prof. Anthony D. Rollett (Co-Principal Investigator) Department of Materials Science and Engineering, Carnegie Mellon University, rollett@andrew.cmu.edu
Prof. Robert M. Suter (Co-Principal Investigator) Department of Physics, Carnegie Mellon University, suter@andrew.cmu.edu
Matthew Wilkin (Graduate Student) Department of Materials Science and Engineering, Carnegie Mellon University, mjwilkin@andrew.cmu.edu

Project Scope

The goal of this project is to observe microplasticity events in 3-D using a combination of high energy X-ray techniques, including Bragg Coherent Diffractive Imaging (BCDI), High Energy Diffractive Imaging (HEDM), and Dark-Field X-ray Microscopy. These methods will allow us to investigate phenomena such as dislocation runback, the loss of elastic moduli during loading, intergranular deformation flow, and the effect of heterogeneous stress fields within grains on critical resolved shear stress (CRSS). If successful, our efforts will play a crucial role in linking nanoscale defect dynamics with mesoscale responses.

Technical Progress

In the past year, we contributed to two beam runs at the Advanced Photon Source (APS) to further the efforts proposed. The current thrust of the project is on Bragg Coherent Diffraction Imaging (BCDI), as this method is currently more readily available to us than Dark Field Microscopy. In BCDI, a single Bragg peak rocked over a small angular interval can be reconstructed to give atomic displacement fields at the nano scale in an individual grain, making it able image individual defects in 3-D [1]. An example of a reconstructed grain can be seen in Figure 1, with 'phase' corresponding to atomic displacement. We have begun pursuing High Energy BCDI at the 1-ID beamline at APS, with substantial involvement by Jun Park (1-ID staff). 1-ID uses X-rays in the range of 40-100 keV, with 52 keV for the current BCDI experiments, which gives it the unique capability among BCDI capable beamlines of imaging grains in bulk metals, rather than thin films. Additionally, this beamline has accumulated extensive experience with High Energy Diffraction Microscopy (HEDM), which allows us to quickly locate specific grains of interest within our sample.

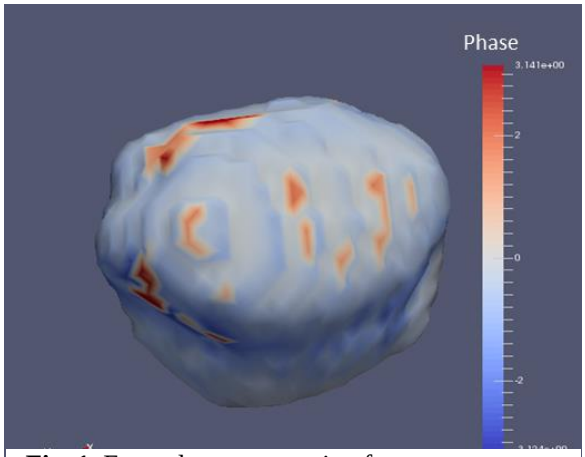

Fig. 1. Example reconstruction from a scan over a single Bragg peak of a gold grain colored by the value of the phase.

This Spring, we wanted to determine whether High Energy BCDI at 1-ID was capable of imaging more complex defects, so we ran HEDM and BCDI on a depleted UO_2 sample, hoping to capture irradiation damage. The results of these runs have yet to be determined as both the HEDM (near-field and far-field) and BCDI datasets are still being reconstructed. As mentioned previously, the experimental setup at 1-ID allows us to collect several peaks from the same grain. This is significant because BCDI measurements from a single peak only provide a displacement field projected along the scattering vector direction for the Bragg peak. To reconstruct a fully resolved strain field, peaks from

three non-colinear directions are needed [2]. Reconstructing the full strain tensor makes BCDI a truly three-dimensional characterization tool and will be invaluable in our future studies of plasticity events on the mesoscale. At our beam time at 1-ID in April 2019, we measured a nanocrystalline Au sample (in addition to the UO_2). Thanks to being able to reconstruct at least the larger grains via far field HEDM we were able to find a pair of grains in twin relationship to each other. We measured 7 Bragg peaks from the parent grain and 5 peaks from the twin—an embarrassment of riches in terms of data, given that only 3 peaks are needed for a fully resolved strain field. With this data, we are attempting a simultaneous reconstruction of all 7 peaks in the parent and another for all peaks in the twin. We hypothesize that a simultaneous reconstruction, rather than independent reconstructions for each peak, will improve strain field convergence, giving us a more accurate reconstruction and paving the way for future experiments which will allow us to image defects more precisely in 3-D. The twin relationship also means that there is almost certainly a flat twin boundary between the two grains (or twin boundaries between multiple lamellar grains) which provides useful shape information for checking the reconstructions.

Future Work

We will continue to develop the aforementioned simultaneous reconstruction code to resolve full the full elastic strain tensor in the grain. This involves a close collaboration with Siddharth Maddali and Stephan Hruszkewycz (staff at ANL). Additionally, the challenges involved in reconstructing Bragg peaks from differently oriented planes will be relevant in our attempts to observe the interactions between neighboring grains in future experimental runs.

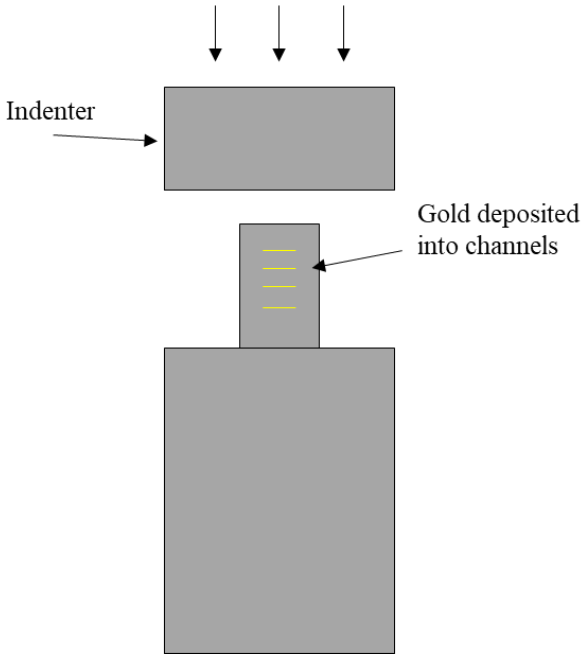

Fig. 2. Planned compression sample for future experiment at 1-ID. Pt will be deposited into channels about 300 nm wide in a column of aluminum alloy.

We will continue to reconstruct the BCDI and near-field HEDM data from the UO_2 sample. Although these grains are well below the spatial resolution of the technique, we hope to be able to provide a map of orientations and center-of-mass positions similar to what is normally obtained from far-field HEDM. These data will be examined to probe the ability to translate the hundred nanometer grains across the one-micron beam and to determine vertical positions from intensity curves. At the same time, this will test beam stability and mechanical motions. Note that, as discussed above, the far-field measurement can be used to determine orientations that are present, but the position resolution is too coarse by roughly two orders of magnitude.

We have begun preparations for another beam run at 1-ID in Fall 2019 to image grains under compression. We have made an Al-6061 compression sample with several trenches cut into it that are approximately 300 nm deep. Pt will be deposited into the channels and annealed, so that the grains will grow to the size of the channel width. The goal will be to compress the platinum by pushing on the top of the sample, as shown in Figure 2. We hypothesize that by indexing the peaks beforehand, we can pick out two neighboring grains and watch them interact during compression; this capability is a major goal of the project, would be a first in the field (as of now), and would help develop a more detailed understanding of how dislocations interact with grain boundaries. By pushing on the aluminum, instead of directly on the

platinum, we aim to control the deformation in the platinum with sufficient precision that we can induce controlled motion of dislocations (in the platinum). The aluminum, which is low-Z and therefore a weak scatterer compared to the Pt, acts in effect as a strain carrier for the material of interest.

In the broader scope of the program, we will collaborate with beam staff at the APS to develop and test the dark field imaging capability. This is a complementary technique to BCDI that uses compound refractive lenses (CRL) to project a diffracted beam onto a detector to image the defect structure in the material.

Relevance to MGI

Our work will further the dependability of predictive models by providing insight into plastic events on the mesoscale. Current continuum-level models are unable to predict plastic behavior at the grain scale and below, and this project will help to close this gap in our understanding by providing important information about stress heterogeneity within grains due to defects and its impact on macroscopic properties.

Broader Impact

Development of advanced imaging techniques serves to expand the scope of problems that user facilities such as the Advanced Photon Source can tackle. Although this effort is focused on imaging dislocations and their motion, there are other defect structures that may be accessible through one or both of the techniques described here.

Accelerating Materials Discovery and Development

By exploring the effects of phenomena such as dislocation dynamics in 3D, our work will illuminate blind spots in current predictive models and help future scientists to more accurately determine material properties from material structure.

Open Access and Data Sharing

In conformance with our Data Management Plan, once each data set has been analyzed and a paper published, the data will be made available on a publicly accessible website such as CMU's *kilthub* system.

References

[1]. Robinson, I., & Harder, R. (2009). Coherent X-ray diffraction imaging of strain at the nanoscale. *Nature materials*, *8*(4), 291.

[2]. Hofmann, F., Phillips, N. W., Das, S., Karamched, P., Hughes, G. M., Douglas, J., ... & Liu, W. (2019). Full, 3D-resolved lattice strain tensor measurements of specific crystallographic defects extracted from a bulk sample. *arXiv preprint arXiv:1903.04079*.

Doping Metallic Grain Boundaries to Control Atomic Structure and Damage Tolerance

Timothy J. Rupert - University of California, Irvine

Program Scope

Grain boundaries and other interfaces often act as nucleation sites for cracks and voids that lead to failure during plastic deformation of metallic materials. While it is known that interface character and structural state can greatly influence this damage nucleation process, the current level of understanding and control over such details is relatively limited. The objective of this research is to obtain fundamental knowledge about our ability to control grain boundary structure by locally and selectively adding other elements, with the idea of inducing planned grain boundary "phases" or ***complexions*** [1]. The effect of these complexions on both mechanical and radiation damage mechanisms is a major focus of this project, with the goal of improving the field's understanding of damage nucleation at interfaces and identifying materials design strategies for extremely tough and radiation-tolerant materials. This research uses a combination of computational, experimental, and characterization techniques to isolate and understand the importance of atomic-level grain boundary structure and interfacial chemistry.

Recent Progress

The project has been ongoing for four years, but this extended abstract touches on progress from the last two years only. We have broken down our recent progress into three distinct areas: (1) fundamental materials design for utilization of complexions, (2) the effect of complexions on important properties, and (3) the extension of the complexion concept to line defects. All three research areas contain complementary computational and experimental tasks.

Fundamental Materials Design

Our early work on complexions and mechanical behavior showed that disordered complexions, or amorphous intergranular films (AIFs), could serve as toughening features which improve both the ductility and strength of nanocrystalline Cu-Zr [2]. These structures allow for efficient dislocation absorption that delays crack nucleation and propagation at internal interfaces, with thicker films giving a more pronounced effect. First, we wanted to be able to find other binary metallic alloys which could sustain AIFs along their grain boundaries, leading us to develop simple materials selection rules that emphasized dopant segregation to grain boundaries and the creation of energetically favorable conditions for an amorphous phase. We found that the transition from ordered to disordered grain boundary complexions in polycrystalline binary metallic alloy can be controlled by an informed selection of enthalpy of segregation (ΔH^{seg}) and enthalpy of mixing (ΔH^{mix}). These rules were applied to all binary transition metal alloys, with our predictions confirmed in multiple Ni-rich alloys (Ni-Zr and Ni-W).

We next explored whether the addition of compositional complexity in the grain boundary region would be beneficial. For bulk metallic glasses, one generally needs three or more atomic elements

to be mixed together. First, we used atomistic modeling to test this theory. While our Monte Carlo/molecular dynamics simulations are limited by the limited availability of interatomic potentials for ternary alloys, we were able to study complementary co-segregation in a few model ternary systems and find that, with the right ratio of the different dopants at the grain boundaries, a ternary alloy can sustain a thicker AIF (Fig. 1(a)). We then turned to experiments to compare binary Cu-Zr with ternary Cu-Zr-Hf samples. All samples had the grain sizes, global compositions, and atomic size mismatches between solvent and solute atoms, making a very clean comparison with only the level of chemical complexity varying. Fig. 1(b) shows high resolution transmission electron microscopy (TEM) images of AIFs in these alloys, with compiled thickness data from >50 boundary films presented in Fig. 1(c). Even with the exact same total amount of dopant, the Cu-Zr-Hf specimen has notably thicker AIFs within the microstructure, especially for the thickest films in the distribution. While it is not required to form amorphous complexions, it is beneficial for the boundaries to be chemically complex. The choice of a better alloy means that one can either (1) sustain thicker amorphous complexions and therefore access improved properties or (2) create AIFs at lower processing temperatures.

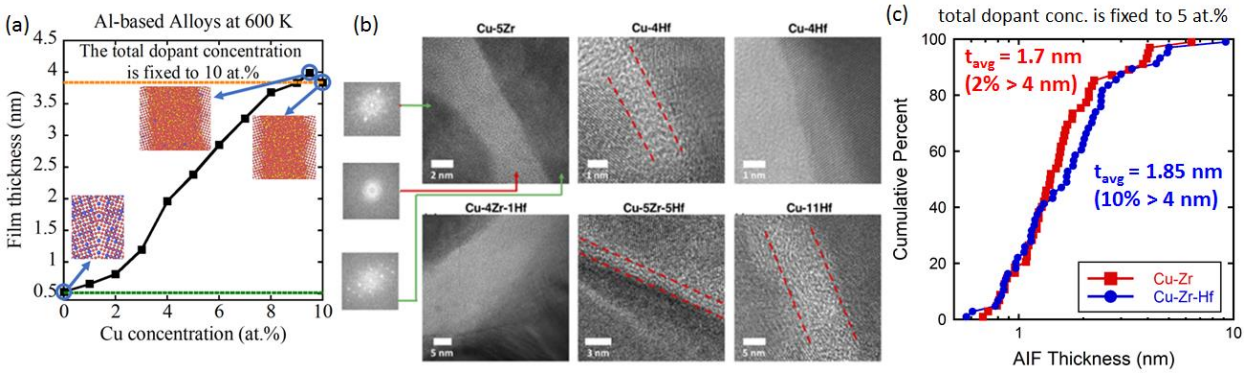

Figure 1. (a) Atomistic models of complexion formation in ternary alloys show that the correct dopant ratio can induce thicker films than binary mixtures. (b) High resolution TEM of AIFs can be used to collect (c) thickness distributions which confirm that ternary alloys are able to have thicker films since the boundary is more chemically complex.

Complexions and Important Properties

Our early work showed that ductility could be improved by the addition of AIFs to a microstructure, so we have moved to understand their effect on more complex properties such as fatigue failure and radiation damage. A Ph.D. student in my group was selected for an Office of Science Graduate Student Research (SCGSR) fellowship, which allowed her to spend 6 months at Sandia National Laboratories hosted by Dr. Brad Boyce and Dr. Khalid Hattar, who are both participants in the current MBRE program. First, we studied the fatigue failure process using in situ TEM experiments where sputtered thin films were heated on a chip and then either slowly cooled (ordered boundaries) or rapidly quenched (AIFs) to alter the complexion state, followed by fatigue deformation. We were specifically interested in understanding the dominant mechanisms associated with crack initiation and propagation in the two types of samples. The sample with ordered boundaries experienced grain growth near the crck and unsteady, accelerating crack growth. Alternatively, the sample with AIFs had a stable grain structure and experienced steady crack growth rates. In addition, the sample with AIFs had plastic events which were distributed

further away from the crack (Fig. 2(a) and (b)), which is much more beneficial than the localized failure experiences in the ordered grain boundary sample.

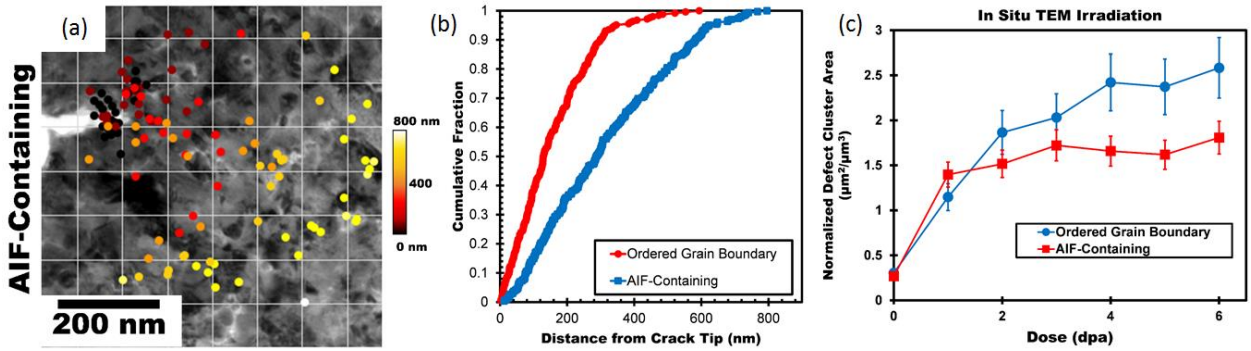

Figure 2. (a, b) Specimens with AIFs experience more distributed plasticity during fatigue as compared to samples with only ordered boundaries. (c) AIFs also lead to improved radiation resistance, as probed by in situ ion irradiation.

We were also able to explore the effect of complexion type on the radiation tolerance of nanocrystalline Cu-Zr. A combination of in situ TEM and ex situ Au ion irradiation were used to induce damage into ball milled materials. As a whole, we found that the sample with AIFs had much lower stored defect densities, with the data from the in situ testing shown in Fig. 2(c). This improved radiation tolerance was connected to the existence of (1) thicker grain boundaries and (2) additional free volume. Interesting corollaries associated with the stability of these amorphous complexions under radiation at elevated temperatures were found.

Extension of Complexion Concept to Dislocations

Grain boundary segregation generally occurs because interfaces have different local structure and stress state as compared to the crystal. Dislocations share these features, leading to the question of whether complexions can be stabilized at line defects as well. A very recent paper from the group of Prof. Dierk Raabe [3] motivated our work. These authors suggested that a local phase transition was found near dislocation in Fe-Mn alloys, arranged as arrays of nanoparticles. We have been using our atomistic modeling tools to (1) understand the details of this complexion transition with improved resolution and (2) explore whether it can be extended to dislocations in different face centered cubic (FCC) alloys. We first modeled segregation and possible complexions transitions along dislocations dipoles in Fe-Ni, as the phase diagram is very similar to Fe-Mn and a reliable interatomic potential is available. Fig. 3(a) shows a dislocation in pure and doped Fe, demonstrating segregation and the nucleation of a chemically ordered complexion. We found that the $L1_0$ phase reported by Raabe and coworkers is actually joined by a metastable B2 phase, which would be impossible to identify using the chosen experimental techniques.

We have recently extended our study of linear complexions to FCC materials. Since all dislocations dissociate into mixed character partial dislocations separated by a stacking fault, there is a much more reliable template for these transformation to occur. We have found at last three new types of linear complexions in FCC alloys, depending on the alloy system that is chosen. For example, a layered, 2D phase can form along the stacking fault, as shown in Fig. 3(b). We have

also made linear complexion diagrams (Fig. 3(c)) that show the local compositions that are needed for a complexion transition at a given temperature, which can guide future experimental validation efforts. In addition, our models show us that stacking fault width is very clearly affected by complexion nucleation in all FCC alloys studied so far, giving us a clear target when pursuing future characterization efforts with high resolution TEM.

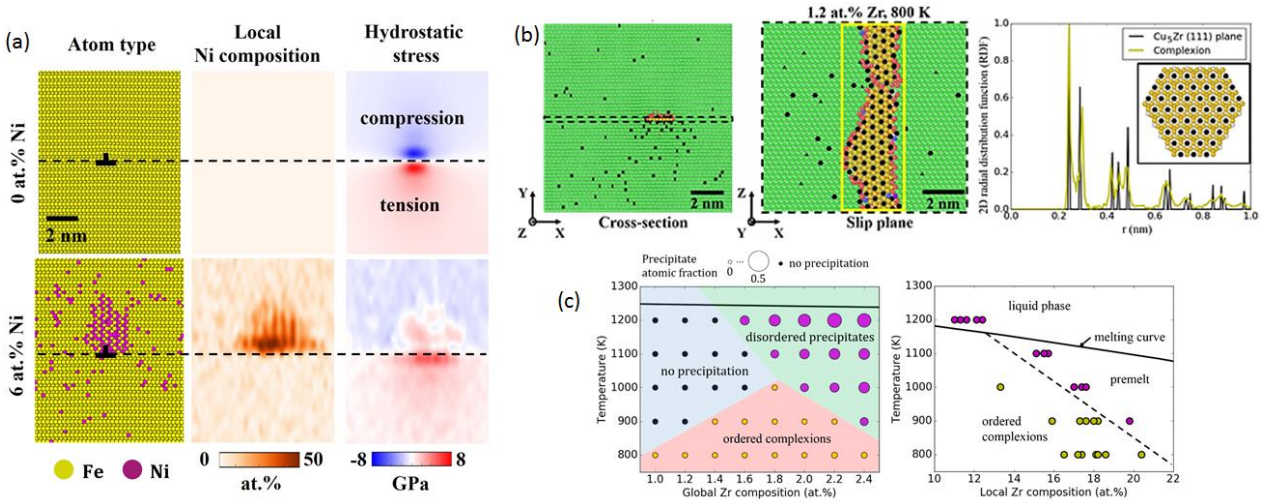

Figure 3. (a) We have discovered new complexions near dislocations that consist of metastable phases. (b) Multiple new complexion types were found in FCC alloys, such as a 2D layered complexion at the stacking fault that resembles one plane taken from the Cu_5Zr intermetallic phase. (c) Linear complexion phase diagrams will guide future study.

Future Plans

Our future work will focus on additional materials discovery, the kinetic aspects of complexion transitions, and the effect of damage on complexion integrity. We plan to develop a greater understanding of how chemical composition at the grain boundary leads to complexions of different types and thicknesses. Specifically, we believe that anisotropic segregation to different boundaries is responsible for the variety of AIF thicknesses within a given sample. We are also probing the effect of controlled cooling rates on the complexion thickness distribution. Although we tried to rapidly quench our original samples, a new sample geometry where heat is extracted through a liquid nitrogen cooled sink gives a complexion distribution that is roughly twice as thick as our preliminary samples, demonstrating that this is an exciting avenue for new work. Finally, there is an open question about how the mechanical damage from incoming dislocations or the radiation damage associated with local cascades and incoming point defects can affect the stability of a complexion. In theory, there must be some limit where the complexion undergoes a transition back to the room temperature state, likely "pushed" by these dynamic processes.

References

1. Cantwell, PR *et al.* "Grain boundary complexions." *Acta Mater.* **62**, 1-48, (2014).
2. Khalajhedayati A, Pan Z, Rupert TJ "Manipulating the interfacial structure of nanomaterials to achieve a unique combination of strength and ductility." *Nature Comm.* **7**, 10802, (2016).
3. Kuzmina M, Herbig M, Ponge D, Sandlöbes S, Raabe D. "Linear complexions: Confined chemical and structural states at dislocations." *Science* **349**, 1080-1083, (2015).

Publications (2017-2019)

(1) Pan Z, Rupert TJ. "Formation of ordered and disordered intergranular films in immiscible metal alloys," *Scripta Materialia*, 130, 91 (2017).

(2) Pan Z, Rupert TJ. "Spatial variation of short-range order in amorphous intergranular complexions," *Computational Materials Science*, 131, 62 (2017).

(3) Pham QN, Larkin LS, Lisboa CC, Saltonstall CB, Qiu L, Schuler JD, Rupert TJ, Norris PM. "Effect of Growth Temperature on the Synthesis of Carbon Nanotube Arrays and Amorphous Carbon for Thermal Applications," *Physica Status Solidi A*, 1600852 (2017).

(4) Schuler JD, Rupert TJ. "Materials selection rules for amorphous complexion formation in binary metallic alloys," *Acta Materialia*, 140, 196 (2017).

(5) Hu Y, Schuler JD, Rupert TJ. "Identifying interatomic potentials for the accurate modeling of interfacial segregation and structural transitions," *Computational Materials Science*, 148, 10 (2018).

(6) Turlo V, Rupert TJ. "Dislocation-assisted linear complexion formation driven by segregation," *Scripta Materialia*, 154, 25 (2018).

(7) Hu Y, Rupert TJ. "Atomistic modeling of interfacial segregation and structural transitions in ternary alloys," *Journal of Materials Science*, 54, 3975 (2019).

(8) Schuler JD, Barr CM, Heckman NM, Copeland G, Boyce BL, Hattar K, Rupert TJ. "In situ high-cycle fatigue reveals the importance of grain boundary structure in nanocrystalline Cu-Zr," *JOM*, 74, 1221 (2019).

(9) Turlo V, Rupert TJ. "Linear complexions: Metastable phase formation and coexistence at dislocations," *Physical Review Letters*, 122, 126102 (2019).

(10) Grigorian CM, Rupert TJ. "Thick amorphous complexion formation and extreme thermal stability in ternary nanocrystalline Cu-Zr-Hf alloys," (under review).

(11) Turlo V, Rupert TJ. "Discovery of a wide variety of linear complexions in face centered cubic alloys," (under review).

(12) Schuler JD, Grigorian CM, Barr CM, Boyce BL, Hattar K, Rupert TJ. "Amorphous intergranular films mitigate radiation damage in nanocrystalline Cu-Zr," (under review).

Role of Heterogeneous Segregation on Shear Localization Mechanisms in Nanocrystalline Alloys

Frederic Sansoz
Department of Mechanical Engineering, The University of Vermont, Burlington VT (USA)

Program Scope

Over the past decade, considerable research effort has been focused on the role of solute segregation in stabilizing nanoscale interfaces to harden metals at near-ideal Hall-Petch strength limits, through extreme grain refinement ($d \leq 50$ nm) [1]. Inevitably, grain boundary (GB) segregation is also associated with a significant deterioration of tensile ductility in nanocrystalline (nc) alloys that generally exhibit poor uniform plastic elongations below 2% [2]. The segregation-induced ductile-to-brittle transition is well-understood in terms of two dominant deformation mechanisms at interfaces: GB embrittlement accelerating intergranular cracking, and glass-like shear localization leading to catastrophic shear banding.

The proposed research aims to deploy state-of-the-art atomistic simulations and experimental studies to fundamentally understand plasticity and shear localization mechanisms in binary nanocrystalline Ag-Ni alloys that have not been well studied so far (other metallic alloys will also be studied as a comparison). Ag-Ni alloys are of interest because recent theoretical models [3] have predicted that GB segregation behavior in nc Ag alloys containing small Ni contents ($\leq$ 2 at%) is intrinsically *heterogeneous*. Heterogeneous segregation is a unique behavior where solute atoms cluster along some GB regions, whereas other GB regions are left solute free. Therefore, it is hypothesized that new shear localization and ductility enhancement mechanisms induced by heterogeneous GB segregation could be controlled by the segregated solute content.

Recent Progress

Recent theory and simulations speculate that the potential of segregating elements to either weaken or strengthen individual GBs governs the type of embrittlement mechanism in nc alloys [4]. Notably, in the case of a GB embrittling element, a recent study in Au-segregated nanocrystalline Pt metals has observed that 10 at% Au promotes brittle-like behavior and fast cracking [5]. Surprisingly, however, this study revealed that a smaller 5 at% content makes possible for the alloy to recover some ductility at same grain size, due to crack arrest at triple junctions induced by *heterogeneous* GB segregation. Yet our basic understanding of this phenomenon remains limited, because common nc alloys studied in the literature, such as Ni-W and Cu-Zr alloys, exhibit *homogeneous* segregation, with solute atoms distributing uniformly along interfaces at all concentrations.

By contrast, in alloys containing GB strengthening elements (e.g. nc Ag-Cu alloys), the loss of toughness and ductility is associated with shear localization mechanisms. Our past work using atomistic simulations showed that the segregation behavior of nanocrystalline-nanotwinned Ag-Cu alloys is of the homogeneous type [6]. Our preliminary results suggest that these materials fail by shear localization-induced embrittlement after segregation. ***Our main hypothesis is that heterogeneous segregation should fundamentally alter the above shear localization mechanisms leading to embrittlement with GB strengthening elements.***

We have performed hybrid Monte-Carlo and molecular-dynamics simulations to study the strengthening effects of homogeneous segregation and heterogeneous segregation on nc Ag alloys doped with either Cu or Ni solutes, respectively, as shown in Figure 1. Our atomistic simulation results presented in Figure 2 show that Cu-doped samples with homogeneous segregation tend to deform through strain localization induced by high GB volume fraction, saturating the strengthening effect at high solute compositions. However, Ni-doped samples with heterogeneous segregation tend to suppress strain localization by forming solute-rich clusters, Figure 1d, leading to a consistent and sustained strengthening effect when increasing the solute concentration. The finding that heterogeneous segregation suppresses strain localization could provide an efficient way to design tough nanostructured materials through GB segregation engineering from different alloy systems with such segregation behavior.

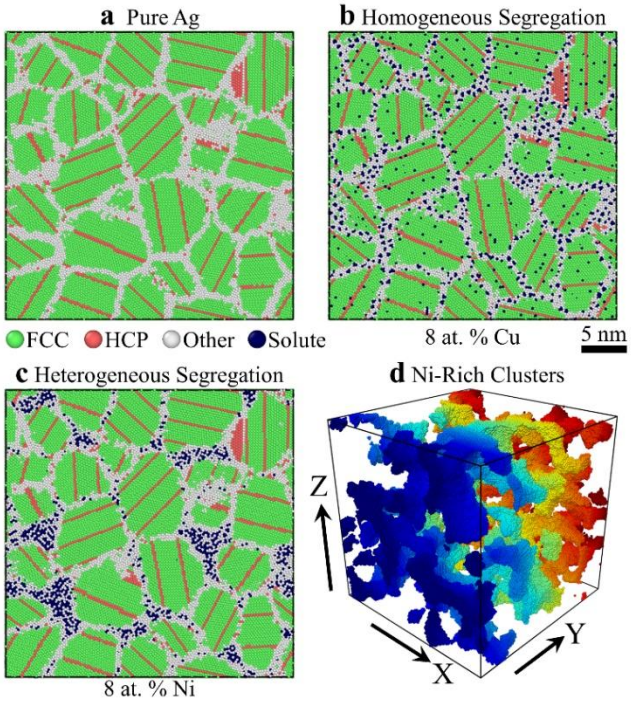

Figure 1. Equilibrium configurations of (a) pure Ag, (b) Cu homogeneous segregation, and (c) Ni heterogeneous segregation. The atoms are colored according to CNA, with face-centered cubic (FCC) atoms colored green, hexagonal close-packed (HCP) atoms red, and other atoms white. The solute atoms are highlighted with dark blue. (d) shows the distribution of Ni-rich clusters inside the simulation box, with atoms colored according to the Y coordinates.

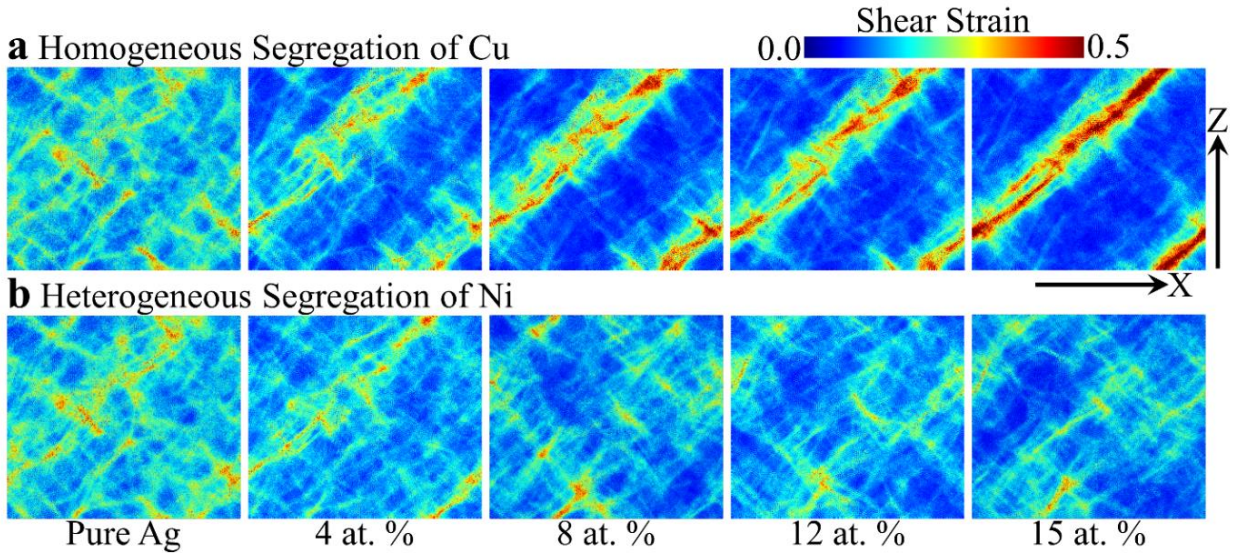

Figure 2. Reduced atomic shear strain map on X-Z plane for (a) Cu and (b) Ni segregated samples at a tensile strain of 10%. Increasing Cu composition tends to deteriorate the strain localization but increasing Ni composition tends to suppress it.

Future Plans

Studying the effects of homogeneous versus heterogeneous segregation behaviors on shear localization mechanisms is challenging, both experimentally and theoretically, because (1) these mechanisms extend over multiple deformation scales from single GB structural units to shear banding across the polycrystal, and (2) nc binary alloys with GB strengthening elements exhibiting heterogeneous segregation remain new. Therefore, our plans for this research are:

(1) **Atomic-scale Quantification of Shear Localization:** To use large-scale atomistic simulations to numerically quantify the contribution of each type of GBs (segregated or non-segregated) in nanocrystalline Ag-Ni metals, to understand how heterogenous segregation affects shear localization mechanisms. These simulations will enable us to pin point the origin of shear localization at GB level and simulate hypothetical materials that could not be achieved experimentally; e.g., Ni-doped Ag metals with homogeneous segregation, as a comparison.

(2) **Microscale Quantification of Shear Localization:** To quantify shear localization at microscopic scale using in-situ SEM/EDS/EBSD tensile tests using newly available experimental equipment at the PI's institution. For that purpose, we will use materials fabricated at Lawrence Livermore National Laboratory (Dr. Morris Wang) using a new high-power impulse sputtering deposition system. Results with this instrument have never been reported before, but the high power should enable us to achieve better microstructure control at smaller grain size (possibly twin size), to match atomistic models more closely.

(3) **Grain-boundary Segregation Analysis:** To understand how interface structure, chemical composition and thermal relaxation influence heterogeneous GB segregation behavior in Ni-Ag alloy bicrystals and polycrystals using hybrid Monte-Carlo/molecular-dynamics simulations, with particular focus on quantifying the Ni cluster fraction, shape and distribution. Since this numerical approach matches only quasi-equilibrium conditions, however, we intend to collaborate with Dr. Daniel Schreiber at Pacific Northwest National Laboratory to conduct 3D atom probe tomography (3D-APT) experiments on sputter-deposited Ni-Ag metals.

References

1. Hu, J., Y.N. Shi, X. Sauvage, G. Sha, and K. Lu, *Grain boundary stability governs hardening and softening in extremely fine nanograined metals.* Science, 2017. **355**(6331): p. 1292.
2. Ovid'ko, I.A., R.Z. Valiev, and Y.T. Zhu, *Review on superior strength and enhanced ductility of metallic nanomaterials.* Progress in Materials Science, 2018. **94**: p. 462-540.
3. Pan, Z., V. Borovikov, M.I. Mendelev, and F. Sansoz, *Development of a semi-empirical potential for simulation of Ni solute segregation into grain boundaries in Ag.* Modelling and Simulation in Materials Science and Engineering, 2018. **26**(7): p. 075004.
4. Gibson, M.A. and C.A. Schuh, *Segregation-induced changes in grain boundary cohesion and embrittlement in binary alloys.* Acta Materialia, 2015. **95**: p. 145-155.
5. Heckman, N.M., S.M. Foiles, C.J. O'Brien, M. Chandross, C.M. Barr, N. Argibay, K. Hattar, P. Lu, D.P. Adams, and B.L. Boyce, *New nanoscale toughening mechanisms mitigate embrittlement in binary nanocrystalline alloys.* Nanoscale, 2018. **10**(45): p. 21231-21243.
6. Ke, X. and F. Sansoz, *Segregation-affected yielding and stability in nanotwinned silver by microalloying.* Phys. Rev. Mater., 2017. **1**(6): p. 063604.

Crack Tip Mechanisms Driving Environmental Degradation

S.M. Bruemmer, D.K. Schreiber, C. Wang, M.J. Olszta, K. Kruska, M.L. Sushko and K.M. Rosso

Pacific Northwest National Laboratory

Program Scope

Environmental degradation and associated nano-to-macroscale cracking are fundamental materials science issues impacting a wide range of current and future energy systems. It is the goal of this research program to reveal the fundamental processes that underlie these interlinked and complex phenomena. To do so, we leverage a cutting-edge suite of in-situ and ex-situ microscopy techniques, multiscale mechanistic modeling, and macroscale mechanical testing under controlled environments to produce a comprehensive picture on the roles of environment, alloying additions, surfaces, interfaces, and microstructural defects on the resulting behavior.

Our overarching hypothesis is that common mechanisms operating at the atomic scale underpin the stress corrosion cracking (SCC) response at the macroscale. Key among these are selective oxidation, vacancy injection, and accelerated interfacial diffusion. These basic processes extend from high-temperature (>600°C) gaseous to moderate-temperature (<360°C) aqueous environments, with surface and interfacial reactions and transport dominating with decreasing temperature. Our research activities are generalized into three synergistic areas:

i) Environmental Degradation and Crack-Tip Behavior: Quantitative crack-growth testing as a function of material and environmental conditions [1,2] is combined with ex-situ, high-resolution characterization of oxidation fronts and crack tips [3,4] via analytical transmission electron microscopy (ATEM) and atom probe tomography (APT) to establish direct correlations.

ii) In-situ and Operando Oxidation: In-situ and operando TEM, performed in a specially designed environmental (E)TEM, complements ex-situ techniques with real-time atomic-scale observations of unique, dynamic processes operating during oxidation or corrosion, including vacancy generation and accumulation, as a function of environment [5,6].

iii) Multiscale Modeling: State-of-the-art hybrid functional DFT calculations of the energetics of oxide and interface formation, ab initio molecular dynamics (AIMD) simulations of bulk matrix and interfacial atomic transport processes, formation and mobilities of vacancies and interstitials, and metal/oxygen/vacancy interactions [7,8]. Ab initio thermodynamics techniques are used to incorporate the role of environment and temperature dependence. Molecular computations bridge into the mesoscale via a novel classical density functional theory (cDFT) approach [9] that, in turn, connects directly with experimental observations.

Recent Progress

Significant progress has been made towards determining the impact of secondary phases inclusions (e.g. intergranular carbides or borides) on corrosion behavior [3.9] and to establish the fundamental differences during oxidation in dry, gaseous versus "wet" environments (water vapor or high-pressure liquid water) [4,5].

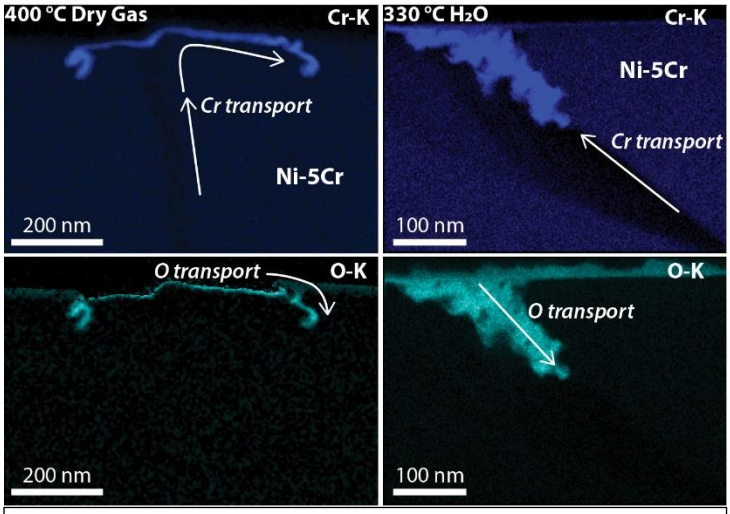

Fig. 1: STEM EDS reveals divergent behavior during oxidation of Ni-5Cr under (left) dry gas and (right) aqueous conditions. Penetrative intergranular attack is found in water, while a thin Cr_2O_3 layer locally protects the grain boundary in dry gas. [4]

It is well established that water enhances the oxidation rate of many materials [10], but the atomic-level detail of this altered response has not been directly determined. Ex-situ testing and microscopy (Fig 1) reveals striking differences in the oxidation behavior of Ni-5Cr under nominally identical oxidizing potentials (Ni/NiO stability) for high-temperature, hydrogenated water and a dry, gaseous Rhines Pack [4]. Selective oxidation of Cr dominates in both cases, but the morphology of the resulting oxide is fundamentally and pragmatically opposite. In the case of water, preferential intergranular oxide penetration results in a massively altered grain boundary chemistry (Cr depletion) and (potentially) localized embrittlement along the oxide/metal interface [1]. Conversely, dry oxidation promotes the formation of a thin, passive Cr_2O_3 film directly above the grain boundary that prevents further intergranular attack. This morphological dichotomy demonstrates that, despite nominally identical oxidation potentials, water promotes the formation of less protective oxides, and that local passivation is possible at surprisingly low Cr concentrations due to enhanced Cr transport along grain boundaries.

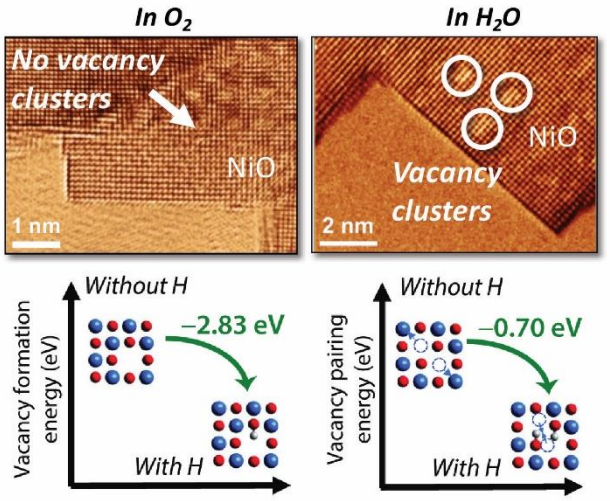

Fig. 2: Operando ETEM reveals atomic processes of Ni-10Cr oxidation in (left) pure O_2 and (right) water vapor. (bottom) DFT calculations show that water dissociation and proton ingress uniquely stabilize vacancies in NiO, resulting in enhanced ion transport and accelerated oxidation [5].

In-situ and operando ETEM provides a way to directly monitor the oxidation of a similar Ni-10Cr alloy under controlled environments (Fig. 2). Here NiO formation is followed at the atomic scale,

in real time, during dry (pure O_2) or wet (water vapor) oxidation [5]. Comparison of the high-resolution TEM images reveals the unique formation of vacancy clusters in the water vapor environment. Complementary DFT calculations demonstrate that interstitial protons, introduced by the dissociation of water molecules, can stabilize both Ni and O vacancies in the oxide, and promote their condensation into the vacancy clusters that are visualized in ETEM. Such a mechanism has been speculated previously, but these operando ETEM studies have provided the first real-time, atomic-scale visualization of the phenomena.

Intergranular secondary phases are also known to influence the SCC response of Ni-base alloys in high temperature, hydrogenated water. Alloy 600 (Ni-16Cr-9Fe) tested in a nominally carbide-free, solution annealed condition exhibits greater susceptibility to SCC than the same material in a thermally treated (carbide containing) condition [9]. To better understand the role of these secondary phases on oxidation, we compared 3D APT measurements of intergranular carbide oxidation with mesoscale calculations of the metal/metal and metal/carbide interfacial oxide formation (Fig. 3). These calculations incorporate first-principles calculations of atomic transport rates in the alloy matrix, along metallic grain boundaries and surfaces [11], and through various oxide defects [7,8]. Both experimental and computational results come to a surprising conclusion: oxide formation is most favorable slightly away from the Cr-rich carbide. In the APT data, a nanoscopic Ni-rich layer separates the Cr_2O_3 shell from the Cr carbide core. This closely mimics the calculation predictions, where Cr favors sitting a few nanometers from the carbide surface. Further observations, particularly to consider where cracks propagate through this unexpected

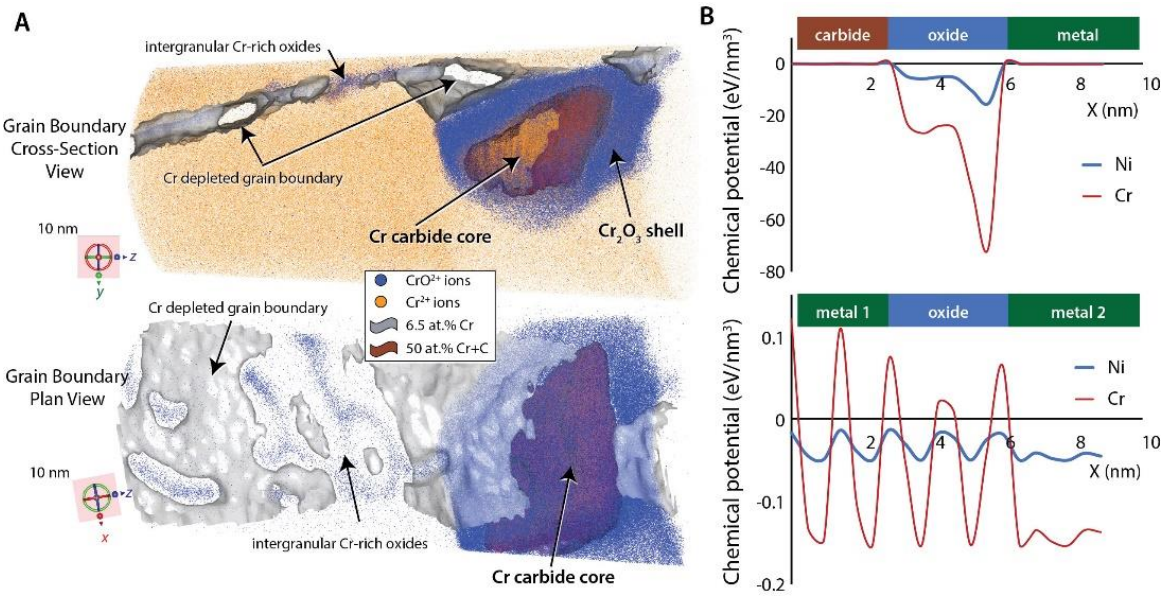

Fig. 3: Combined experimental and mesoscale modeling of intergranular attack in Ni-16Cr-9Fe with a Cr carbide precipitate. (left) 3D APT reconstruction of oxidation enveloping a Cr carbide and (right) corresponding mesoscale cDFT calculations. Both results show that oxide growth is more favorable when spatially separated from the carbide. Experimentally, this results in a nanoscopic metallic Ni layer separating the Cr_2O_3 shell from the Cr carbide core. [9]

nanostructure, are planned to understand the impact of these features on the corresponding SCC behavior.

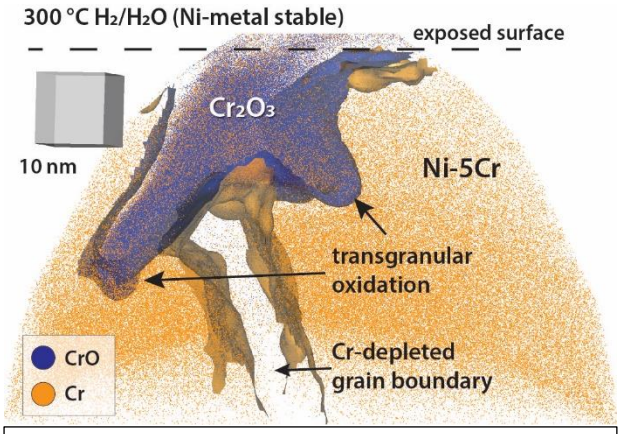

Fig. 4: 3D APT characterization of Ni-5Cr after exposure to 300°C H_2/H_2O steam reveals a Cr_2O_3 passivating layer resulting in transgranular oxidation. A similar passive film forms during dry oxidation at the external surface (Fig 1), while steam favors subsurface passivation. [unpublished results]

Future Plans

Selective oxidation, defect formation, vacancy injection and atomistic transport, especially along interfaces, continue to be primary areas of interest. Recent progress comparing oxidation under water-bearing and dry environments have revealed some unexpected phenomena, including the local passivation of grain boundaries at relatively low Cr concentrations in Ni-5Cr. Steam exposures may bridge the observations between dry Rhines Pack studies and behavior in liquid water. Steam at elevated temperatures (420–480°C) is oftentimes used for accelerated testing conditions mimicking pressurized water, but preliminary observations of steam exposure of Ni-5Cr (Fig 4) suggest that steam more closely mimics dry gaseous oxidation than aqueous corrosion at the grain boundary. Additional studies, including SCC testing in steam versus water versus dry gas, will be performed to extend our understanding of the impact of stress on these localized passivation phenomena. In-situ and operando ETEM studies will also be extended to include controlled H_2/H_2O ratios, with partner AIMD simulations of environment-dependent transport kinetics, to probe and understand selective oxidation processes of more reactive species with the ultimate goal of studying dynamic grain boundary phenomena. Select studies are also planned to leverage the isotopic sensitivity of APT to understand dominant transport pathways during oxidation. For example, ^{18}O tracers can highlight active diffusion pathways through nominally passive or porous oxide microstructures to indicate the relative importance of interfacial, bulk and surface diffusion. These observations will provide direct feedback to modeling activities to refine our focus on the most critical phenomena.

References

[1] Bruemmer et al. *Corros. Sci.,* **131** (2018) 310. [2] Zhai et al. *Corros. Sci.,* **123** (2017) 76. [3] Schreiber et al. *Proceedings of 18th Env. Deg*. (2018), p. 359. [4] Kruska et al. *Corros. Sci.*, **139** (2018) 309. [5] Luo et al. *Nature Mater.*, **17** (2018) 514. [6] Luo et al. *Scripta Mater*., **114** (2016) 129. [7] Medasani et al. *J. Phys. Chem. C*, **122** (2018) 12984. [8] Medasani et al. *J. Phys. Chem. C*, **121** (2017) 1817. [9] Sushko et al. *Scripta Mater*., **156** (2018) 51. [10] Saunders et al. *Prog. Mater Sci*., **53** (2008) 775. [11] Alexandrov et al. *Corros. Sci.*, **113** (2016) 26.

Publications (2017-Present)

Kruska, K., D. K. Schreiber, M. J. Olszta, B. J. Riley and S. M. Bruemmer (2019). "Comparison of selective oxidation in Ni-based alloys exposed to PWR primary water and Rhines Pack environments," 19th International Conference on Environmental Degradation of Materials in Nuclear Power Systems - Water Reactors. (*In Press)*

Dong, Y., A. Etienne, A. Frolov, S. Fedotova, K. Fujii, K. Fukuya, C. Hatzoglou, E. Kuleshova, K. Lindgren, A. London, A. Lopez, S. Lozano-Perez, Y. Miyahara, Y. Nagai, K. Nishida, B. Radiguet, D. K. Schreiber, N. Soneda, M. Thuvander, T. Toyama, J. Wang, F. Sefta, P. Chou and E. A. Marquis (2019). "Atom probe tomography interlaboratory study on clustering analysis in experimental data using the maximum separation distance approach," *Microscopy and Microanalysis* **25**: 356-366.

Taylor, S. D., J. Liu, X. Zhang, B. W. Arey, L. Kovarik, D. K. Schreiber, D. E. Perea and K. M. Rosso (2019). "Visualizing the iron atom exchange front in the Fe(II)-catalyzed recrystallization of goethite by atom probe tomography," *Proceedings of the National Academy of Sciences* **116**: 2866-2874.

Luo, L, M. Su, P. Yan, L. Zou, D. K. Schreiber, D. R. Baer, Z. Zhu, G. Zhou, Y. Wang, S. M. Bruemmer, Z. Xu and C. Wang (2018). "Atomic origins of water-vapour-promoted alloy oxidation," *Nature Materials* **17**: 514-518.

Badwe, N., X. Chen, D. K. Schreiber, M. J. Olszta, N. R. Overman, E. K. Karasz, A. Y. Tse, S. M. Bruemmer and K. Sieradzki (2018). "Decoupling the role of stress and corrosion in the intergranular cracking of noble-metal alloys," *Nature Materials* **17**: 887-893.

Bruemmer, S. M., M. J. Olszta, M. B. Toloczko and D. K. Schreiber (2018). "Grain boundary selective oxidation and intergranular stress corrosion crack growth of high-purity nickel binary alloys in high-temperature hydrogenated water," *Corrosion Science* **131**: 310-323.

Kruska, K., D. K. Schreiber, M. J. Olszta, B. J. Riley and S. M. Bruemmer (2018). "Temperature-dependent selective oxidation processes for Ni-5Cr and Ni-4Al," *Corrosion Science* **139**: 309-318.

Sushko, M.L., D. K. Schreiber, K. M. Rosso and S. M. Bruemmer (2018). "Role of Cr-rich carbide precipitates in the intergranular oxidation of Ni-Cr alloys," *Scripta Materialia* **156**: 51-54.

Medasani, B., M. L. Sushko, K. M. Rosso, D. K. Schreiber and S. M. Bruemmer (2018). "First-principles investigation of native interstitial diffusion in Cr_2O_3," *Journal of Physical Chemistry C* **122**: 12984-12993.

Exertier, F., A. La Fontaine, C. Corcoran, S. Piazolo, E. Belousova, Z. Peng, B. Gault, D. W. Saxey, D. Fougerouse, S. M. Reddy, S. Pedrazzini, P. A. J. Bagot, M. P. Moody, B. Langelier, D. E. Moser, G. A. Botton, F. Vogel, G. B. Thompson, P. T. Blanchard, A. N. Chiaramonti, D. A. Reinhard, K. P. Rice, D. K. Schreiber, K. Kruska, J. Wang and J. M. Cairney (2018) "Atom probe tomography analysis of the reference zircon GJ-1: An interlaboratory study," *Chemical Geology* **495**: 27-35.

Broberg, D., B. Medasani, N. E. R. Zimmermann, G. Yu, A. Canning, M. Haranczyk, M. Asta and G. Hautier (2018). "PyCDT: A Python toolkit for modeling point defects in semiconductors and insulators." *Computer Physics Communications* **226**: 165-179.

Taylor, S. D., J. Liu, B. W. Arey, D. K. Schreiber, D. E. Perea and K. M. Rosso (2018). "Resolving iron(II) sorption and oxidative growth on hematite (001) using atom probe tomography." *The Journal of Physical Chemistry C* **122**: 3903-3914.

Schreiber, D. K., M. J. Olszta, K. Kruska and S. M. Bruemmer (2017). "Role of grain boundary Cr_5B_3 precipitates on intergranular attack in alloy 600." in: M. Wright, J. Jackson, D.J. Paraventi (Eds.) 18th International Conference on Environmental Degradation of Materials in Nuclear Power Systems - Water Reactors, TMS, Portland, OR, pp. 359-374.

Medasani, B., M. L. Sushko, K. M. Rosso, D. K. Schreiber and S. M. Bruemmer (2017). "Vacancies and vacancy-mediated self diffusion in Cr_2O_3: A first-principles study." *The Journal of Physical Chemistry C* **121**(3): 1817-1831.

Zhai, Z., M. B. Toloczko, M. J. Olszta and S. M. Bruemmer (2017). "Precursor evolution and SCC initiation in cold-worked alloy 690 in simulated PWR primary water." *Corrosion J.* 73-10: 1224-1236.

Kruska, K., Z. Zhai, and S. M. Bruemmer (2017). "Characterization of SCC initiation precursors in cold-worked alloy 690." In: *Proc. of Corrosion 2017,* NACE International, Paper 9717.

Zhai, Z., M. B Toloczko, M. J. Olszta and S. M. Bruemmer (2017). "Stress corrosion crack initiation of alloy 600 in PWR primary water." *Corrosion Science* 123: 76-87.

Correlating Structure, Local Atomic Dynamics, and Composition to Reveal the Origin of Fracture Toughness in Metallic Glasses

Jan Schroers, Yale University

Program Scope

Fracture toughness quantifies a material's ability to resist catastrophic failure in the presence of a crack. Understanding the fracture toughness of glassy materials, which lack long-range crystalline order and are characterized by intrinsically disordered non-equilibrium structures, is a pressing problem in general and particularly for metallic glasses. The wide range of fracture toughness of metallic glasses with their seemingly similar atomic structure has been puzzling the metallic glass community for the last 15 years. Several challenges have prevented a deeper understanding of fracture toughness in the past. i) the lack of a theoretical understanding of the intrinsically disordered, non-equilibrium glassy states of matter, ii) techniques to generate well-reproduced, well-defined glassy states, and iii) accurate and reproducible fracture toughness samples and measurements. During the previous funding period, we addressed ii) and iii) and were able to gain some theoretical understanding of aspects of i). Specifically, we developed an alternative method to measure fracture toughness in BMGs, based on thermoplastic forming of BMGs [1, 2]. This fabrication method drastically reduces most of the previously identified extrinsic contributions. As a consequence, highest repeatability and relative accuracy in fracture toughness measurements of BMGs has been achieved. When quantifying critical test sample geometries, we revealed a flaw tolerance behavior in metallic glasses, where below a certain flaw size the BMGs' response is indistinguishable [2]. Utilizing developed method and gained knowledge about sample size and flaw tolerance, we were able to tackle major open questions of fracture toughness of BMGs. We quantified the processing dependence [3], measured in the fictive temperature dependence of fracture toughness [4], and revealed a mechanical glass transition [5], which separates rate dependent ductile from brittle behavior in metallic glasses. Besides the fictive temperature, the chemical composition of a BMG can be expected to have the largest influence on its fracture toughness. Proposed research will build on our research during the previous funding periods. We will measure fracture toughness for a large number of alloys representing the material class of BMGs. For selected BMGs, we will determine shear and cavitation strength, quality factor, elastic constants, fragility, atomic structure through high-energy synchrotron x-ray experiments, and response to mechanical/thermal cycling. A central quantity, are low barrier events, which we characterize through quality factor measurements. The availability of this large set of complementary data will be used to develop a mechanistic understanding of fracture toughness in metallic glasses.

Recent Progress

Effect of Processing on the Fracture Toughness of Metallic Glasses, Critical Fictictive Temperature, and Mechanical Glass Transition

When glasses are cooled with different rates, they assume different structures. Those structures, which correspond to states in the potential energy landscape, can be correlated with a fictive temperature, T_f. Together with the glasses' chemistry, T_f of a glass defines its structure and properties.

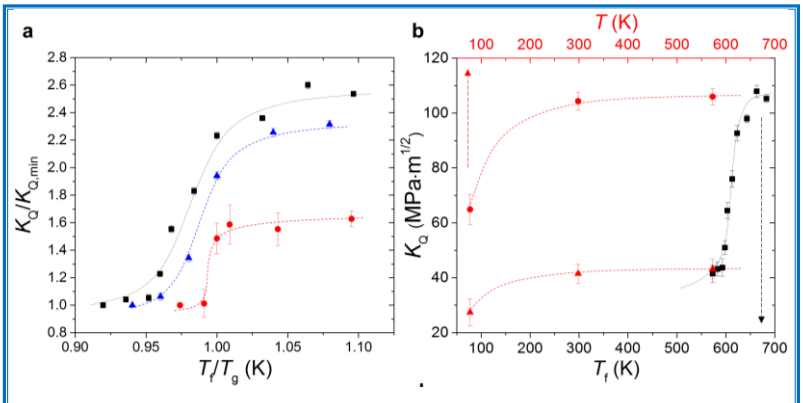

Figure 1: Dramatic transition as a function of fictive temperature, T_f in K_q for metallic glasses. (a) The notch fracture toughness K_Q, normalized by its minimal value $K_{Q,min}$, as a function of T_f, normalized by the glass temperature T_g, for $Zr_{44}Ti_{11}Ni_{10}Cu_{10}Be_{25}$ (black squares), $Pd_{43}Cu_{27}Ni_{10}P_{20}$ (red circles), and $Pt_{57.5}Cu_{14.7}Ni_{5.3}P_{22.5}$ (blue triangles). The error bars represent one standard deviation of five samples per data point. The dashed lines serve as a guide to the eye. (**b**) K_Q for $Zr_{44}Ti_{11}Ni_{10}Cu_{10}Be_{25}$ as a function of T_f (measured at room temperature, black symbols – bottom axis) and T (red symbols – top axis, measured at T) with T_f =683K > T_f^{DB} (red circles) and T_f =583K < T_f^{DB} (red triangles). The dashed lines represent polynomial fits of the data.

Contrary to the understanding of the research community of how fracture toughness should depend on the structure of the glass, we found during the previous funding period an abrupt, toughening transition as a function of the fictive temperature (T_f) (Fig. 1). The previous understanding assumed a continuous change of K_q with either cooling rate or fictive temperature of the glass For the ordinary temperature, which has been previously associated with a ductile-to-brittle transition, we found that it plays a minimal role. We interpret the observed transition to result from a competition between the T_f-dependent plastic relaxation-rate and an applied strain-rate. This would result in a similar toughening transition as a function of strain-rate, which we also observed experimentally [5]. The observed mechanical toughening transition bears strong similarities to the ordinary glass transition and explains previously reported large scatter in fracture toughness data and ductile-to-brittle transitions. Our results have also significant practical implications. They offer a well-defined procedure to realize the practically maximal fracture toughness of metallic glasses defined by their composition and by the strain-rate in a specific application. Such realization can be achieved by carefully controlling T_f through annealing protocols. As a consequence, the observed $K_Q(T_f)$ defines a critical cooling rate (setting $\tau_{plastic}$) to achieve ductile behavior, distinct from the critical cooling rate for glass formation.

Composition Dependence of Fracture Toughness in Metallic Glasses

The other main aspect defining fracture toughness in metallic glasses (besided T_f) is the BMGs composition. We did first experiments on the compositional dependence of fracture toughness in BMGs. For this we considered 13 BMGs from 12 BMG system (Fig. 2). We measured fracture toughness, elastic constants, and yield strength. To also compare BMGs within one alloy system, we considered $Zr_x(Al_{0.25}Ni_{0.25}Cu_{0.5})_{100-x}$ with x = 65, 60, 55, 50 and $Pd_x(NiCu_2)_{(80-x)/3}P_{20}$ with x = 62, 56, 50, 44, 38, 32 (Fig. 2 bottom).

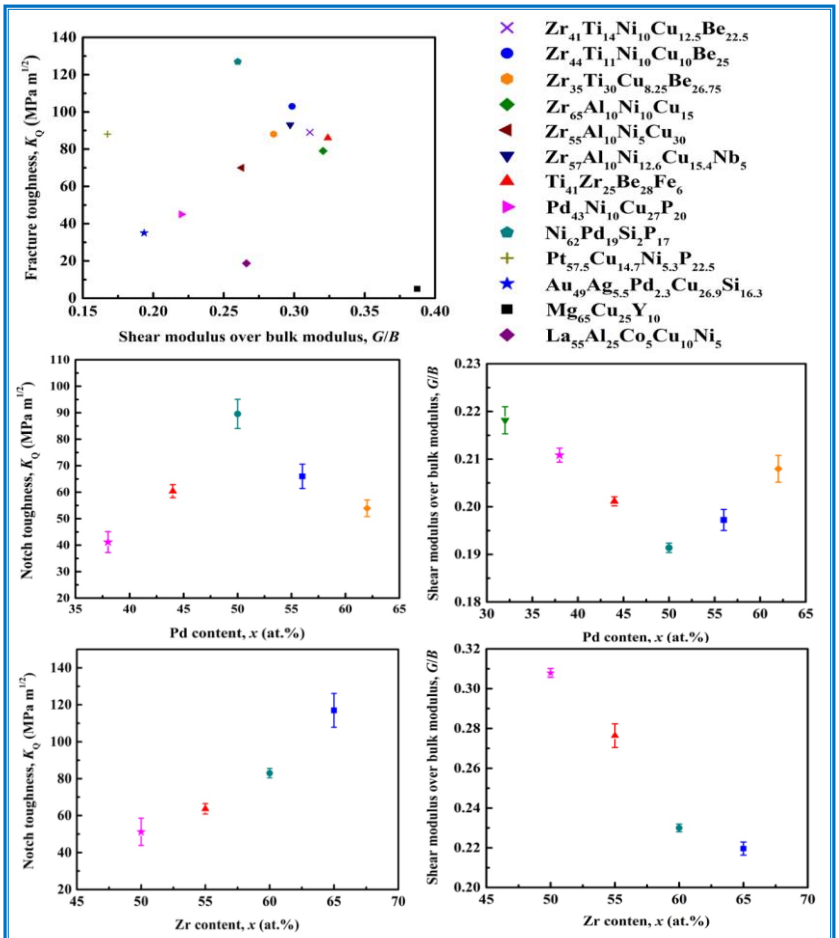

Figure 2: Top: Fracture toughness as a function of yield strength for a 13 BMGs from 12 different alloy systems. Bottom: Fracture toughness and elastic constants for $Zr_x(Al_{0.25}Ni_{0.25}Cu_{0.5})_{100-x}$ with x = 65, 60, 55, 50 and $Pd_x(NiCu_2)_{(80-x)/3}P_{20}$ with x = 62, 56, 44, 38, 32.

Our preliminary conclusion is that the fracture toughness varies dramatically within the materials class of BMGs and such variations *are not* correlated with elastic constants (G/B) and that the fracture toughness varies significantly within one BMG forming alloy system and such variations *are* correlated with elastic constants (G/B).

These preliminary findings have raised several critical questions which we proposed to address in this proposal through proposed research tasks. For example, what causes the non-monotonic behavior of $K_q(c)$? Also for both alloy systems dK_q/dc is large and suggest that within only small composition regions very ductile and very brittle glasses are present.

Future Plans

Correlation of Low Barrier Events Causing Anelasticity/Plasticity with Fracture Toughness:

This task is motivated and aims to answer the following questions:

- *Are low barrier events essential for the fracture toughness in metallic glasses?*
- *Do the low barrier events control T_f^{DB} by setting time scale of plastic relaxation?*

Until recently it was though that metallic glasses are perfectly elastic with an elastic strain limit of ~2% [6]. Recently however, more and more experimental and theoretical evidence has revealed that essentially for any strain in the previously reported "elastic strain limit" anelastic and plastic events occur. Even though it is reasonable to assume that these events can be associated with free volume [7], shear transformation zones [8], soft spots, flexibility volume, core-shells and flow units they provide new insights into metallic glasses. In contrast to the above listed concepts, such "low barrier events" can be quantified in terms of size, quantity, and energetics [9]. They can be considered as low barrier events as within the potential energy landscape, they exhibit a low activation barrier for α-relaxation. In order to investigate the influence of the low barrier events on fracture toughness we propose to characterize their influence on the quality factor, *Q*-factor. As the *Q*-factor measures the dissipation of energy within a system, we can directly correlate it with the low barrier events. We have developed and build a system to drastically reduce external effects on energy dissipation such as clamping and viscoelastic losses which enables us to measure internal dissipation mechanism created by the low barrier events. We will consider three BMG forming compositions, Pd-Ni-Cu-P, Zr-Ti-Ni-Be, and Ni-Pd-B-Si in various conditions. All glasses will be considered in their ductile state, $T_F > T_F^{DB}$ and brittle state, $T_F < T_F^{DB}$. For the same BMGs and conditions where we determine *Q*-factor, fracture toughness will be measured.

References

[1] W. Chen, J. Ketkaew, Z. Liu, R.M.O. Mota, K. O'Brien, C.S. da Silva, J. Schroers, Does the fracture toughness of bulk metallic glasses scatter?, Scripta Materialia 107 (2015) 1-4.

[2] W. Chen, Z. Liu, J. Ketkaew, R.M.O. Mota, S.H. Kim, M. Power, W. Samela, J. Schroers, Flaw tolerance of metallic glasses, Acta Materialia 107 (2016) 220-228.

[3] W. Chen, H.F. Zhou, Z. Liu, J. Ketkaew, N. Li, J. Yurko, N. Hutchinson, H.J. Gao, J. Schroers, Processing effects on fracture toughness of metallic glasses, Scripta Materialia 130 (2017) 152-156.

[4] G. Kumar, P. Neibecker, L. Yanhui, J. Schroers, Critical Fictive Temperature for ductility in metallic glasses, Nature Communications 4 (2013) 1536.

[5] J. Ketkaew, W. Chen, H. Wang, A. Datye, M. Fan, G. Pereira, U.D. Schwarz, Z. Liu, R. Yamada, W. Dmowski, M.D. Shattuck, C.S. O'Hern, T. Egami, E. Bouchbinder, J. Schroers, Mechanical glass transition revealed by the fracture toughness of metallic glasses, Nature Communications 9 (2018).

[6] W.L. Johnson, Bulk glass-forming metallic alloys: Science and technology, Mrs Bulletin 24(10) (1999) 42-56.

[7] F. Spaepen, Homogeneous flow of metallic glasses: A free volume perspective, Scripta Materialia 54(3) (2006) 363-367.

[8] A.S. Argon, Plastic-Deformation in Metallic Glasses, Acta Metallurgica 27(1) (1979) 47-58.

[9] J.D. Ju, D. Jang, A. Nwankpa, M. Atzmon, An atomically quantized hierarchy of shear transformation zones in a metallic glass, Journal of Applied Physics 109(5) (2011).

Publications

1. 1. J. Ketkaew, W. Chen, H. Wang, A. Datye, M. Fan, G. Pereira, U.D. Schwarz, Z. Liu, R. Yamada, W. Dmowski, M.D. Shattuck, C.S. O'Hern, T. Egami, E. Bouchbinder, and J. Schroers, *Mechanical glass transition revealed by the fracture toughness of metallic glasses.* Nature Communications, 9, (2018).

2. W. Chen, H.F. Zhou, Z. Liu, J. Ketkaew, L. Shao, N. Li, P. Gong, W. Samela, H.J. Gao, and J. Schroers, *Test sample geometry for fracture toughness measurements of bulk metallic glasses.* Acta Materialia, 145, 477, (2018).

3. P. Zhang, J.J. Maldonis, Z. Liu, J. Schroers, and P.M. Voyles, *Spatially heterogeneous dynamics in a metallic glass forming liquid imaged by electron correlation microscopy.* Nature Communications, 9, (2018).

4. H.T. Zhang, D. Lee, Y. Shen, Y.C. Miao, J. Bae, Y.H. Liu, J. Schroers, Y. Xiang, and J.J. Vlassak, *Combinatorial temperature resistance sensors for the analysis of phase transformations demonstrated for metallic glasses.* Acta Materialia, 156, 486, (2018).

5. M. Shayan, J. Padmanabhan, A.H. Morris, B. Cheung, R. Smith, J. Schroers, and T.R. Kyriakides, *Nanopatterned bulk metallic glass-based biomaterials modulate macrophage polarization.* Acta Biomaterialia, 75, 427, (2018).

6. Ketkaew, J., M. Fan, M.D. Shattuck, C.S. O'Hern, and J. Schroers, *Structural relaxation kinetics defines embrittlement in metallic glasses.* Scripta Materialia, 149, 21, (2018).

7. Ze Liu, Guoxing Han, Sungwoo Sohn, Naijia Liu, Jan Schroers, *Nanomolding of crystalline metals: The smaller the easier*, Physical Review Letters, 036101 (2019)

8. R.M.O Mota, T.E. Graedel, E. Pekarskaya, and J. Schroers, *Criticality in Bulk Metallic Glass Constituent Elements.* Jom, 69, 2156, (2017).

9. L. Shao, A. Datye, J.K. Huang, J. Ketkaew, S.W. Sohn, S.F. Zhao, S.J. Wu, Y.M. Zhang, U.D. Schwarz, and J. Schroers, *Pulsed Laser Beam Welding of Pd43Cu27Ni10P20 Bulk Metallic Glass.* Scientific Reports, 7, (2017).

10. W. Chen, H.F. Zhou, Z. Liu, J. Ketkaew, N. Li, J. Yurko, N. Hutchinson, H.J. Gao, and J. Schroers, *Processing effects on fracture toughness of metallic glasses.* Scripta Materialia, 130, 152, (2017).

11. W. Chen, Z. Liu, J. Ketkaew, R.M.O. Mota, S.H. Kim, M. Power, W. Samela, and J. Schroers, *Flaw tolerance of metallic glasses.* Acta Materialia, 107, 220, (2016).

Discovery and Design of Stable Nanocrystalline Alloys: The Grain Boundary Segregation Genome

Principal Investigator: Christopher A. Schuh, Department of Materials Science and Engineering, Massachusetts Institute of Technology

Program Scope

Nanocrystalline alloys exhibit superior properties compared to coarse-grained alloys, including mechanical, optical and magnetic properties unattainable at larger grain sizes. However, most nanostructured materials are unstable due to their large volume fraction of excess-energy-bearing grain boundaries; they are prone to accelerated grain growth even at low temperatures, quickly compromising their advanced properties. Recent work has shown that nanocrystalline alloys can be designed to be stable by *intentional grain boundary segregation*: by using alloying elements that will segregate to the boundaries and lower the grain boundary energy, the driving force for grain growth can be attenuated or even eliminated. However, the complexity of screening alloys and designing a successful one on this basis is much higher than in conventional alloy design because of the multitude of grain boundary environments and the effects of solutes upon their energies.

The main thermodynamic data necessary for predicting stability in nanocrystalline alloys is the segregation strength of the alloying element, quantified by the segregation energy. At present, the state of the art in estimating segregation energy is a semi-empirical estimate—a guess—at a single 'average' value for a given system over all grain boundaries. The field has relied upon on intuition and iterative experiments to evaluate such guesses' viability in reality. The challenge addressed in this project is to map and understand the full spectral dependency of segregation energy on grain boundary structure, temperature and solute-solute interactions at the boundary. With ~10^{10} different types of grain boundaries each having up to hundreds of separable segregation sites, added to the combinatorics of chemical composition for binary or ternary transition metal alloys, the problem involves a search space that is on the order of >10^{15} alloy configurations. More alarming yet is that most of this space is inaccessible to the most accurate computations, because density functional theory (DFT) modeling can only simulate a handful of highly symmetric boundaries, and the generalization of those results to the broader problem has yet to be confronted systematically. This project is developing a data science/machine-learning (DS/ML) framework to explore the high-dimensional structural and compositional design space for nanocrystalline alloys to dramatically accelerate their design and development.

Future Work

We will leverage high-throughput atomistic simulations matched with advanced data science methods, to tackle this search space most efficiently. We aim to connect (a) the full complexity of a nanocrystalline alloy with solute segregation on the grain boundaries, to (b) spectral representations of the full suite of grain boundary segregation states for a general alloy, which (c) may be rapidly calibrated for any arbitrary alloy on the basis of a few low-overhead computations. The path from (a) to (c) is to be connected in detail using DS/ML methods that are trained across alloys, structures, and even across different types of modeling. Unlike many ML methods aimed at atomistic problems, we do not aim to learn interatomic potentials relevant to GB environments, but rather to train ML models to directly infer thermodynamic segregation energy spectra from a few limited simulations, bypassing the need for potentials.

In the coming first project year, we will first elucidate and study the spectrum of grain boundary segregation sites in polycrystals, and identify statistical conditions for a stable representative spectrum. We will proceed to develop the criterion that connects the spectrum to thermodynamic stability in nanocrystalline alloys, and begin a high-throughput computational search of many possible binary alloys.

Microparticle Supersonic Impact: A Testbed for the Exploration of Metals under Extreme Conditions

Principal Investigators: Christopher A. Schuh[1] and Keith A. Nelson[2]
Massachusetts Institute of Technology, (1) Department of Materials Science and Engineering and (2) Department of Chemistry

Program Scope

Understanding material behavior under high velocity impact is the key to addressing a variety of fundamental phenomena including impact-induced plasticity, adhesion or cold welding, phase transformations, erosion and ballistic penetration. In this area, researchers have repeatedly observed "critical velocities", thresholds above which supersonic particles transition their mode of interaction with the substrate. For example, there is a critical velocity at which they may adhere to the substrate instead of rebounding, and another where the adhesion gives way to erosion.

We are advancing an in-house-designed setup to accelerate single micron-sized metallic particles, to track them, and to observe the entire deformation/adhesion/erosion process in real time as they impact a substrate (*1*). In our setup, a laser excitation pulse is focused onto a launching pad assembly from which single metallic particles are ejected. Particles are accelerated to supersonic speeds, controllable (from 100 m/s to ~2 km/s) by adjusting the laser excitation pulse energy. The particle impacts a metallic target whose deformation is captured by a high frame rate camera that records up to 16 images with a time resolution as short as 3 ns. The time resolution is enough to capture the deformation event at such extreme impact, which typically takes place over a 50 ns time window. The setup uniquely enables us to study metals response to a wide range of impact velocity, pressure and deformation rate. Figure 1a shows snapshots taken for 45-micron Al particles impacting an Al target with a velocity of 600 m/s (i) and 800 m/s (ii). At

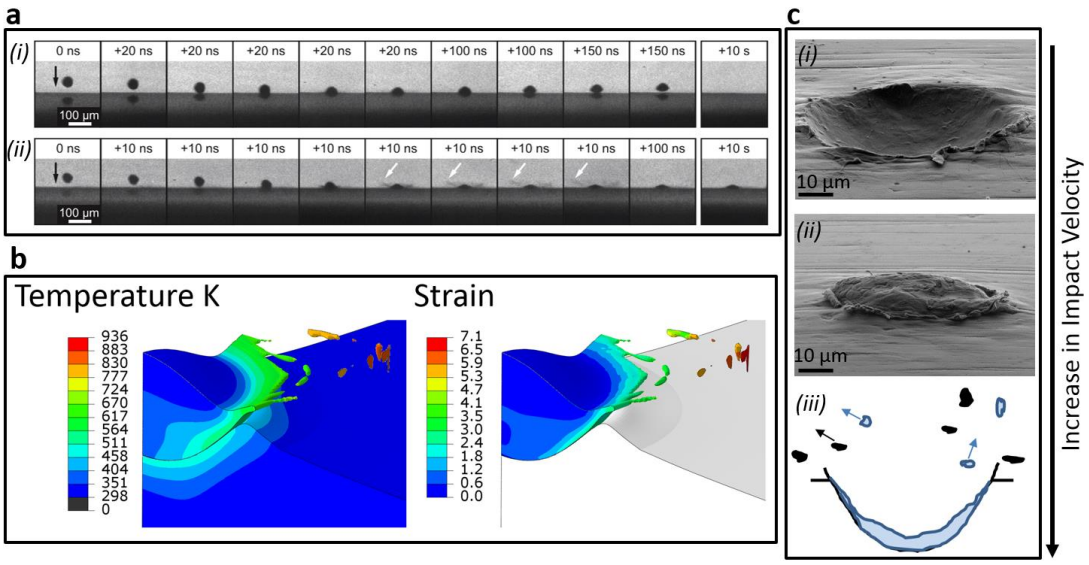

Figure 1. a) Multi-frame sequences with 5 ns exposure time and variable inter-frame time showing single Al particle impacts on Al targets. The inter-frame time relative to the previous frame is shown at the top the frames. (i) Impact at 600 m/s showing particle rebound. (ii) Impact at 800 m/s showing particle adhesion. Material ejection is indicated by white arrows. **b)** The deformation, temperature and strain distribution in Al particle as a result of impact at 800 m/s velocity, featuring extreme thermo-mechanical conditions induced at the contact region during a short amount of time (~50 ns). **c)** Surface deformation at different supersonic impact regimes: (i) rebound (SEM); (ii) adhesion (SEM); and (iii) erosion (schematic).

the lower impact velocity, the particle rebounds with clear flattening and permanent deformation. At the higher impact velocity, there is significantly more deformation accompanied by very fast lateral material ejection at the periphery of the particle, formation of an interfacial jet, and material ejection. The particle does not rebound, but instead adheres to the substrate. We model such impacts using, e.g., finite element simulations, which reveal strain rates up to 10^9 /s, hundreds of percent of plastic strain, temperature rises of hundreds of degrees, all in tens of nanoseconds. *These are truly extreme conditions, which we can now study in real-time and through direct observation of the particle deformation*.

Recent Results

Over the past two project years, through our real-time observations, we have now mapped out three behavioral regimes as the impact velocity rises during metal-on-metal impact. Figures 2a-c show exemplar snapshots capturing tin microparticles impacting tin substrates. As impact velocity increases the impacting microparticle first bounces off as shown in Fig. 2a, then adhesively bonds to the substrate as shown in Fig. 2b, and eventually produces a material splash involving ejected fragments of material. Covering a wide range of impact velocity from 0.1 to 1.1 km/s, Fig. 2e shows how the rebound velocity normalized with the impact velocity (coefficient of restitution) varies with the impact velocity. Transition velocities can be precisely determined using such a plot. We observe an apparent linear decrease in v_i/v_r for the impact

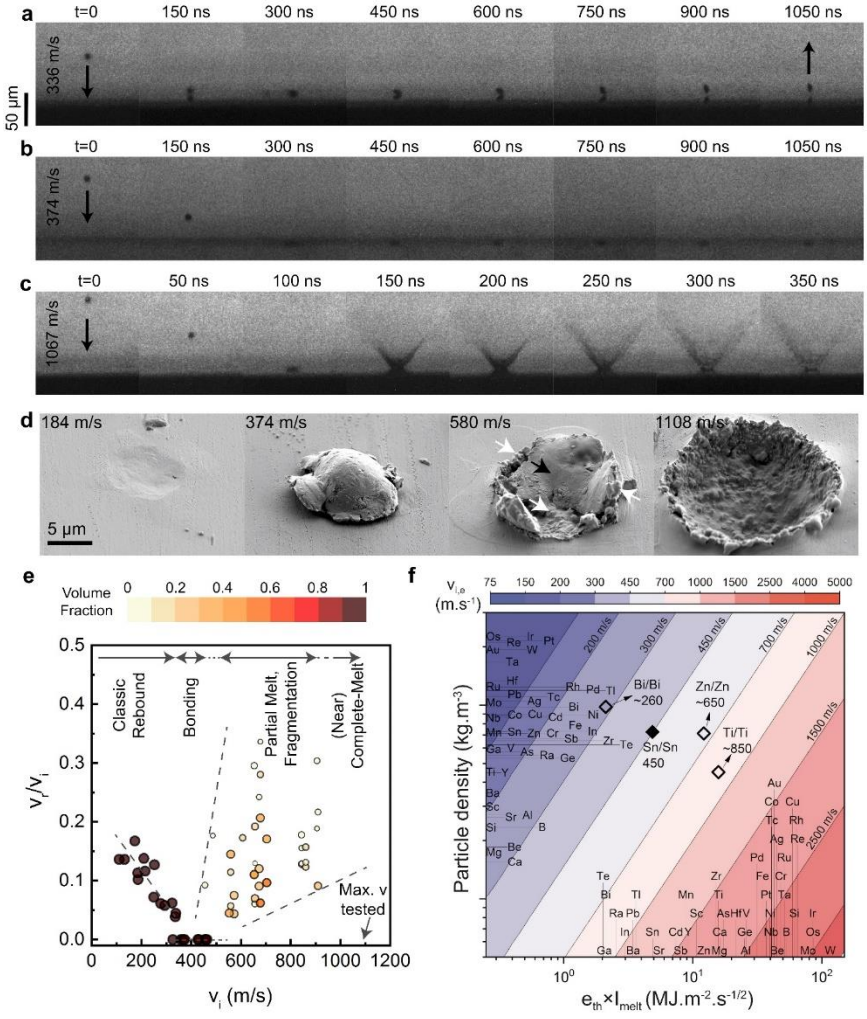

Figure 2.**(a-c)** Multi–frame sequences with 5 ns exposure times showing (a) 9-µm-, (b) 9-µm-, and (c) 10-µm-tin particles arriving from the top of the field of view and impacting tin substrates at (b) 336, (c) 374, (e) 1067 m/s, velocities, spanning from the rebound regime to the bonding and the erosion regimes. (d) Scanning electron micrographs of the impact areas after tin particles impacted the tin substrate at 184, (b) 374, 580, and 1108 m/s velocities, showing rebound, bonding, partial melt, and full melt. Corresponding in-situ observations confirm material loss in the last two cases. **(e)** Coefficient of restitution of the rebounding tin particles and fragments. **(f)** Melt-driven erosion map: Impact velocity at which melt-driven erosion is triggered for different combinations of particle/substrate materials. Particle material is populated on the y-axis. Material of interest in which erosion occurs (primarily substrate in the present context) is located on the x-axis.

velocity range of 100-350 m/s, which is the regime where the particle bounces. The sharp decrease in this ratio to zero values at ~350 m/s identifies the transition from rebound to bonding. We also observe a second transition at around 450 m/s, to a third regime of behavior where material is ejected, in the form of splash and fragments with non-zero v_i/v_r values. As splash and fragmentation lead to material loss, we refer to this regime as the erosion regime; this is the first time this regime has been explicitly mapped out at high velocities.

Post-mortem observations of the impact sites confirm these three behavioral regimes identified in-situ. In the rebound regime, an indentation such as shown in the first image in panel d is left behind on the substrate. Particles exceeding the critical bonding velocity, such as the one in the second image, adhere to the substrate without substantial material loss. The third and the last ones show residue behind where erosion sets on. At 580 m/s the residue exhibits two different morphologies, one indicated by black arrows that appears formed by solid plasticity, and a second indicated by white arrows that is rounded and smooth and suggestive of melting and resolidification. At 1108 m/s we exclusively see splashes in-situ, and the impact site appears to be a completely melted and resolidified crater, as shown in Fig. 2d.

Adhesion transition

The first transition in this sequence, from bouncing to adhesion, is related to the ability of the particle to cold-weld upon impact. We have analyzed this situation as being akin to a micro-scale explosion weld, and the critical feature of the transition is the formation of a jet such as seen in Fig. 1a for aluminum-on-aluminum impact. We have reported direct observations of such jets in both aluminum and in gold (*2*). This jet is not related to melting or any phase transition, but is rather an observation of spall: the reflected pressure wave after the initial impact event leads to spall (solid state rupture), which takes on a jet shape for a convergent geometry such as at the particle-substrate edge. The spall process and its related jet formation are critical to cold welding, because they involve large strains that clean the surface of oxide and flatten nanoscale asperities, permitting clean metallic contact. We have analyzed the results of experiments on a significant number of metals in the past year, including: Al, Ti, Ni, Zn, Sn, Au, Ag (*2*, *3*). In every case, we are able to quantitatively correlate the measured adhesion transition velocity with expectations based on a spall mechanism.

Erosion transition

The second transition that occurs at higher velocities and involves large splashes and significant material loss is related to fundamentally different physics, namely, that of the melting phase transformation. Combining our postmortem and in-situ observations reveals that significant material loss and melting emerge concurrently at the transition velocity between the bonding and the erosion regimes. In other words, erosion appears to be melt-driven, and this is mechanistically unforeseen based on prior work on erosion, which has usually attributed erosion to either a cutting action (*4*) or a combined forging-extrusion action of the eroding particles (*5*).

At the onset of melt-driven erosion we balance the input kinetic energy dissipated with the energy required to heat and melt an affected volume of material, to make a prediction of what conditions will lead to impact melting. Our analysis leads to a view that two critical thermal parameters are important, namely, $e_{th} = \left(\rho k C_p\right)^{1/2}$, called the thermal effusivity, which combines thermal conductivity k, specific heat C_p

and density ρ, and $I_{melt} = T_m - T_0 + \frac{H_f}{C_p}$ a melting index that describes the amount of temperature rise/heat absorption needed to raise the temperature from ambient T_0 to melting T_m. Figure 2f shows a map constructed based on these parameters, using density as the y-axis to locate the particle material, and the product of effusivity and the melting index on the x-axis to locate the substrate material. Thus, for a given particle (vertical line) and substrate (horizontal line) there is an intersection position that is associated with a critical erosion velocity. The range of erosion velocities that we predict to occur is represented by a series of contours in the present map. Superimposing the in-situ measurement of erosion velocity for tin particles impacting a tin substrate onto the map with a black diamond, and three more cases based on limited impact tests with open diamonds, a reasonable agreement between the predictions of the map and the experimental measurements is noted. What is more, $e_{th} \times I_{melt}$ is introduced as a material index to rank substrate materials performance against erosive impacts. This result was the subject of a major publication in the past project year (*6*).

Future Plans

With a basic understanding of the controlling physics of the adhesion transition (spall) and the erosion transition (melting), we are proceeding to evaluate more complex situations and their effects on those mechanisms. For example, we have recently completed a series of works systematically varying particle size, and mapping the adhesion transition. We are developing a theoretical interpretation of those results presently. We have also conducted experiments that involve finer-resolution microscopy in-situ, to explore in more detail the process of jet formation and conditions needed to evolve a jet. This includes some exploration of non-normal incidence impacts. Finally, we have begun to explore impacts with mismatched materials systems. In the case of metal-on-ceramic impact, we find that adhesion is controlled by the ability of the metal to penetrate surface roughness on the ceramic (*7*), and our work looking at ceramic on metal impacts is still in progress.

References

1. M. Hassani-Gangaraj, D. Veysset, K. A. K. A. Nelson, C. A. C. A. Schuh, In-situ observations of single micro-particle impact bonding. *Scr. Mater.* **145**, 9–13 (2018).
2. M. Hassani-Gangaraj, D. Veysset, K. A. Nelson, C. A. Schuh, Impact-bonding with aluminum, silver, and gold microparticles: Toward understanding the role of native oxide layer. *Appl. Surf. Sci.* (2019), doi:10.1016/j.apsusc.2019.01.111.
3. M. Hassani-Gangaraj, D. Veysset, V. K. Champagne, K. A. Nelson, C. A. Schuh, Adiabatic shear instability is not necessary for adhesion in cold spray. *Acta Mater.* **158** (2018), doi:10.1016/j.actamat.2018.07.065.
4. I. Finnie, Erosion of surfaces by solid particles. *Wear*. **3**, 87–103 (1960).
5. R. Bellman, A. Levy, Erosion mechanism in ductile metals. *Wear*. **70**, 1–27 (1981).
6. M. Hassani-Gangaraj, D. Veysset, K. A. K. A. Nelson, C. A. C. A. Schuh, *Nat. Commun.*, in press, doi:10.1038/s41467-018-07509-y.
7. S. I. Imbriglio, M. Hassani-Gangaraj, D. Veysset, M. Aghasibeig, R. Gauvin, K. A. Nelson, C. A. Schuh, R. R. Chromik, Adhesion strength of titanium particles to alumina substrates: A combined cold spray and LIPIT study. *Surf. Coatings Technol.* (2019), doi:10.1016/j.surfcoat.2019.01.071.

Radiation Response of Low Dimensional Carbon Systems

Lin Shao, Di Chen, S.V. Verkhoturov

Texas A&M University, College Station, TX 77845

Program Scope

The project is aimed at understanding the fundamentals of radiation response of low dimensional carbon systems and irradiation-induced mechanical property changes, with focus on the unique phenomena arising from their geometry, boundary, and quantum size effects. In comparison with their bulk counterparts (graphite), radiation responses of low dimensional carbon systems are substantially different. The differences exist at almost each stage of defect development, namely, displacement creation, damage cascade and thermal spike formation, defect recombination, defect clustering, and structural reconstruction. Many traditional concepts in ion-solid interaction theory are not applicable at the nanoscale level or require substantial modification to fit their observed response. In our previous project "Radiation response of low dimensional carbon systems", we systematically studied various aspects of radiation damage development in graphene and carbon nanotubes (CNTs). The project was renewed in 2018. The new project shifts the irradiation source from using "traditional" single ions to using cluster ions, and includes the following parallel tasks: (1) Cluster ion irradiation of a stack of well-separated graphene layers for controllable nanopore formation which images cascade damage volume changes as a function of penetration depth; (2) Cluster ion irradiation of a stack of bilayer graphene to form controllable nanopores which have "welded" edges and unique electronic properties; (3) Swift ion irradiation of graphite for controllable growth of CNTs; (4) Ion irradiation of stressed graphene to control defect clustering; and (5) Ion irradiation of twisted bilayer graphene to study effects of periodic corrugations on defect clustering, a technique that may pave new ways to form periodic vacancy clusters.

Recent Progress

C_{60} ion source Different from low energy bombardment which creates a large damage cascade by a single atom, high energy cluster ion bombardment is unique due to its capability to create highly localized and significantly overlapping individual damage cascades arising from nonlinear sputtering and stopping. Local melting and shock wave creation may occur. For this project, the ion source is a custom-built device which contains a C_{60} cluster effusion source. The source includes an oven containing C_{60} powder. Upon heating to ~400°C, C_{60} clusters are evaporated and then diffuse through a hollow tube to enter the ionization chamber. The chamber includes a Ta plate which emits electrons upon heating. The emitted electrons are accelerated to >100 eV to allow energetic interactions with C_{60}, causing formation of positively charged C_{60}. The ionized C_{60} clusters are then accelerated through a bias >10 kV, and focused and steered via a series of lens. The C_{60} source is used for impact on the front side of the bulk target at an incidence angle of 25° from normal. Secondary ions are emitted and detected in the reflection direction. The

detection device includes a linear time-of-flight, (ToF), mass spectrometer, and an electron emission microscope, EEM. The EEM was used to detect secondary electrons for the ToF start signal.

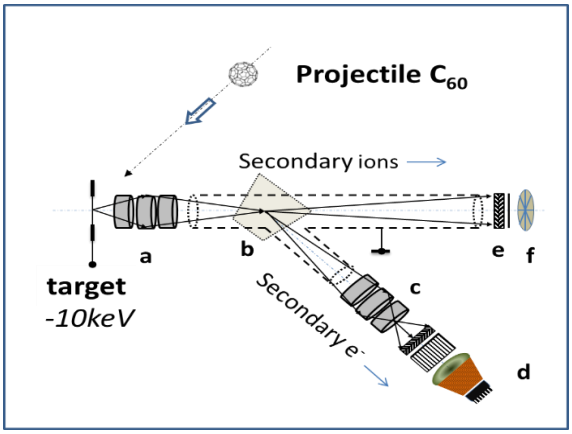

Fig. 1. Schematic picture of C_{60} ion source.

Surface coated graphene to reduce substrate sputtering under ion/cluster bombardment

Modeling: By using molecular dynamics (MD) simulations, we have found that a surface graphene layer (one monolayer) can effectively reduce sputtering caused by ion/cluster bombardment. Due to strong C-C bonding of the graphene layer, the coating layer can slow down atom movement toward the surface and thereby reduce sputtering of substrate atoms lying beneath the graphene layer. Figure 2 shows MD simulations of Ge sputtering by 10 keV C_{60}. Fig. 2A is for uncoated Ge and Fig. 2B is for graphene-coated Ge (with a single layer of graphene on its surface). The effect of graphene coating is obvious. At a time of 10 ps after starting the bombardment, significant Ge sputtering (Fig. 2 A-1) and energy deposition (Fig. 2 A-2) occurs, leading to formation of a crater about 10 nm in dimeter (Fig. 2 A-3). In comparison, the number of sputtered atoms is greatly reduced if Ge is coated with a one atom thick graphene layer (Fig. B-1 and B-2). The damage cascade creates a nanopore on the graphene surface (Fig. B3).

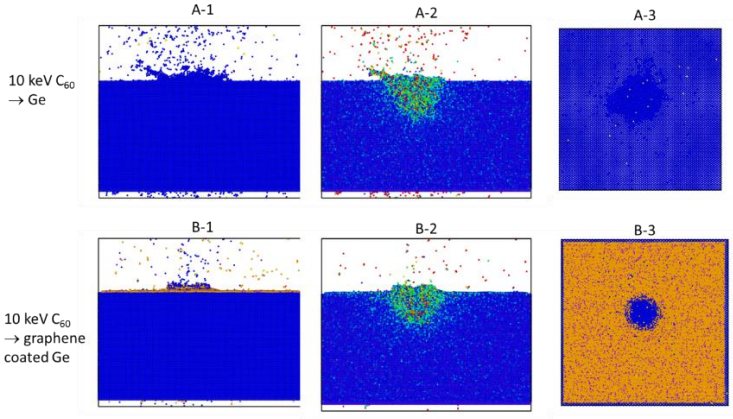

Fig. 2 MD simulations of sputtering by one 10 keV C_{60} cluster for (A1-3) Ge without graphene and (B1-3) Ge with one atom-thick graphene layer. (1) Atom displacements, (A-2) kinetic energy distributions (using different colors), and (A-3) top view of the surface morphology.

Our MD simulations suggest two interesting physical mechanisms: One is that the surface-coated graphene layer serves as a protection layer to stop sputtering, particularly at low bombarding energies at which displacements are relatively low in energy. The other mechanism is that, due to the superior thermal conductivity of graphene, near surface damage cascades have better thermal dissipation, leading to accelerated quenching and reduced sputtering/evaporation in the time period corresponding to formation of local melting zones. The above effects occur only at relatively low C_{60} bombardment energies, since graphene can only slow down and block sputtering of low energy Ge atoms. At higher C_{60} energies, the sputtered atoms are too energetic to be blocked by graphene. The sputtering yields, with or without graphene coating, are largely different at low energies, but the difference disappears at higher energies.

Experiments: We have studied sputtering of both Ge and PMMA with or without 1L (one layer) graphene coating, upon bombardment by C_{60} cluster ions. In order to differentiate C atoms sputtered from the substrate (PMMA) and those from the top graphene layer, our 1L graphene is made from ^{13}C, instead of ^{12}C. The capability of event-by-event bombardment-detection allows the selection of specific impacts. For C_{60} bombarding graphene coated Ge, we are able to identify (1) impacts on bare Ge, when the emitted ions are Ge atomic ions and Ge cluster ions, and (2) impacts on surface of graphene, when the emitted atoms include ^{13}C. Our studies show that the sputtering yields of 1G graphene coated Ge is about half of that from uncoated region. Experimental observations are in good agreements with modeling results. The sputtering suppression effect is even more significant for PMMA. Figure 3 compares the mass spectra of bombarded PMMA covered and uncovered by 1L graphene. For graphene covered PMMA, for instance, for fragments at m = 55, and 85 amu, which correspond to $C_2H_3CO^-$ and $C_4H_5O_2^-$ in the mass spectrum of PMMA (blue, bottom), the yields are 25 times less for the PMMA covered by graphene (top, red).

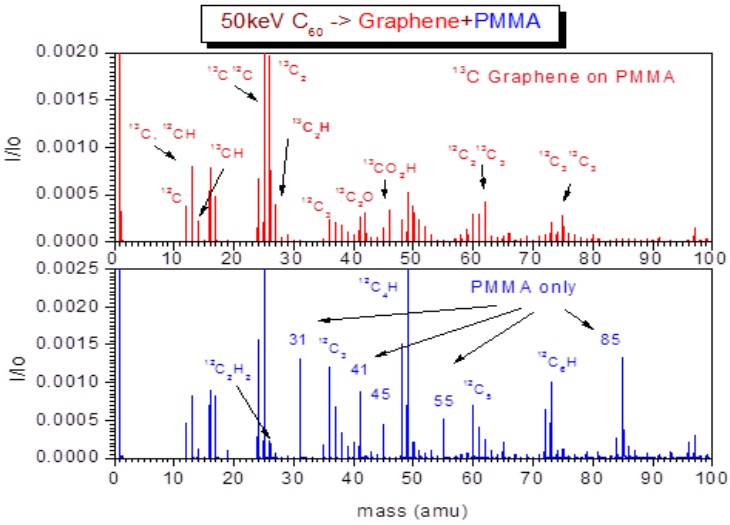

Fig. 3. Mass spectrum of PMMA coated and uncoated with 1G graphene, bombarded with 50 keV C_{60}.

Using damage cascades as pinning sites to immobilize graphene rotation in a two-layer system

Recently it was found that two layers of graphene can have electronic properties tunable from insulator to superconductor characteristics [1,2]. These findings have stimulated intensive research interests and open the door for graphene applications for various types of devices. The key parameter is to precisely control the graphene misalignment angle. However, it was also reported in numerous subsequent studies that precise control of misalignment angles is very challenging. When one graphene layer is released to bond with another graphene layer under a specific misalignment angle, the inter-layer interactions attend to realign both layers when they are close to each other. Hence, the misalignment control is completely lost. Figure 4 shows our MD simulations of this re-alignment process, in which the top graphene is slowly moving towards the bottom one. The misalignment creates a periodic pattern as viewed from the top. With decreasing distance, the periodic pattern disappears. In this project, we have invented a novel method to pin graphene layers and stop their automatic rotation when positioned close to each other. C_{60} clusters are used to bombard graphene layers, which create damage zones in each layer. When two irradiated layers are moving close to each other, defects from irradiation damaged zones prefer to interact with each other, hence acting as pinning sites to immobilize further graphene rotation. Figure 5 shows a top and also side view of periodic pattern evolution while moving two irradiated graphene close to each other. Both layers are irradiated by three C_{60} clusters prior to the movement. When two layers touch to become a two-layer system, there is no change in the periodic patterns, which demonstrates the feasibility of the technique. We are currently in the stage of experimental demonstration.

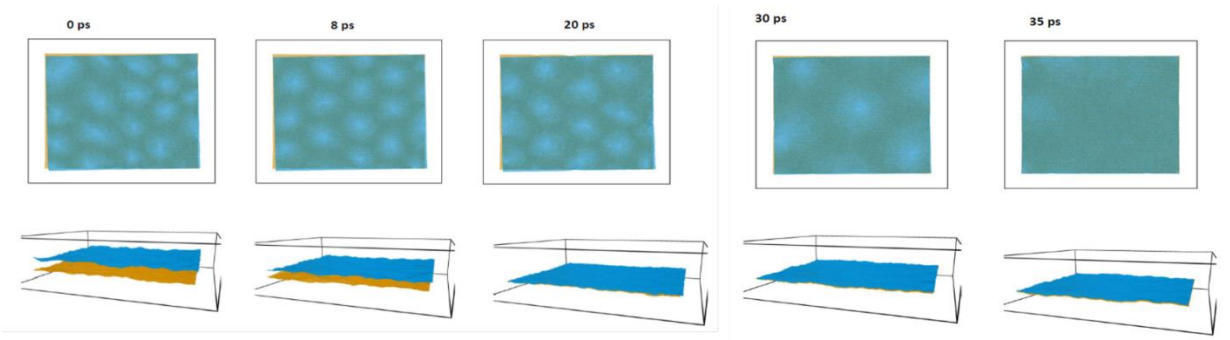

Fig. 4 MD simulations of the top view and side view of two graphene layers moving closer to each other as a function of time. The periodic patterns disappear when two layers touch.

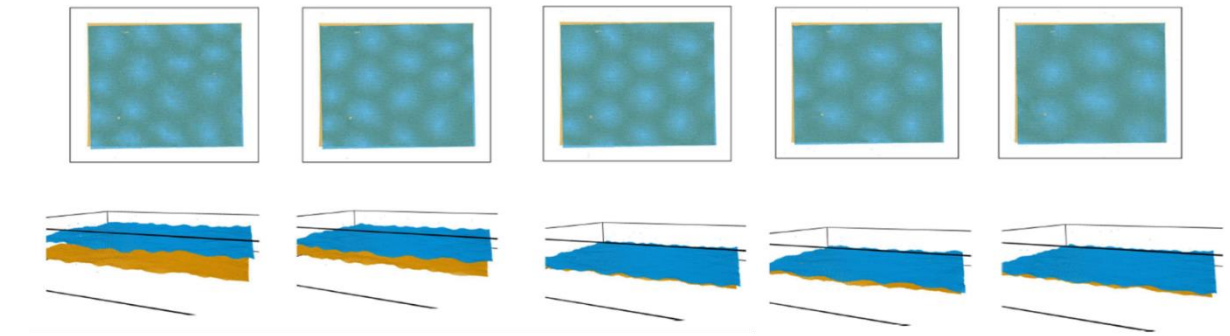

Fig. 5 MD simulations of two irradiated graphene layers moving closer to each other. Prior to movement, the two layers were bombarded with three 50 keV C_{60} clusters which are energetic enough to penetrate through both layers and leave three damage cascade regions on each layer. These damage layers serve as pinning sites to preclude graphene rotation.

Future Plans

The first year has been focused primarily on developing the C_{60} ion source. We are now at the stage to harvest results using this unique capability. We will continue C_{60} ion bombardment on graphene-coated vs. non-coated substrates to study the role of a surface graphene layer on the sputtering mechanism. The study will extend to energy dependence, to confirm the observations from MD simulations. Using cluster ion bombardment to pin two-layer graphene layers is technologically important and its experimental demonstration will be our next focus. We will soon start cluster ion bombardments on well-separated graphene layers for nanopore formation arising from damage cascade explosion. In this exciting task, cluster ions will become dissociated and explode with increasing penetration depth, thereby producing nanopores with sizes first increasing and then decreasing, due to the nature of cluster ion-solid interactions.

References

[1] Y. Cao, V. Fatemi, S. Fang, K. Watanabe, T. Taniguchi, E. Kaxiras, P. Jarillo-Herrero, Unconventional superconductivity in magic-angle graphene superlattices, Nature 556 (2018) 43.

[2] Y. Cao, V. Fatemi, A. Demir, S. Fang. S.L. Tomarken, J. Y. Luo, J.D. Sanchez-Yamagishi, K. Watanabe, T. Taniguchi, E. Kaxiras, R.C. Ashoori, P. Jarillo-Herrero, Correlated insulator behaviour at half-filling in magic-angle graphene superlattices, Nature 556 (2018) 80.

Publications (2018-Present)

[1] X. Zhao, J. Ma, X. Xiao, Q. Liu, L. Shao, D. Chen, S. Liu, J. Niu, X. Zhang, Y. Wang, R. Cao, W. Wang, Z. Di, H. Ly, S. Long, M. Liu, Breaking the current-retention dilemma in cation-based resistive switching devices utilizing graphene with controlled defects, Advanced Mater. 30 (2018) 1705193.

[2] Jing Wang, Di Chen, Lin Shao, The edge effect on structural stability of individual graphene layers in few-layer graphene under electron irradiation, Sci. Rep., under review

[3] Joseph Wallace, Jing Wang, Lin Shao, Irradiation-enhanced torsional buckling capacity of carbon nanotube bundles: a study from molecular dynamics simulations, Carbon, under review.

Toughening mechanisms in ceramic nanocomposites with one and two dimensional reinforcements

Brian W. Sheldon, Huajian Gao, Nitin Padture, Brown University, Providence, RI

Jun Lou, Rice University, Houston, Texas

Program Scope

Although ceramic materials have inherent advantages for applications at high temperatures and in chemically aggressive surroundings, their poor mechanical properties (relative to metals) often prevent implementation in these types of harsh environments. Thus, the research community has long focused on methods for improving these properties, particularly the fracture toughness. Numerous studies have reported evidence of substantial fracture toughness improvements in ceramic nanocomposites reinforced with carbon nanotubes (CNTs), graphene, and reduced graphene oxide (r-GO). However, an understanding of the mechanisms that lead to increased toughness in these types of materials is lacking. In comparison with conventional ceramic composites, reducing the reinforcement dimensions by roughly two orders of magnitude leads to important new questions – in particular, the extent to which existing continuum mechanics laws are applicable. Because the scale over which fracture and decohesion occur are comparable to the reinforcement dimensions (e.g., nanotube diameter or number of graphene layers), phenomena at atomic or near-atomic length scales must now be carefully addressed. Exploring the ways in which these inherently smaller size scales will impact toughening mechanisms is the central motivation of the work being pursued in this project.

In this research, several different processing methods are being employed to carefully control defects and other structural features. These well controlled materials are then being used to enable systematic experiments. Investigations of toughening mechanisms employ *in situ* mechanical testing capabilities that have been developed at both Brown and Rice Universities. This approach allows us to observe and monitor fracture mechanisms in ways that go well beyond prior studies. The experimental investigations are also closely integrated with multiscale modeling efforts. Through this combination of careful processing, in situ testing, and modeling, we expect to greatly expand the existing understanding of nanoscale toughening in ceramic nanocomposites.

Recent Progress

Toughening Mechanisms in CNT Reinforced Ceramics

Ion implantation has been used to modify internal structures, close collaboration with Izabela Szlufarska at the University of Wisconsin (her contributions are supported by a separate DOE-BES award). SiC specimens with and without MWCNT reinforcements were prepared by spark plasma sintering, and then ion-implanted with either protons (p^+) or C^{2+} ions. The implantation depths here are on the order of several microns, and thus large scale fracture tests are not appropriate for investigating the relevant effects. Thus, microcantilevers prepared with FIB milling were employed to investigate fracture. Figure 1 compares the measured bridging toughness contributions with reported ΔK_{IC}^{br} values for ceramics reinforced with randomly oriented MWCNTs. Almost all of the reports are in the range $\Delta K_{IC}^{br} \cong$ 1.5 - 2.5 MPa.m$^{1/2}$. In comparison, the implanted values for the high carbon materials are more than two times larger.

The much higher toughness improvements for the carbon implanted materials are striking. The bridging toughness increase here (4 - 5 MPa.m$^{1/2}$) is more than twice as large as other reliable values for similar MWCNT reinforced ceramics that have been reported in the literature. Raman spectroscopy on materials with and without implantation also reveals important information about changes in the carbon structure. The ratio between the D and G peak intensities can be related to the defect density in the material, and this comparison shows that the ion implantation introduces large numbers of defects. The shift of the G-band to higher wavenumbers is associated with the stress state of the CNTs. Residual stress during the fabrication process occurs because of the CTE difference between SiC and the CNTs. This is calculated to be 0.5 GPa. The ion-implanted composites show much higher residual stresses, up to 5.3 GPa for the higher carbon dosage, which indicates that implantation-induced swelling produces large compressive stresses CNTs. This is one likely cause of the increased toughness. Detailed TEM also shows partial amorphization of the MWCNTs. The combined effects of modifying the reinforcing material's structure and stress state lead to substantial increases in energy dissipation that can be interpreted in terms of changes at the SiC/MWCNT interfaces. However, the interfacial properties here appear to be determined by more than just the atomic scale boundary between the two phases, with toughness improvements that are also due to the changes that occur inside of the MWCNTs. More broadly, this work also shows that controlling defects in MWCNTs can substantially improve mechanical properties compared to what is possible with high quality, low defect density nanotubes.

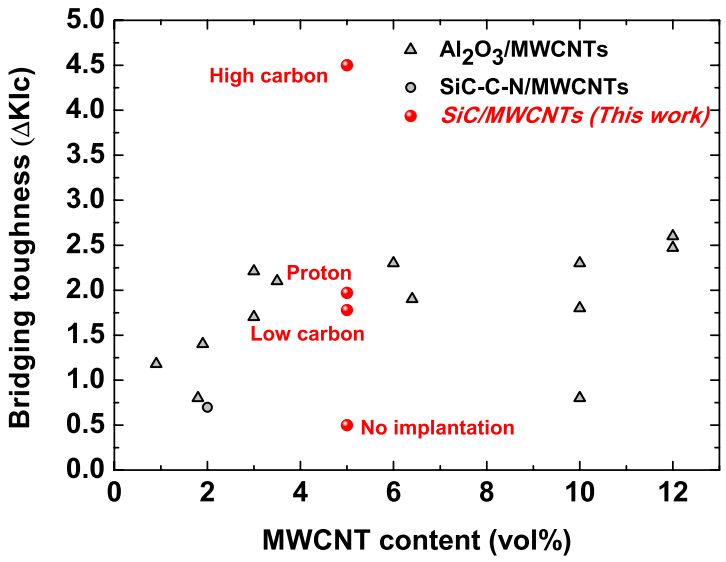

Figure 1. Toughness improvements due to bridging, ΔK_{Ic}^{br}. Ion implantation results are compared to reported ΔK_{Ic}^{br} for other ceramics reinforced with randomly oriented MWCNTs.

Mechanical Behavior of rGO Reinforced Ceramics

Nanocomposites of reduced graphene oxide (rGO) and Al_2O_3 were investigated in terms of the following: (a) process Al_2O_3/rGO nanocomposites with tailored microstructures; (b) evaluate the toughness of these materials; and (c) understand fundamental relationship between the microstructure of these nanocomposites and their fracture toughness.

The toughness measurements were conducted using the surface crack in flexure (SCF) method. These results are summarized in Figure 2. The Al_2O_3/5vol% rGO mixed in ethanol with cross-section orientation (E5-cros) has the greatest toughening effect among all samples investigated to date. It has a fracture toughness of 7.25 MPa·m$^{1/2}$, which is a substantial 190% increase compared to the unreinforced Al_2O_3 matrix (2.50 MPa·m$^{1/2}$). The variations seen in these results indicate that toughening is highly directional for these nanocomposite materials. With the cross-sectional

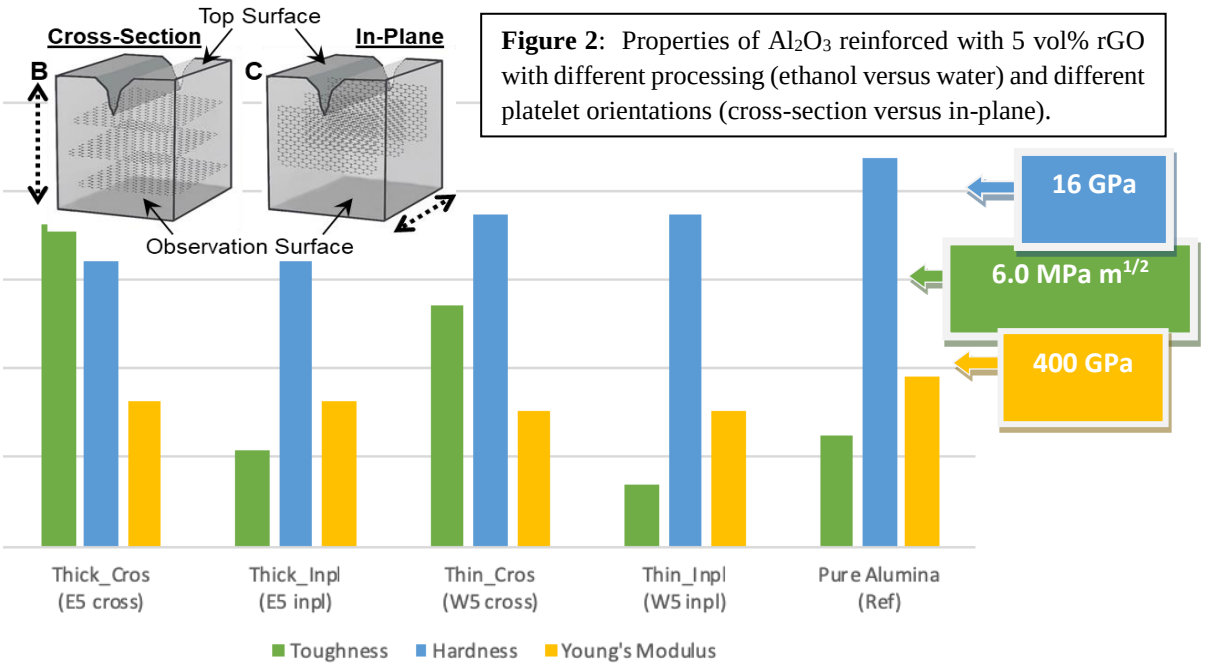

Figure 2: Properties of Al_2O_3 reinforced with 5 vol% rGO with different processing (ethanol versus water) and different platelet orientations (cross-section versus in-plane).

orientation, as the crack propagates it encounters numerous rGO platelets on the surface which prevent the crack from growing.While with the in-plane orientation the crack encounters rGO platelets on the edges, which are the weakest points on rGO layers due to high defect concentration. It is also noteworthy that effective bridging is largely due to the thicker rGO platelets, rather than the thin rGO platelets.

The materials described here provide us with a valuable system for analyzing toughening mechanisms in a ceramic nanocomposite with 2D reinforcements. In particular, the dense alumina/rGO composites with different exfoliation levels prepared by SPS show that both platelet orientation and platelet thickness have a large impact on toughening mechanisms. These effects were not anticipated, and they are currently under further investigation.

Fracture and Interfacial Properties In Individual Reinforcements

A detailed understanding of nanocomposite fracture requires knowledge of the reinforcement properties, including the interfaces which are critically important in dictating the overall composite performance. Careful experiments and modeling to obtain this information are a central component of this program. A major focus over the past year has been study of the shear strength of the interface between h-BN nanosheets (a 2D reinforcement) and a polymer derived ceramic (PDC) matrix. The in-situ mechanical test was carried out in SEM using the Agilent nanoindentation system to quantify the shear strain and shear stress of BN/PDC nanocomposites interface and monitor the pull-out process simultaneously. Interfacial strength can be calculated from these measurements. In addition to the shear at the interface, the elongation of the suspended BN also contributes to the raw displacement. This introduces difficulties in the interpretation of the measured mechanical response. In this regard, seven Pt fiducial markers were deposited on the surface of the BN nanosheet in the FIB system, and the real shear displacement between the BN nanosheet and PDC matrix was determined by image correlation methods. As shown in Figure 3a, the marker 0 served as the reference, since it was not on the movable sample regime at all.

The shear deformation took place at the BN/PDC interface underneath the markers 1 to 5, and the suspended BN with the markers 6 and 7 only experienced elastic elongation. The schematic in Figure 3d shows where all the fiducial markers were deposited. Figure 3b shows the sample under loading and the real displacement of each marker. Figure 3c shows the image of the sample right before it was completely pulled out. The real displacement of each marker is plotted in Figure 3e. As the marker gets closer to the right interface boundary, the displacement gradually increases. At the suspended BN region, the displacement increases linearly. Quantitative interpretation of these measurements is based on a finite element model of the experimental configuration.

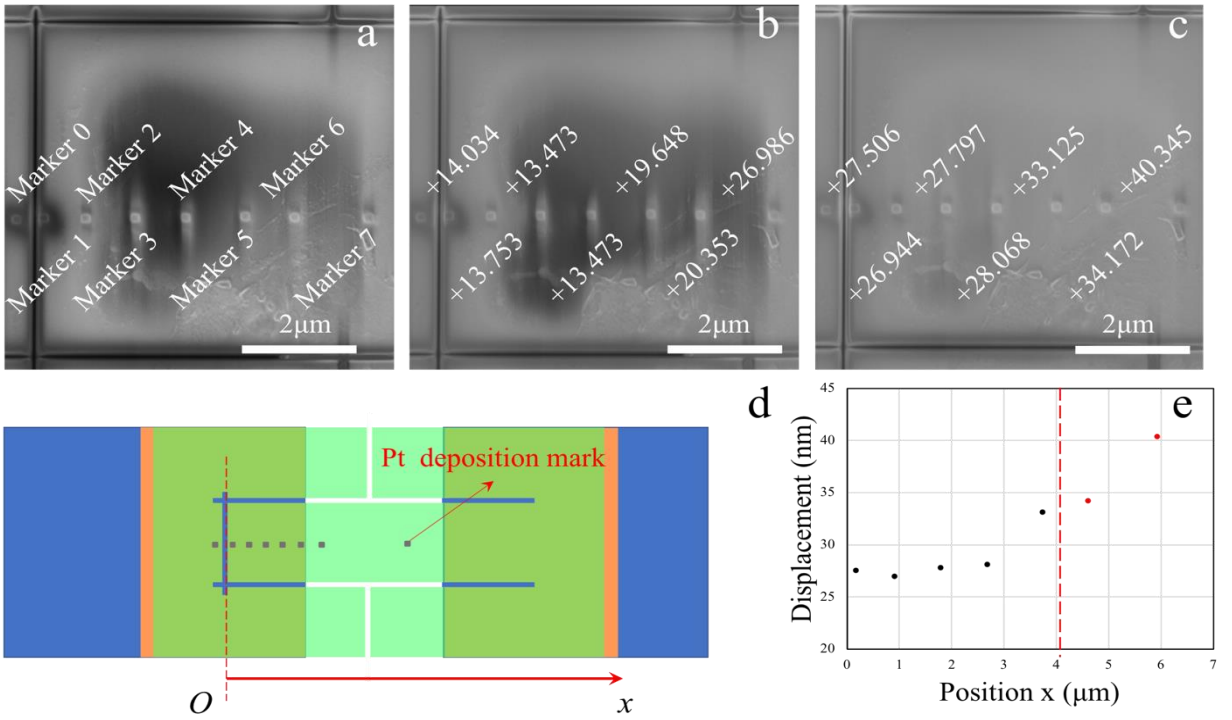

Figure 3. True strain measurement in pull-out tests. (a-c) SEM images of the BN/PDC sample with fiducial markers before the test, under loading and before failure, respectively. (d) Schematic of the BN/PDC sample with fiducial markers. (e) The true displacement of each marker.

Future Plans

Research efforts for the next year are designed to create an integrated understanding of toughening mechanisms in ceramic composites with nanoscale reinforcements. Key activities are:

- Mechanical behavior will be investigated with the unique set of *in situ* methods that have been developed at Brown and Rice. This work includes ongoing modeling efforts, that allow us to better interpret and guide the experimental efforts.
- Carefully controlled modifications of reinforcement properties will address the extent to which interface properties can be decoupled from internal defects.
- Initial evidence indicates that 2-D reinforcements can provide more effective toughening than CNTs. This has opened up a set of questions about nanoscale toughening that we will address with a combination of well-controlled materials, systematic in situ experiments, and detailed modeling. More than 50% of our efforts in the next year will be related to 2-D materials.

Publications

Xin Liang, Yingchao Yang, Jun Lou, and Brian W. Sheldon, "The impact of core-shell nanotube structures on fracture in ceramic nanocomposites", *Acta Materialia* **122**, 82-91 (2017).

Yingchao Yang, Cristina Ramirez, Xing Wang, Zhixing Guo, Anton Tokranov, Ruiqi Zhao, Izabela Szlufarska, Jun Lou, and Brian W. Sheldon, **"**Impact of carbon nanotube defects on fracture mechanisms in ceramic nanocomposites", *Carbon* **115**, 402-408 (2017).

Lukas Porz, Tushar Swamy, Brian W. Sheldon, Daniel Rettenwander, Till Frömling, Henry L. Thaman, Stefan Berendts, Reinhard Uecker, W. Craig Carter, and Yet-Ming Chiang, "Mechanism of Lithium Metal Penetration through Inorganic Solid Electrolytes", *Advanced Energy Materials* **7**, 1701003 (2017).

Cristina Ramírez, Qizhong Wang, Manuel Belmonte, Pilar Miranzo, M. Isabel Osendi, Brian W. Sheldon, and Nitin P. Padture, "Direct *In Situ* Observation of Toughening Mechanisms in Nanocomposites of Silicon Nitride and Reduced Graphene-Oxide", *Scripta Materialia* **149**, 40-43 (2018).

Tushar Swamy, Richard Park, Brian W. Sheldon, Daniel Rettenwander, Lukas Porz, Stefan Berendts, Reinhard Uecker, W. Craig Carter and Yet-Ming Chiang, "Lithium Metal Penetration during Electrodeposition through Single-Crystal Garnet Solid Electrolyte", *J. Electrochemical Society* **165** (16), A3648-A3655 (2018).

C. Sui, Z. Pan, R. J. Headrick, Y. Yang, C. Wang, J. Yuan, X. He, M. Pasquali, J. Lou, "Aligned-SWCNT Film Laminated Nanocomposites: Role of the Film on Mechanical Reinforcement", *Carbon*, Vol. 139, 680-697, 2018. DOI: 10.1016/j.carbon.2018.07.025

C. Sui, Y. Yang, R.J. Headrick, Z. Pan, J. Wu, J. Zhang, S. Jia, X. Li, W. Gao, O.S. Dewey, C. Wang, X.D. He, J. Kono, M. Pasquali, J. Lou, "Directional sensing based on flexible aligned carbon nanotube film nanocomposites", *Nanoscale*, Vol. 10(31), 14938-14946, 2018. DOI: 10.1039/c8nr02137f

E. Hacopian, Y. Yang, B. Ni, Y. Li, X. Li, Q. Chen, H. Guo, J.M. Tour, H. Gao, J. Lou, "Toughening Graphene by Integrating Carbon Nanotubes", *ACS Nano*, Vol. 12(8), 7901-7910, 2018

I.A. Kinloch, J. Suhr, J. Lou, R.J. Young, P.M. Ajayan, *Composites with carbon nanotubes and graphene: An outlook*, Science, Vol. 362(6414), 547-553, 2018. DOI: 10.1126/science.aat7439

Y. Zhou, C. Chen, S. Zhu, C. Sui, C. Wang, Y. Kuang, U. Ray, D. Liu, A. Brozena, U.H. Leiste, N. Quispe, H. Guo, A. Vellore, H.A. Bruck, A. Martini, B. Foster, J. Lou, T. Li, L. Hu, "A printed, recyclable, ultra-strong, and ultra-tough graphite structural material", *Materials Today*, published online, 2019. DOI:https://doi.org/10.1016/j.mattod.2019.03.016

Christos. E. Athanasiou, Tomonori Baba, Cristina Ramirez, Hongliang Zhang, Jianqi Xi, Wei Zhang, Nitin P. Padture, Izabela Szlufarska, Brian W. Sheldon, "Ultra-high toughness nanoreinforced ceramics via ion implantation*", submitted.*

Y. Yang, Z. Song, G. Lu, Q. Zhang, B. Ni, C. Wang, X. Li, L. Gu, X. Xie, H. Gao, J. Lou, "Lattice Asymmetry Induced Intrinsic Toughening and Stable Crack Propagation in Monolayer h-BN", *submitted*.

Qizhong Wang, Cristina Ramírez, Lin Zhang, Connor S. Watts, Oscar Borrero-López , Angel L. Ortiz, Brian W. Sheldon, Nitin P. Padture**, "**Toughening Mechanisms and Sliding-Wear Resistance in Nanocomposites of Alumina and Reduced Graphene-Oxide"*, in preparation.*

Dynamic Fracture in Dealloying Induced Stress Corrosion Cracking

PI: Karl Sieradzki, Fulton School of Engineering, Arizona State University, Tempe, Arizona 85287-6106

Program Scope

When metallic alloys are exposed to a corrosive environment that selectively dissolves one or more of the alloy components, porous nanoscale morphologies spontaneously form that can adversely affect the mechanical integrity of critical engineering structures composed of nickel-base alloys and stainless steels [1]. In order to investigate this phenomenon we use model Ag-Au alloys in order to avoid any possible contribution of hydrogen embrittlement to the cracking mechanism. If this stress-corrosion process were purely electrochemical, a form of Faraday's law would be able to predict the crack propagation rate. However, researchers have shown that Faraday's law can underestimate the cracking rates by factors of 10 – 1000 [2,3]. Consequently, we have hypothesized that there is a pure mechanical component active in this stress-corrosion process [4]. The picture that emerges is the following. A thin dealloyed nanoporous layer (~ hundreds of nanometers in thickness) forms at the tip of an advancing crack within which a high-speed micro-crack is nucleated that is subsequently injected for a short distance into the un-corroded parent phase alloy prior to coming to arrest by plastic processes. This process is discontinuous: a nanoporous layer forms by dealloying corrosion, then the crack propagates exposing more parent-phase to the electrolyte which in-turn corrodes and the cycle repeats [5]. The scope of our program has three primary components.

Sequential ligament tearing and crack injection in dealloying induced stress-corrosion cracking (DISCC): The main aim of this portion of the research is to examine how the current density and the corresponding nanoporous gold (NPG) volume ahead of a crack together with loading conditions (e.g., strain rate) affect the nucleation frequency and distance of crack injection events in to the un-dealloyed parent phase.

Sample size effects on the ductile-brittle transition in NPG: One possible criterion for brittle crack nucleation is connected to attaining a "critical" physical volume of NPG at fixed mean ligament diameter, $\langle \mathcal{L} \rangle$, in front of a propagating stress-corrosion-crack. Based on our previous results for this transition we estimate, for example, that the transition volume for $\langle \mathcal{L} \rangle \sim 150$ nm is about 10^{-11} m^3. We are studying this by examining tensile behavior of 10 μm diameter crack-free monolithic NPG wires.

Room temperature IGSCC of sensitized stainless steel: The room temperature IGSCC of sensitized stainless steels was examined in some detail in the late 1970's and into the 1980's. Since that time most SCC work on stainless steels has focused on cracking that occurs at higher temperature (~300 °C), and in electrolyte chemistries typical of that in power generating nuclear reactors [6]. Importantly, progress in the development of aprotic ionic liquid (iL) electrolytes allows us to separate possible hydrogen effects from the type of stress-corrosion process described above [7]. Aberration-corrected STEM is used to characterize GBs in commercial purity 304 stainless with C contents ~ 0.07 wt% following sensitization and after GB dissolution experiments. Dissolution experiments and SCC experiments are conducted in two general types

electrolytes. One is an aqueous electrolyte containing e.g., 0.5M NaS_2O_3. The other electrolyte is an aprotic iL electrolyte, e.g., 1-butyl methylpyrrolidinium-bis-(trifluoromethylsulfonyl)imide ([BMPyr] [NTf2]).

Recent Progress

Results that we are currently preparing for publication involved dynamic fracture experiments in monolithic NPG samples in an experimental realization of the infinite strip geometry [8]. In this geometry the sample is loaded at fixed displacement and the stored elastic energy per unit area in the sample, *W*, is given by $Eb\varepsilon^2/2(1-\nu^2)$, where all the terms have their usual significance and *b* is the half-width of the strip [9]. While under fixed displacement, a dynamic crack is started by dropping a guillotine across the mid-plane edge of the sample [10]. During the fracture process the crack is interacting with elastic shear waves reflecting from the vertical boundary of the sample, which imparts an inertial term to the crack tip equation of motion. Marder has shown that under these conditions [11]:

$$\Gamma(v) = W\left(1 - \frac{b\dot{v}}{c_l^2}\frac{1}{\left[1-\left(v/c_R\right)^2\right]^2}\right).$$

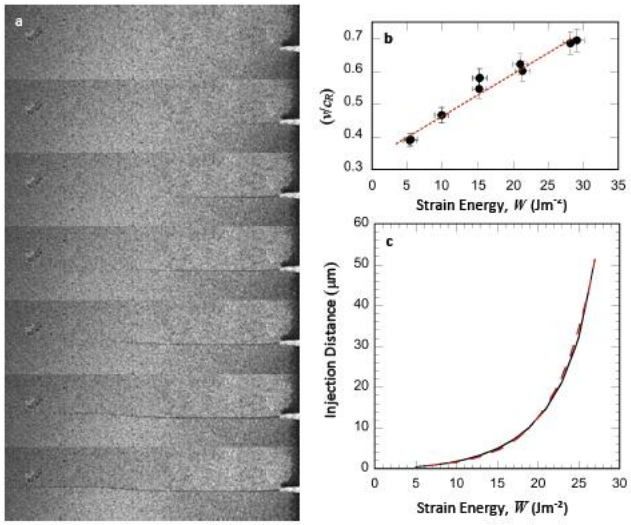

Figure 1 | Results of dynamic fracture tests for the strip geometry. **(a)** Sequential images at 4.34 μs per frame showing crack propagation over ~ 4 mm of crack growth at 200 m/s. **(b)** Summary of the normalized crack velocity ($c_R = 400$ m/s in NPG) as a function of the imposed strain energy, *W*. **(c)** Crack injection distance as a function of the strain energy *W* (or parametrically the exit velocity of a crack from a NPG layer) in the sample for $\Gamma(v) = \Gamma_s(c_R/v)$, where Γ_s corresponds to the energy dissipated in the fracture process for a crack traveling at the Rayleigh wave velocity (1500 m/s) in the undealloyed parent phase. The dashed red line shows an exponential fit with the crack injection distance, $l = 0.22exp(0.20W)$.

Here $\Gamma(v)$ is the energy dissipated per unit area of crack advance, c_l is the longitudinal sound velocity, c_R is the Rayleigh velocity, v is the crack velocity, and $\dot{v}$ the crack acceleration. $\Gamma(v)$ can only be determined experimentally and for the case of a high-speed crack moving in an otherwise ductile solid, this quantity is not accessible. In our application of this equation, the crack exits the NPG with some initial velocity determined by W (see Fig. 1a,b) and enters into the parent phase. Making the substitution, $\dot{v} = vdv/dl$, we have solved this equation for the crack injection distance, as shown in Figure 1c, for various physically motivated forms of $\Gamma(v)$.

Recently, we have become interested in addressing the question of how the parent phase crystallography affects the formation and resulting nanoporous gold morphology. In order to address this we examine dealloying and the resultant NPG structure for two different parent phase crystal structures of the same composition.

The systems that we chose for this study is ordered Cu_3Au that has the $L1_2$ crystal structure and it's disordered counterpart, $Cu_{0.75}Au_{0.25}$ which has a random FCC structure. The reason that we believe that there may differences in resultant NPG morphologies is that the crystallographic orientation of NPG is determined by the orientation of the un-dealloyed parent phase. This is not a surprising given that as the less noble element (say Cu or Ag) is selectively dissolved, Au atoms surface diffuse and effectively epitaxially "deposit" on the un-dealloyed parent phase. Dealloying of the ordered Cu_3Au presents an interesting dilemma in this regard, since this process necessarily results in a phase change from the $L1_2$ parent phase structure to FCC gold. Additionally, the rate of surface diffusion on the ordered and disordered parent-phase "substrates" are likely to be different enough to result in differences in the NPG morphologies.

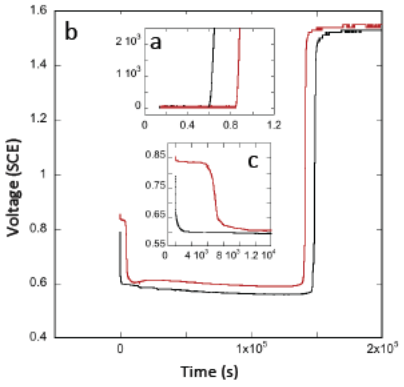

Figure 2 | Dealloying of ordered and disordered Cu3Au. (a) inset shows LSV. **(b)** CP at 1 $mAcm^2$ **(c)** inset shows a magnified view of the first 12,000 s of CP.

Cu-Au alloy sheets of 75 at.% copper and 25 at.% gold were cut, polished with 0.05 µm alumina suspension, and encapsulated in quartz ampules that were evacuated and backfilled with a mixture of 5% H_2 and Argon (by volume). The samples to be structurally ordered were heat treated at 850°C for 72 hours, lowered to 380°C, held for 72 hours, and then slowly cooled by lowering the temperature 10°C every 24 hours to room temperature. This heat treatment protocol takes about 30 days to complete. The samples to have a disordered crystal structure were heat treated at 850°C for 72 hours and water quenched. Electron dispersive spectroscopy (EDS) was used to ascertain the compositional homogeneity of the samples, prior to and post dealloying. X-ray diffraction (XRD) was used to confirm whether or not long range ordered and disordered structures were obtained.

All of the EDS measurements showed that to within ± 1 at.% the composition of both alloy sets prior to and post dealloying was compositionally uniform. Figure 2a shows the linear sweep voltammetry (LSV) for these sets of alloys in in 0.5M Na_2SO_4 + 0.5M H_2SO_4. The results show a difference in critical potentials of 250 mV. In order to insure equal dealloying rates, the ordered and disordered samples were dealloyed at a fixed current density of 1 mA/cm^2. Following this dealloying protocol, EDS showed that in each of the alloys the NPG structures retained ~ 1at.% Cu. Figure 2b shows representative chronopotentiometry (CP) for this process. Figure 2c is a magnified view of the first 12,000 s of dealloying. These results reveal that dealloying in each of the alloys is a two-stage process. The first stage shows a variation in voltage at fixed current density and the second stage occurs virtually at constant voltage. In the first stage, the process is activation controlled, while the second stage, is controlled by a surface diffusion process. We speculate that the ~ 30 mV difference in potential between the ordered and disordered alloy observed in the second stage reflects the difference in the activation energies for surface diffusion. A brief summary of our morphology results is presented in Figure 3.

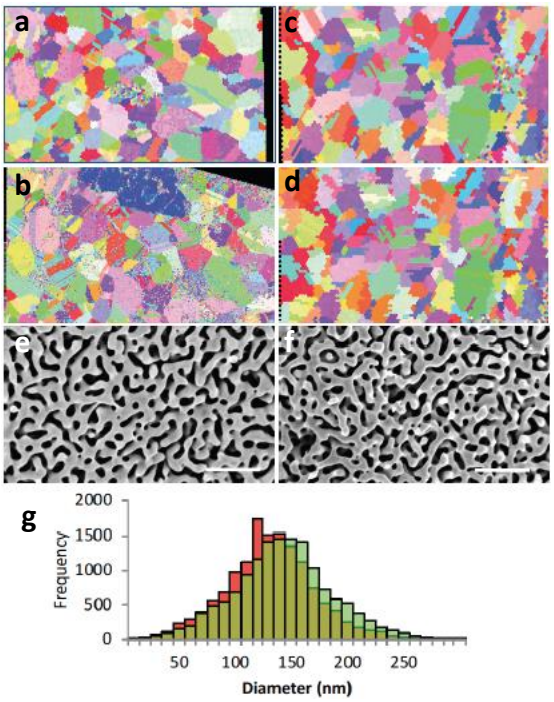

Figure 3 | Dealloyed morphology following 2 x **10^5 s of dealloying of ordered and disordered Cu_3Au. (a)** EBSD of the ordered alloy prior to and **(b)** after dealloying. **(c)** EBSD of the disordered alloy prior to and (**d)** after dealloying. **(e)** NPG morphology of the ordered alloy. Scale bar 100 μm. **(f)** NPG morphology of the disordered alloy. Scale bar 100 μm. **(g)** Superimposed ligament diameter distribution of the ordered alloy (red) and the disordered alloy (green).

Future Plans

- Sequential ligament tearing and crack injection in experiments aimed at defining the loading parameters for the frequency of current transients and sequential ligament tearing in the SCC of single crystal Ag-Au alloys.
- Characterization of GB porosity of sensitized 304 stainless steel (in collaboration with PNNL) and stress corrosion cracking of this material in aqueous and ionic liquid electrolytes.
- Mechanical testing of monolithic NPG with the aim of elucidating sample size effects on the ductile-brittle transition.
- Development of a quantitative model of dealloying induced SCC.
- Completion of the work examining NPG formed from ordered and disordered Cu-Au alloys.

References

[1] Badwe, N., Chen, X, Schreiber, D.K. Olszta, M.J., Overman N.R., Karasz, E.K., Tse, A.Y., Bruemmer, S.M., Sieradzki, K., *Nat. Mater.*,**17,** 887-893 (2018).
[2] Stewart, J., Wells, D.B., Scott, P.M., & Williams D.E., *Corros. Sci*., **33,** 73-88 (1992).
[3] Serebrinsky, S. A. & Galvele, J. R. *Corros. Sci*. **46**, 591–612 (2004).
[4] Sieradzki, K., & Newman, R.C. *Philos. Mag*. **A51,** 95-132 (1985).
[5] Sun, S., Chen, X., Badwe, N. & Sieradzki, K. Potential-dependent dynamic fracture of nanoporous gold. *Nat. Mater.* **14**, 894-898 (2015).
[6] Bruemmer, S.M., Olszta, M.J., Toloczko, M.B. & Schreiber, D.K, *Corros. Sci*., **131,** 310-323 (2018).
[7] Dilasari, B., Jung, Y. &Kwon, K., *Electrochem. Comm*., **73,** 20-23 (2016).
[8] Chen, X, Karasz, E.K, Sieradzki *in preparation*
[9] J. R Rice, "Mathematical Analysis in the Mechanics of Fracture", Chapter 3 of Fracture: An Advanced Treatise (Vol. 2, Mathematical Fundamentals) (ed. H. Liebowitz), Academic Press, N.Y., 1968, pp. 191-311.

[10] Goldman, T. Livine, A., Fineberg, J., Acquisition of Inertia by a Moving Crack, Phys. Rev. Lett., **104,** 114301 (2010).
[11] Marder, M., *Philos. Mag*. B, **78,** 203-214 (1998).

2-Year List of Publications

N. Badwe, X. Chen, K. Sieradzki, *Mechanical Properties of Nanoporous Gold in Tension*, Acta Materialia, Vol. 129, 251-258 (2017).

N. Badwe, X. Chen, D.K. Schreiber, M.J. Olszta, N.R. Overman, E.K. Karasz, A.Y. Tse, S.M. Bruemmer, K. Sieradzki, *Decoupling the role of stress and corrosion in the intergranular cracking of noble-metal alloys*, Nat. Mater., Vol. 17, 887-893 (2018).

Role of nanoscale coherent precipitates on the thermo-mechanical response of martensitic materials

Alejandro Strachan (PI), Michael Titus (Co-PI)
School of Materials Engineering, Purdue University, Indiana USA

Program Scope

Martensitic phase transitions are first order, diffusionless, solid-to-solid, transformations that underlie shape memory, superelasticity, and strengthening in modern steels, impacting a wide range of technologies. While shape memory and superelasticity in traditional alloys are well understood from a mechanistic point of view,[i,ii] recent unexpected results by our group and others indicate a much richer set of phenomena yet to be characterized and with significant potential to result in unprecedented properties. Specifically, martensitic materials with coherent precipitates or nanoscale variations in composition have been experimentally shown to exhibit uncharacteristic martensite microstructures,[iii] broad diffraction patterns,[iv] anomalous softening and continuous stress-induced transformation.[v] From an applied point of view, ultra-high fatigue resistance[vi] and low stiffness with high strength[v,vii] have been demonstrated in martensites with coherent second phases. With on-going support from BES, PI Strachan and his group used theory and high-fidelity atomistic simulations to demonstrate that a tailored coherent second phase can modify the *free energy landscape* that governs the martensitic transformation and achieve notable changes in response. Our team demonstrated the ability to control the hysteresis and temperature of the phase transition[viii,ix], and the design of metamaterials with ultra-low stiffness.[vii] We predicted Young's moduli as low as 2GPa, a value typical of soft materials, in full density and strength metallic nanomaterials. This remarkable result is possible by the stabilization of a thermodynamically unstable state with negative stiffness via interfacial stresses caused by a coherent second phase.

In summary, coherent second phases can have a profound effect on the properties and performance of martensitic materials and we lack a comprehensive, mechanistic understanding of the underlying processes. This limits our ability to rationally design second phases to tailor the response of martensitic materials. To address this situation, this project will develop a mechanistic, predictive understanding of the thermal and mechanical response of martensitic materials with nanoscale coherent heterogeneities, see Figure 1. A synergistic combination of atomistic simulations and experiments will be used to relate the local properties of each phase (in particular, their free energy landscape) and the material nanostructure (volume fraction, shape and size of second phase precipitates, and defects that may disrupt coherency) to the overall materials response. The focus will be on second phases expected to induce phenomena or properties not otherwise achievable: second order martensitic transformation in SMAs, ultra-low stiffness, increased control of transition temperatures, and fatigue resistance.

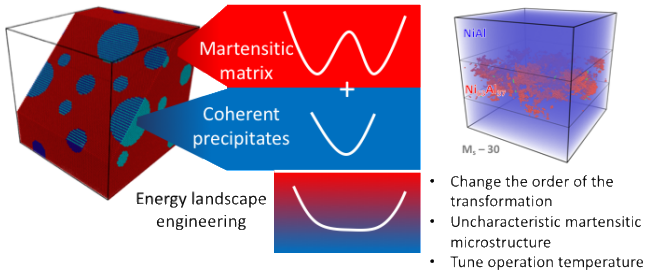

Figure 1. Project overview. White lines represent the free energy as a function of lattice parameter in the martensitic phase and in the coherent precipitates. Their combined landscapes (bottom) can exhibit properties not achievable otherwise.

Recent progress

This poster summarizes the main results of our team over the last two years, including preliminary results from a newly added experimental effort. The poster will be organized along three complementary topics.

Modifying the nature of martensitic transformations

Phase transformations are fascinating from a scientific point of view and critical for human development, from the production of early bronzes to today's phase change materials used in nanoelectronics[1] and ferroelectrics.[2,3,4] Solid-to-solid martensitic transformations in metallic alloys underlie shape memory, superelasticity, and strengthening in many high-performance steels.[5,6] Quite remarkably, while most phase transformations, e.g. ferroelectric or ferromagnetic, can be of first order (i.e. involve discontinuous jumps in properties) or second order (continuous), martensitic transformations in metallic alloys are nearly universally first order. While specific compositions can lead to continuous behavior[7], we lack an external field to tune the nature of these transformations and achieve criticality as in the vast majority of cases. In this Letter, we demonstrate that epitaxial stress originating from the incorporation of a tailored second phase can modify the free energy landscape that governs the phase transition in martensitic alloys and change its order from first to second. High-fidelity molecular dynamics (MD) simulations show a remarkable change in the character of the martensitic transformation in Ni-Al alloys near the critical point. We observe continuous transformation, uncharacteristic martensitic microstructures, and scaling described by power-law exponents comparable to similar transitions. This work provides a theoretical foundation for recent and quite unexpected experimental and computational results.

Martensitic transformation and role of interfacial strain in lightweight MgSc alloys

Low density makes Mg-Sc shape memory alloys attractive for a wide range of applications, but the use of these alloys is hindered by a low martensitic transformation temperature (173K). We use density functional theory to characterize the energetics associated with the martensitic transformation in a Mg-Sc (19.44 at.% Sc) alloy from a disordered body centered cubic (BCC) austenite to a disordered orthorhombic martensite. The simulations predict lattice parameters and diffraction patterns in good agreement with experiments and the martensite to be 10.5 meV/atom lower in energy than austenite at 0 K, consistent with the low martensitic transformation temperature. We explore the effect of epitaxial strain on the relative energy between the two phases with the objective of increasing the martensitic transformation temperature. Compressive strain along [100] and tensile strain along $[0\bar{1}1]$ on the closest packed plane (011) stabilize the martensite phase with respect to austenite. Bi-axial strain between 5 and 7% increases the zero-temperature energy difference between the phases by over 60%. Similar stabilization of the martensite phase can be achieved by the addition of pure Mg as a coherent second phase. Superlattices with 50 at. % Mg results in an energy difference of 18.1 meV/atom between the two phases at zero temperature. These results indicate that coherency strains can be used to increase the martensitic transformation and operation temperature of Mg-Sc alloys to room temperature.

Fabrication and characterization of alloys with coherent second phase

Using thermodynamic databases to guide alloy design, a series of Ni-Al + (Cu,Ti) alloys have been fabricated to investigate the role of a coherent second phase embedded within a known shape memory alloy matrix. The alloys consist of a B2-(NiAl) matrix with and without nanometer-

scale $L2_1$-(Ni_2AlTi) precipitates. To precipitate the $L2_1$ phase, we have performed a series of heat treatments 1000, 1100, and 1200 °C, followed by water quenching. Preliminary results indicate a fine dispersion of coherent $L2_1$ precipitates embedded in the B2-(NiAl) matrix. If the precipitates exhibit a $(100)_{B2} \parallel (100)_{L21}$ - $<100>_{B2} \parallel <100>_{L21}$ orientation relationship, the precipitates are expected to enable low-stiffness materials based on strain energy calculations. While the additions of Ti and the coherent $L2_1$ precipitates are expected to stabilize the austenite phase and decrease the M_s temperature, we anticipate that Cu additions will help to stabilize the martensitic phase and offset or even raise the M_s temperature. However, no shape memory behavior has yet to be observed, even as low as -150 °C. We believe this may be due oxygen uptake during annealing at elevated temperatures. Heat treatments are currently being conducted in protective atmospheres to prevent oxygen uptake, and micro/nanoindentation will be performed as a function of temperature to investigate alterations to elastic modulus.

Future Plans

Having demonstrated the effect of coherent second phases on martensitic transformation in simple geometries, the main focus of the theoretical work will now switch to characterizing the effect of microstructure. Specifically, we seek to characterize the effect of defects that affect coherency, such as interfacial dislocations, on the effect of the second phase. In addition, new alloys with coherent second phases are being developed, and non-conventional processing paths are being explored to fabricate nanolaminate materials.

References cited

[i] Bhattacharya, K., Conti, S., Zanzotto, G. & Zimmer, J. Crystal symmetry and the reversibility of martensitic transformations. *Nature* **428,** 55 (2004).

[ii] Bhattacharya K, Microstructure of martensite: why it forms and how it gives rise to the shape-memory effect, Oxford University Press (2004).

[iii] Cui, J. P., Hao, Y. L., Li, S. J., Sui, M. L., Li, D. X., & Yang, R, Reversible movement of homogenously nucleated dislocations in a β-titanium alloy. *Physical review letters*, *102*(4), 045503 (2009).

[iv] Wang, H. L. *et al.* Elastically confined martensitic transformation at the nano-scale in a multifunctional titanium alloy. *Acta Materialia* **135,** 330–339 (2017).

[v] Hao, Y. L. *et al.* Superelasticity and Tunable Thermal Expansion across a Wide Temperature Range. *Journal of Materials Science & Technology* **32,** 705–709 (2016).

[vi] Chluba, C. et al. Ultralow-fatigue shape memory alloy films. Science. **348**, 1004–1007 (2015).

[vii] Reeve, S. T., Belessiotis-Richards, A. & Strachan, A. Harnessing mechanical instabilities at the nanoscale to achieve ultra-low stiffness metals. *Nat. Commun.* **8,** 1137 (2017).

[viii] Guda Vishnu, K. & Strachan, A. Shape memory metamaterials with tunable thermo-mechanical response via hetero-epitaxial integration: A molecular dynamics study. J. Appl. Phys. **113**, 103503 (2013).

[ix] Reeve, S. T., Guda Vishnu, K., Belessiotis-Richards, A. & Strachan, A. Tunability of martensitic behavior through coherent nanoprecipitates and other nanostructures. *Acta Materialia* **154**, 295-302 (2018).

Publications

1. “Tunability of martensitic behavior through coherent nanoprecipitates and other nanostructures” Samuel T Reeve, KG Vishnu, A Belessiotis-Richards, A Strachan, Acta Materialia. (2018).
2. “Harnessing mechanical instabilities at the nanoscale to achieve ultra-low stiffness metals”, Samuel T Reeve, A Belessiotis-Richards, A Strachan, Nature Communications 8 (1), 1137 (2017).

Coupled Effects of Radiation and Chemical Environment on Interfaces in SiC

PI: ***Izabela Szlufarska***
Department of Materials Science & Engineering, University of Wisconsin – Madison

Program Scope

High-temperature ceramics are a promising class of materials for applications in advanced nuclear reactor systems. These materials have been studied in the context of various high-temperature applications, including jet engines, gas turbines for electrical power and steam generation, and thermal coatings for hypersonic vehicles. However, an important distinguishing feature of nuclear applications is that the promising properties of these materials (i.e., corrosion resistance, mechanical strength) have to be maintained during irradiation. Not surprisingly, lack of understanding of corrosion of ceramics under reactor environments has been identified as a critical knowledge gap in the design of ceramic composites for nuclear applications. Preferential corrosion of interfaces, such as grain boundaries (GBs) and fiber/matrix interphase in composites, can lead to a subcritical crack growth and therefore understanding of corrosion is also important for design of materials with superior mechanical strength.

The goal of this project is to develop a scientific basis for design of ceramic materials that can withstand the harsh conditions of nuclear reactors, including radiation, high-temperature, and corrosive environments. The current focus of this project is on discovering structural and chemical changes that takes place at ceramics interfaces during irradiation and on how these radiation-induced changes impact environmental degradation.

Recent Progress

We have previously shown that there is radiation-induced segregation (RIS) in SiC, which is surprising given that it is a line-compound and that segregation of constituent species has not been previously reported in ceramics. The limitations of our earlier results were that we demonstrated this effect on a small number of samples (one GB for each temperature) and that we did not investigate the GB type (which was challenging to determine in our earlier experiments). We have now confirmed the presence of RIS effect on a larger number of samples and demonstrated that the observed effects are not due to the different GB types investigated at each temperature. We have also discovered that RIS does depend on the GB type. Specifically, the effect is pronounced on random high-energy GBs (the majority of GBs in SiC) but it is absent in small-angle tilt and twin boundaries in this material (***Figure 1***). A manuscript on this topic is being revised. These results are consistent with predictions from our multiscale models (also supported by this project) that showed evolution of chemical and structural evolution of GBs under irradiation [1, 2].

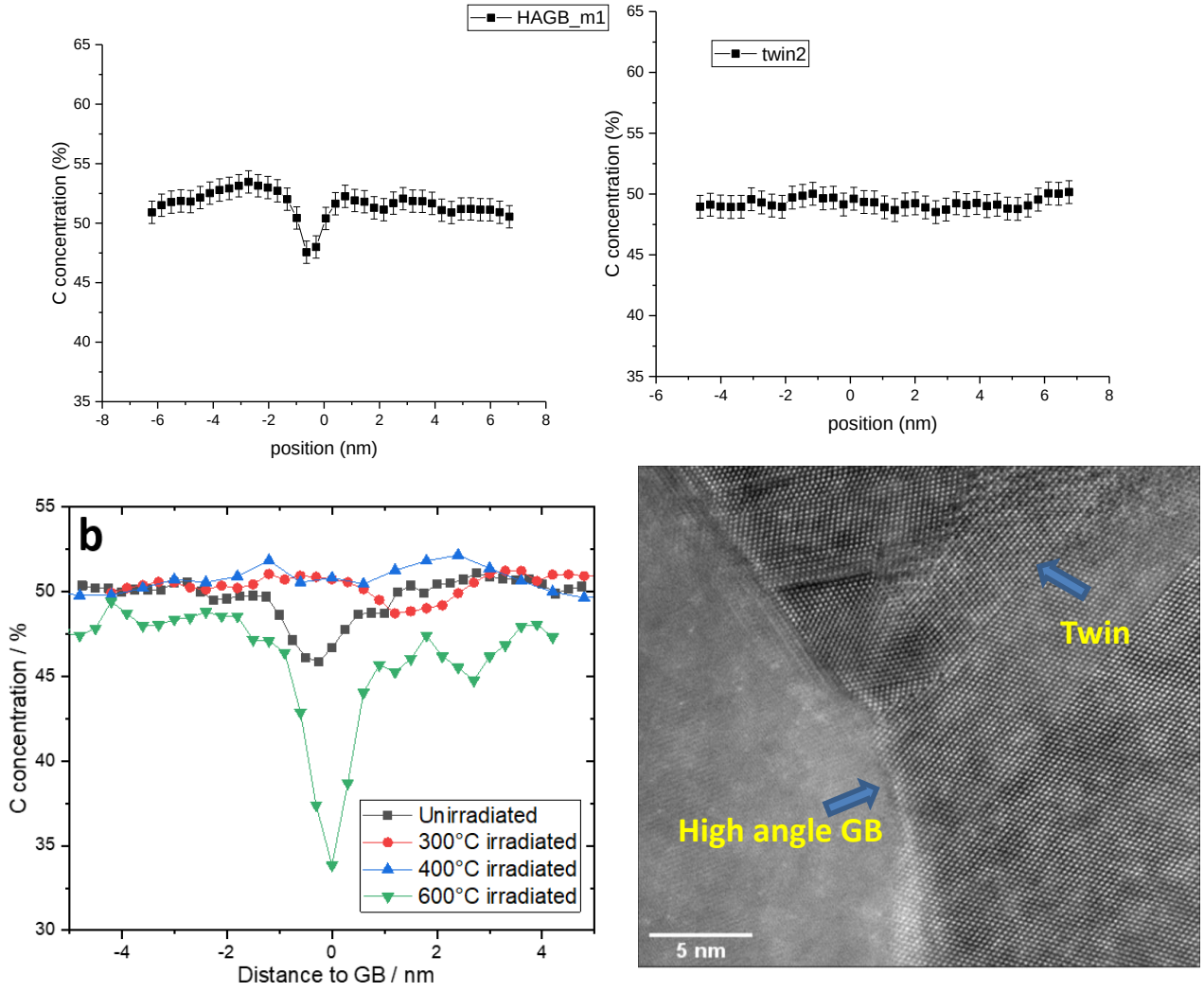

Figure 1 RIS in SiC demonstrated on multiple GBs. Top row shows concentration profiles determined using electron energy loss spectroscopy near unirradiated GBs in CVD grown SiC. High energy GBs are consistently depleted in C, which is not true of low-angle and twin GBs. Bottom left shows changes in concentration profile as a function of irradiation temperature. RIS is found to be a non-monotonic function of temperature. Bottom right: high resolution TEM showing interfaces in SiC.

We have made the following advances toward understanding how radiation-induced defects (including those in GBs) and corrosion are coupled to each other: (i) we provided fundamental insights into mechanisms of environmental degradation of SiC surfaces in molten salts [3], dry oxygen [4], and high-temperature water [5] (major environments relevant for applications in nuclear reactors); (ii) we determined how GBs affect environmental degradation (focusing for now on dry oxidation); and (iii) we predicted through simulations the impact of RIS (discovered and experimentally confirmed in this project) on oxidation.

As an example of fundamental insight into corrosion mechanisms, I will discuss the case of hydrothermal corrosion. Under hydrothermal conditions, protective oxide layer does not form

on SiC and it has been postulated that SiC either directly dissolves into the water or it forms an oxide that then immediately dissolves. Understanding fundamental mechanisms of dissolution is an important first step to determine how these mechanisms depend on the microstructure (e.g., the presence of GBs), the coolant chemistry, or radiation-induced defects in the solid. This understanding can also provide guidance as to conditions under which an oxide film will form on ceramics exposed to water.

We have broken down the corrosion process of ceramics in water into three stages: (1) water dissociation on the surface; (2) chemical attack of the surface that involves breaking of bonds and formation of new surface species; (3) transition of surface species into an oxide or dissolution of surface species into water. So far, we succeeded in addressing the first two stages.

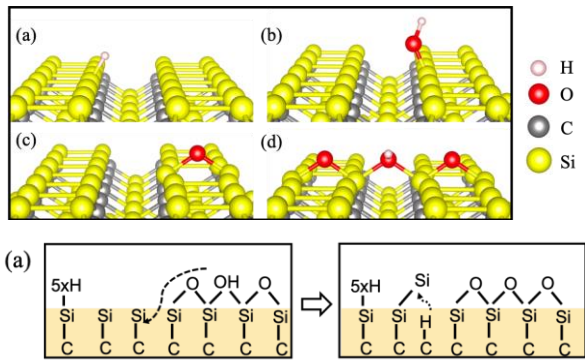

Figure 2 Top row: Possible products of water dissociation on SiC surface. Bottom row: Schematic representation of the H scission reaction.

It has been hypothesized that water attack on SiC occurs by oxygen from H_2O molecules breaking Si-C back-bonds and being incorporated into the sub-surface region. This kind of mechanism has been previously proposed and confirmed on Si. We discovered that in the case of SiC, oxygen attack in pure water is energetically unfavorable. Instead attack of water on SiC occurs by hydrogen scission reaction in which H from a H_2O molecule breaks a Si-C bond, pushing out Si above the surface and making Si vulnerable to further chemical reactions with water. We found that multiple subsequent scission reactions occur and facilitate formation of $Si(OH)_3$ motifs, which are known to be precursors to oxide formation and/or dissolution. Using a combination of reactive force fields in classical molecular dynamics (MD) simulations and DFT calculations we discovered that H scission reaction is initiated by metastable species (i.e., hydroxyl bridge Si–OH–Si) formed on the surface of SiC during water dissociation. Interestingly, this species have not been previously reported and they have been found for the first time in our MD simulations. The reason is that these species are not stable in isolation and most (if not all) of the earlier DFT calculations of water dissociation on SiC surface were performed for a single H_2O molecule. Using DFT calculations we confirmed earlier predictions of the three most stable species, i.e., -H, -OH, and Si-O-Si bridge. The Si-O-Si is most stable and is likely to be the dominant species on a corroding SiC surface. It turns out that as the concentration of Si-O-Si bridges increases, a new metastable species is stabilized (Si-OH-Si bridge) and it can form even on MD time scales in high temperature water. The Si-OH-Si bridge can subsequently transforms to a more stable Si-O-Si bridge and the released H atom either passivates available surface sites or attacks the Si-C back-bond through H scission reaction. H scission reaction is energetically unfavorable from the other stable species on a perfect SiC surface. H scission is schematically shown in Fig. 2.

To understand the effect of GBs on environmental degradation, we have performed MD simulations of oxidation of bicrystals with coherent and incoherent GBs. Briefly, we have found that incoherent GBs provide a faster oxidation path than the single crystal whereas coherent GBs do not accelerate oxidation [4]. We have also considered the effect of radiation-induced defects on oxidation. In single crystal SiC, all point defects were found to accelerate oxidation. Interestingly, the situation is different in the case of GB. We discovered that C antisites in incoherent GBs (C segregates to GBs due to RIS – see Fig. 1) suppress oxidation rate in comparison to stoichiometric GBs. The key to fast oxidation along GBs is the presence of a continuous path of highly-reactive Si atoms (Si atoms are preferred by oxygen) and introducing C atoms disrupts this fast oxidation pathway [6].

Future Plans

- Fabricate SiC bicrystals to control GB type and determine if GB can be engineered to control RIS.
- Irradiate bicrystals and determine the effects of radiation on GB corrosion.
- Understand the role of SiC/carbon nanotube (CNT) interfaces on radiation resistance of SiC/CNT composites. We have found [7] in collaboration with Prof. Brian Sheldon from Brown University (results not shown in this abstract) that radiation-induced defects in SiC/CNT composites significantly increase fracture toughness. They key to this exciting phenomenon is radiation-induced swelling of CNTs and evolution of the SiC/CNT interfaces. We plan to investigate these processes in detail with both simulations and experiments and to determine if such composites could have a better resistance to radiation-induced amorphization than pure SiC.

References

1. H. Jiang and I. Szlufarska, *"Small-angle twist grain boundaries as sinks for point defects"*, Scientific Reports 8, 3736 (2018)
2. H. Jiang, X. Wang, I. Szlufarska, "*The Multiple Roles of Small-Angle Tilt Grain Boundaries in Annihilating Radiation Damage in SiC",* Scientific Reports, 7, 42358 (2017)
3. J. Xi, H. Jiang, C. Liu, D. Morgan, I. Szlufarska, "*Corrosion of Si, C, and SiC in molten salt",* Corrosion Science, 146, 1-9 (2019)
4. C. Liu, J. Xi, I. Szlufarska, "*Sensitivity of SiC grain boundaries to oxidation"* J. Phys. Chem. C**,** 123, 11546-11554 (2019)
5. J. Xi, C. Liu, D. Morgan, I. Szlufarska, "*Molecular mechanisms of early oxidation of SiC in high-temperature water",* Submitted (2019)
6. C. Liu, J. Xi, I. Szlufarska, "*Effect of point defects on oxidation of 3C-SiC",* To be submitted (2019)
7. C. E. Athanasiou, H. Zhang, C. Ramirez, J. Xi, T. Baba, X. Wang, W. Zhang, N. P. Padture, I. Szlufarska, B. Sheldon, "*Ultra-high toughness ceramic nanocomposites via ion implantation",* Submitted (2019)

Publications

1. H. Jiang, X. Wang, I. Szlufarska, *The Multiple Roles of Small-Angle Tilt Grain Boundaries in Annihilating Radiation Damage in SiC,* ***Scientific Reports***, 7, 42358 (2017)
2. Ko, H., Kaczmarowski, A., Szlufarska, I. & Morgan, D. *Optimization of self-interstitial clusters in 3C-SiC with genetic algorithm*. ***J. Nucl. Mater.*** 492, 62-73 (2017)
3. Tangaptjaroen, C., Grierson, D., Shannon, S., Jakes, J. & Szlufarska, I. *Size effects in nanoscale wear of silicon carbide*. ***ACS Applied Materials and Interfaces*** 9, 1929-1940 (2017).
4. Y. Yang, C. Ramirez, X. Wang, Z. Guo, A. Tokranov, R. Zhao, I. Szlufarska, J. Luo, B. W. Sheldon, *Impact of Carbon Nanotube Defects on Fracture Mechanisms in Ceramic Nanocomposites*, ***Carbon*** 115, 402-408 (2017)
5. M-J. Zheng, X. Wang, I. Szlufarska, D. Morgan, *Continuum model for hydrogen pickup in zirconium alloys of LWR fuel cladding* ***J. Appl. Phys.*** 121, 135101 (2017)
6. H. Jiang and I. Szlufarska, *Small-angle twist grain boundaries as sinks for point defects*, ***Scientific Reports*** 8, 3736 (2018)
7. C. Liu and I. Szlufarska, *Distribution of defect clusters in the primary damage of ion irradiated 3C-SiC,* ***J. Nuclear Mat.*** 509, 392-400 (2018)
8. D. R. Sahoo, I. Szlufarska, D. Morgan, N. Swaminathan, *Role of pre-existing point defects on primary damage production and amorphization in silicon carbide*, ***Nuclear Inst. And Methods in Physics Research B,*** 414, 45-60 (2018)
9. J. Xi, H. Jiang, C. Liu, D. Morgan, I. Szlufarska, *Corrosion of Si, C, and SiC in molten salt****, Corrosion Science***, 146, 1-9 (2019)
10. C. Liu, J. Xi, I. Szlufarska, *Sensitivity of SiC grain boundaries to oxidation* ***J. Phys. Chem. C,*** 123, 11546-11554 (2019)
11. C. E. Athanasiou, H. Zhang, C. Ramirez, J. Xi, T. Baba, X. Wang, W. Zhang, N. P. Padture, I. Szlufarska, B. Sheldon, *Ultra-high toughness ceramic nanocomposites via ion implantation*, ***Submitted*** (2019)
12. J. Xi, C. Liu, D. Morgan, I. Szlufarska, *Molecular mechanisms of early oxidation of SiC in high-temperature water*, ***Submitted*** (2019)

<u>To be submitted</u>

13. C. Liu, J. Xi, I. Szlufarska, *Effect of point defects on oxidation of 3C-SiC*, To be submitted (2019)
14. X. Wang, Hao Jiang, Cheng Liu, Juan-Carlos Idrobo, Dane Morgan, Paul M. Voyles, Izabela Szlufarska ***"****Radiation-induced compositional evolution of grain boundaries in 3C-SiC"*, To be submitted (2019)

Grain Boundary Microstates: Exploring the Metastability of Sink Efficiency

PIs: Mitra Taheri (Johns Hopkins), Jaime Marian (UCLA), & Dave Srolovitz (U. Penn)

Despite a history of research linking grain boundary (GB) structure to its effect on properties (such as radiation-induced segregation), defect absorption rates do not follow a clear trend with macroscopic GB descriptors (misorientation, inclination). Recent simulations that classify GBs according to microstates, or phases, present an opportunity to sharpen our understanding of sink efficiency, to explain the resulting denuded zone variations, and to glean a predictive understanding of interfaces to realize radiation tolerant microstructures. GB stability may be defined as the ability of a GB to continue to absorb point defects without becoming saturated and without changing its macroscopic degrees of freedom (misorientation, inclination), or "DOFs." To maintain "stability," we hypothesize that GBs evolve metastable microstates as point defects are added to the GB. Our preliminary work suggests that adding or removing atoms can change the GB microstate, and that the impact of changes of such GB microstates on the ability of GBs to influence radiation damage or how radiation damage leads to evolution of the micro-states. *It is this interplay between GB microstates and radiation damage that is our focus. In particular, our goal is to understand the role that damage plays in inducing these metastable microstates that will allow for their possible use as building blocks toward damage tolerant microstructures.*

This project is just starting.

Disorder & Diffusion in Complex Oxides: Towards Prediction & Control

Blas Pedro Uberuaga, Los Alamos National Laboratory

Program Scope

Complex oxides such as pyrochlores and spinels have multiple technological applications, including nuclear waste forms, ionic conductors, and magnets. Factors such as cation disorder and microstructure are critical for performance. However, there is still much that is not understood about the relationship between cation arrangements and mass transport, particularly for complex oxides containing multiple A and/or B cations. We postulate that these types of chemistries can form ordered superstructures with their own mass transport characteristics. Further, we can induce these superstructures using irradiation. We pursue an integrated experimental and theoretical effort that examines the structure/property relationship between cation arrangements and mass transport. We use irradiation to induce both metastable structures and thermodynamically preferred structures inaccessible via conventional synthesis routes. Our experimental efforts focus on AC impedance measurements of conductivity in oxide thin films. We complement irradiations with *in situ* x-ray diffraction and transmission electron microscopy annealing studies to determine how cations diffuse, how grain boundaries modify cation distributions, and how phase structure evolves. These experiments are coupled with density functional theory and accelerated molecular dynamics simulations that target ordering in these mixed oxides and unit mechanisms responsible for the thermodynamic and kinetic behavior of these materials. The insights from this work not only provide a foundation for understanding ionic conductivity and radiation damage in complex oxides, but will also lead to design principles for advanced materials with enhanced functionality.

Recent Progress

During the last two years, the primary results of this project focused around demonstrating that the cation distributions in pyrochlore, one specific complex oxide that has been the center of our activities, greatly impacts the transport properties of the material. This is both true for metastable disordered structures, where our experimental efforts demonstrated a profound effect on ionic conductivity, and for ordered ground state structures in mixed complex oxides, as revealed from accelerated molecular dynamics (AMD) simulations. Finally, we have been pursuing novel microscopy measurements to reveal the complex structures formed during irradiation.

Experimental Demonstration of the Role of Disorder on Ionic Conductivity

There have been conflicting experimental reports on the role of disorder in modifying the ionic conductivity in pyrochlores [1,2]. Typically, disorder is induced in these materials via chemistry, substituting one species for another to achieve a pyrochlore that has a greater tendency towards disorder. Thus, these experiments are measuring the effects of multiple changes at once. To clarify the true role of disorder on ionic conductivity, in work published in *J. Mater. Chem. A*, we used irradiation to induce disorder while keeping the chemistry constant [3]. Thin films of one

pyrochlore – $Gd_2Ti_2O_7$ – were irradiated to varying fluences with 200 keV He ions. AC impedance spectroscopy was used to quantify the ionic conductivity in these films as a function of He fluence and, thus, cation disorder. The results are highlighted in Fig. 1. We find that, as the disorder increases, the conductivity also increases. More surprising is the sensitivity of the conductivity to disorder. Introducing only a few percent cation disorder leads to a great change in conductivity, after which the conductivity remains relatively insensitive to the disorder. There is another rise once the material amorphizes. Thus, these experiments clearly show that introducing disorder alone leads to a large enhancement in conductivity. We are currently working on a defect model of the system to determine exactly how the defect content responsible for the conductivity changes with fluence.

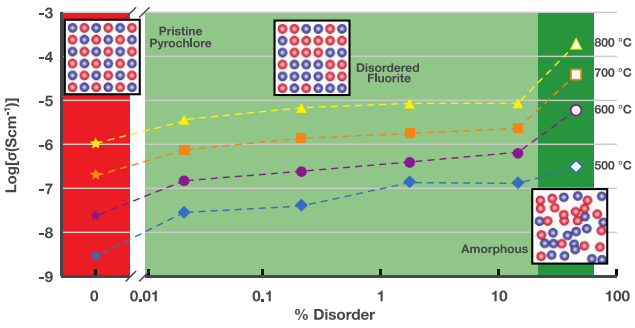

Figure 1. Irradiation-induced changes in disorder and conductivity in $Gd_2Ti_2O_7$. Even a few percent increase in disorder leads to a significant increase in the conductivity, which then remains relatively constant until the material amorphizes.

Ordered Superstructures in Mixed Complex Oxides

It is now well established that mixing two perovskites (ABO_3), to form so-called double perovskites ($AA'BB'O_6$), leads to structures with specific orderings of cations on the A and B sublattices [4], which have an impact on the defect kinetics [54]. The question naturally arises whether such "double" compounds can form in other mixed complex oxides. We considered the case of pyrochlore, using the two end members of $Gd_2Ti_2O_7$ and $Gd_2Zr_2O_7$ as starting points. As highlighted in Fig. 2, we used DFT to compute the energies of a large number of combinations of cation arrangements and found that there are stable mixtures of these compounds that exhibit longer-range order than the parent pyrochlore structure [5]. In the most stable structure with a chemistry of $Gd_2(Ti_{0.25}Zr_{0.75})_2O_7$, the ordering is stabilized by a significant distortion of the Zr environment in which, as compared to normal pyrochlore in which the Zr cations are coordinated by six oxygen, some of the Zr cations in this structure are coordinated by seven oxygen ions. Using temperature accelerated dynamics (TAD), an accelerated molecular dynamics (AMD) method that utilizes high temperature MD trajectories to evolve a system at low temperature, we examined how structures such as those shown in Fig. 2 impact defect kinetics [6]. For systems with the chemistry and stoichiometry but different cation ordering, we predict a difference in the diffusivity of the vacancy

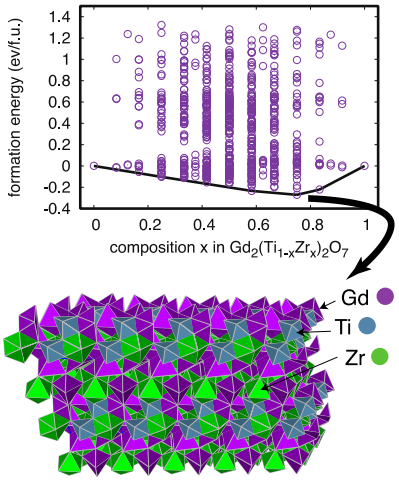

Figure 2. DFT predictions of ordered superstructures in $Gd_2(Ti_xZr_{1-x})_2O_7$ pyrochlore. Structures with a negative energy are more stable than either end-member.

of nearly 50 times at 1500 K. Thus, one must know the detailed cation arrangement to determine how mass will flow through that structure.

Advanced Microscopy for Understanding Complex Oxides

In order to understand the detailed structure of complex oxides such as pyrochlore and spinel and the changes induced by irradiation, we have used advanced electron microscopy techniques. First, we have used in situ heating to look at the kinetics of recrystallization of irradiated pyrochlore. Using a He-implanted sample that was amorphized, we observed the recrystallization of the material directly in the microscope. Figure 3 shows the structure before and after. The goal is to determine how the damage layer – here characterized by a layer of bubbles and pores – impacts the recrystallization. We observe that nucleation occurs in two stages. First, homogeneous nucleation occurs at the amorphous/crystalline interface, driven by the ability of the amorphous region to epitaxially match the unirradiated substrate. However, this recrystallization front is impeded by the bubble layer. Thus, after some time, heterogeneous nucleation begins at the top of the bubble layer, leading to a polycrystalline layer at the top of the recrystallized film. Second, via a user proposal with the Molecular Foundry at Lawrence Berkeley National Laboratory, we have been using 4D scanning transmission electron microscopy (4D STEM) [7] to examine the cation structure in the material. Figure 6.10b shows a micrograph of a partially recrystallized pyrochlore film (the recrystallization was interrupted between the two stages shown in Fig. 3). 4D STEM diffraction patterns for different regions of the material are shown in the insets, revealing that, at the crystal/amorphous interface, the material is not fully ordered into pyrochlore, but exhibits some level of disorder.

Future Plans

The central theme of our future work revolves around the postulates that the cation distributions in complex oxides, especially those with more than one A and/or B cations, dictate the mass transport characteristics of the material and that various forms of these distributions can be induced by irradiation. Ultimately, cation distributions will be governed by a number of factors:

- The thermodynamics of mixing multiple A and/or B cations.
- The metastability of structures that can be achieved via irradiation.
- Interfaces, and the qualitatively different energy landscape they represent for cation ordering and mixing.

In our future work, we will control cation distributions, moving the material up and down in stability, via irradiation. We will then determine the impact that the resulting structures have on mass transport. Our work targets the physical phenomena necessary to understand and control the cation structures of these mixed complex oxides. Further, our understanding of how irradiation-induced damage interacts with the cation structure of these systems will provide new insight into the design of ceramics with enhanced radiation tolerance.

We have already seen that cation disorder dramatically changes ionic conductivity in pyrochlore. In the future, we will focus on irradiation-induced orderings in more complex oxides, both structures that are thermodynamically more preferred than the as-synthesized state and metastable structures that can be induced by irradiation. In some cases, these will still contain some level of cation disorder, but in others the cations will form ordered super-structures as compared to the simpler end members. We expect that these more chemically complex systems exhibit their own surprises in terms of ionic conductivity. To understand these systems, we are using both modeling and experiment to understand the structure and kinetics associated with these more complex systems.

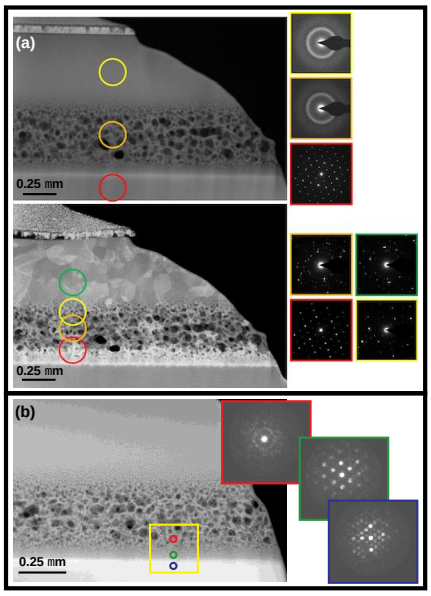

Figure 3. (a) In situ heating of amorphous GTO, leading to the recrystallization of the material. (b) 4D STEM measurements of the irradiated material, showing representative diffraction patterns across the sample.

Further, we have shown how microstructural features such as surfaces [8] and grain boundaries [9] can change the local level of disorder and thus the mass transport characteristics of the system. Our future work involves examining this behavior in more detail. In particular, we hypothesize that, under irradiation, disorder will preferentially occur at grain boundaries and thus these will act as fast diffusion pathways for oxygen. This offers a novel route to engineering materials for fast ion conductor applications.

Most of our work has focused on pyrochlores. In the future, however, we will study the properties of Mg-bearing spinels (AB_2O_4). Depending on the chemistry of the spinel, they can be either ordered (normal) or disordered (random or inverse) [10]. The same considerations that dictate mass transport in pyrochlore are relevant for these spinels. Further, by studying a different class of materials, we will be able to compare and contrast how crystal structure impacts trends that are revealed in this project.

References

[1] K. J. Moreno, et al., *Physical Review B* **75**, 184303 (2007).
[2] H. Tuller. *J. Phys. Chem.* Solids **55**, 1393 (1994).
[3] C. R. Kreller, et al., *Journal of Materials Chemistry A* **7**, 3917-3923 (2019).
[4] M. T. Anderson, et al., *Progress in Solid State Chemistry* **22**, 197-233 (1993).
[5] G. Pilania, et al., *npj Computational Materials* **5**, 7 (2019).
[6] B. P. Uberuaga, et al., *Physical Chemistry Chemical Physics* **21**, 5956-5965 (2019).
[7] T. C. Pekin, et al., *Ultramicroscopy* **176**, 170-176 (2017).
[8] J. Wen, et al., *Acta Materialia* **110**, 175 (2016).
[9] R. Perriot, et al., *Nanoscale* **9**, 6826 (2017).
[10] H.St.C. O'Neill and A. Navrotsky, *American Mineralogist* **68**, 181-194 (1983).

Publications

Intellectually led by this FWP

2017

- T.G. Holesinger, J.A. Valdez, M.T. Janish, Y.Q. Wang, B.P. Uberuaga, Potential benefit of amorphization in the retention of gaseous species in irradiated pyrochlores, *Acta Materialia* **164**, 250-260 (2019).
- C.R. Kreller, J.A. Valdez, T.G. Holesinger, J. Morgan, Y.Q. Wang, M. Tang, F.G. Garzon, R. Mukundan, E.L. Brosha, B.P. Uberuaga, Massively enhanced ionic transport in irradiated crystalline pyrochlore, *Journal of Materials Chemistry A* **7**, 3917 (2019).
- G. Pilania and B.P. Uberuaga, Predictions of Novel Chemistry-Driven Strong Local Distortions in Ordered $A_2BB'O_7$ Mixed Pyrochlores: Origins and Implications, *npj Computational Materials* **5**, 7 (2019).
- B.P. Uberuaga, R. Perriot, G. Pilania, The impact of chemical order on defect transport in mixed pyrochlores, *Physical Chemistry Chemical Physics* **21**, 5956 (2019).

2018

- B.P. Uberuaga, E. Martinez, D. Perez, and A.F. Voter, Discovering mechanisms relevant for radiation damage evolution, *Computational Materials Science* **147**, 282 (2018). *Uberuaga led this paper, with contributions from the other authors.*

2017

- M. Tang, J.A. Valdez, J. Zhang, Y.Q. Wang, B.P. Uberuaga, and K.E. Sickafus, Ion irradiation-induced phase transformations in fully inverse spinel $MgIn_2O_4$, *Scripta Materialia* **125**, 10 (2016).

Collaborative publications

2019

- R. Batra, G. Pilania, B.P. Uberuaga, R. Ramprasad, Multi-fidelity Information Fusion with Machine Learning: A Case Study of Dopant Formation Energies in Hafnia, *ACS Applied Materials and Interfaces* **11**, 24906-24918 (2019).
- J. Chapman, R. Batra, B.P. Uberuaga, G. Pilania, R. Ramprasad, A Comprehensive Computational Study of Adatom Diffusion on the Aluminum (100) Surface, *Computational Materials Science* **158**, 353-358 (2019)
- P.P. Dholabhai and B.P. Uberuaga, Beyond Coherent Oxide Heterostructures: Atomic-scale Structure of Misfit Dislocations, *Advanced Theory and Simulations*, in press; DOI: 10.1002/adts.201900078.

2018

- A. Debelle, J.-P. Crocombette, A. Boulle, E. Martinez, B. P. Uberuaga, D. Bachiller-Perea, Y. Haddad, F. Garrido, L. Thome, M. Behar, How relative defect migration energies drive contrasting temperature-dependent microstructural evolution in irradiated ceramics, *Physical Review Materials* **2**, 083605 (2018).

- A.J. Samin, D.A. Andersson, E.F. Holby, B.P. Uberuaga, On the role of electro-migration in the evolution of radiation damage in nanostructured ionic materials, *Electrochemistry Communications* **96**, 47 (2018).
- B. P. Uberuaga, D. Perez, A. F. Voter, Accelerated molecular dynamics methods for long-time simulations in materials, invited chapter for a book honoring William Goddard: *Computational Materials, Chemistry, and Biochemistry: From Bold Initiatives to the Last Mile*.
- R.J. Zamora, D. Perez, E. Martinez, BP Uberuaga, A.F. Voter, Accelerated molecular dynamics methods in a massively parallel world, *Handbook of Materials Modeling. Volume 1 Methods: Theory and Modeling*, 1 (2018).

Mechanically modulated electrochemistry in solid-state ion conductive materials and interfaces: Enabling design of predictable energy conversion and storage

Krystyn J. Van Vliet (Lead PI), W. Craig Carter, Yet-Ming Chiang, Ju Li, Harry L. Tuller, and Bilge Yildiz, Massachusetts Institute of Technology, Cambridge, MA 02139 USA

Program Scope

Portable, reliable, and deployable devices for energy storage and conversion require fundamental changes in design of solid-state composites comprising ceramics and metals. These materials comprise the electrodes and electrolytes of next-generation solid-oxide fuel cells and all solid-state batteries, forming solid-state functional composites. The advent of solid-state batteries – which replace liquid electrolytes with solid electrolytes capable of lithium ion transport for reliable energy storage in portable batteries – and the increased demand space for all solid-state fuel cells capable of oxygen reduction at intermediate temperatures remain important challenges for improved material stability and decreased system cost. However, little is understood about key couplings between mechanics and electrochemistry of materials in this energy design space for solid-state energy applications.

The COFFEI Group comprises expertise from materials science and engineering to integrate unique *in situ* experiments, simulations, and fabricated interfaces that address these fundamental questions in solid-state interfaces of nanoscale composites that will guide solid-state electrochemistry, transport kinetics, and mechanical deformation for nonstoichiometric materials that enable such applications. In particular, we build on COFFEI's understanding of ***chemomechanical coupling*** among defect concentrations, ionic transport, electron transport, and stored elastic energy that is particularly acute in the far-from-equilibrium conditions typical of energy device applications (Fig. 1).

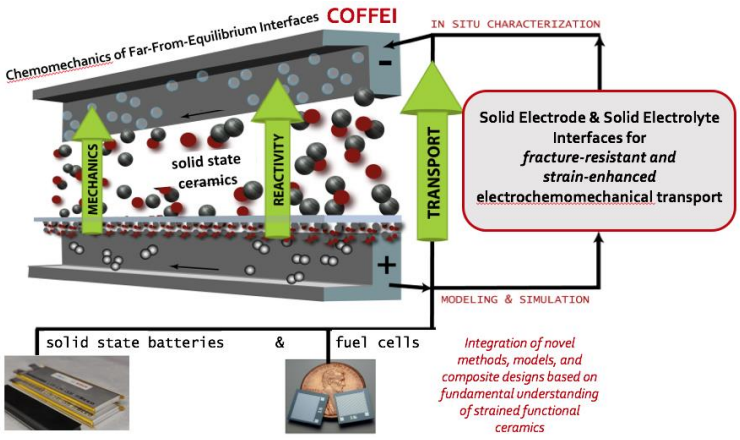

Figure 1: COFFEI Group focuses on fundamental scientific challenges and key design opportunities in solid-state interfaces, specifically the coupling between mechanics and electrochemistry for functional ceramics enabling portable, solid-state energy conversion and storage.

By tailoring our focus to solid-state interfaces, COFFEI addresses these important issues by (*a*) applying

advanced *in-situ* and *ex-situ* characterization tools to characterize model materials and interfaces synthesized with molecular-level control, under both laboratory-controlled and extreme environments representative of energy device operation; and (*b*) employing computational modeling and simulation frameworks to predict transport mechanisms, reactivity and stability of these materials and interfaces under strains typical of energy device operation.

Recent Progress

COFFEI Phase 4 focuses on **mechanically modulated electrochemistry in solid-state materials and interfaces**, including strain-modulated conductivity, reactivity, and microstructural integrity across interfaces. Our motivating hypothesis is as follows: Interfacial strain can significantly promote or modulate ionic/electronic conductivity and reactivity for solid-state energy conversion. Our recent progress includes study and enhancement of ion mobility, particularly at lower temperatures relevant to device operation where the activation energy for ionic motion can be larger than at higher temperatures due to association effects. The primary ions of interest for energy conversion and storage in our studies are oxygen ions and lithium ions, within materials and across electrode-electrolyte interfaces. Selected recent progress against these goals is organized around three supporting subquestions:

A. Can we predict defect equilibrium and charge transfer kinetics under strain? Specifically, what are the effects of oxygen vacancies and applied fields on these unit processes in functional oxides?

A.1. **Measuring impact of oxygen non-stoichiometry on near-ambient ionic mobility in mixed-ionic-electronic-conducting thin films.** We applied a novel approach for measuring ionic conductivity in nano-dimensioned thin films based on cyclic voltammetry measurements, allowing one to overcome the above-mentioned limitations (Kaleav et al., 2018). We focus our study initially on the model $Pr_xCe_{1-x}O_2$ (PCO) system, whose defect chemical and ionic transport properties have been previously studied by our COFFEI team (Bishop et al., 2011; Kim et al., 2012). By carefully processing the PCO layer, sandwiched between transparent conducting electrodes, it becomes possible to quench in different degrees of oxygen non-stoichiometry to room temperature and to confirm it by optical absorption measurements and Raman spectroscopy. By combining this information with the mobility data extracted from the analysis of cyclic voltammetry measurements, we observe impact of non-stoichiometry on ionic mobility close to room temperature. This offers valuable insights for a variety of devices operating under near ambient conditions, where knowledge about the as-prepared non-stoichiometry is generally lacking. Moreover, this methodology offers the opportunity for future systematic examination of the impacts of alternative stimuli (e.g., high field or strain) on ionic mobility.

A.2. Computational predictions of strain-induced conductivity changes in bulk, lithium conducting solid electrolytes. In order to identify materials yielding high Li-ion conductivity upon strain and underlying atomic-scale mechanisms/scenarios, an extensive literature survey of up-to-date (2018–2019) research on strain-alteration of Li-ion conductivity in solid state

electrolytes was performed. The following key-scenarios of conductivity strain-alteration were selected as promising: (i) (Trivial) decrease of Li-ion migration barriers; (ii) Modification of crystal structure, e.g. a (local) change from less conducting HCP to more facile BCC anion-framework enabling faster Li-ion migration and better interconnection of diffusion pathways; (iii) Promotion of concerted multiple-ion migration mechanism (as opposed to single-ion migration), since it enables faster conductivity due to low migration barriers.

B. Can we predict differences in thin films with interfaces, compared to bulk? Specifically, how can we relate interface-rich experiments and computational modeling to predict interfaces of strain-modulated transport?

B.1. High-Temperature Chemical Expansion of Thin-Film Praseodymium Cerium Oxide Characterized by Laser Doppler Vibrometry. Expansion of oxides, induced by changes in temperature and/or oxygen partial pressure p_{O2}, known as chemical expansion, enables a new generation of very high-temperature actuators (Swallow 2018). We have been investigating chemical expansion utilizing thin-film $Pr_{0.1}Ce_{0.9}O_{2-\delta}$ (PCO) as a model system. Samples consisting of PCO deposited on yttria stabilized zirconia (YSZ) substrates exhibited considerable expansion at temperatures of up to at least 800°C. We expanded our studies of such phenomena by application of in-situ by high-temperature laser Doppler vibrometry (LDV) that enables us to reach higher temperatures and a much wider range of oxygen partial pressures. This is being studied both with membranes with a pin-type support to solely reflect film expansion as well as full supports in which lateral stresses in the PCO film cause measurable deflection of the full sample. For example, superposition of the increase in film thickness and associated sample deflection results in a displacement of 110 nm at 800°C.

B.2. Experimental validation of our predictions regarding strain-induced changes in electronic defect dominance in oxygen ion-conducting thin films. We developed an experimental approach that facilitates application of in-plane strain to functional oxide thin films continuously on the same substrate, through multipoint bending and concurrent conductivity measurement of a thin film-on-substrate device. This simple yet remarkable new approach to controlled strain in *operando* conditions is accessible to a wide temperature range (room temperature to 700℃) and precise gas control (oxygen partial pressure down to 1 ppm without reactive gas) relevant to mixed ionic-electronic conducting oxides. We can strain and measure the transport properties of the same functional oxide thin film at high temperature in situ, including PCO as discussed in B.1, over a range of strains applied to a single system.

C. Can we increase transport (electronic and/or ionic) and reactivity via strain sufficiently to improve performance including enhanced transport at lower driving forces?

C.1. Tailoring non-stoichiometry and mixed-ionic electronic conductivity in PCO/STO heterostructures. We demonstrated that substantial changes in the non-stoichiometry of $Pr_{0.1}Ce_{0.9}O_{2-\delta}$ (PCO), a model mixed ionic-electronic conductor,can be achieved by fabricating multilayers with another, relatively inert material, $SrTiO_3$ (STO). We fabricated heterostructures using pulsed laser deposition, keeping the total thickness of PCO and STO constant while

varying the number of layers and thickness or each individual layer. We confirmed that this change was due to variations in non-stoichiometry, by optical transmission measurements, and show that the lower oxygen content is consistent with a decrease in the effective oxygen reduction enthalpy of PCO. This greatly reduces experimental time and enables in-situ control of both single and multilayer (or VAN) oxide thin films. We demonstrated that the optical measurement enable one to access the ionic defect concentration. These results exemplify the dramatic differences in properties achievable by interface engineering.

C.2. Computational predictions and experimental validation of electrochemomechanical flaw propagation at solid electrode-solid electrolyte interfaces. Our prior COFFEI experiments of electrochemical fatigue in solid electrolytes and simple electrode-electrolyte interfaces (Porz 2017, McGrogan 2018) motivated our current computational study of the propagation of metal dendrite propagation in solid state electrolytes via finite element analysis. We developed an elastic-plastic finite element model to investigate mechanisms by which Li metal electroplating and electronic conduction could proceed through solid electrolytes. We confirmed that Li plating can generate tensile stresses ahead of pre-existing flaws, and identified relationships among the applied bias (and thus charging rate), maximum allowable processing flaw size, and fracture toughness of the solid electrolyte. We also determined a strong dependence of the fracture criterion on the plastic behavior of metallic Li, identifying two distinct mechanisms by which Li plasticity may assist with prevention of electrolyte fracture. This provides a simple computational model to test electrode-electrolyte failure hypotheses.

C.3. Experimental demonstration of microscale flaws in electrochemomechanical perturbation at solid interfaces. We also extended our previous work identifying the chemomechanical origins of metal penetration through solid electrolytes (Porz et al., 2017). That prior COFFEI work has been highly cited, receiving 94 citations in <2 yrs (Google Scholar). Key new findings concern the relative length scales of solid electrolytes and electrodes that lead to spatial variation in dendrite formation and growth from inherent surface flaws. *Operando* lithium electrodeposition experiments were performed using $Li_6La_3ZrTaO_{12}$ single crystals grown by collaborators in Austria and Germany. General and quantitative design rules for solid-state cell design were established for avoidance of chemomechanical stress concentrators with respect to the relative lateral dimensions of positive and negative electrodes and the electrolyte layer thickness; these effects were found to dominate over intentionally introduced large indentation defects.

Future Plans

A. After further optimizing multilayer cells utilizing Au and/or TCO electrodes, we will apply the nonlinear I-V characterization technique on other MIEC materials of interest for use as SOFC electrodes, particularly those with semimetallic character. We also plan to upgrade our existing sputtering system, recently renovated, by adding a new RF source and 1inch sputtering gun. The later will enable us to deposit oxide materials technologically challenging or costly to produce sputtering targets. RF

sputtering enables one to grow thin films from amorphous to highly epitaxial one that especially important in the study of the interface effects on the ionic defects concentration and kinetic properties. Finally, we will complete our first-principles calculations on enhanced oxygen-ion mobility in a series of electrode/electrolyte systems to investigate how electrochemically tuned oxygen-ion mobility influences the mechanical properties in the above materials via experiments and simulations.

B. We will next include the effects of interfaces on the measured chemical expansion. For example, grain boundaries are believed to result in the accumulation of Pr^{3+} relative to the grains due to space charge effects. By comparing expansion of near epitaxial PCO layers with nanocrystalline layers, this feature can be tested. We are also planning to expand this study to other PCO compositions and MIECs such as $SrTi_{1-x}Fe_xO_3$ to see how these materials respond chemomechanically. We will complete testing of the stability and reproducibility of the setup. We have also conducted several impedance measurements on single crystal YSZ with the device. We will also combine atomistic simulation technique, density functional theory, to calculate the migration barrier for ionic transport under different strains, aiming to strengthen our experimental observations.

C. Previously we demonstrated that optical spectroscopy is powerful characterization tool for the oxygen vacancy monitoring and surface oxygen exchange kinetics. We will next complete our study on the effects of mechanical stresses and strains applied to solid electrolyte-metal electrode interfaces on metal dendrite propagation via a mechanical fracture-driven mechanism. Following this, we intend to explore the effects of strain on Li-ion transport in solid state conductors using Li conducting garnets and sulfides as model systems.

References

Bishop, S. et al., Understanding chemical *expansion* in non-stoichiometric oxides, Annual Review of Materials Research 41, 369-398 (2011).

Kim, J.J. et al., Investigation of Redox Kinetics by Simultaneous In Situ Optical Absorption Relaxation and Electrode Impedance Measurements: Pr Doped Ceria Thin Films, ECS Trans 57, 1979-1984 (2013).

Swallow, J.G. et al., Dynamic chemical expansion of thin-film non-stoichiometric oxides at extreme temperature, Nature Materials, 16, 749-754 (2017).

McGrogan, F.P. et al., "Connecting particle fracture with electrochemical impedance in LiXMn2O4," J. Electrochem. Soc. 164 A3709-A3717 (2017).

Porz, L. et al., Mechanism of Lithium Metal Penetration through Inorganic Solid Electrolytes**,** Adv Energy Mat., 7, 1701003 (2017).

Publications

Swallow, J.G, Lee, J., Defferriere,T. , Hughes,G.M , Raja,S.N., Tuller,H.L ., Warner,J.H., and Van Vliet, K.J. ACS Nano. 12, 1359-1372 (2018).

Schmidtchen,S. Fritze,H. , Bishop,S.R. , Chen,D., and Tuller,H.L., Chemical Expansion of Praseodymium-Cerium Oxide Films at High Temperatures by Laser Doppler Vibrometry. Solid State Ionics, 319, 61-67 (2018).

Kalaev,D., Tuller,H.L, Riess,I., Measuring Ionic Mobility in Mixed-Ionic-Electronic-Conducting Nano-Dimensioned Thin Films at Near Ambient Temperatures, Solid State Ionics, 319, 291-295 (2018).

Swamy, T., Park, R., Sheldon, B.W., Rettenwander, D., Porz, L., Berendts, S., Uecker, R., Carter, W.C., Chiang, Y-M., Metal Penetration Induced by Electrodeposition through Solid Electrolytes: Example in Single-Crystal $Li_6La_6ZrTaO_{12}$ Garnet, Journal of the Electrochemical Society (2018).

McGrogan, F.P., Raja, S.N., Chiang, Y.-M., and Van Vliet, K.J., Electrochemomechanical fatigue: Decoupling mechanisms of fracture-induced performance degradation in LiXMn2O4,"J. Electrochem. *Soc.*, 165 A2458-A2466, 2018.

Cho, Y., Ogawa, M., Oikawa, I. , Tuller, H.L., Takamura, H., Stabilizing Coexisting N-Type Electronic and Oxide-Ion Conductivities in Donor-Doped Ba-In-Based Oxides under Oxidizing Conditions - Roles of Oxygen Disorder and Electronic Structure, Chem. Mater. 31 2713-2722 (2019).

Perry,N., Kim,N., Ertekin,E., Tuller, H.L., Origins and Control of Optical Absorption in a Non-Dilute Oxide Solid Solution: $Sr(Ti,Fe)O_{3-x}$ Perovskite Case Study, Chem. Mater., 31 (3), 1030–1041 (2019).

Harrington, G.F., Sun,L., Yildiz,B., Sasaki,K., Perry, N.H. and Tuller,H.L., The Interplay and Impact of Strain and Defect Association on the Conductivity of Rare Earth Substituted Ceria. Acta Materialia, 166, 447-458 (2019).

Polfus,J.M., Yildiz,B., Tuller,H.L., Origins and Control of Optical Absorption in a Non-Dilute Oxide Solid Solution: $Sr(Ti,Fe)O_{3-x}$ Perovskite Case Study. Chem. Mater., 31 (3), 1030–1041 (2019).

Lu,Q., Vardar,G., Jansen,M., Bishop,S.' Waluyo,I., Tuller,H.L. and Yildiz, B., Surface Defect Chemistry and Electronic Structure of $Pr_{0.1}Ce_{0.9}O_{2-\delta}$ Revealed in operando. Chemistry of Materials, 30 [8], 2600-2606 (2018)

Lu, Q., Bishop, S.R., Lee, D., Lee, S., Bluhm,H., Tuller, H.L., Lee, H.N. and Yildiz, B., Electrochemically Triggered Metal-Insulator-Transition Between VO_2 and V_2O_5, Advanced Func Mat. 28 [34], 1803024 (2018).

Schröder,S., Fritze,H., Bishop,S.R, Chen,D. and Tuller,H.L,, Thin-Film Nano-thermogravimetry Applied to Praseodymium-Cerium Oxide Films at High Temperatures, Appl. Phys. Lett. 112 [21], 213502 (2018).

Huber,T.M, Navikas,E., Sasaki,K., Yildiz,B., Hutter,H., Tuller,H.L, Fleig,J. , Interplay of Grain Size Dependent Electronic and Ionic Conductivity in Electrochemical Polarization Studies On Sr-Doped $LaMnO_3$ (LSM) Thin Film Cathodes, J. Electrochem. Soc. 165 (9) F1-F8 (2018).

Polfus,J.M., Yildiz,B., Tuller,H.L., Bredesen,R. , Adsorption of CO_2 and Facile Carbonate Formation On $BaZrO_3$ Surfaces, J. Phys. Chem. C, 122, 307-314 (2018).

Localized Deformation and Intergranular Fracture of Irradiated Alloys under Extreme Environmental Conditions

Gary S. Was
2355 Bonisteel Blvd., University of Michigan, Ann Arbor, MI 48109 gsw@umich.edu

Ian M. Robertson
1415 Engineering Drive, University of Wisconsin-Madison, Madison WI 53706
ian.robertson@wisc.edu

Diana Farkas
201A Holden Hall, Virginia Tech, Blacksburg, VA 24061, diana@vt.edu

Program Scope

The overall objective of this project is to determine the basic processes by which localized deformation in irradiated materials leads to intergranular cracking in alloys in aggressive environments at high temperature. We will utilize a mesoscale science approach that provides linkage from atomistic simulations of dislocation responses to the accommodation and emission of dislocations from grain boundaries, through direct observation of dislocations with irradiation defects and grain boundaries, to macroscale experiments. The consequence of this combined effort will be the identification of the factors most likely responsible for establishing not only the local stress state at grain boundaries prone to failure but also their location with respect to the macroscopic applied stress. The grain boundaries and local conditions at which disruption of the surface oxide and hence, exposure to the water environment is most probable, have been identified. Having isolated these conditions, we are poised to address why this failure does not occur at every grain boundary that is favorably oriented, why it remains isolated at one channel over others along the same grain boundary, and what is the role of environment in inducing the cracking. We are focusing on the following sub-objectives are designed to bring us closer to determining the mechanism of irradiation assisted stress corrosion cracking, IASCC.

- Does a threshold stress for initiation of IASCC exist and if so, how can the magnitude of it be determined? Is the likelihood of IASCC initiation determinable from the value of the local normal stresses at dislocation channel-grain boundary intersections, and if so, what is that value and how does it depend on the slip systems active in the dislocation channel (DC) impinging on the grain boundary (GB), the grain boundary character, and the composition of the alloy?
- The water environment plays a critical role in the cracking process because straining at the same temperature and strain rate in an inert environment does not result in grain boundary cracking. What is the role of the environment/oxide film on the initiation of IASCC cracks coupled with high local stresses on the grain boundary? Does the oxidation process create a susceptibility to cracking which is initiated by the high local stresses where dislocation channels intersect grain boundaries? What is the nature of the induced "sensitivity" of the grain boundary to cracking and why is it location specific?

Recent Progress

We conducted high resolution electron backscattering detection (HREBSD) scans of a Fe-13Cr-15Ni tensile bar, which had been strained to 3.5% plastic strain in an argon environment at 288°C after being irradiated to 5 dpa at 360°C at the Michigan Ion Beam Laboratory. To date 75 scans at discontinuous channel – grain boundary interaction sites. Samples were then strained in BWR-NWC at 288°C an additional 1.5% to induce IGSCC. Figure 1 shows a compilation of the calculated grain boundary normal stress made for both the susceptible Fe-13Cr-15Ni alloy and the non-susceptible Fe-21Cr-32Ni alloy as a function of the grain boundary orientation defined by the product of the Schmid factor and the cosine of the angle between the grain boundary normal and the tensile axis. Note that 1) the stresses normal to the grain boundary are highest for the boundaries oriented closest to normal to the applied stress; 2) there appears to be a stress threshold below which cracking does not occur in the Fe-13Cr-15Ni alloy, 3) the distribution of normal stresses in the Fe-21Cr-32Ni alloy parallels that of the Fe-13Cr-15Ni alloy but none of these sites exhibited IASCC. These results confirm that a high localized stress is induced by the termination of a dislocation channel at the grain boundary and that this stress is a major driver of irradiation assisted stress corrosion cracking. They also show that increasing the chromium content of the alloy is an effective strategy for suppressing IASCC. However, the magnitude of the normal stress is not the only factor as evidenced by the fact that not all such oriented boundaries crack.

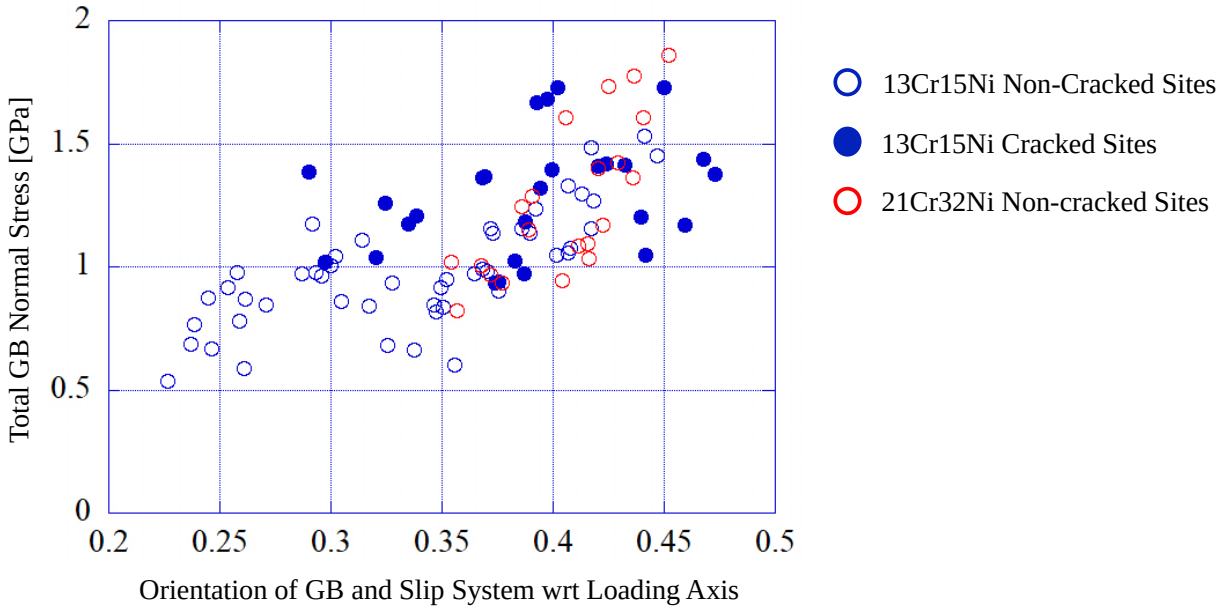

Figure 1. Stress normal to the grain boundary at discontinuous dislocation channel – grain boundary sites as a function of grain boundary orientation for alloys Fe-13Cr-15Ni and Fe-21Cr-32Ni and their cracking susceptibility following straining in BWR-NWC to 4.5% at 288°C.

As in our previous studies, the composition of the grain boundary and the thickness of the inner protective oxide appears to be an important factor. The crack initiation site correlated with the local maximum of GB Cr content (local minimum of GB Ni content), which may lead to an insufficient protection by the inner oxides over that particular site. By combining this data, with that of Rigen et al. [M.R. He, et al., Acta Mater. 2017, 138: 61], the susceptibility of a specific

location on a grain boundary to cracking, assuming the oxide is ruptured and the boundary is exposed to the environment, occurs at locations with a nickel concentration that is less than 20 wt.%, a Cr content less than about 10 wt. %, and an effective protection (thickness of the inner protective oxide and the maximum Cr content) of between 8.5 and 10 nm, Figure 2. This compositional variation along the grain boundary can be attributed to radiation induced segregation and the fact that grain boundary diffusion can be affected by the local structure of the boundary.

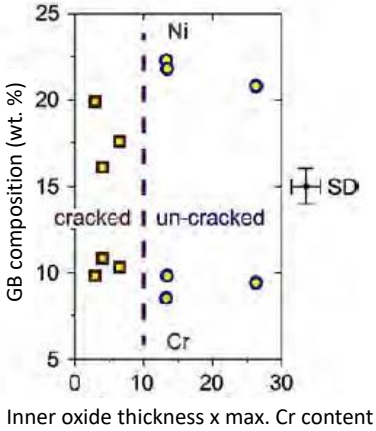

Figure 2. Summary of all measurements to date shows the correlation between GB composition (upper: Ni; lower: Cr) at the far field and the effectiveness of protection, evaluated as the product of thickness and maximum Cr content, of the inner oxide layer.

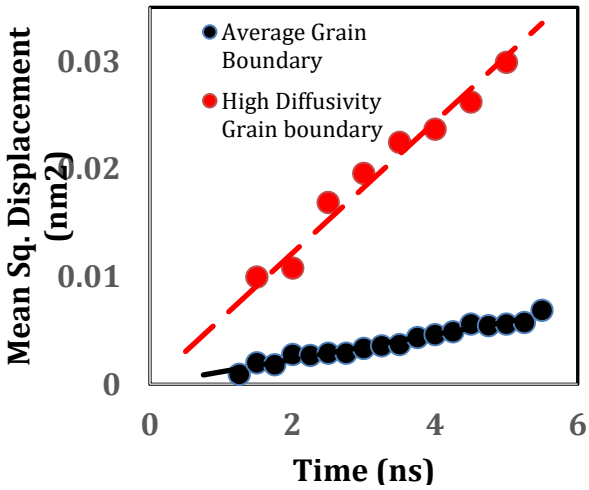

Figure 3. Mean square displacements as a function of simulation time. The data in red are for a high diffusivity boundary. The data in black are the averages for all boundaries in the sample.

We have utilized large-scale molecular dynamics simulations to address some of the kinetic issues that may be important in understanding stress corrosion cracking in irradiated materials. Simulations addressed the diffusion process along grain boundaries, revealing the individual atomic jumps within a particular grain boundary.These simulations complement the experimental observations and an analysis of how diffusion phenomena can affect IASSC. The first set of

studies was aimed at understanding how diffusion is affected by the local structure of the boundary by tracking individual atom displacements in the boundary region during a 1 ns simulation at 800K. A polycrystalline sample containing random tilt boundaries around the {110} axis revealed that the diffusion behavior depends very strongly on the misorientation and local structure of the boundary. Two grain boundaries show high diffusivity with the rest not showing the same level of atomic jumps. These results show that the diffusion behavior is critically dependent on the misorientation and local structure of the grain boundary. In order to quantify these differences Fig. 8 shows the mean square displacement in the boundaries as a function of simulation time. Data for a high diffusivity boundary (in red) are significantly higher than than the average of the boundaries in the sample (in black).

Future Plans

Experiments are planned to test the behavior of DC-GB sites upon further straining to determine if the local stress continues to increase and if the propensity for cracking also changes.

The composition and structure of oxides above the grain boundary in the IASCC-resistant alloy Fe-21Cr-32Ni is being analyzed to determine if they are consistent with boundaries that resist cracking in the more susceptible Fe-13Cr-15Ni alloy. An irradiated sample was also tested in Ar and BWR-NWC at 360°C at a slower strain rate to permit the development of larger grain boundary migration zones to more easily tie these zones to the diffusion of Cr to for protective surface oxides.

Modeling efforts are aimed at determining the dependence of grain boundary diffusion on the nature of the grain boundary in an effort to explain why some boundaries appear to more easily transmit Cr to the surface than others.

Recent Publications

B. Kuhr and D. Farkas, "Dislocation Content in Random Grain Boundaries, Model. Sim Mater. Sci. Engin. 27 (2019) 045005.

D. C. Johnson, B. Kuhr, D. Farkas, G. S. Was, "Quantitative Linkage between the Stress at Dislocation Channel- Grain Boundary Interaction Sites and Irradiation Assisted Stress Corrosion Cracking," Acta Mater. 170 (2019) 166-175.

L. Smith, D. Farkas, "Connecting Interatomic Potential Characteristics with Deformation Response in FCC Materials," Compu. Mater. Sci. 147 (2018) 18-27.

L. Smith, D. Farkas, "Deformation Response of Grain Boundary Networks at High Temperature," J. Mater. Sci. 53 (2018) 5696-5705.

B. Kuhr, D. Farkas, I. M. Robertson, G. S. Was, D. C. Johnson, "Stress Localization Resulting from Grain Boundary Dislocation Interactions in Relaxed and Defective Grain Boundaries," submitted to Mater. Metall. Trans. A.

Mo-Rigen He, Drew C. Johnson, Gary S. Was, Ian M. Robertson. "Insights into the Site-Specific Initiation of Irradiation-Assisted Stress Corrosion cracking." *(in preparation)*

Electronic and Atomic Response of Ceramic Structures to Irradiation

William J. Weber[1,2], Yanwen Zhang[1], Eva Zarkadoula[1] and Fuxiang Zhang[1]

[1]Materials Science & Technology Division, Oak Ridge National Laboratory
[2]Department of Materials Science & Engineering, The University of Tennessee

Program Scope

The overarching goal of this research is to understand and predictively model the dynamic response of ceramic structures to energy deposition from ion irradiation at the level of electrons and atoms. The design of radiation tolerant materials and creation of new functional materials by ion beam modification demand a comprehensive understanding and predictive models of energy transfer and exchange processes between the electronic and atomic structures. To achieve this goal, this research focuses on two specific aims: (1) the dynamic and coupled response of the electronic and atomic structures to single ion events; and (2) the collective effects from energy deposition and dissipation processes on damage accumulation, nanostructure formation, phase transformations, and recovery processes from multiple ion events over a broad range of conditions. Novel experimental and computational approaches are integrated to investigate the separate and coupled dynamics of electronic and atomic processes over a range of irradiation conditions to elucidate the underlying mechanisms. This research utilizes unique experimental capabilities for *in situ* luminescence and ion channeling measurements to characterize and quantify defect evolution in ceramics under ion irradiation over a range of temperatures. Scientific advances from this work will lead to new design principles for self-healing and radiation tolerant materials in extreme radiation environments, as well as provide the atomic-level foundation for the design and control of new functionalities in oxide electro-ceramics to enable broad advances in sustainable energy technologies and national security.

Recent Progress

$SrTiO_3$ has been irradiated over a wide range of ion fluences at 300 K with different ion species in order to investigate the effects of varying the energy loss to electrons and atomic nuclei [1]. The ion channeling results (Fig. 1) unambiguously show a dramatic difference in behavior for $SrTiO_3$ irradiated with light ions (Ne, O) compared to heavy ions (Ar and Au). While damage accumulation and amorphization under Ar and Au ion irradiation are consistent with previous

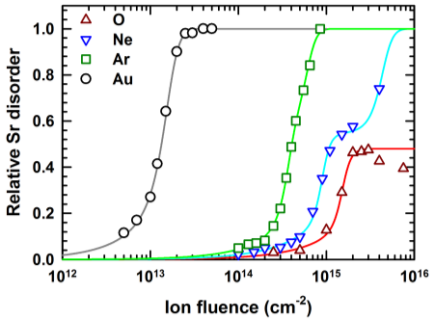

Fig. 1. Relative Sr disorder at 300 K vs. ion fluence in $SrTiO_3$ single crystals irradiated with different ions [1].

observations and existing models, damage accumulation under Ne irradiation reveals a quasi-saturation state at a disorder level of 0.54 for an ion fluence corresponding to a dose of 0.5 dpa; this is followed by further increases in disorder with increasing ion fluence. In the case of O ion irradiation, the damage accumulation at the damage peak closely follows that for Ne ion irradiation up to a fluence corresponding to a dose of 0.5 dpa, where a quasi-saturation of fractional disorder level occurs at about 0.48; however, in this case, the disorder at the damage peak decreases slightly with further increases in fluence. This behavior is associated with changes in kinetics due to irradiation-enhanced diffusional processes that are dependent on electronic energy loss.

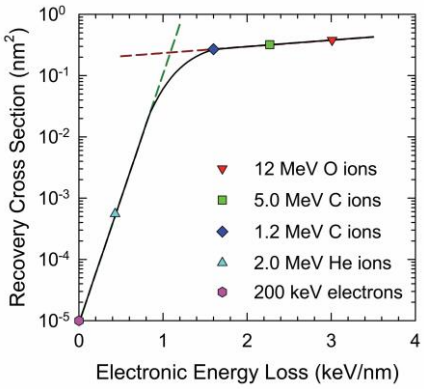

Fig. 2. Dependence of ionization-induced recovery cross sections on electronic energy loss [unpublished].

While high energy ions contribute to damage production in $SrTiO_3$ above a threshold electronic energy loss of ~6.5 keV/nm [2], the effects of electronic energy loss below this threshold have not been studied in detail. To address this, pre-damaged surface layers of $SrTiO_3$ has been irradiated with 2 MeV He, 1.2 MeV C, 5 MeV C and 12 MeV O ions. While melt-quenching does not occur for these ions, the inelastic thermal spike causes enough local heating to induce defect recovery. The results indicate two distinct regimes of ionization-induced recovery (Fig. 2). From ~ 1.1 to 4 keV/nm, the ionization-induced thermal spike is sufficient to induce recrystallization. Below ~1.1 keV/nm, recrystallization is associated with electronic excitations that enhance defect mobility.

Using *in situ* luminescence, the origin of the blue emission at 2.8 eV in $SrTiO_3$ has been investigated as a function of irradiation fluence, electronic excitation density, and temperature (100 to 300 K) over a range of ion energies and masses [3]. The emission does not show any correlation with the concentration of vacancies generated by irradiation and is greatly enhanced under heavy-ion irradiation. The intensity ratio of the 2.8 and 2.5 eV bands is independent of fluence at all temperatures but increases with excitation rate. A new model for the blue emission is proposed consisting of a radiative transition from un-bound (CB) states to the ground self-trapped exciton (STE) level (Fig. 3). The green and blue emissions are associated with transitions of the STE center, involving either localized states (2.5 eV), or pairs of localized and unbound states in the conduction band (2.8 eV). This represents a novel feature associated with high electronic excitation densities achieved by both pulsed laser and ion irradiations. Our analysis provides a unified description of the

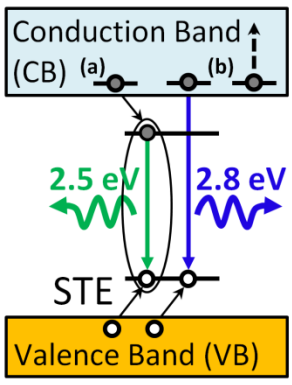

Fig. 3. Proposed mechanisms for emissions at 2.5 and 2.8 eV in ion irradiated $SrTiO_3$ [3].

emission mechanisms and demonstrates the unique potential of ion luminescence to unravel the rich and complex variety of effects associated with electronic carriers and defects in complex oxides.

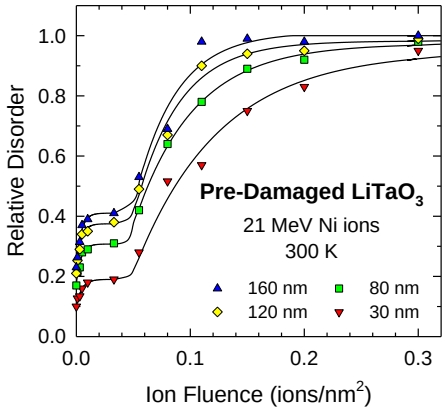

Fig. 4. Relative disorder as a function of 21 MeV Si ion fluence for pre-damaged $LiTaO_3$ at different depths [4].

Separate and combined effects of electronic and nuclear energy deposition in $LiTaO_3$ have been investigated [4]. Irradiation of pristine $LiTaO_3$ samples with 2 MeV Ta ions leads to amorphization due to atomic displacement damage that is described by a disorder accumulation model. Irradiation of pristine $LiTaO_3$ with 21 MeV Si ions does not produce significant damage at similar ion fluences. Irradiation with 2 MeV Ta ions to introduce a partially disordered, but crystalline, structure sensitizes $LiTaO_3$ to the electronic energy loss by 21 MeV Si ions that leads to amorphous track formation via a synergistic two-stage phase transition process (Fig. 4). During the first stage, a possible ferroelectric phase transformation occurs that sufficiently changes the electronic structure, which promotes the formation of amorphous tracks by 21 MeV Si ions during the second stage.

Ion irradiation of $KTaO_3$ has been performed to investigate the evolution of irradiation damage with and without significant electronic energy deposition [5]. Damage accumulation under irradiation with 2 MeV Au ions follows a direct-impact/defect-stimulated model, and occurs more rapidly than in $SrTiO_3$ under similar conditions. Electronic energy deposition from 21 MeV Ni ions creates negligible damage in pristine $KTaO_3$ to depths of 1 micron; however, damage is greatly enhanced in samples containing pre-existing defects, as evidenced by rapid amorphization due to track formation. The cross-sections for amorphous tracks show a nearly linear dependence on initial disorder, comparable to that previously observed in $SrTiO_3$.

The modification of the local structure in cubic perovskite $KTaO_3$ irradiated with 3 MeV and 1.1 GeV Au ions has been studied by Raman and x-ray absorption spectroscopy, complemented by density functional theory (DFT) calculations [6]. In the case of irradiation with 3 MeV Au ions, where displacement cascade processes are dominant, the Ta L_3-edge x-ray absorption measurements indicate that a peak corresponding to the Ta–O bonds in the TaO_6 octahedra splits, which is attributed to the formation of Ta_K antisite defects that are coupled with oxygen vacancies, V_O. This finding is consistent with the DFT calculations. Under irradiation with 1.1 GeV Au ions, the intense ionization and electronic energy deposition lead to a blue shift and an intensity reduction of active Raman bands. In the case of sequential irradiations with 3 MeV Au ions followed by 1.1 GeV Au ions, extended x-ray absorption fine structure measurements reveal a decrease in concentration of coupled Ta_K-V_O defects, compared to irradiation with just 3 MeV Au ions, due to the intense ionization and electron energy loss.

The TRIM code is commonly applied to predict radiation damage dose, and we have resolved the controversy over the inconsistencies (factor of ~2) in determining atomic displacement numbers using full-cascade and quick (modified Kinchin–Pease) TRIM modes [7]. Full-cascade TRIM simulations are consistent with full-cascade simulations using other modern Monte Carlo codes with the same ZBL scattering cross sections and SRIM electronic stopping powers. Furthermore, full-cascade TRIM simulations agree with numerical solutions for displacement functions determined from coupled integro-differential equations, which supports the accuracy of full-cascade TRIM simulations. The discrepancies between full-cascade and quick TRIM simulations are due in part to misunderstandings regarding the derivation of the modified Kinchin-Pease model and limitations of the energy partition model employed, which often provides inaccurate predictions (up to a factor of 2) of the energy loss by recoils to electrons and is not valid for polyatomic materials.

Future Plans

We will complete the separate effects studies on SiC to better understand the effects of temporal and spatial coupling of energy deposition from electronic and ballistic processes on damage evolution along an ion trajectory. This is critical for both accurate modeling damage evolution processes in SiC under irradiation, as well as for selecting appropriate ions and energies to be used in experiments to emulate fast neutron irradiation damage processes.

References

1. G. Velisa, E. Wendler, H. Xue, Y. Zhang, and W. J. Weber, Revealing ionization-induced dynamic recovery in ion-irradiated $SrTiO_3$, *Acta Mater.* **149**: 256-264 (2018).
2. H. Xue, E. Zarkadoula, R. Sachan, Y. Zhang, C. Trautmann and W. J. Weber, Synergistically-enhanced ion track formation in pre-damage strontium titanate by energetic heavy ions, *Acta Mater.* **150**: 351-359 (2018).
3. M. L Crespillo, J. T. Graham, F. Agulló-López, Y. Zhang, and W. J. Weber, The Blue Emission at 2.8 eV in Strontium Titanate: Evidence for a Radiative Transition of Self-trapped Excitons from Unbound States, *Mater. Res. Lett.* **7**: 298-303 (2019).
4. N. Sellami, M. L. Crespillo, Y. Zhang, and W. J. Weber, Two-state synergy of electronic energy loss with defects in $LiTaO_3$ under ion irradiation, *Mater. Res. Lett.* **6**: 339-344 (2018).
5. K. Jin, Y. Zhang, and W. J. Weber, Synergistic effects of nuclear and electronic energy deposition on damage production in $KTaO_3$, *Mater. Res. Lett.* **6**: 531-536 (2018).
6. F. X. Zhang, J. Xi, Y. Zhang, T. Tong, H. Xue, R. Huang, C. Trautmann and W. J. Weber, Local structure and defects in ion irradiated $KTaO_3$, *J. Phys.: Condens. Matter*, **30** [14]: 145401 (2018).
7. W.J. Weber and Y. Zhang, Predicting Damage Production in Monoatomic and Multi-elemental Targets using Stopping and Range of Ions in Matter Code: Challenges and Recommendations, *Curr. Opin. Solid State Mater. Sci.* (2019) in press. https://doi.org/10.1016/j.cossms.2019.06.001

Publications (past 2 years)

1. W.J. Weber and Y. Zhang, Predicting Damage Production in Monoatomic and Multi-elemental Targets using Stopping and Range of Ions in Matter Code: Challenges and Recommendations, *Current Opinion in Solid State & Materials Science* (2019) in press. https://doi.org/10.1016/j.cossms.2019.06.001
2. M. L Crespillo, J. T. Graham, F. Agulló-López, Y. Zhang, and W. J. Weber, The Blue Emission at 2.8 eV in Strontium Titanate: Evidence for a Radiative Transition of Self-trapped Excitons from Unbound States, *Materials Research Letters* **7**: 298-303 (2019).
3. A. Debelle, L. Thomé, I. Monnet, F. Garrido, O. H. Pakarinen, and W. J. Weber, Ionization-induced thermally activated defect-annealing processes, *Physical Review Materials* **3**: 063609 (2019).
4. F. Zhang, T. Tong, H. Xue, J. K. Keum, Y. Zhang, A. Boulle, A. Debelle, and W. J. Weber, Strain engineering 4H-SiC with ion beams, *Applied Physics Letters* **114**: 221904 (2019).
5. W. A. Hanson, M. K. Patel, M. L. Crespillo, F. Zhang, S. J. Zinkle, Y. Zhang, and W. J. Weber, Ionizing vs collisional radiation damage in materials: Separated, competing, and synergistic effects in Ti_3SiC_2, *Acta Materialia* **173**: 195-205 (2019).
6. G. Velisa, E. Wendler, L.-L. Wang, Y. Zhang and W. J. Weber, Amorphization kinetics in strontium titanate at 16 and 300 K under argon irradiation, *Journal of Materials Science* **54**: 6066-6072 (2019).
7. K. Jin, G. Velisa, H. Xue, T. Yang, H. Bei, W. J. Weber, L. Wang, and Y. Zhang, Channeling analysis in studying ion irradiation damage in materials containing various defect types, *Journal of Nuclear Materials* **517**: 9-16 (2019).
8. J.-M. Costantini, G. Gutierrez, H. Watanabe, K. Yasuda, S. Takaki, G. Lelong, M. Guillaumet, and William J. Weber, Optical spectroscopy study of modification induced in cerium dioxide by electron and ion irradiations, *Philosophical Magazine* **99**: 1695-1714 (2019).
9. M. L. Crespillo, J. T. Graham, F. Agulló-López, Y. Zhang, and W. J. Weber, Recent Advances on Carrier and Exciton Self-Trapping in Strontium Titanate: Understanding the Luminescence Emissions, *Crystals* **9**: 95 (2019).
10. R. Sachan, M. F. Chisholm, X. Ou, Y. Zhang, and W. J. Weber, Energetic ion irradiation-induced disordered nanochannels for fast ion conduction, *JOM* **71** [1]: 103-108 (2019).
11. Z. Liao, M. Brahlek, J. M. Ok, L. Nuckols, Y. Sharma, Q. Lu, Y. Zhang, and H. N. Lee, Pulsed-laser epitaxy of topological insulator Bi2Te3 thin films, *APL Materials* **7** [4]: 041101 (2019).
12. C. Sohn, E. Skoropata, Y. Choi, X. Gao, A. Rastogi, A. Huon, M. A. McGuire, L. Nuckols, Y. Zhang, J. W. Freeland, D. Haskel, and H. N. Lee, Room-Temperature Ferromagnetic Insulating State in Cation-Ordered Double-Perovskite $Sr_2Fe_{1+x}Re_{1-x}O_6$ Films, *Advanced Materials* **31** [4]: 1805389 (2019).
13. K. Nordlund, S. J. Zinkle, A. E. Sand, F. Granberg, R. S. Averback, R. E. Stoller, T. Suzudo, L. Malerba, F. Banhart, W. J. Weber, F. Willaime, S. L. Dudarev, and D. Simeone, Primary

radiation damage: A review of current understanding and models, *J. Nuclear Materials* **512**: 450-479 (2018).
14. M. L. Crespillo, J. T. Graham, F. Agulló-López, Y. Zhang, and W. J. Weber, Isolated oxygen vacancies in strontium Titanate shine red: Optical identification of Ti^{3+} polarons, *Applied Materials Today* **12**: 131-137 (2018).
15. C. Ostrouchov, Y. Zhang, and W. J. Weber, pysrim: Automation, Analysis and Plotting of SRIM Calculations, *The Journal of Open Source Software* **3** [28]: 829 (2018).
16. K. Jin, Y. Zhang, and W. J. Weber, Synergistic effects of nuclear and electronic energy deposition on damage production in $KTaO_3$, *Materials Research Letters* **6** [9]: 531-536 (2018).
17. R. Sachan, E. Zarkadoula, X. Ou, C. Trautmann, Y. Zhang. M. F. Chisholm, and W. J. Weber, Sculpting Nanoscale Functional Channels in Complex Oxides Using Energetic Ions and Electrons, *ACS Applied Materials & Interfaces* **10** [19]: 16731-16738 (2018).
18. A.-M. Seydoux-Guillaume, X. Deschanels, C. Baumier, S. Neumeier, W. J. Weber, and S. Peuget, Why natural monazite never becomes amorphous: experimental evidence for alpha self-healing, *American Mineralogist* **103** [5]: 824-827 (2018).
19. H. Xue, E. Zarkadoula, R. Sachan, Y. Zhang, C. Trautmann and W. J. Weber, Synergistically-enhanced ion track formation in pre-damage strontium titanate by energetic heavy ions, *Acta Materialia* **150**: 351-359 (2018).
20. G. Velisa, E. Wendler, H. Xue, Y. Zhang, and W. J. Weber, Revealing ionization-induced dynamic recovery in ion-irradiated $SrTiO_3$, *Acta Materialia* **149**: 256-264 (2018).
21. F. X. Zhang, J. Xi, Y. Zhang, T. Tong, H. Xue, R. Huang, C. Trautmann and W. J. Weber, Local structure and defects in ion irradiated $KTaO_3$, *J. Phys.: Condens. Matter*, **30** [14]: 145401 (2018).
22. N. Sellami, M. L. Crespillo, Y. Zhang, and W. J. Weber, Two-state synergy of electronic energy loss with defects in $LiTaO_3$ under ion irradiation, *Materials Research Letters* **6** [6]: 339-344 (2018).
23. K. Nordlund, S. J. Zinkle, A. E. Sand, F. Granberg, R. S. Averback, R. Stoller, T. Suzudo, L. Malerba, F. Banhart, W. J. Weber, F. Willaime, S. Dudarev, and D. Simeone, Improving atomic displacement and replacement calculations with physically realistic damage models, *Nature Communications* **9**: 1084 (2018).
24. J.-M. Costantini, S. Miro, N. Touati, L. Binet, G. Wallez, G. Lelong, M. Guillaumet, and W. J. Weber, Defects induced in cerium dioxide single crystals by electron irradiation, *J. Applied Physics* **123** [2]: 025901 (2018).
25. S. Jesse, B. M. Hudak, E. Zarkadoula, J. Song, A. Maksov, M. Fuentes-Cabrera, P. Ganesh, I. Kravchenko, P. C. Snijders, A. R. Lupini, A. Y. Borisevich, and S. V. Kalinin, "Direct atomic fabrication and dopant positioning in Si using electron beams with active real-time image-based feedback," *Nanotechnology* **29** [25]: 255303 (2018).
26. Y. Zhang, H. Xue, E. Zarkadoula, R. Sachan, C. Ostrouchov, P. Liu, X. Wang, S. Zhang, T. S. Wang, and W. J. Weber, Coupled electronic and atomic effects on defect evolution in

silicon carbide under irradiation, *Current Opinion in Solid State & Materials Science* **21** [6]: 285-298 (2017).
27. S. Zhao, Y. Zhang, and W. J. Weber, Ab Initio Study of Electronic Excitation Effects on $SrTiO_3$, *J. Physical Chemistry C* **121** [48]: 26622-26628 (2017).
28. M. L. Crespillo, J. T. Graham, F. Agulló-López, Y. Zhang, and W. J. Weber, Correlation between Cr^{3+} Luminescence and Oxygen Vacancy Disorder in Strontium Titanate under MeV Ion Irradiation, *J. Physical Chemistry C* **121** [36]: 19758-19766 (2017).
29. H. Xue, Y. Zhang, and W. J. Weber, In-cascade ionization effects on defect production in 3C silicon carbide, *Materials Research Letters* **5** [7]: 494-500 (2017).

Irradiation Tailoring of Deformation-Induced Phase Transformations

Janelle P. Wharry [1]

[1] Purdue University

Program Scope

The objective of this project is to understand how irradiation enables deformation-induced phase transformations in fcc metallic alloys. Low-temperature deformation of face centered cubic (fcc) metals and alloys can occur through several modes, one of which is martensitic transformation, wherein fcc γ-Fe austenite reverts to hexagonal close packed (hcp) ε-martensite or body centered cubic (bcc) α'-martensite. Irradiation is believed to enhance the tendency for this transformation to occur, considering that irradiation similarly enhances other low-temperature deformation modes such as dislocation channeling and deformation twinning. However, the mechanisms underlying the irradiation enhancement of martensitic transformations remain unknown. Most studies on deformation of irradiated fcc alloys have focused on deformation twinning rather than on the martensitic transformation, and have tended to simply ascribe any martensites to the twinning associated with irradiation-induced dislocation loops [1–4]. But recently, porosity has been shown to enhance the martensitic transformation in shape memory alloys [5–7] through surface energy effects. Thus, the role of both interstitial-type (e.g. loops) and vacancy-type (e.g. cavities) irradiation defects on the phase transformation must be understood. An altered tendency to phase transform can have severe implications on the performance of load-bearing materials exposed to irradiation, such as nuclear reactor structural materials. More scientifically, using irradiation to tailor the austenite-to-martensite phase transformation can facilitate materials design and innovation across numerous energy generation applications.

This project hypothesizes that the type (i.e. interstitial or vacancy), morphology, and distributions of irradiation defects enable precise tuning of the deformation mechanism. The hypothesis will be tested through three scientific questions:

1) How does irradiation enable the deformation mechanism to evolve from dislocation-mediated or twinning, to martensitic transformation?
2) How do the relative populations of irradiation-induced vacancy- and interstitial-type defects modulate the martensitic transformation pathway?
3) How does the stacking fault energy (SFE) vary locally at irradiation-induced defects, and how does this variation affect the deformation pathway?

Recent Progress

This project will begin in September 2019.

Future Plans

This project will use a multiscale approach that combines novel small-scale mechanical testing

and *in situ* electron microscopy investigations with mechanics models that will help us interpret and expand the parametric space of our experiments. Work will focus on Fe-*x*Mn alloys irradiated with He^{+} and/or Fe^{2+} ions to create tailored microstructures that are dominated either by vacancy-type or interstitial-type defects, or some combination of these extremes. We will utilize small-scale mechanical testing techniques to introduce deformation. Nanoindentation will rapidly check for twinning or martensitic transformations over a range of irradiation and loading conditions, and post-indentation microstructure characterization will enable us to associate specific irradiation conditions with deformation mechanisms. Transmission electron microscopic (TEM) *in situ* deformation will reveal nano/micro-scale mechanisms of twinning and deformation-induced martensite nucleation at specific irradiation-induced defects. Coupled phase field-crystal plasticity models will elucidate the role of irradiation-induced changes in interfacial/surface energy and SFE, in the transition from deformation twinning to martensitic transform.

References

[1] A.H. Cottrell, B.A. Bilby, LX. A mechanism for the growth of deformation twins in crystals, Philos. Mag. 42 (1951) 573–581.

[2] J.A. Venables, The martensite transformation in stainless steel, Philos. Mag. 7 (1961) 35–44.

[3] J.A. Venables, Deformation twinning in face-centred cubic metals, Philos. Mag. 6 (1961) 379–396.

[4] N. Hashimoto, S.J. Zinkle, A.F. Rowcliffe, J.P. Robertson, S. Jitsukawa, Deformation mechanisms in 316 stainless steel irradiated at 60°C and 330°C, J. Nucl. Mater. 283–287 (2000) 528–534.

[5] M. Chmielus, X.X. Zhang, C. Witherspoon, D.C. Dunand, P. Müllner, Giant magnetic-field-induced strains in polycrystalline Ni-Mn-Ga foams, Nat. Mater. 8 (2009) 863–866.

[6] W.Z. Han, J. Zhang, M.S. Ding, L. Lv, W.H. Wang, G.H. Wu, Z.W. Shan, J. Li, Helium Nanobubbles Enhance Superelasticity and Retard Shear Localization in Small-Volume Shape Memory Alloy, Nano Lett. 17 (2017) 3725–3730.

[7] V.A. Levin, V.I. Levitas, K.M. Zingerman, E.I. Freiman, Phase-field simulation of stress-induced martensitic phase transformations at large strains, Int. J. Solids Struct. 50 (2013) 2914–2928.

Publications

None yet; this project will begin in September 2019.

Center for Thermal Energy Transport Under Irradiation

David Hurley[1], Jian Gan[1], Anter El-Azab[2], Krysztof Gofryk[1], Michael Manley[3], Yongfeng Zhang[1], Chris Marianetti[4], Matthew Mann[5], Lingfeng He[1], Janelle Wharry[2], Madhab Neupane[6], Marat Khafizov[7], Jason Harp[3], Zilong Hua[1], Mukesh Bachhav[1]

[1] Idaho National Laboratory; [2] Purdue University; [3] Oak Ridge National Laboratory; [4] Columbia University; [5] Air Force Research Laboratory; [6] University of Central Florida; [7] Ohio State University

Program Scope

The Center for Thermal Energy Transport under Irradiation (TETI) will provide the foundational work necessary to accurately model and ultimately control electron- and phonon-mediated thermal transport in 5*f* electron materials in extreme irradiation environments. To efficiently capture the energy of the nuclear bond, advanced nuclear reactor concepts aim to use fuels that must withstand unprecedented temperature and radiation extremes. In these advanced fuels, thermal energy transport under irradiation is directly related to reactor efficiency as well as reactor safety, and is arguably one of the most important material properties.

Degradation of thermal properties is strongly tied to atomic-scale stoichiometric changes caused by nuclear fission, cooperative effects of multiple defect types, and self-organized defect clusters in oxide fuel or fission gas bubble superlattices in metallic fuel. However, the fundamental relationships between defects and thermal transport remain unknown. TETI will reveal these relationships, in order to ultimately improve the function of nuclear fuel thermal transport by controlling defect evolution under irradiation. We hypothesize that thermal transport in nuclear fuels can be enhanced by mesoscopic defect ordering under irradiation. TETI will achieve two main project goals: (1) predict self-organization of equilibrium and irradiation-induced defects in oxide and metallic fuels, together with the individual and cooperative influence of these defects on the scattering of thermal energy carriers (phonon and electrons), and (2) use fundamental knowledge of microscopic phonon and electron transport physics to predict and validate mesoscopic thermal transport under irradiation in oxide and metallic fuels.

Recent Progress

Science Question 1: What is the impact of 5f electrons on phonon and electron structure in $Th_{1-x}U_xO_2$ and U-Zr?

We have computed the phonons and phonon interactions using density functional theory (DFT) for the parent materials α-U, δ-U, and ThO_2. We have computed the cubic phonon interactions in ThO_2, which will allow the computation of phonon linewidth and thermal conductivity. Finally, we have computed the Gruneisen parameters in ThO_2, finding one branch with unusually large Gruneisen parameters, corresponding to the mode that softens upon sufficient volume expansion and leads to the oxygen sublattice melting.

The analysis of phonon density of states measurements of UO_2 as a function of temperature has been completed. Heat capacity has two regimes: <300 K, the harmonic heat capacity from phonons can account for the measured heat capacity at constant pressure, but >300 K, the heat capacity can be decomposed into a harmonic and an anharmonic term based on measured phonon

density of states and an electron contribution. We also measured heat capacity of UO_2 single crystals. To unveil the nature of 5*f* electrons in correlated uranium metallic phases such as α- and δ-uranium (UZr_2), we have performed detailed magnetic, thermodynamic, and transport measurements of these phases. Time-domain Brillouin scattering (TDBS) has been used to generate and detect lattice vibrations associated with the propagation of quasi-longitudinal and quasi-shear elastic phonon modes along various crystallographic directions in ThO_2. Measurements of the temperature-dependent change in phonon velocities have been performed (Fig. 1).

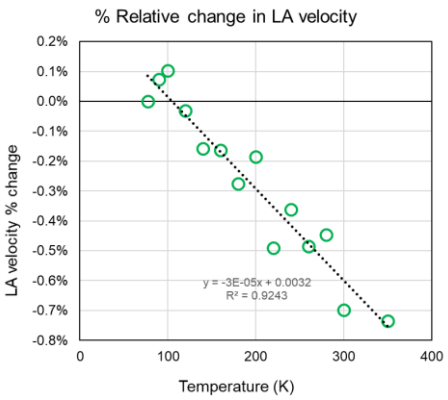

Figure 1. Change in the low frequency LA mode velocity versus temperature for ThO_2.

To directly compare with electronic structure of 5*f*-systems, we studied the electronic structure of 4*f*-electron systems. Through a detailed electronic structure study using high-resolution angle-resolved photoemission spectroscopy (ARPES) and high field magnetoresististivity (MR), we demonstrated detailed characterization of the electronic structure of HoSb, revealing a highly anisotropic bulk band with a small gap at the corner of the Brillouin zone and a Rashba-type surface state within the bulk gap.

Science Question 2: How do intrinsic and irradiation-induced defects self-organize in $Th_{1-x}U_xO_2$ and U-Zr, and what are their impacts on electron and phonon scattering?

Hydrothermal growth of (100), (111), and (311) single-crystal ThO_2 was achieved at 600-650°C (Fig. 2). Additionally, three δ-UZr_2 (UZr_2, $U_{31}Zr_{69}$, $U_{28}Zr_{72}$) and three Zr-doped α-U ($U_{99}Zr_1$, $U_{98}Zr_2$ and $U_{97}Zr_3$) alloys were prepared by arc melting and arc casting.

Figure 2. Large ThO_2 single crystal grown hydrothermally.

Atom probe tomography (APT)-based quantitative chemical analysis of high bandgap materials (e.g. ThO_2 bandgap of ~6 eV) is not straightforward: the physics of field evaporation are not well understood, and laser and field interaction with semiconducting materials introduce thermal complexities. We have established proper APT parameters to accurately quantify the stoichiometry of ThO_2. A computational model to investigate the off-stoichiometry x in $ThO_{2\pm x}$ and $Th_{1-y}U_y O_{2\pm x}$ subjected to various temperature and oxygen pressure has been completed. ThO_2 remains stoichiometric up to ~1300 K and becomes oxygen-deficient >1300 K. The model analyzes the disorder caused by vacancies and interstitials of Th and O; investigation was expanded to the $Th_{1-y}U_yO_2$ system. Molecular dynamics (MD) simulations studied defect production and evolution in α-U subject to electron irradiation at 300K and 600K to a dose of 0.02 displacements per atom (dpa). At both temperatures, limited defect diffusion precludes dislocation loop formation. A large number of interstitial clusters are observed, although vacancy clusters are rarely seen (Fig. 3). Single interstitials take a [001] dumbbell structure, with another two nearest neighbor atoms pushed

away, giving a 2D interstitial configuration in the (100) plane. The interstitial clusters also take 2D configurations in the (100) plane. Phase transformation from α to γ was also studied. Two γ variants with different crystal orientations can result from the transformation, with a Σ3 twin boundary in between. A new shear and shuffle transformation mechanism is identified.

Science Question 3: What are the collective effects of defects, defect ordering, and defect supersaturation on thermal transport $Th_{1-x}U_xO_2$ and U-Zr?

SQ3 focuses on the computational modeling of the phonon and electron-transport/scattering processes using the Boltzmann Transport Equation (BTE) framework and the confrontation of the computed conductivities with measured values in materials with carefully controlled defects. The initial focus has been on the trial use of the theoretical, computational and experimental tools until the specimens of materials of interest are available.

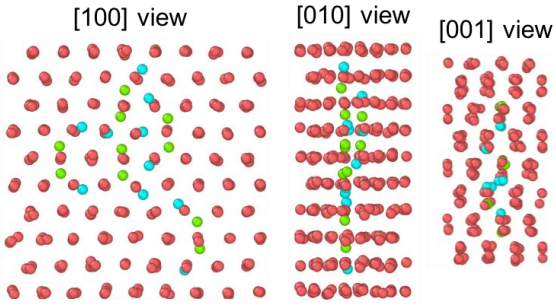

Figure 3. Atomic configuration of a 2D interstitial cluster in the (100) plane identified from molecular dynamics simulations. The green atoms are those in [001] dumbbells, and the blue ones are displaced away from their lattice sites by the dumbbell. From left to right, the configuration is projected along the [100], [010] and 001] directions, respectively.

We have recently tested several phonon relaxation time models along with a novel Brillouin zone (BZ) integration scheme that yielded accurate thermal conductivity of solid Ar. This same class of phonon relaxation time models was used to assess phonon transport in UO_2 and is currently being applied to ThO_2. Thermal anisotropy in cubic UO_2 has been measured, as a first step in addressing the same questions for ThO_2. We have also measured heat capacity of ThO_2 single crystals over a wide temperature range to help elucidate vibrational properties, especially details of the phonon density-of-states. Finally, because point defects and small defect clusters can lead to activation of Raman vibrational modes, we have evaluated the applicability of Raman spectroscopy approaches by demonstrating these measurements on proton irradiated CeO_2 (Fig. 4). Raman spectra exhibit notable width and position changes in the intrinsic F_{2g} peak, and emergence of a defect peak previously attributed to vacancies.

Future Plans

Science Question 1 – DFT calculations to predict phonons, electrons, and transport will continue, with a focus on phonon linewidths and shifts in ThO_2, the temperature-pressure phase diagram of U, and the temperature dependence of the thermal conductivity and elastic constants of U and ThO_2. Neutron & x-ray scattering measurements of linewidth and dispersion in ThO_2 and $U_{(1-y)}Th_{(y)}O_2$ will be carried out. Resultant phonon density of states and the temperature-dependent behavior will be compared to aforementioned DFT simulations.

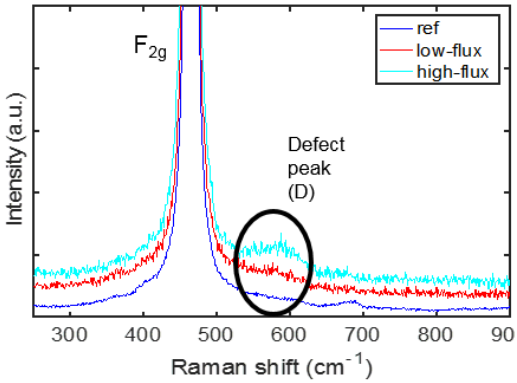

Figure 4. Raman spectra in proton irradiated CeO_2, showing intrinsic F_{2g} mode accompanied by a defect peak associated with O vacancies.

We will carry out systematic and fundamental studies of UZr_2 to understand electronic structure, quantum oscillation, and phonon and electron contribution to thermal transport. Thermal expansion measurements will help understand lattice anharmonicity, and TDBS will be used to measure the temperature-dependent refractive index of ThO_2.

Science Question 2 – The first $Th_{1-y}U_yO_{2\pm x}$ single crystal samples will be prepared. Single crystal α-U will also be grown, and the fabrication method for α-U(Zr) will be refined. Ion irradiations will be conducted on ThO_2, U-doped ThO_2, and UZr. Subsequently, transmission electron microscopic (TEM) and APT characterization of the irradiated specimens will proceed. These experimental results will provide the number and size distribution of defects as functions of temperature, to calibrate cluster dynamics simulations for the materials. Thermodynamic and kinetic properties will be calculated for various defects, and we will also simulate how defect and defect cluster configurations scatter energy carriers such as phonons. A cluster dynamics model will be completed to investigate the formation of defect clusters under irradiation. The model will be integrated with the Boltzmann transport equation solution for phonon transport. Research will then progress to implement a phase field model of microstructure evolution under irradiation in ThO_2 and $Th_{1-y}U_yO_2$.

Science Question 3 – A BTE code will be implemented to investigate thermal conductivity of ThO_2 and U-doped ThO_2, including phonon scattering by extrinsic and intrinsic defects. Dispersion curves and anharmonic force constants required to implement the BTE approach for ThO_2 and α-U will be obtained using DFT modeling. We will complete detailed thermal property measurements on U-doped ThO_2, including thermoelectric power, thermal conductivity and electrical resistivity (including in high magnetic fields to gain insight on the role of 5*f* electrons on transport properties), and magneto-resistance measurements to obtain the electronic and lattice contributions to the total thermal conduction. We will also investigate the crystallographic anisotropy of thermal conductivity of ThO_2 with different types/concentrations of defects. We will study the effects of radiation damage on the phonon dispersion and linewidths in α-U and δ-UZr_2 using inelastic x-ray scattering (IXS). We will also use Raman spectroscopy to characterize irradiation induced defects in pure and doped ThO_2, the results from which will be compared to TEM and APT results.

Publications

1. D.H. Hurley, Characterization of material nano/microstructure using pump-probe laser ultrasonics, Accepted November 2018, *IEEE Nanotechnology Magazine*.
2. K. Rickert, T.A. Prusnick, E. Hunt, M.M. Kimani, S. Chastang, D.L. Brooks, E.A. Moore, J.C. Petrosky, J.M. Mann, Inhibiting laser oxidation of UO2 via Th substitution, *Journal Nuclear Materials*, 517, 254 (2019).
3. Yuzhou Wang, David H Hurley, Zilong Hua, Gaofeng Sha, Samuel Raetz, Vitalyi E Gusev, Marat Khafizov, Nondestructive characterization of polycrystalline 3D microstructure with time-domain Brillouin scattering, *Scripta Materialia*, 166, 34 (2019).

Mesoscale Defect Interaction Mechanisms in Structural Alloys

Haixuan Xu, The University of Tennessee Knoxville

Program Scope

This project aims to obtain a mesoscale mechanistic understanding of radiation-induced defect interaction in model structural alloys. The conventional understanding of mesoscale defect interaction in structural alloys is inadequate due to practical limitations of available tools to capture processes or phenomenon in meso-timescale (nanoseconds to milliseconds or more) as they are too fast for experimental techniques like transmission electron microscopy (TEM) and too slow for conventional atomistic simulations like molecular dynamics. [1-7] This also limits our understanding of how microscale defects interact collectively, which leads to potential errors when extrapolating to macroscale phenomena and materials performance. This project will employ the Self-Evolving Atomistic kinetic Monte Carlo [8-10] to investigate mesoscale defect dynamics and eliminate some of the assumptions or approximations in traditional models and simulations. Particularly this project will focus on (i) The bias factors of interstitial dislocation loops (especially small <100> loops) in bcc iron and iron-based alloys; (ii) collective interaction between multiple dislocations and radiation-induced defects in model alloys. The knowledge gained will provide new insights of void swelling and radiation-induced hardening, which may lead to a useful means of avoiding failure mechanisms such as dislocation channeling. In addition, this project will advance computational capabilities at the mesoscale, which will be widely applicable to other fields of materials science, physics, and chemistry.

Recent Progress

For the dislocation bias model, we have obtained most migration energy barriers (MEBs) for point defects (a vacancy and a dumbbell in bcc iron) near an (edge and screw) dislocation and dislocation loops (both ½<111> and <100> types) with different sizes. Comparatively, we have also calculated the MEBs of point defects near voids. The binding energies of point defects near dislocation loops are also examined. The barriers that are in close proximity to the dislocation loops still need further detailed examined. Preliminary estimations of sink strengths and bias factors of a void based on the kinetic Monte Carlo (KMC) approach have been performed.

For the collective behavior of multiple dislocations with obstacles, we have been focusing on the computational setup and influences of various factors on the simulations. We have 1) verified the simulation setup and structures of one single edge/screw dislocation in Fe and Cu. 2) Performed Peierls stress calculations using the configurations obtained in 1). 3) Studied the interaction of

one single edge/screw dislocation in Fe/Cu with different sizes of voids. 4) Found that a void can be completely absorbed by interacting with multiple dislocations, detailed mechanistic analysis is still in process. 5) Achieved a pile-up configuration of multiple dislocations, with the presence of a coherent twin boundary in fcc Cu or a Σ3 <1 1 0> (1 1 1) symmetrical tilt grain boundary (STGB) in bcc Fe.

For advanced computational capabilities at the mesoscale, integrated approaches of machine learning and parallel computing are working in progress to improve the computational time and accuracy.

Future Plans

The first year of the grant has focused on the theoretical framework. For the coming year, KMC simulations to obtain the bias factors of dislocations loops with different sizes in bcc iron will be carried out. This will allow us to establish the size dependences of dislocations loops on the bias factors. In addition, efforts will be started to investigate bias factors in bcc tungsten, in which the dominant self-interstitial atom is a crowdion. Simulations to examine the mechanisms of multiple dislocations with obstacles will continue and initial simulations of dislocations using SEAKMC will start.

References

1. Bulatov, V., et al., *Connecting atomistic and mesoscale simulations of crystal plasticity*. Nature, 1998. **391**(6668): p. 669-672.

2. Li, J., et al., *Atomistic mechanisms governing elastic limit and incipient plasticity in crystals.* Nature, 2002. **418**(6895): p. 307-310.

3. Yamakov, V., et al., *Grain-boundary diffusion creep in nanocrystalline palladium by molecular-dynamics simulation.* Acta Materialia, 2002. **50**(1): p. 61-73.

4. Yamakov, V., et al., *Dislocation processes and deformation twinning in nanocrystalline Al.* Iccn 2002: International Conference on Computational Nanoscience and Nanotechnology, 2002: p. 283-286.

5. Yamakov, V., et al., *Dislocation processes in the deformation of nanocrystalline aluminium by molecular-dynamics simulation.* Nature Materials, 2002. **1**(1): p. 45-48.

6. Yamakov, V., et al., *Deformation-mechanism map for nanocrystalline metals by molecular-dynamics simulation.* Nature Materials, 2004. **3**(1): p. 43-47.

7. Osetsky, Y.N. and D.J. Bacon, *An atomic-level model for studying the dynamics of edge dislocations in metals.* Modelling and Simulation in Materials Science and Engineering, 2003. **11**(4): p. 427-446.

8. Xu, H.X., Y.N. Osetsky, and R.E. Stoller, *Self-Evolving Atomistic Kinetic Monte Carlo: Fundamentals and Applications.* Journal of Physics-Condensed Matter, 2012. **24**: p. 375402.

9. Xu, H.X., et al., *Solving the Puzzle of < 100 > Interstitial Loop Formation in bcc Iron.* Physical Review Letters, 2013. **110**(26): p. 265503.

10. Xu, H.X., et al., *Self-Evolving Atomistic Kinetic Monte Carlo simulations of defects in materials.* Computational Materials Science, 2015. **100**: p. 135-143.

Publications

N/A

Understanding Multiscale Defect Formation Process and Phase-Switching Behavior in Shape Memory Functional Oxides

Mohsen Asle Zaeem, Colorado School of Mines (Lead Principle Investigator)
Doyl Dickel, Mississippi State University (Principal Investigator)
Michael Baskes, Mississippi State University (Co-Investigator)

Program Scope

Different stimuli (e.g., mechanical load or temperature change) can promote martensitic phase transformation in some ceramic oxides, and similar to many metallic systems, the phase fractions and morphologies of martensitic phases determine the properties of these materials. It is recently revealed that some micron- and submicron-sized ceramics show recoverable martensitic phase transformation that can provide superelastic and shape memory properties. However, experimental tests reveal that degradation of shape recovery and premature failure happen in these materials only after a few loading cycles. The underlying nanoscale phase-switching behavior and defect formation and evolution process of these shape memory functional oxides (SMFOs) are not fully understood yet. In this work, a combination of large scale atomistic simulations and phase-field modeling is proposed to study the effects of intrinsic and extrinsic characteristics on the deformation mechanism, phase-switching property, and defect formation/evolution process in single crystalline and polycrystalline nano- and micropillars of yttria-stabilized tetragonal ZrO_2 (YSTZ) and $BiFeO_3$.

SMFOs are solid-state transducers and may sense thermal, mechanical and electric stimulus, making them useful in a wide variety of applications ranging from actuation, energy damping, energy harvesting, etc. Development of advanced quantitative computational models for fundamental understanding of phase-switching behavior and defect formation process and predicting the properties of SMFOs are necessary for the future design of shape memory ceramics that can function for a high number of thermo-electro-mechanical fatigue cycles.

Recent Progress

Specimen- and grain-size effects on nanoscale plastic deformation mechanisms and mechanical properties of polycrystalline yttria-stabilized tetragonal zirconia (YSTZ) nanopillars were studied by molecular dynamics simulations [1]. Through uniaxial compression of YSTZ columnar nanopillars, intergranular and transgranular deformation mechanisms are investigated. Cooperative intergranular deformations including grain boundary sliding and migration, grain rotation, and amorphous phase formation at grain boundaries are revealed Figure 1). Results also reveal formation of partial dislocations, which act as splitters of large grains and play a significant role in facilitating the rotation of grains, and consequently promote amorphous-to-crystalline phase transition in-between neighboring grains. An increase in free surface-to-volume ratio is found to be responsible for specimen size-induced softening phenomenon, where a decrease in Young's modulus and strength is observed when the specimen width decreases from 30 nm to 10 nm. Also, a decrease in Young's modulus and strength is revealed with the decrease of average grain size from 15 nm to 5 nm. Grain boundary density is identified to be responsible for the observed grain size-induced softening behavior in polycrystalline YSTZ nanopillars. A transition in dominant deformation mechanism is observed from amorphous phase formation at grain boundaries to a competition between intergranular grain boundary sliding and transgranular phase transformation. Furthermore, an inverse Hall-Petch relationship is revealed describing the

correlation between grain size and strength for polycrystalline YSTZ nanopillars with grain sizes below 15 nm.

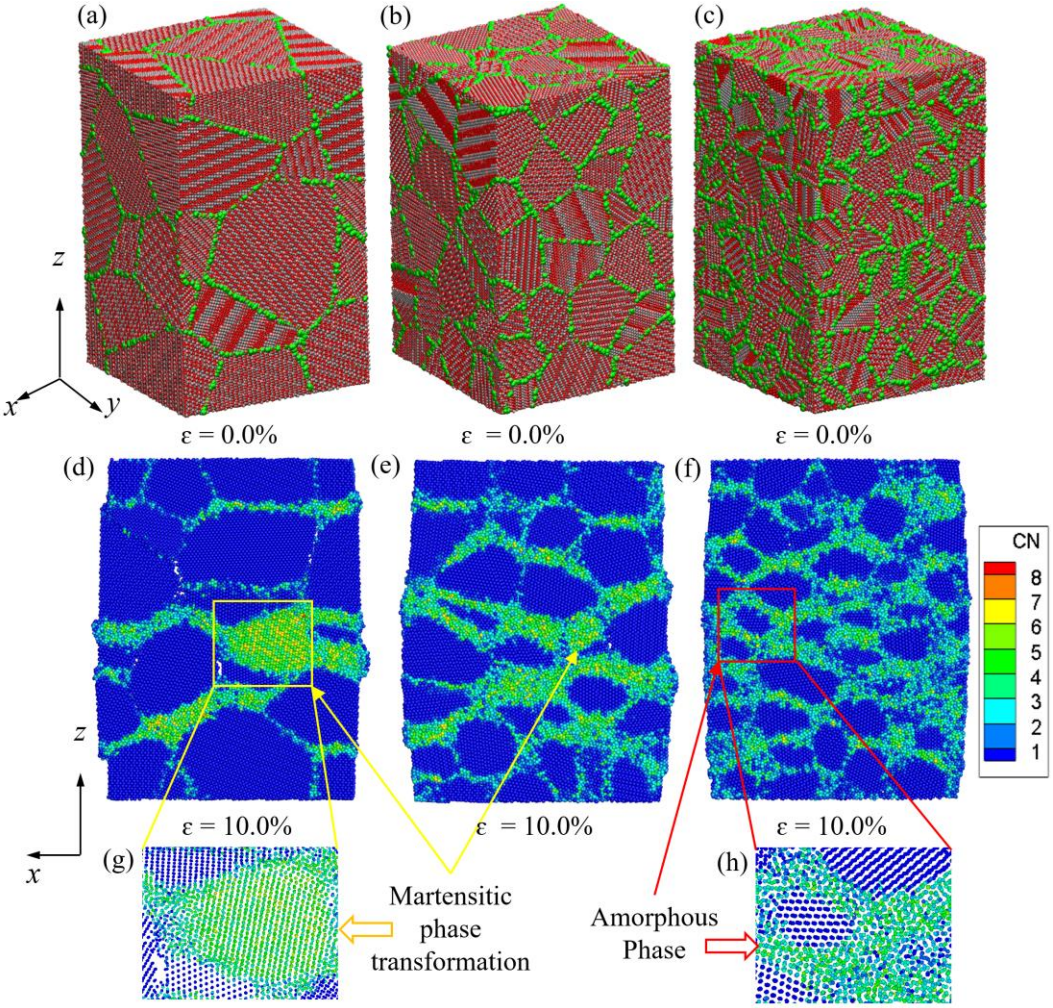

Figure 1. Representative polycrystalline YSTZ nanopillars with average grain sizes of (a) 14.7 nm, (b) 7.8 nm and (c) 5.4 nm for grain size effect study. Atoms with grey, red and pink colors are Zr, O and Y, respectively. (d-f) show the corresponding cross-sectional side views of atomic configurations in (a-c) at strain of 10.0%. The atomic arrangements regarding transgranular phase transformation and amorphous phase formation on GBs are enlarged and shown in (g) and (h), respectively. Coordination number (CN) is adopted to track the evolution of deformation in (d)-(h). Blue color represents YSTZ with tetragonal structure, while green and other colors represent GBs and high strained atoms [1].

The defect evolution behaviors in YSTZ nanopillars were investigated by atomistic simulations [2]. Two characteristic orientations of $[01\bar{1}]$ and [001] are selected to represent the dominant deformation mechanisms of phase transformation and dislocation migration, respectively. Volume expansion associated with the tetragonal to monoclinic phase transformation is observed to promote healing of crack and void. Atom stress analyses reveal stress concentrations along the newly formed monoclinic phase bands. A critical crack/void width is identified, less than which the crack/void can be fully closed in compression (Figure 2). For [001]-oriented YSTZ nanopillars, dislocation migration leads to formations of an amorphous phase, which also assist the crack and void closure process. The revealed crack/void healing mechanisms may provide a path for mitigating internal defects that influences the mechanical properties and deformation mechanisms of SM ceramics.

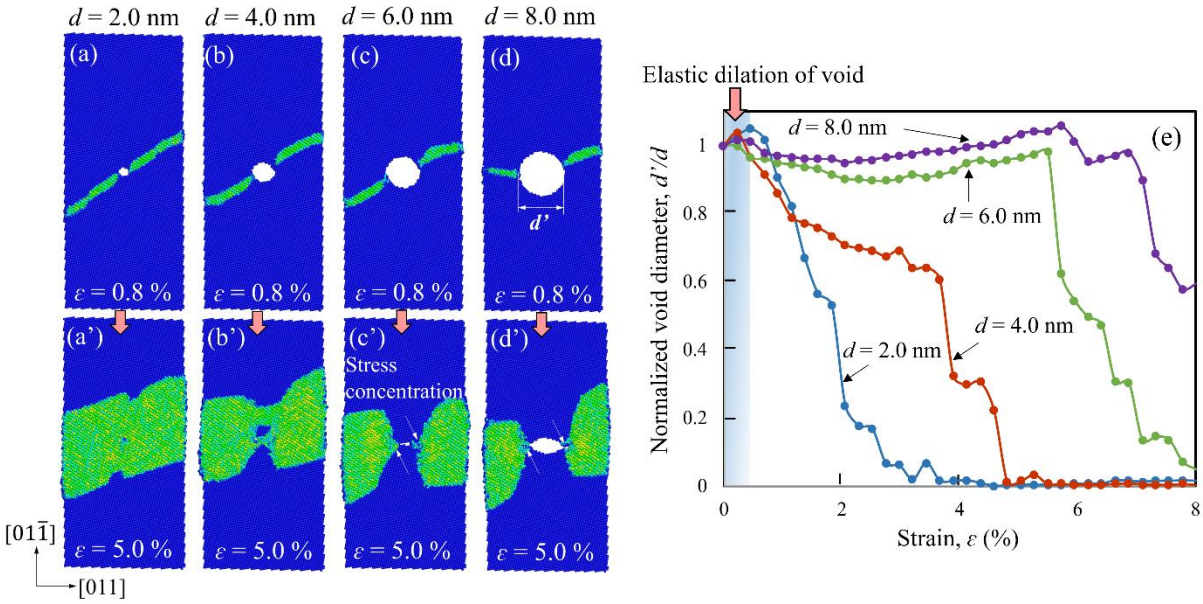

Figure 2. Atomic configurations of [01$\bar{1}$]-oriented YSTZ nanopillars with different pre-existing void sizes under compressive strains of (a-d) 0.8% and (a'-d') 5.0%. Atoms are colored by coordination number, where blue and green colors denote atoms with tetragonal and monoclinic crystal structures, respectively. (e) Evolution of normalized void diameter (*d'/d*) during compression as a function of strain for YSTZ nanopillars with pre-existing diameters of 2.0 nm, 4.0 nm, 6.0 nm and 8.0 nm. The blue shadow region on the left indicates the original elastic dilation of crack [2].

Future Plans

In annealing of yttria-stabilized tetragonal zirconia (YSTZ), {011}-specific twins and sub-surface defects are often observed, however their effects on the martensitic phase transformation and deformation behavior of YSTZ have never been investigated. We will study the roles of twin boundaries (TBs) and pre-existing defects in determining the mechanical properties and subsequent deformation mechanisms of YSTZ nanopillars.

We also plan to the investigate the flaw tolerance in polycrystalline YSTZ nanopillars by creating polycrystalline models with different grain sizes and pre-existing defects. The goal is to find a relationship between grain orientation, grain and defect/void size in order to design nano/microstructures that increase the flaw tolerance of polycrystalline YSTZ.

And finally, we are working on developing new sets of interatomic potentials for SMFOs. First we will focus on $BiFeO_3$, and we will investigate the effects of crystallographic orientation on shape memory, phase-switching, and defect formation process of single-crystal and bicrystal $BiFeO_3$ nanopillars by large scale molecular dynamics simulations.

Publications

[1] N. Zhang and M. Asle Zaeem. Understanding specimen- and grain-size effects on nanoscale plastic deformation mechanisms and mechanical properties of polycrystalline yttria-stabilized tetragonal zirconia nanopillars. European Journal of Mechanics / A Solids 76 (2019) 80-90.

[2] N. Zhang and M. Asle Zaeem. Nanoscale self-healing mechanisms in shape memory ceramics. npj Computational Materials 5 (2019) 54.

[3] M. Asle Zaeem, N. Zhang, M. Mamivand. A review of computational modeling techniques in study and design of shape memory ceramics. Computational Materials Science 160 (2019) 120-136.

Deformation mechanisms of nanotwinned Al and binary Al alloys

Xinghang Zhang
School of Materials Engineering, Purdue University, West Lafayette, IN 47907
Phone: (765) 494-1641; Email: xzhang98@purdue.edu

Program Scope

The objective of this project is to investigate, at a fundamental level, the deformation mechanism of nanotwinned (nt) Al and binary Al alloy films with high density **twin boundaries (TBs)** and **stacking faults (SFs)**. To achieve this goal, we will test the following hypotheses:

1) Nanotwinned (nt) Al with high stacking fault energy (SFE) may have strengthening mechanisms drastically different from those of nt Cu with low SFE.

2) ITBs and SFs may enable high ductility in nt Al. Although there are abundant studies that show CTBs promote work hardening in nt Cu, there are few studies that investigate the influence of ITBs and SFs on tensile ductility of nt Al.

3) ***Certain solutes in nt Al alloys may enable substantial increase of strength and plasticity and significantly enhance the mechanical and thermal stability of TBs in nt Al alloys.*** *The addition of certain solutes may enable us to tailor (reduce) the SFE of Al alloy, so that we can introduce greater density of twins/SFs in nt Al alloys, tailor strengthening and deformation mechanisms in nt Al alloys and accomplish increase of strength with little loss in ductility in nt Al alloys.*

Recent Progress

1) High-Strength Nanotwinned Al Alloys with 9R Phase (Adv. Materials 30, 1704629, 2018)

We fabricated high-strength, nt Al-xFe (x=1-10 at.%) solid solution alloys with a substantial fraction (~ 25 vol.%) of 9R phase. *In situ* SEM micrographs in Fig. 1a show ductile deformation of pure Al, as evidenced by barreling of the pillar, and the specimen exhibits a flow stress of ~ 200 MPa (Fig. 5D). The SEM snapshots of Al-2.5%Fe alloys (Fig. 1b) show extensive deformation of the pillar, with a reverse conical shape. The flow stress of Al-2.5%Fe exceeds 1 GPa. Similar geometry change was observed in the Al-5.9%Fe micropillars (Figure 1c). Interestingly, no shear offsets were observed in the deformed specimens. At 10% strain, the flow stress of the Al-5.9%Fe exceeds 1.5 GPa (calculations represent lower bound of stress).

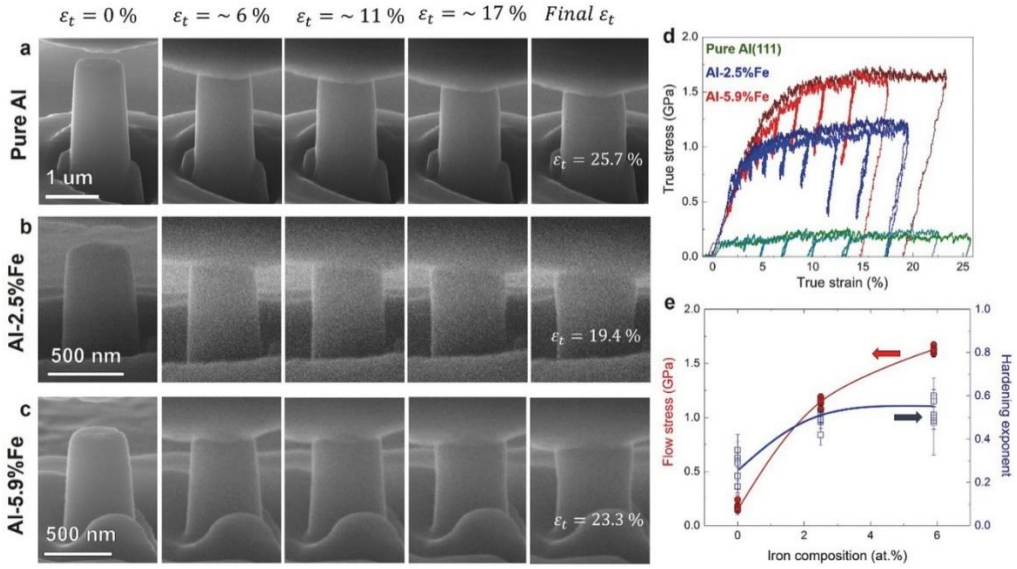

Figure 1. *In situ* micropillar compression tests on Al (111) and nt Al-Fe films performed inside a scanning electron microscope. (a-c) SEM micrographs of Al(111) and Al-xFe (x = 2.5 or 5.9 at.%) pillars captured during *in situ* compressions to different strains. (d) True stress-strain curves of the pillars show that the flow stress of Al-2.5%Fe and Al-5.9% Fe exceeds 1.0 and 1.5 GPa, respectively. (e) The flow stresses at ~ 10% strain shows that the Al-Fe alloy films have significantly higher flow stress than monolithic Al films. The strain hardening exponent, n, of the Al-Fe films is greater than that of monolithic Al films.

2) Mechanical behavior and strengthening mechanisms of nanotwinned AlMg alloys.
(Invited paper, Journal of Materials Research 33, 3739-3749, 2018)

We introduce twins into sputtered AlMg films by using a Ag seed layer as shown in Fig. 2. By adding more Mg solute, the strength of the nt AlMg films raises significantly due to the solid-solution and grain boundary strengthening. *In situ* micropillar compression technique is also employed to obtain stress-strain behaviors, and the flow stress of nt Al-Mg films reached 0.8 GPa, correlated well with the hardness measured by nanoindentation. Furthermore, compression studies show nt AlMg has an excellent strain hardening capability.

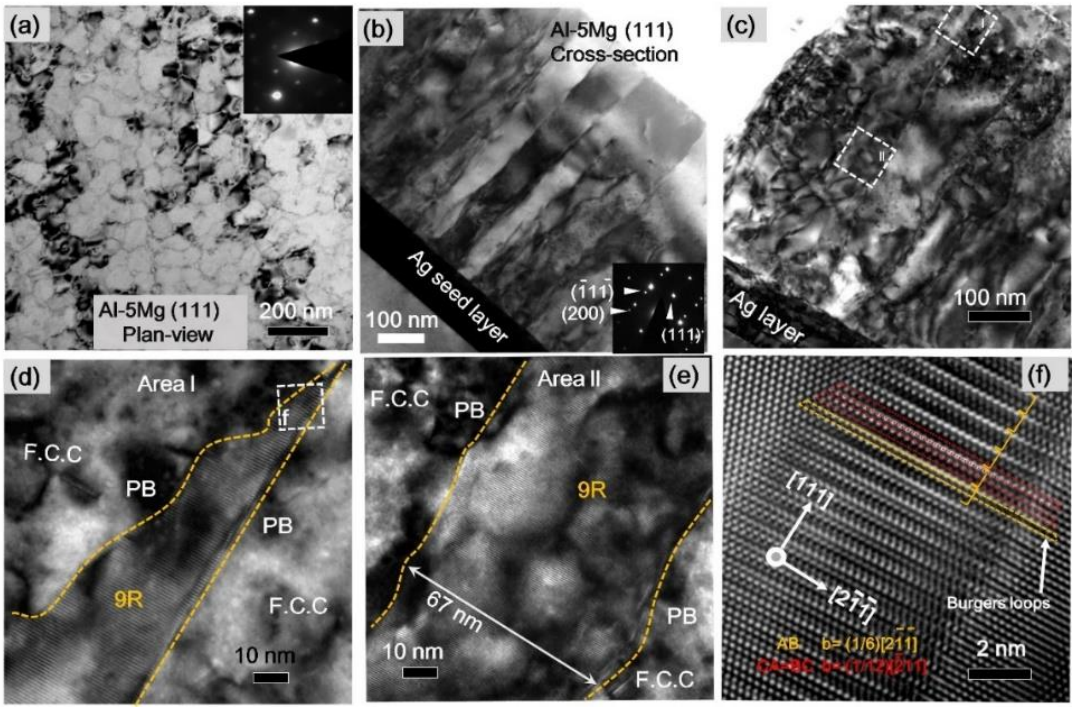

Figure 2.TEM images of Al-5Mg thin film. (a) Plan-view TEM micrograph showing domain boundaries. The inserted selected area (SAD) diffraction pattern showing the formation of epitaxial films. (b) A cross-section TEM (XTEM) micrograph showing columnar grain boundaries. (c) A low magnification XTEM showing the incoherent twin boundaries (ITBs) decorated with 9R phase. (d) The width of 9R phase decreases from interface to the film surface. (c) A higher magnification TEM micrograph showing the typical 9R phase, ~ 67 nm, formed in the middle of the film. (f) A HRTEM image shows the 9R phase from white box f in Figure 2d.

3) Ultra-strong nanotwinned Al-Ni solid solution alloys with significant plasticity.
(Nanoscale 10 (46), 22025-22034, 2018)

In this paper, we show, by using a small amount of Ni solutes, high-density twin boundaries and stacking faults form in the sputtered Al-Ni solid solution alloys. First-principle density function theory calculations show that Ni solute facilitates the formation of stacking faults and stabilizes nanotwins in Al-Ni solid solutions. *In situ* micropillar compression tests were performed on selected nt Al-Ni alloys. The Al-4.5 Ni and Al-9.3Ni pillars have flow stress (at 8% strain) of 1.0 and 1.75 GPa, respectively. Also, Al-4.5Ni and Al-9.3Ni have much higher work hardening rate than pure Al.

4) Thermal and microstructural stability of high-strength nanotwinned Al-Fe alloys.
(Acta Materialia 165, 142-152, 2019)

Al alloys have widespread applications but often suffer from low yield strength. Nanotwinned Al-Fe solid solution alloys have shown high flow stress (> 1.5 GPa), ascribed to nanograins with abundant incoherent twin boundaries and solute-stabilized 9R phase. However, the high temperature mechanical behaviors of high-strength twinned Al-Fe alloys remain unknown. In this study, we show that nanotwinned microstructures are stable up to 280 ˚C, followed by recrystallization at 300˚C. The precipitation first nucleated at free surface of the films at 280 ˚C. Precipitation and recrystallization formed through the samples at 300 ˚C. The Al_6Fe is determined to possess an orthorhombic structure.

To unveil the real-time mechanical response of the Al-Fe solid solution alloys, in situ micropillar compression has been conducted inside a SEM microscope. As show in Figure 3b, Al-5.5% Fe has a flow stress of ~ 1.67 and 1.63 GPa, after annealing at 100 and 200˚C, slightly lower than that of the as-deposited specimen. The significant drop of flow stress to ~ 0.88 GPa after annealing at 300˚C is due to grain coarsening.

The improved thermal stability of the nt Al-Fe is attributed to several aspects. First, although ITBs carry boundary energy of 223-354 mJ/m^2, similar to the 324 mJ/m^2 of high angle GBs, most of the ITBs in the Al-Fe alloys are diffuse TBs. These diffuse ITBs are less mobile, comparing to sharp ITBs. Second, the Fe solute significantly stabilizes extended ITBs, i.e. 9R phase, as proved by our recent molecular dynamic simulations.

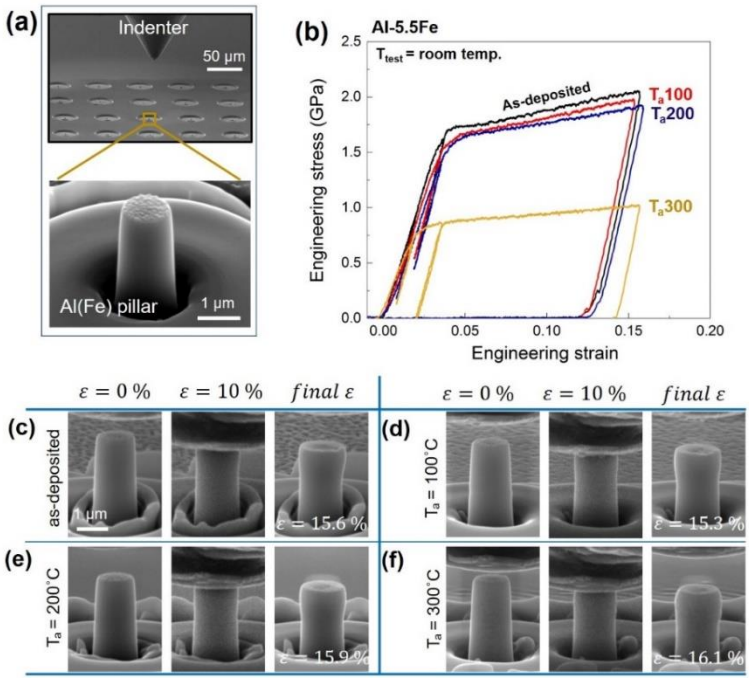

Figure 3. Room temperature in-situ compression tests on Al-5.5Fe specimens annealed at various temperatures: (a) An SEM image demonstrates a typical in-situ experiment. (b) Typical engineering stress-strain curves of Al-5.5 Fe treated at different temperatures. (c-f) Corresponding SEM snapshots captured at different strains during in-situ tests of as-deposited and annealed specimens. T_{anneal} and T_{test} stands for annealing temperature and test temperature, respectively.

Future Plans

In the next fiscal year, we plan to undertake the following tasks:

1) Investigate the tensile behavior of nanotwinned Al alloys.
2) Examine the mechanical behavior of nanotwinned binary Al alloys.
3) Explore the solute effect on twin formation in binary Al alloy systems.
4) Explore the thermal stability of nanotwins in Al and Al alloys.

Publications-patent through this program, 2016-2019

1. Q. Li, J. Cho, S. Xue, X. Sun, Y. Zhang, Z. Shang, H. Wang, X. Zhang, High temperature thermal and mechanical stability of high-strength nanotwinned Al alloys, **Acta Materialia**, 165 (2019) 142-152.

2. S. Xue, Q. Li, D.Y. Xie, Y.F. Zhang, H. Wang, H. Wang, J. Wang, X. Zhang, High strength, deformable nanotwinned Al–Co alloys, **Materials Research Letters**, 7 (2019) 33-39.

3. Y.F. Zhang, Q. Li, S.C. Xue, J. Ding, D.Y. Xie, J. Li, T. Niu, H. Wang, H. Wang, J. Wang, X. Zhang, Ultra-strong nanotwinned Al–Ni solid solution alloys with significant plasticity, **Nanoscale**, 10 (2018), 22025-22034.

4. Q. Li, S. Xue, J. Wang, S. Shao, A. H. Kwong, A. Giwa, Z. Fan, Y. Liu, Z. Qi, J. Ding, H. Wang, J. R. Greer, H. Wang, X. Zhang, High-Strength Nanotwinned Al Alloys with 9R Phase, **Advanced Materials** 30 (2018) 1704629.

5. S. Xue, Q. Li, Z. Fan, H. Wang, Y. Zhang, J. Ding, H. Wang, X. Zhang, Strengthening mechanisms and deformability of nanotwinned AlMg alloys, **Journal of Materials Research** 33 (2018), 3739-3749 (invited paper).

6. S. Xue, W. Kuo, Q. Li, Z. Fan, J. Ding, R. Su, H. Wang, X. Zhang, Texture-directed twin formation propensity in Al with high stacking fault energy, **Acta Materialia,** 144 (2018) 226-234.

7. Y.F. Zhang, S. Xue, Q. Li, C. Fan, R. Su, J. Ding, H. Wang, H. Wang, X. Zhang, Microstructure and mechanical behavior of nanotwinned AlTi alloys with 9R phase, **Scripta Materialia,** 148 (2018) 5-9.

8. S. Xue, Z. Fan, B. Lawal O, R. Thevamaran, Q. Li, Y. Liu, K. Y. Yu, J. Wang, E. L. Thomas, H. Wang, X. Zhang, High-velocity projectile impact induced 9R phase in ultrafine-grained aluminium, **Nature Communications**, 8 (2017) 1.

9. Y. Zhang, Q. Li, S. Xue, J. Ding, T. Niu, R. Su, H. Wang, X. Zhang, Size dependent strengthening in high-strength nanotwinned Al/Ti multilayers, **Acta Materialia,** 175 (2019) 466-476.

10. C. Fan, Y. Chen, Jin Li, Jie Ding, H.Wang, X.Zhang, Defect evolution in heavy ion irradiated nanotwinned Cu with nanovoids, **Journal of Nuclear Materials, 496** (2017) 293-300.

11. C. FAN, JIN LI, ZHE FAN, H. WANG, and X. ZHANG, In Situ Studies on the Irradiation-Induced Twin Boundary-Defect Interactions in Cu, **Metall. Trans. A**, 2017, DOI: 10.1007/s11661-017-4293-5.

ENERGY DISSIPATION TO DEFECT EVOLUTION (EDDE)

K.L. More,[1] W.J. Weber,[2,1] D.S. Aidhy,[3] H. Bei,[1] M. Caro,[4] A. Correa,[5] T. Egami,[2,1] Y.N. Osetskiy,[1] I.M. Robertson,[6] G.D. Samolyuk,[1] G.M. Stocks,[1] L. Wang,[7] E. Zarkadoula,[1] F. Zhang,[1] and Y. Zhang,[1,2]

[1.] Oak Ridge National Laboratory (lead institution); [2.] University of Tennessee-Knoxville; [3.] University of Wyoming; [4.] Virginia Tech; [5.] Lawrence Livermore National Laboratory; [6.] University of Wisconsin-Madison; [7.] University of Michigan-Ann Arbor

Program Scope

EDDE's Mission is to develop a fundamental understanding of energy dissipation and defect evolution mechanisms in tunable concentrated solid solution alloys (CSAs) and ultimately to control defect evolution in a radiation environment. We hypothesize that modifying alloy chemical complexity will enable us to control defect production and dynamics at the early stage of damage formation and ultimately enhance late stage radiation-tolerance under extreme radiation conditions.

Recent Progress

The effort to develop metallic alloys with increased structural strength and improved radiation performance has focused on the incorporation of either solute elements or microstructural inhomogeneities to mitigate damage. Over a decade ago, complex concentrated alloys (CCAs) composed of multiple elements, all at high concentrations, have emerged that presents unforeseen opportunities for materials discovery. Among CCAs, single–phase concentrated solid-solution alloys (SP-CSAs) have drawn great attention. SP-CSAs are a unique group of CCAs, that have tunable chemical complexity, but lack microstructural inhomogeneities (e.g., nanoclusters, secondary phases, grain boundaries, interfaces). Single–phase high-entropy alloys (SP-HEAs), a subset of SP-CSAs, commonly contain five or more elemental species. An example of the tunable chemical complexity is specified in Fig. 1. A progression from elemental Ni to quinternary SP–CSAs—including the corresponding binary, ternary, and quaternary subsystems in Fig. 1 left—offers a powerful means to explore the influences of chemical complexity on energy dissipation and defect evolution. For example, the ability to tailor the chemical complexity of SP-SCAs can be used to control energy dissipation via energy carriers that transport charge, heat, and spin (Fig. 1 top center) and to modify the energy landscape (Fig. 1 bottom center) in order to control defect evolution resulting from kinetic energy transfer and mass transport during and after radiation events, e.g., collision cascades and defect migration. Manipulation of a material's ability to dissipate radiation energy can control the very early stages

of defect dynamics and subsequently impact the microstructural evolution under prolonged high-dose irradiation, (Fig. 1 right).

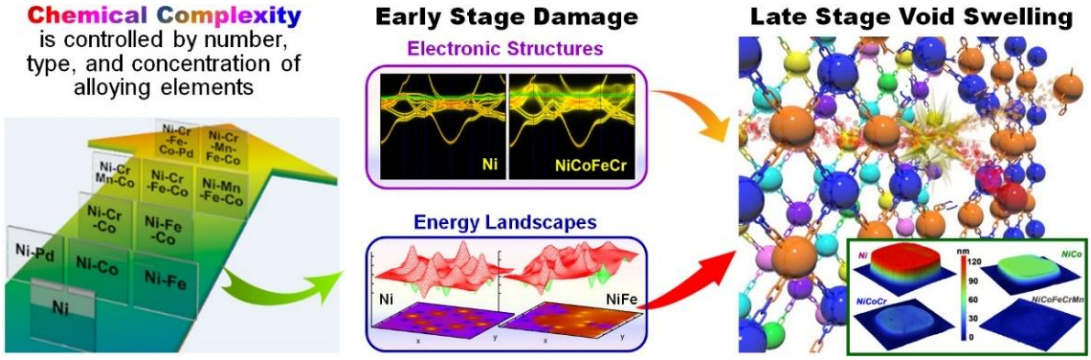

Fig. 1. SP-CSAs are alloys with tailored chemical complexity tunable via the intrinsic elemental disorder. The tunable chemical complexity (e.g., left: a subset of SP-CSAs) represents a powerful tool for dramatically modifying properties at the level of electrons and atoms (middle: electronic structure and energy landscapes in pure nickel and CSAs) and ultimately enhancing radiation tolerance (right: schematic drawing of an atomic collision and the radiation-induced swelling from step-height measurements).

To elucidate the impact of chemical complexity, we focus on SP-CSAs that do not have complications resulting from microstructural inhomogeneities. Recent progress is summarized from five aspects, starting at the level of electrons and atoms to microstructure progression.

1. Electronic effects—Electrons, magnons, and electronic structure affect energy transfer and defect properties. Knowledge of the electronic structure and magnetic characteristics of 3*d* SP-CSAs and their element-based temperature-dependent intrinsic properties has provided critical insights into energy dissipation processes. We show that modified electronic structure is due to magnetic frustration. Orders-of-magnitude reductions in electron mean free paths and localized electron-electron interactions are achieved by controlling chemical complexity [1]. Further study discovers the hidden Mn magnetic-moment disorder and a ground state in fcc NiCoMn to be the most energetically favorable in the presence of spin noncollinearity [2]. The *d* electron characteristics are shown to control the defect properties of 3*d* SP-CSAs. A substantial reduction in the capability to dissipate energy with increasing differences in the 3*d* electron count is demonstrated, and more localized heat is shown to enhance defect recombination. These findings suggest a path forward to study magnetism-controlled electronic structure and energy dissipation.

2. *Atomic effects—Complex energy landscapes significantly tailor defect migration and atomic transport.* In SP-CSAs, extensive chemical disorder and elemental diversity result in rich atomic-level inhomogeneities [3,4]. Defects experience a complex energy landscape that affects transport properties and defect behavior [5]. A wide distribution of defect energetics and chemically biased mass transport resulting from chemical disorder, as well as electronic effects on defect stabilization, are revealed. The high atomic-level stresses and modified atomic motion facilitate rapid annealing and prevent growth of extended defects.

3. *Coupled electronic and atomic effects—Pronounced ionization effects alter the atomic processes, modify defect dynamics, and affect microstructure evolution.* We show nonadiabatic interactions of electrons with ions. First principles and time-dependent DFT based codes [6,7] are developed to account for almost all the energy loss to target atoms. Closely coupled elastic and inelastic interactions under ion irradiation, in which the inelastic energy deposited to electrons significantly affects atomic processes, as the energy returned to the lattice via electron-phonon (*e-ph*) coupling enhances defect recombination and produces more isolated defects [8-10]. More pronounced coupling effects are observed in more complex SP-CSAs due to lower thermal conductivity and stronger *e-ph* coupling, compared with Ni or dilute alloys.

4. *Defect evolution—Local chemical disorder affects phase stability, radiation-induced segregation, and microstructure evolution.* Complex chemical complexity is shown as being a unique tool to intrinsically suppress damage evolution under irradiation. Just as dislocations are pinned by defects in conventional alloys, defects in SP-CSAs are pinned by chemical disorder. However, the pinning strength depends on the nature of the defects and chemical environment. The remarkably slow defect evolution and therefore delayed damage accumulation are attributed to the intrinsic "self-healing" property of chemically complexed SP-CSAs [11,12].

5. *Microstructure progression—Complex chemical disorder delays microstructure degradation, retards void swelling, and suppresses helium bubble growth.* Increasing complexity has been shown to significantly suppress void swelling, by two orders of magnitude, at elevated temperatures. Alloying with Pd effectively delay the growth of dislocation loops than alloying with Mn, and Pd-HEAs have shown stronger suppression of void growth at higher temperatures [13]. EDDE work provides clear evidence of chemical effects on He behavior in CSAs and evidence that strategies by tailoring chemical complexity can alter vacancy and interstitial migration energies, thereby suppressing bubble formation and growth during irradiation [14].

EDDE research in SP-CSAs has clearly shown that extreme chemical complexity is conceptually different from dilute solutes or nanoscale features. The current understanding of electronic and atomic effects, defect evolution, and microstructure progression suggests that radiation energy dissipates in SP-CSAs at different interaction strengths via the energy carriers (electrons, phonons, and magnons). Modification of electronic- and atomic-level heterogeneities and tailoring of atomic transport processes can be realized through tuning of the chemical complexity of SP-CSAs via the selection of elements and their concentrations. Alloy design should take the electronic, atomic, and coupled effects fully into account. Due to the high chemical complexity, CSAs offer wide ranges of variation in electronic and structural properties that allow several knobs to be turned in designing materials for the desired functionality.

Future Plans

Studies worldwide have shown that nano-scale features can significantly affect defect dynamics and microstructural evolution. Integration of above understanding from SP-CSAs with

knowledge on nano-scale features by adding low level of substitutional additions, nanoparticles, grain boundaries in CSAs allows further improvement of radiation performance, already demonstrated in our preliminary work on *Thermal Stability and Irradiation Response of Nanocrystalline CoCrCuFeNi HEA* [15]. We will continue the investigation on nanostructured CSAs under extreme environments. Tuning chemical complexity and controlling microstructural complexity represent a powerful tool to improve radiation performance and may ultimately lead to alloy design criteria to meet various application requirements.

References

[1] S. Mu, G.D. Samolyuk, S. Wimmer, M.C. Troparevsky, S. Khan, S. Mankovsky, H. Ebert, G.M. Stocks, *npj Comput. Mater.* **5**, 1 (2019).

[2] S. Mu, J. Yin, G.D. Samolyuk, S. Wimmer, Z. Pei, M. Eisenbach, S. Mankovsky, H. Ebert, G.M. Stocks, *Phys Rev. Materials* **3**, 014411 (2019).

[3] Y. Tong, K. Jin, H. Bei, J. Y. P. Ko, D. C. Pagan, Y. Zhang, F. X. Zhang, *Mater. Des.* **155**, 1–7 (2018).

[4] F.X. Zhang, Y. Tong, K. Jin, H. Bei, W.J. Weber, A. Huq, T. Lanzirott, M. Newville, D.C. Pagan, J.Y.P. Ko, a Y. Zhang, *Mater. Res. Lett.* **6**, 450 (2018).

[5] S. Zhao, Y. Osetsky, G.M. Stocks, Y. Zhang, *npj Comput. Mater.* **5**, 13 (2019).

[6] R. Ullah, E. Artacho, A. Correa, *Phys. Rev. Lett.* **121**, 116401 (2018).

[7] A. Tamm, M. Caro, A. Caro, G.D. Samolyuk, M. Klintenberg, A. Correa, *Phys. Rev. Lett.* **120**, 185501 (2018).

[8] A.A. Leino, G.D. Samolyuk, R. Sachan, F. Granberg, W.J. Weber, H. Bei, J. Lie, P. Zhai, Y. Zhang, *Acta Mater.* **151**, 191 (2018).

[9] R. Sachan, M.W. Ullah, M.F. Chisholm, J. Liu, P. Zhai, D. Schauries, P. Kluth, C. Trautman, H. Bei, W.J. Weber, Y. Zhang, *Mater. Des.* **150**, 1 (2018).

[10] N. Sellami, A. Debelle, M.W. Ullah, H.M. Christen, J.K. Keum, H. Bei, H. Xue, W.J. Weber, Y. Zhang, *Curr. Opin. Solid State Mater. Sci.* **23**,107 (2019).

[11] G. Velişa, E. Wendler, S. Zhao, K. Jin, H. Bei, W.J. Weber, Y. Zhang, *Mater. Res. Lett.* **6**, 136 (2018).

[12] T. Yang, C. Lu, G. Velisa, K. Jin, P. Xiu, M. Crespillo, Y. Zhang, H. Bei, L. Wang, *Acta Mater.* **151**, 159–168 (2018).

[13] C. Lu, T. Yang, K. Jin, G. Velisa, P. Xiu, M. Song, Q. Peng, F. Gao, Y. Zhang, H. Bei, W.J. Weber, L. Wang, *Mater. Res. Lett.* **6**, 584 (2018).

[14] Z. Fan, S. Zhao, K. Jin, D. Chen, Y. Osetskiy, Y. Wang, H. Bei, K. More, Y. Zhang, *Acta Mater.* **164**, 283 (2019).

[15] Y. Zhang, M. A. Tunes, M. L. Crespillo, F. Zhang, W. L. Boldman, P.D. Rack, L. Jiang, C. Xu, G. Greaves, S. E. Donnelly, L. Wang, and W. Weber, *Nanotechnology* **30**, 294004 (2019).

Publications (since 2018)

1. S. Zhao, Y. Zhang, and W.J. Weber, Stability of vacancy-type defect clusters in Ni based on first-principles and molecular dynamics simulations, *Scr. Mater.* **145**, 71-75 (2018).

2. G. Velişa, E. Wendler, S. Zhao, K. Jin, H. Bei, W.J. Weber, and Y. Zhang, Delayed damage accumulation by athermal suppression of defect production in concentrated solid solution alloys, *Mater. Res. Lett.* **6**, 136-141 (2018).

3. S. Zhao, T. Egami, G. M. Stocks, and Y. Zhang, Effect of d electrons on defect properties in NiCoCr and NiCoFeCr concentrated solid solution alloys, *Phys. Rev. Materials* **2**, 013602 (2018).

4. S. Shi, M.-R. He, K. Jin, H. Bei and I. Robertson, Evolution of ion damage at 773K in Ni-containing concentrated solid-solution alloys, *J. Nucl. Mater.* **501**, 132-142 (2018).

5. E. Zarkadoula, G. Samolyuk, and W. J. Weber, Effects of electronic excitation in 150 keV Ni ion irradiation of metallic systems, *AIP Advances* **8**, 015121 (2018).

6. D. Chakraborty, A. Harms, M. W. Ullah, W. J. Weber, and D. S. Aidhy, Effect of atomic order/disorder on vacancy clustering in concentrated NiFe alloys, *Comput. Mater. Sci.* **147**, 194-203 (2018).

7. K. Jin, C. Zhang, F. Zhang, and H. Bei, Influence of compositional complexity on interdiffusion in Ni-containing concentrated solid solution Alloys, *Mater. Res. Lett.* **6**, 293-299 (2018).

8. A.A. Leino, G. Samolyuk, R. Sachan, F. Granberg, W.J. Weber, H. Bei, J. Lie, P. Zhai, and Y. Zhang, GeV ion irradiation of NiFe and NiCo: Insights from MD simulations and experiments, *Acta Mater.* **151**, 191-200 (2018).

9. T. Yang, C. Lu, G. Velisa, K. Jin, P. Xiu, M. Crespillo, Y. Zhang, H. Bei, and L. Wang, Effect of alloying elements on defect evolution in Ni-20X binary alloys, *Acta Mater.* **151**, 159-168 (2018).

10. R. Sachan, M. W. Ullah, M. F. Chishol, J. Liu, P. Zhai, D. Schauries, P. Kluth, C. Trautman, H. Bei, W. J. Weber, and Y. Zhang, Radiation-induced extreme elastic and inelastic interactions in concentrated solid solutions, *Mater. Des.* **150**, 1-8 (2018).

11. M. Caro, A. Tamm, A. A. Correa, and A. Caro, On the local density dependence of electronic stopping of ions in solids, *J. Nucl. Matter.* **507**, 258-266 (2018).

12. A. Tamm, M. Caro, A. Caro, G. Samolyuk, M. Klintenberg, and A. Correa, Langevin dynamics with spatial correlations as a model for electron-phonon coupling, *Phys. Rev. Lett.* **120**, 185501 (2018).

13. K. Jin and H. Bei, Single-phase concentrated soild-solution alloys: Bridging intrinsic transport properties and irradiation resistance, *Front. Mater.* **5**, 26 (2018).

14. A. Correa, Calculating electronic stopping power in materials from first principles, *Comput. Mater. Sci.* **150**, 291-303 (2018).

15. F.X. Zhang, Y. Tong, K. Jin, H. Bei, W.J. Weber, A. Huq, T. Lanzirott, M. Newville, D.C. Pagan, J. Y. P. Ko, and Y. Zhang, Chemical complexity induced local structure distortion in NiCoFeMnCr high entropy alloy, *Mater. Res. Lett.* **6**, 450-455 (2018).

16. Y. Tong, K. Jin, H. Bei, J. Y. P. Ko, D. C. Pagan, Y. Zhang, F. X. Zhang, Local lattice distortion in NiCoCr, FeCoNiCr and FeCoNiCrMn concentrated alloys investigated by synchrotron X-ray diffraction, *Mater. Des.* **155**, 1-7 (2018).

17. F. X. Zhang, M. W. Ullah, S. Zhao, K. Jin, Y. Tong, G. Velisa, H. Xue, H. Bei, R. Huang, C. Park, W. J. Weber, and Y. Zhang, Local structure of NiPd solid solution alloys and its response to ion irradiation, *J. Alloy Compd.* **755**, 242-250 (2018).

18. C. Lu, T. Yang, L. Niu, Q. Peng, K. Jin, M. L. Crespillo, G. Velisa, H. Xue, F. Zhang, P. Xiu, Y. Zhang, F. Gao, H. Bei, W. J. Weber, and L. Wang, Interstitial migration behavior and defect evolution in ion irradiated pure nickel and Ni-xFe binary alloys, *J. Nucl. Mater.* **509**, 237-244 (2018).

19. Y. N. Osetskiy, L. Beland, A. Barashev, and Y. Zhang, On the existence and origin of sluggish diffusion in chemically disordered concentrated alloys, *Curr. Opin. Solid State Mater. Sci.* 22, 65-74 (2018).

20. G. Bonny, D. Chakraboty, S. Pandey, A. Manzoor, N. Castin, S. Phillpot and D. S. Aidhy, "Classical interatomic potential for quaternary Ni-Fe-Cr-Pd solid solution alloys," Modelling Simul. Mater. Sci. Eng. 26, 065014 (2018).

21. Y. Tong, S. Zhao, K. Jin, H. Bei, Y. J. P. Ko, D. C. Pagan, Y. Zhang, and F. X. Zhang,"A comparison study of local lattice distortion in $Ni_{80}Pd_{20}$ binary alloy and FeCoNiCrPd high-entropy alloy, *Scr. Mater.* **156**, 14-18 (2018).

22. A. Manzoor, S. Pandey, D. Chakraborty, S. Phillpot and D. S. Aidhy, Entropy contributions to phase stability in binary random solid solutions, *npj Comput. Mater.* **4**, 47 (2018).

23. B. Lu, T. Yang, K. Jin, G. Velisa, P. Xiu, M. Song, Q. Peng, F. Gao, Y. Zhang, H. Bei, W. J. Weber, and L. Wang, Enhanced void swelling in NiCoFeCrPd high-entropy alloy by indentation-induced dislocations, *Mater. Res. Lett.* **6**, 584-591 (2018).

24. T. Yang, C. Li, S. J. Zinkle, S. Zhao, H. Bei, and Y. Zhang, Irradiation responses and defect behavior of single-phase concentrated solid solution alloys, *J. Mater. Res.* **33**, 3077-3091 (2018).

25. G.D. Samolyuk, S. Mu, A.F. May, B.C. Sales, S. Wimmer, S. Mankovsky, H. Ebert, and G.M. Stocks, Temperature dependent electronic transport in concentrated solid solutions of the 3d-transition metals Ni, Fe, Co and Cr from first principles, *Phys. Rev. B* **98**, 165141 (2018).

26. Y. Tong, G. Velisa, S. Zhao, W. Guo, T. Yang, K. Jin, C. Lu, H. Bei, J. Y. P. Ko, D. C. Pagan, Y. Zhang, L. Wang, F. X. Zhang, Evolution of local lattice distortion under irradiation in medium- and high-entropy alloys, *Mater.* **2**, 73 – 81 (2018).

27. B. Kombaiah, K. Jin, H. Bei, P. Edmondson, and Y. Zhang, Phase stability of single phase $Al_{0.12}$CrNiFeCo high entropy alloy upon irradiation, *Mater. Des.* **160**, 1208-1216 (2018).

28. E.E. Quashie and A.A. Correa, Electronic stopping power of protons and alpha particles in nickel, *Phys. Rev. B* **98**, 235122 (2018).

29. Z. Fan, S. Zhao, K. Jin, D. Chen, Y. Osetskiy, Y. Wang, H. Bei, K. More and Y. Zhang, Helium irradiated cavity formation and defect energetics in Ni-based binary single-phase concentrated solid solution alloys, *Acta Mater.* **164**, 283-292 (2019).

30. T. Yang, C. Lu, G. Velisa, K. Jin, P. Xiu, Y. Zhang, H. Bei and L. Wang, Influence of irradiation temperature on void swelling in NiCoFeCrMn and NiCoFeCrPd, *Scripta Mater.* **158**, 57-61, (2019).

31. X. Wang, K. Jin, D. Chen, H. Bei, Y. Wang, W.J. Weber, Y. Zhang, and K. L. More, Effects of Fe concentration on helium bubble formation in NiFex single-phase concentrated solid solutions alloys, *Materialia* **5**, 100183 (2019).

32. F. Zhang, Y. Tong, K. Jin, H. Bei, W. Weber and Y. Zhang, Lattice distortion and phase stability of Pd-doped NiCoFeCr solid-solution alloys, *Entropy* **20**, 900 (2018).

33. B. Kombaiah, P. D. Edmondson, Y. Wang, L. A. Boatner, and Y. Zhang, Mechanisms of radiation-induced segregation around He bubbles in a Fe-Cr-Ni crystal, *J. Nucl. Mater.* **514**, 139 - 147 (2019).

34. S. Zhao, Y. Osetsky, G. M. Stocks, and Y. Zhang, Local-environment dependence of stacking fault energy in concentrated solid–solution alloys, *npj Comput. Mater.* **5**, 13 (2019).

35. S. Mu, G. D. Samolyuk, S. Wimmer, M. C. Troparevsky, S. Khan, S. Mankovsky, H. Ebert, G. M. Stocks, "Uncovering electron scattering mechanisms in NiFeCoCrMn derived concentrated solid solution and high entropy alloys, *npj Comput. Mater.* **5**, 1 (2019).

36. S. Mu, J. Yin, G. D. Samolyuk, S. Wimmer, Z. Pei, M. Eisenbach, S. Mankovsky, H. Ebert and G. M. Stocks, Hidden Mn magnetic-moment disorder and its influence on the physical properties of medium-entropy NiCoMn solid solution alloys, *Phys Rev. Materials* **3**, 014411 (2019).

37. K. Jin, Y. Xia, M. Crespillo, H. Xue, Y. Zhang, Y. F. Gao, and H. Bei, Quantifying early stage irradiation damage from nanoindentation pop-in tests, *Scripta Mater.* **157**, 49-53 (2018).

38. R. Ullah, E. Artacho, and A. Correa., Core electrons in the electronic stopping of heavy ions, *Phys. Rev. Lett.* 121, 116401 (2018).

39. Y. N. Osetsky, A. Barashev and Y. Zhang, On the mobility of defect clusters and their effect on microstructure evolution in fcc Ni under irradiation, *Materialia* **4**, 139-146 (2018).

40. M. He, C. Wu, M. V. Shugaev, G. D. Samolyuk, and L. V. Zhigilei, Computational study of short-pulse laser-induced generation of crystal defects in Ni-based single-phase binary solid-solution alloys, *J. Phys. Chem. C* **123**, 2202-2215 (2019).

41. K. Jin, G. Velisa, H. Xue, T. Yang, H. Bei, W. J. Weber, L. Wang and Y. Zhang, Channeling analysis in studying ion irradiation damage in materials containing various types of defects, *J. Nucl. Mater.* **517**, 9-16 (2019).

42. Z. Fan, G. Velisa, K. Jin, M. Crespillo, H. Bei, W. Weber, and Y. Zhang, Temperature-dependent defect accumulation and evolution in Ni-irradiated NiFe concentrated solid-solution alloy, *J. Nucl. Mater.* **519**, 1-9 (2019).

43. E. Zarkadoula, G. Samolyuk, and W. J. Weber, Effects of electron-phonon coupling and electronic thermal conductivity in high energy molecular dynamics simulations of irradiation cascades in nickel, *Comput. Mater. Sci.* **162**, 156-161 (2019).

44. M. A. Tunes, V. M. Vishnyakov, O. Camara, G. Greaves, P. D. Edmondson, Y. Zhang and S.E. Donnelly, A candidate accident tolerant fuel system based on a highly concentrated alloy thin film, *Mater. Today Energy* **12**, 356-362 (2019).

45. M-R He, S. Wang, K. Jin, H. Bei, K. Yasuda, S. Matsumura, K. Higashida, and I. M. Robertson, A comparative characterization of defect structure in NiCo and NiFe equimolar solid solution alloys under in situ electron irradiation, *Scripta Mater.* **166**, 96–101 (2019).

46. M.A. Tunes, H. Le, G. Greaves, C.G. Schön, H. Bei, Y. Zhang, P. Edmondson, S. Donnelly, Investigating sluggish diffusion in a concentrated solid solution alloy using ion irradiation with in situ TEM, *Intermetallics* 110, 106461 (2019).

47. M. Caro, A. Tamm, A. A. Correa, and A. Caro, Role of electrons in collision cascades in solids. Part I: Dissipative model, *Phys. Rev. B* **99**, 174302 (2019).

48. A. Tamm, M. Caro, A. Caro, and A. A. Correa, "Role of electrons in collision cascades in solids. Part II: Molecular dynamics", *Phys. Rev. B* **99**, 174301 (2019).

49. Y. Zhang, M. A. Tunes, M. L. Crespillo, F. Zhang, W. L. Boldman, P.D. Rack, L. Jiang, C. Xu, G. Greaves, S. E. Donnelly, L. Wang, and W. Weber, Thermal Stability and Irradiation Response of Nanocrystalline CoCrCuFeNi High-entropy Alloy, *Nanotechnology* **30**, 294004 (2019).

50. S. Zhao, Y. Osetsky, and Y. Zhang, Frenkel defect recombination in Ni and Ni–containing concentrated solid–solution alloys, *Acta Mater.* **173**, 184-194 (2019).

51. C. Lu, T.-N. Yang, K. Jin, G. Velisa, P. Xiu, Q. Peng, F. Gao, Y. Zhang, H. Bei, W.J. Weber, L.Wang, Irradiation effects of medium-entropy alloy NiCoCr with and without pre-indentation, *J. Nucl. Mater.* **524**, 60-66 (2019).

52. A. Barashev, Y. N. Osetsky, H. Bei, C. Lu, L. Wang, and Y. Zhang, Chemically-Biased Diffusion and Solute Segregation Impedes Void Growth in Irradiated Ni-Fe Alloys, *Curr. Opin. Solid State Mater. Sci.* **23**, 92-100 (2019).

53. N. Sellami, A. Debelle, M. W. Ullah, H. M. Christen, J. K. Keum, H. Bei, H. Xue, W. J. Weber, and Y. Zhang, Effect of electronic energy dissipation on strain relaxation in irradiated concentrated solid solution alloys, *Curr. Opin. Solid State Mater. Sci.* **23**, 107–115 (2019).

54. S. Zhao, Y.Osetsky, and Y. Zhang, Diffusion of point defects in ordered and disordered Ni-Fe alloys, *Journal of Alloys and Compounds*, accepted.

55. R.W. Harrison, G. Greaves, H. Le, H. Bei, Y. Zhang, S.E. Donnelly, Chemical effects on He bubble superlattice formation in high entropy alloys, *Current Opinion in Solid State & Materials Science*,(2019) in press. https://doi.org/10.1016/j.cossms.2019.07.001.

56. X. Wang, C.M. Bar, K. Jin, H. Bei, K. Hattar, W.J. Weber, Y. Zhang, K.L. More, Defect evolution in Ni and NiCoCr by in situ 2.8 MeV Au irradiation, *J. Nucl. Mater.* (2019), in press. https://doi:10.1016/j.jnucmat.2019.05.026.

57. W.J. Weber and Y. Zhang, Predicting damage production in monoatomic and polyatomic targets using Stopping and Range of Ions in Matter code: Challenges and Recommendations has been accepted for publication in *Curr. Opin. Solid State Mater. Sci.* (2019), in press. https://doi.org/10.1016/j.cossms.2019.06.001.

Author Index

Participant List

Last Name	Organization	Email
Agnew, Sean	University of Virginia	agnew@virginia.edu
Aifantis, Katerina	University of Florida	kaifantis@ufl.edu
Aitkaliyeva, Assel	University of Florida	aitkaliyeva@mse.ufl.edu
Allison, John	University of Michigan	johnea@umich.edu
Anderson, Peter	The Ohio State University	anderson.1@osu.edu
Asle Zaeem, Mohsen	Colorado School of Mines	zaeem@mines.edu
Athanasiou, Christos	Brown University	christos_edouardos_athanasiou@brown.edu
Baker, Ian	Dartmouth College	marge.heggison@dartmouth.edu
Balk, Thomas	University of Kentucky	john.balk@uky.edu
Bellon, Pascal	University of Illinois, Urbana-Champaign	bellon@illinois.edu
Beyerlein, Irene	University of California, Santa Barbara	irene.beyerlein@gmail.com
Bhattacharyya, Jishnu	University of Virginia	jjb4cp@virginia.edu
Boyce, Brad	Sandia National Laboratories	blboyce@sandia.gov
Branicio, Paulo	University of Southern California	branicio@usc.edu
Byun, Thak Sang	Pacific Northwest National Laboratory	thaksang.byun@pnnl.gov
Cai, Wei	Stanford University	caiwei@stanford.edu
Capolungo, Laurent	Los Alamos National Laboratory	laurent@lanl.gov
Chi, Yen-Ting	Massachusetts Institute of Technology	yenting@mit.edu
Dauskardt, Reinhold	Stanford University	dauskardt@stanford.edu
Ding, Jun	Lawrence Berkeley National Laboratory	ding@lbl.gov
Dingreville, Remi	Sandia National Laboratories	rdingre@sandia.gov
Eisenlohr, Philip	Michigan State University	eisenlohr@egr.msu.edu
El-Azab, Anter	Purdue University	aelazab@purdue.edu
Farkas, Diana	Virginia Tech	diana@vt.edu
Fullwood, David	Brigham Young University	dfullwood@byu.edu
Gan, Jian	Idaho National Laboratory	Jian.Gan@inl.gov
Gao, Yipeng	Idaho National Laboratory	yipeng.gao@inl.gov
George, Easo	Oak Ridge National Laboratory	georgeep@ornl.gov
Gersten, Bonnie	US Department of Energy	bonnie.gersten@science.doe.gov
Ghazisaeidi, Maryam	The Ohio State University	ghazisaeidi.1@osu.edu
Han, Songyang	Michigan State University	hansong7@msu.edu
Hemker, Kevin	Johns Hopkins University	hemker@jhu.edu
Kacher, Joshua	Georgia Institute of Technology	josh.kacher@mse.gatech.edu

Kerch, Helen	US Department of Energy	helen.kerch@science.doe.gov
Kim, Seong H.	Pennsylvania State University	shk10@psu.edu
Kreller, Cortney	Los Alamos National Laboratory	ckreller@lanl.gov
Krogstad, Jessica	University of Illinois, Urbana-Champaign	jakrogst@illinois.edu
Kube, Sebastian	Yale University	Sebastian.Kube@yale.edu
Kwong, Anthony	California Institute of Technology	akwong@caltech.edu
Lee, Seok-Woo	University of Connecticut	seok-woo.lee@uconn.edu
Li, Lin	University of Alabama	lin.li@eng.ua.edu
Li, Qizhen	Washington State University	qizhen.li@wsu.edu
Li, Qun	University of Illinois, Urbana-Champaign	qunli2@illinois.edu
Lou, Jun	Rice University	jlou@rice.edu
Madden, Nathan	University of Illinois, Urbana-Champaign	njmadde2@illinois.edu
Mariyappan, Arul Kumar	Los Alamos National Laboratory	marulkr@lanl.gov
Miller, Matthew	Cornell University	mpm4@cornell.edu
Misra, Amit	University of Michigan	amitmis@umich.edu
Nygren, Kelly	Cornell University	k.nygren@cornell.edu
Osmundsen, Rachel	Thayer School of Engineering at Dartmouth	Rachel.D.Osmundsen.TH@dartmouth.edu
Pederson, Mark	US Department of Energy	mark.pederson@science.doe.gov
Pierron, Olivier	Georgia Institute of Technology	olivier.pierron@me.gatech.edu
Qi, Liang	University of Michigan	qiliang@umich.edu
Riedo, Elisa	New York University	elisa.riedo@nyu.edu
Ritchie, Robert	Lawrence Berkeley National Laboratory	roritchie@lbl.gov
Rollett, Anthony	Carnegie Mellon University	rollett@andrew.cmu.edu
Rosso, Kevin	Pacific Northwest National Laboratory	kevin.rosso@pnnl.gov
Rupert, Timothy	University of California, Irvine	trupert@uci.edu
Sansoz, Frederic	University of Vermont	frederic.sansoz@uvm.edu
Schreiber, Daniel	Pacific Northwest National Laboratory	daniel.schreiber@pnnl.gov
Schuh, Christopher	Massachusetts Institute of Technology	schuh@mit.edu
Shao, Lin	Texas A&M University	lshao@tamu.edu
Sheldon, Brian	Brown University	brian_sheldon@brown.edu
Sieradzki, Karl	Arizona State University	Karl.Sieradzki@asu.edu
Strachan, Alejandro	Purdue University	strachan@purdue.edu
Szlufarska, Izabela	University of Wisconsin	szlufarska@wisc.edu
Taheri, Mitra	Johns Hopkins University	mtaheri4@jhu.edu
Thompson, Gregory	University of Alabama	mrobinso@bama.ua.edu

Titus, Michael	Purdue University	titus9@purdue.edu
Uberuaga, Blas	Los Alamos National Laboratory	blas@lanl.gov
Van Vliet, Krystyn	Massachusetts Institute of Technology	krystyn@mit.edu
Vetrano, John	US Department of Energy	john.vetrano@science.doe.gov
Wagoner, Robert	The Ohio State University	wagoner.2@osu.edu
Wang, Jian	University of Nebraska, Lincoln	jianwang@unl.edu
Weber, William	University of Tennessee	wjweber@utk.edu
Wharry, Janelle	Purdue University	jwharry@purdue.edu
Xie, Yu Xuan Kelvin	Texas A&M University	kelvin_xie@tamu.edu
Xu, Haixuan	University of Tennessee, Knoxville	xhx@utk.edu
Yang, Ying	Oak Ridge National Laboratory	yyangtan@gmail.com
Zhang, Xinghang	Purdue University	xzhang98@purdue.edu
Zhang, Yanwen	Oak Ridge National Laboratory	zhangy1@ornl.gov